This is to certify that the
dissertation entitled

SIMULTANEOUS WALL-PRESSURE AND VELOCITY MEASUREMENTS IN THE FLOW FIELD DOWNSTREAM OF AN AXISYMMETRIC BACKWARD-FACING STEP

presented by

LAURA MICHELE HUDY

has been accepted towards fulfillment
of the requirements for the

Ph.D. degree in MECHANICAL ENGINEERING

Ahmed M. Naguib
Major Professor's Signature

12/14/2005
Date

MSU is an Affirmative Action/Equal Opportunity Institution

SIMULTANEOUS WALL-PRESSURE AND VELOCITY MEASUREMENTS
IN THE FLOW FIELD DOWNSTREAM OF AN AXISYMMETRIC
BACKWARD-FACING STEP

By

Laura Michele Hudy

A DISSERTATION

Submitted to
Michigan State University
in partial fulfillment of the requirements
for the degree of

DOCTOR OF PHILOSOPHY

Department of Mechanical Engineering

2005

ABSTRACT

SIMULTANEOUS WALL-PRESSURE AND VELOCITY MEASUREMENTS IN THE FLOW FIELD DOWNSTREAM OF AN AXISYMMETRIC BACKWARD-FACING STEP

By

Laura Michele Hudy

Surface-pressure and planar, Particle Image Velocimetry measurements were obtained in the separating/reattaching flow region downstream of an axisymmetric, backward-facing step. Data were acquired for a two-dimensional (2D) separating boundary layer at four different Reynolds numbers based on step height (Re_h), spanning 5900-18500. The experimental set-up consisted of an array of 32 flush-mounted microphones beneath the separation bubble. These microphones were used to detect the wall-pressure signature that was acquired *simultaneously* with the PIV measurements of the velocity field above the surface.

The surface-pressure and PIV measurements were used to characterize the wall-pressure distribution and the flow field in terms of Reynolds number dependencies. Statistics from these measurements were consistent with findings in the literature. In addition, the evolution of coherent structures in the flow field was investigated using proper orthogonal decomposition (POD) and multi-point, linear, stochastic estimation (LSE). POD was used to determine the dominant convective modes in the pressure signature. Two convective modes were found to be responsible for 60% of the energy of the pressure signature. Multi-point LSE was used to estimate the dominant flow structures above the wall from convective-mode, wall-pressure signatures over a series of

time steps. It was found that a large-scale, coherent structure develops in place at approximately half the reattachment distance. Once this structure reaches a height equivalent to the step, it sheds and accelerates downstream. This growth in place and then shedding resembles a wake mode, which describes the flow field downstream of bluff bodies. The wake mode has been observed in numerical simulation studies of long cavities and backward-facing steps, where two dimensionality is controllable. The present study shows for the first time evidence for the existence of a wake mode in an experimental study of a backward-facing step. This is believed to be related to the good two dimensionality (i.e., axisymmetry) of the test geometry and the ability to track the temporal-evolution of structural features through LSE. Finally, it was observed that, unlike behind bluff bodies, the wake mode in the back-step flow is intermittent, switching on/off in an apparently random manner.

DEDICATION

To my parents,

for their unwavering support, dedication, and love

ACKNOWLEDGEMENTS

I would like to acknowledge support for this research project from the National Science Foundation (Contract #CTS0116907) and supplemental support from the Office of Naval Research. I would also like to acknowledge the support of William (Tony) M. Humphreys and Scott Bartram at NASA Langley Research Center in Hampton, Virginia. Both Tony and Scott provided their expertise and gave countless hours towards the successful completion of this project. I am forever grateful for their contribution.

On a personal note, there are several individuals that I must acknowledge for the role they played in my 11 years at Michigan State University. First, I must take a moment to reflect on undergrad. Thank you to my freshman roommate, Eve, who patiently listened to me (for hours) regarding whether I should change my major from Journalism to Mechanical Engineering and to Jil, for introducing me to the Society of Women Engineers. I must also thank my friend, Kristine, for answering all the "911-phone-calls" regarding classes. Thank you to my friend, Judy, for acting as a sounding board all these years as I worked to meet the challenges of both undergrad and grad school. Finally, I must mention my friends for making the time outside of school fun including Kate, Brad, Mark, Matt, Brady, Scott, Floria, Correna, Heather, and KJ. From soccer games to tailgating, Florida to Aachen, themed parties to Thanksgiving dinners, Albert to Elizabeth Street, the fun never stopped! Thanks for the memories!

As for grad school, I need to start by thanking Dr. Naguib, who has been a wonderful teacher, mentor, and friend. I have enjoyed working with Dr. Naguib over the past six years and I could not imagine going through this degree with any other advisor.

Dr. Naguib is the reason I stayed at MSU for my Ph.D. and I could not be happier with my decision. You have changed my life, Doc, and I am forever grateful to you.

Thank you to several professors at MSU including Dr. Radcliffe, Dr. Pierre, Dr. Shih, Dr. Koochesfahani, Dr. Zhuang, and Dr. Foss for their input regarding my research and their support during my graduate career. I would also like to extend my appreciation to Jill for all our wonderful chats and to Roy and Mike for their help in the machine shop.

A thank you must also be given to my friends at both EB and RCE. Thank you to Scott for his guidance regarding classes, research, and especially presenting at conferences. Also, thank you to the individuals of the Flow Physics and Controls Lab including Yongxiang, Mohamed, Chad, Tony, and Barry for helping me take data and for your company throughout the years. A special thanks goes out to Al and Chee who I have known since undergrad and who have offered so much peer support over the years.

Outside of the academic world, I have spent countless hours on the soccer field with Melinda, Parks, H, Cara, Sarah, Shannon, and Nat. I will miss playing the game with "the ladies of soccer." Also, here's to the Art's soccer team, which has had many faces over the years and many more shoopers. Oh and I cannot forget the 2002 MSU Floor Hockey Champion Intramural team Jedi Mind Trick – wisdom beats age any day!

A special thanks to my roommates in grad school: Shannon, Nikki, and Sarah. Woohoo! You girls rock! We have had a lot of fun over the years…may it continue even though we are miles apart. Big Squeeze and Sweet Cheeks - here's to the Hog Wild Roadhouse and parking tickets. And let us not forget game nights (Gestures, anyone?) at Wardcliff, Wardcliff West and Wardcliff West-North. I also must mention the MSU

Spartan basketball games and loyal fans: Brad, Kate, Drew, Nikki, Chee, and Kristen. I had a blast yelling "Go Spartans" with y'all!!!

I must to extend a very special thank you to three wonderful people in my life. Brad, all I can say is THANK YOU for lunch. Kate, we have been friends all my years at MSU. You are the "bestest" of best friends! I cannot thank you enough for all you have done for me and for all the fun times we have had together. And Barry, your support this past year has been amazing. Thank you for always being there for me.

Next to last, I need to recognize my extended family, especially my Grandma. Grandma always knows how to make you smile no matter the type of day. In addition, thank you to the family members of the "Spartan Tailgating Crew" who started tailgating and attending MSU football games back in the Fall of 1994. Eleven years later the same group is still cheering at Spartan football games. Some of my greatest memories come from standing with them on cold fall nights under the lights at Spartan Stadium. I would like to say a special thanks to my Uncle Tom for keeping it fun during college and for all his study advice. Also, thank you to my cousin, Kristen, for allowing me to make dinners for her over the years at MSU. And to all my extended family on both sides, thank you!

Finally, I must thank my immediate family. First, thank you to my brother Dave, for always bringing me back down to earth and for serving in the United States Navy. I am so proud of him. Last, but not least, I must thank my mom and my dad. My dad encouraged me to go into engineering and I thank him for his vision. My parents have always been my number one fan and they have given so much to me over the years. For their love and devotion, I dedicate this work to them. Thank you, Mom and Dad!

TABLE OF CONTENTS

LIST OF TABLES

LIST OF FIGURES

LIST OF SYMBOLS

Symbol	Definition
A_u	linear stochastic estimation coefficient term for streamwise velocity component
A_v	linear stochastic estimation coefficient term for normal velocity component
$A_{u,quad}$	linear stochastic estimation coefficient term for streamwise velocity component (in quadratic estimation)
$A_{v,quad}$	linear stochastic estimation coefficient term for normal velocity component (in quadratic estimation)
a	amplitude coefficient for POD mode functions
B_u	quadratic stochastic estimation coefficient term for streamwise velocity component
B_v	quadratic stochastic estimation coefficient term for normal velocity component
b	intercept of the least squares line
C_f	skin-friction coefficient = $2(u_\tau/U_\infty)^2$
C_p	mean pressure coefficient
$C_{p'}$	RMS fluctuating pressure coefficient
c	intercept of the mean-velocity distribution in the log region, when plotted on semi-log scale
$\vec{d}$	average displacement vector over a PIV interrogation cell
E	expectation or average of the square of the error
e	error between the estimated and measured fluctuating velocity components
f	frequency [Hz]
H	total height of the fence

Symbol	Definition
H_{12}	boundary layer shape factor = δ^{*}/θ
h	step height
i_{width}	image width
k	Von Karman constant
k_t	time-delay index in correlation function
k_x	streamwise wavenumber
m	camera magnification for PIV images
m_s	slope
N	total number of points measured in the time record
n	time shift, or delay
o_{width}	object width
p	mean surface-pressure
p'	fluctuating surface-pressure
p'_{RMS}	root mean square value of p'
p_r	reference mean pressure
p_s	surface mean pressure
Re	Reynolds number
Re_h	Reynolds number based on step height
Re_θ	Reynolds number based on momentum thickness thickness of the boundary layer at separation
$R_{p'p'}$	normalized auto-correlation function
$R_{u'p'}$	normalized cross-correlation between streamwise velocity and surface-pressure

Symbol	Definition
$R_{v'p'}$	normalized cross-correlation between normal velocity and surface-pressure
$r_{p'p'}$	discrete-time auto-correlation function
ΔT	time delay between light pulses from the two different lasers
t	time
U	mean streamwise velocity component
U_c	mean convection velocity
U_∞	freestream velocity
U^+	non-dimensional mean streamwise velocity component = U/u_τ
u	streamwise velocity component
u'	fluctuating streamwise velocity component
u'_{RMS}	root mean square value of u'
u_τ	wall-friction velocity = $(\tau_w/\rho)^{1/2}$
$\overline{u'v'}$	Reynolds shear stress
V	mean normal velocity component
V_{cc}	power source voltage for the microphones
$\vec{V}$	velocity vector field
v	normal velocity component
v'	fluctuating normal velocity component
v'_{RMS}	root mean square value of v'
x	streamwise coordinate
x_r	reattachment distance
y	wall-normal coordinate

Symbol	Definition
y^+	non-dimensional wall-normal coordinate = yu_τ/ν
z	spanwise coordinate
δ	boundary layer thickness
δ^*	displacement thickness of boundary layer
Γ	circulation
ϕ	azimuthal angle
ϕ_I	mode functions for i^{th} POD mode
$\phi_{p'p'}$	power spectrum of p'
λ	wavelength
ν	kinematic viscosity
θ	momentum thickness of boundary layer
ρ	fluid density
τ	time shift
τ_w	average (mean) wall-shear stress
ω_z	out-of-plane vorticity component
$\bar{\omega}$	vorticity vector
ξ_{ij}	strain rate tensor field
ξ_{xy}	in-plane shear strain component
ξ_{zz}	out-of-plane linear strain component
ξ_{xx}	in-plane linear strain component in streamwise direction
ξ_{yy}	in-plane linear strain component in normal direction

1 Introduction

1.1 Background

One important class of fluid flow that is encountered frequently in engineering applications is separated flows. These applications include flow over airplane wings, in dump combustors, and through turbines and compressors, to mention a few. Extensive research has been done in the area of separated flows in order to understand the dominant flow structures, or flow motions, in the separated shear layer and the general characteristics of the flow field. Some of the research has been focused on understanding the flow generation mechanisms of wall-pressure fluctuations, which is important in engineering applications involving flow-induced noise/vibrations and flow-structure interaction. The ability to understand these and other flow physics concerning separated flows can lead to the development of simplified models for prediction of wall-pressure fluctuations and the implementation of active or passive flow control techniques for optimizing the flow state above the surface and/or minimizing the adverse flow effects on the wall.

An example of a canonical separated-flow configuration is the backward-facing step (BFS) geometry shown in Figure 1.1 along with the average flow pattern above the surface. This flow is frequently adopted for the purpose of research studies as an idealization of real, separated-flow problems. Generally speaking, flow separation occurs where the flow detaches from the boundary of a solid surface, which is at the step edge in the case of the BFS. When the boundary layer separates, it forms a shear layer that may reattach along the same surface depending on the length and contour of the geometry. Beneath the shear layer is a primary and a secondary, recirculation region. Beyond the mean reattachment point, the reattached boundary layer begins to "relax" as it redevelops into an equilibrium turbulent boundary layer for a sufficiently long surface.

The generally accepted view of the BFS flow field in the literature is that large-scale, turbulent structures develop in the highly-unstable, separated shear layer and grow in size and strength as they convect downstream towards reattachment. As will become clear in Chapters 6 and 7, the findings in this study indicate, in agreement with a handful existing studies, an alternate view. Specifically, it will be shown that the large-scale turbulent structures found in the separation zone grow in size and strength while stationary at about half of the reattachment length before shedding from the shear layer and accelerating downstream.

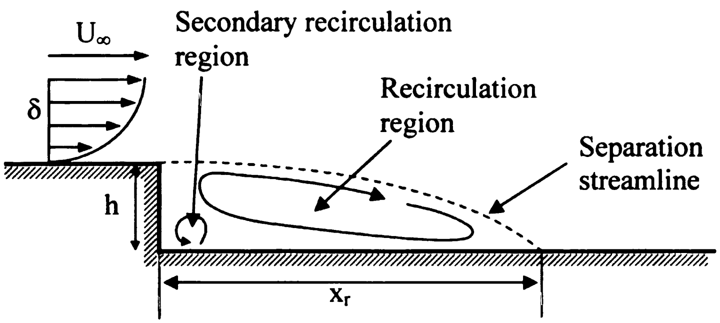

Figure 1.1 Example of separated flow in a backward-facing step

Most of the separating/reattaching flow research to date has been on "2D flows" in *planar* canonical geometries such as a backward-facing step, a splitter plate, or a splitter-plate-with-fence. Classic studies of these geometries include, but are not exclusive to, Eaton and Johnston[1] (BFS), Cherry *et al.*[2] (splitter plate), Castro and Haque[3] (splitter-plate-with-fence), and many others. In these studies, mean flow two dimensionality was assumed due to the large aspect ratio (width of the model divided by the step height). Brederode and Bradshaw[4] showed that three-dimensional effects along the centerline in a planar BFS may be neglected by ensuring a model aspect ratio greater than ten. However, Ruderich and Fernholz[5] provide striking evidence of strong secondary flow patterns within the recirculation region as well as near reattachment using oil-flow pictures in a splitter-plate/fence configuration, which has similar flow characteristics to a BFS. This was true for aspect ratios as high as 22, even with the utilization of end plates. More recently, in Hudy[6], a large aspect ratio of 36 was used for a splitter-plate-with-fence model. It was found that the spanwise distribution of the surface pressure varied between 10 – 30% from the centerline values, suggesting that the flow field was inherently three dimensional. Thus, although three dimensionality effects may be reduced along the centerline of planar separated flow models, the flow exhibits large variation in the spanwise direction, which could substantially influence the flow features observed along the centerline.

The current research project investigates the separating/reattaching flow over an axisymmetric, backward-facing step (BFS). The general, mean-flow characteristics surrounding the axisymmetric BFS are similar to those seen in a planar BFS, except in the axisymmetric BFS the mean flow characteristics are the same in every azimuthal plane. This invariance in the azimuthal direction eliminates the three-dimensional effects that are typically seen in planar BFS and improves the quality of the two dimensionality along the measurement plane. Figure 1.1 shows the ideal two-dimensional, mean-flow field downstream of a planar BFS, which is the same as seen in a single, azimuthal plane downstream of the axisymmetric BFS. An infinite number of these azimuthal planes make up the axisymmetric geometry; and, thus, the mean flow characteristics are the same all the way around the cylindrical model. Based on this explanation and for clarification purposes, the axisymmetric flow developing around the step will frequently be referred to as two dimensional (2D) in this document since the average flow field in the plane perpendicular to the wall and parallel to the freestream velocity is invariant in one of the three spatial dimensions, i.e., the azimuthal direction.

One study that did investigate the flow field in an axisymmetric backward-facing step is Li and Naguib[7]. In 2005, the authors employed the same axisymmetric BFS model used in the present study. Li and Naguib[7] measured the wall-shear stress at different Reynolds numbers using a high-frequency oscillating hot-wire sensor. The sensor was embedded in the wall of the model at different streamwise positions spanning 0.3 to 10 step heights downstream of the step edge and measured both skin friction magnitude and direction. Data were acquired within the viscous sublayer at a height of 97 μm above the wall, which corresponds to $y^+ = 3.1$ ($y^+ = yu_\tau/\nu$ and $u_\tau = (\tau_w/\rho)^{1/2}$, where y is the distance normal to the wall, ν is the kinematic viscosity of the fluid, τ_w is the shear stress at the wall and ρ is the fluid density). Nonetheless, the study was limited to using skin friction measurements and to comparing results with existing planar BFS studies. The present study adds to the work completed by Li and Naguib[7] by investigating both the wall-pressure signature and the flow field above the wall in the axisymmetric geometry. This is accomplished by using *simultaneous* wall-pressure-array and Particle Image Velocimetery (PIV) measurements.

It is the overall goal of this research project to bring further understanding to the flow-physics community in the area of 2D (i.e., axisymmetric) flow separation. Although the backward-facing-step flow field has been investigated extensively over the past few decades, only one other study (Lee and Sung[8]) has utilized an array of microphones to investigate the spatio-temporal statistics. Nonetheless, this study only examined the flow in a planar BFS. In addition, the few PIV studies of the BFS flow have all been conducted in a planar flow geometry. Finally, to the best of the author's knowledge, no studies have investigated the relation between the velocity field and the wall-pressure in an axisymmetric backward-facing step in order to identify the flow structures/mechanisms generating the surface-pressure signature. Thus, considering these motivating factors, the objectives for the present study are the following:

1. To investigate the wall-pressure signature and the velocity field in an axisymmetric separating boundary layer flow field in order to understand the flow and wall-pressure physics using spatio-temporally-resolved measurements of the wall-pressure and spatially-resolved flow-field data
2. To explore and identify Reynolds-number dependencies in the flow
3. To identify the flow structures that generate the surface-pressure signature using wall-pressure-based, single-point linear- and quadratic-stochastic estimation, and multi-point, linear, stochastic estimation
4. To employ stochastic estimation to facilitate an investigation into the time evolution of the flow structures that are linked to the wall-pressure-generation-process within the shear layer and downstream of reattachment

1.2 Organization of document

The present document is divided into seven chapters including the Introduction. The axisymmetric, backward-facing step model is described in Chapter two in terms of the general design and overall construction. Chapter two also highlights the experimental set-up used to acquire surface pressure measurements and Particle Image Velocimetry images simultaneously in the axisymmetric, backward-facing-step model. The general flow field characteristics are discussed in detail in Chapter three, including the reattachment distance, the boundary-layer state at separation, and the mean-pressure distribution along the surface of the model. Chapter four is dedicated to investigating Reynolds-number effects on the wall-pressure measurements. Auto-correlation; cross-correlation; and frequency-wavenumber contour plots are utilized in exploring the spatio-temporal characteristics of the wall-pressure. Similar analyses are presented in Chapter five for the velocity field measurements. The streamwise and normal fluctuating velocity components for different Reynolds-number cases are discussed along with the Reynolds shear stress in each flow field. Mean-vorticity plots are also compared between Reynolds -number cases. Chapter six links all the information together regarding the wall-pressure and above-surface, velocity measurements. In this chapter, the flow structures that generate the wall-pressure signature are investigated using stochastic estimation and proper orthogonal decomposition. A final discussion is given in Chapter seven. The Appendix provides supplementary information regarding the construction of the axisymmetric, backward-facing-step model, measurement techniques implemented, and signal processing techniques utilized. Finally, each chapter contains its own literature review and list of references.

1.3 References

[1] Eaton, J. K. and Johnston, J.P., "A Review of Research on Subsonic Turbulent Flow Reattachment," *AIAA Journal*, Vol. 19, No. 9, 1981, pp. 1093-1099.

[2] Cherry, N. J., Hillier, R., Latour, M.E.M.P., "Unsteady Measurements in a Separated and Reattaching Flow," *Journal of Fluid Mechanics*, Vol. 144, 1984, pp. 13-46.

[3] Castro, I.P. and Haque, A., "The Structure of a Turbulent Shear Layer Bounding a Separation Region," *Journal of Fluid Mechanics*, Vol. 179, 1987, pp. 439-468.

[4] Brederode, V. de and Bradshaw, P., "Three-dimensional flow in nominally two-dimensional separation bubbles. I. Flow behind a rearward-facing step," *Imperial College Aero Report 72-19*, Imperial College of Science and Technology, London, 1972.

[5] Ruderich, R. and Fernholz, H. H., "An Experimental Investigation of a Turbulent Shear Flow with Separation, Reverse Flow, and Reattachment," *Journal of Fluid Mechanics*, Vol. 163, 1986, pp. 283-322.

[6] Hudy, L.M., "Simultaneous wall-pressure array and PIV measurements in a separating/reattaching flow region," Masters thesis, Michigan State University, 2001.

[7] Li, Y. and Naguib, A.M., "High-Frequency Oscillating-Hot-Wire Sensor for near-Wall Diagnostics in Separated Flows," *AIAA Journal*, Vol. 43, No. 3, 2005, pp. 520.

[8] Lee, I. and Sung, H.J., "Characteristics of wall pressure fluctuations in separated and reattaching flows over a backward-facing step," *Experiments in Fluids*, Vol. 30, 2001, pp. 262-272.

2 Experimental Apparatus, Instrumentation, and Measurement Techniques

2.1 Wind Tunnel Facility

The experiment was completed in the Subsonic Basic Research (Wind) Tunnel (SBRT) at NASA Langley Research Center in Hampton, Virginia. The open-circuit, low-speed, wind tunnel has a 6:1 contraction ratio upstream of a 0.57 m-wide by 0.82 m-high by 1.85 m-long test section. An adjustable, false floor was placed in the test section and was set at a slight angle so that the pressure gradient in the test section was zero over most of the test-section's length (see Appendix 8.1). The nominal height of the test section with the false floor installed was 0.62 m. The blockage ratio with the model inside the test section was 3.6% and the turbulence intensity within the test section was less than one percent. More details describing the wind tunnel facility are located in Appendix 8.1.

2.2 The Model

The model used for generating the separating/reattaching flow was an axisymmetric backward-facing step as shown in Figure 2.1, where x represents the streamwise coordinate, y is the wall-normal coordinate, ϕ is the azimuthal angle, h represents the step height, and U_∞ represents the freestream velocity. The model was a circular cylinder with its axis parallel to the x direction, thus making the test geometry axisymmetric.

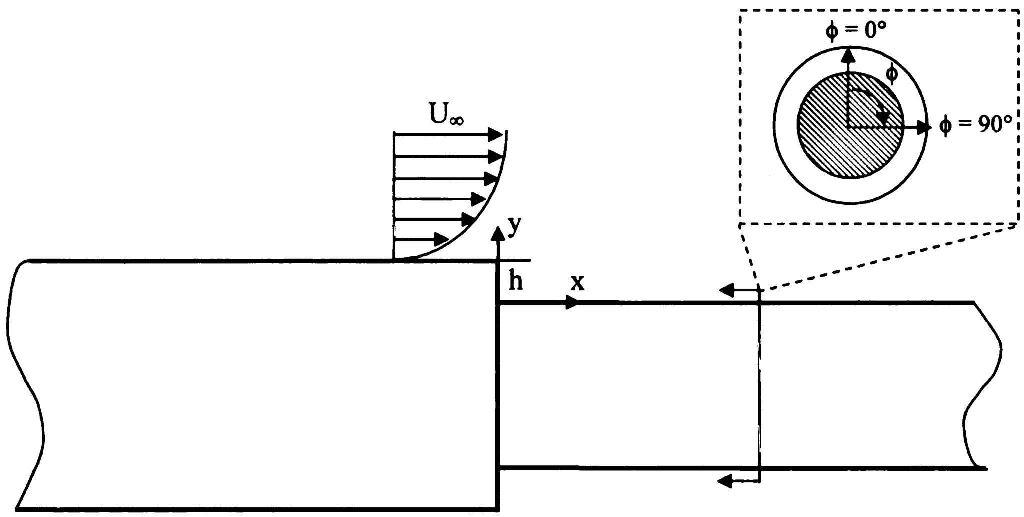

Figure 2.1 Axisymmetric, backward-facing-step configuration

The design of the axisymmetric BFS is shown in Figure 2.2 and Figure 2.3 with intricate construction detail outlined in Appendix 8.2. The model was designed and manufactured in cooperation with JBJ Products and Machinery located in Williamston, Michigan. The model measures 2.37 m in length, 0.124 m in diameter upstream of the step, and 0.10 m in diameter downstream of the step. The height of the step is 12.2 mm, and details regarding the selection of the height of the step can be found in Appendix 8.2. A spherical nose at the leading edge transitions the flow over the model relatively smoothly; although, there is a step discontinuity in the radius of curvature between the nose and the stationary section immediately downstream that may cause a flow disturbance. Because it was desired to establish a turbulent boundary layer at separation, this flow disturbance only aided in the quicker development of the boundary layer to a turbulent state; and, therefore, it was considered beneficial. Downstream of the nose is the 2D section module, measuring 0.35 m in length. This region allows the flow to settle into a 2D boundary layer after transitioning over the nose. In addition, at the upstream end of the 2D section, sandpaper was used to hasten the boundary-layer transition. At the aft end of the model, a conical tail prevents an abrupt transition of the flow surrounding the model into the flow region farther downstream. Moderating the step-like feature at the end of the model helps to prevent the development of disturbances that could propagate upstream, i.e. acoustically, and possibly change the flow conditions in the separating/reattaching flow zone of interest.

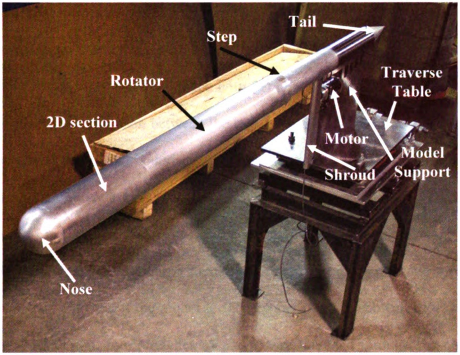

Figure 2.2 Axisymmetric, backward-facing-step model – "Images in this dissertation are presented in color"

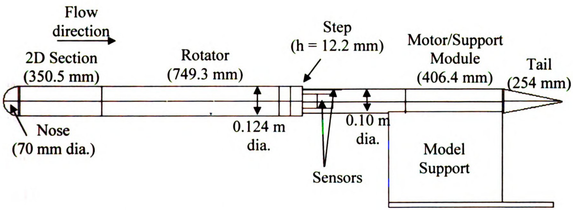

Figure 2.3 Side view of the axisymmetric, backward-facing step

The model was designed to allow the establishment of boundary layers with/without cross-flow velocity component. To accommodate the provisions for establishing the cross flow, the model was hollow with a 25.4 mm-diameter steel shaft that runs the entire length of the model at its center for increased rigidity. Inside the model, a drive shaft, connected to a 1/15 hp motor, rotated the 0.75 m long rotator section upstream of the step to introduce the cross-flow component, establishing what is known in the literature as three-dimensional (3D) boundary layer at separation. Without rotation, the boundary layer is 2D. Since both 2D and 3D boundary layers can develop along the surface, a comparison between the two cases within the same geometry can be made. The results for the 3D boundary layer case are not the focus of this thesis but, for the interested reader, they may be found in Hudy *et al.*[1] Approximately 0.37 m or 30 step heights (6.7 x_r, where x_r is the reattachment length) downstream of the step is a steel motor/support module, which housed the pulley for the electric motor and provided the stability necessary to connect the model to the support stand as shown in Figure 2.2 and Figure 2.3. In addition, four stretches of piano wire threaded through the nose of the model and secured near the four corners of the test section were used to support the front end of the cantilever-beam-like model.

Figure 2.4 shows a front view of the model as "seen" by the freestream flow. In this figure, the model is divided into four quadrants and labeled north, south, east, and west with the corresponding azimuthal angle given. These labels will be used throughout the text to explain the location around the model of the area being discussed. In Figure 2.4, the instrument plates (i.e., plugs employed for the insertion of wall sensors) can be seen. The main instrument plate that houses both microphones and static pressure taps is located on the north side of the model. The instrument plate on the east side contained static pressure taps. For the study of Li[2], this plate also contained two oscillating hotwire sensors that were used for acquiring wall-shear-stress measurements. Finally, two more instrument plates containing only static pressure taps were placed on the south and west sides for the purpose of alignment of the model. All wiring and static-pressure tubes were stored inside the model as discussed in further detail in sections 2.3.

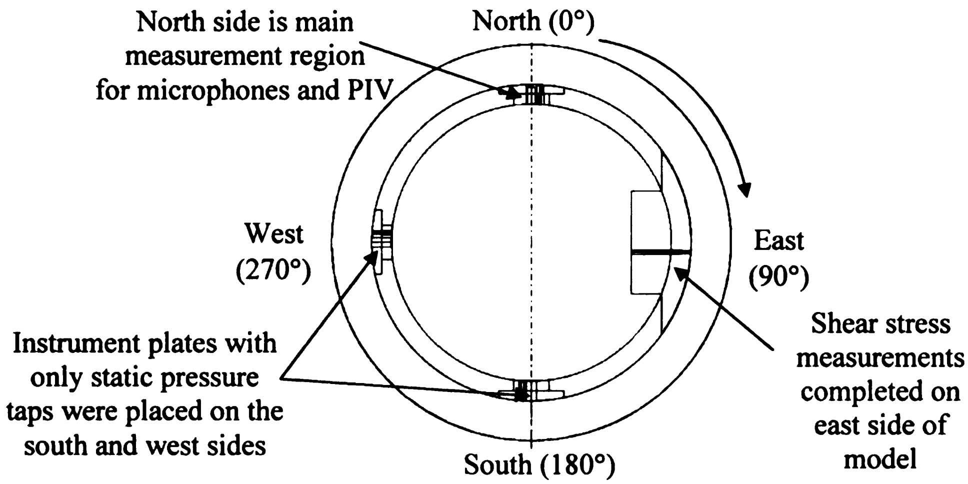

Figure 2.4 Labeling system for the axisymmetric, backward-facing step viewed from the approaching flow direction

It is important to note that the results found in this study are limited to a specific geometric ratio of the step height to the radius (r) of the model. Changing the ratio can affect the flow field downstream of separation. For instance, if the radius is large compared to the step height (r >> h), then the affect due to the curvature of the model is reduced. In such a case, the geometry would be similar to a planar BFS and this may cause the reattachment length to be longer. The r/h for the present model is 5.2. Thus, the results presented are specific to the axisymmetric geometry used in this experiment.

.

2.3 Instrumentation and Measurement Techniques

Several measurement techniques were used to acquire an extensive pressure and velocity dataset. A single hotwire was used to examine the alignment of the model inside the test section in terms of azimuthal uniformity. Appendix 8.3 has the procedure and the results of this test.

The axisymmetric, backward-facing step described in Section 2.2 was also instrumented, downstream of the step, with 56 static pressure taps and 32 Emkay microphones. The microphones and taps were embedded in a 222.25 mm (18 h) long by 20.6 mm (1.7 h) wide anodized instrument plate (I-plate) shown in Figure 2.5. The I-plate was located on the top side of the model and was secured to the model by two ¼-20 screws located at either end of the I-plate. The upstream portion of the I-plate was instrument-free for placement of a 50.3 mm-long "step ring", which was used to form the separation edge. The center of the most upstream microphone was located 5.3 mm (0.43 h) downstream of the step-ring edge. The wiring and tubing for the instrumentation was stored inside the model within a 12.7 mm-wide annular space (see Appendix 8.2 for model construction details). The taps were used to characterize the mean flow surrounding the model and to align the model in the wind tunnel. The microphones were used to measure the unsteady pressure along the surface.

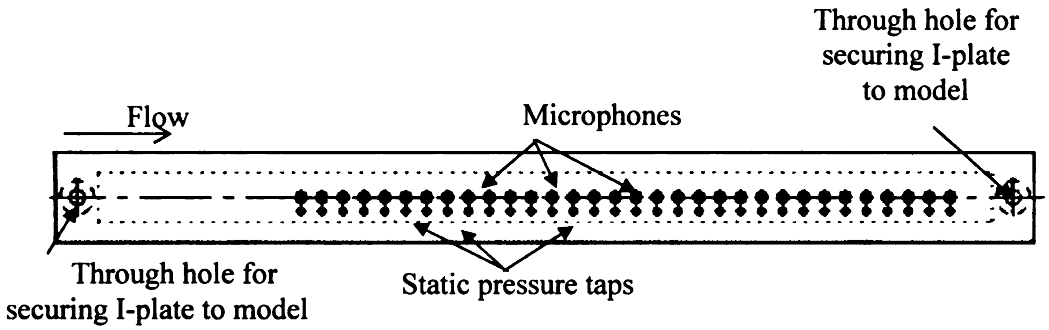

Figure 2.5 A schematic of the top view of the Microphone and static-pressure-tap instrument-plate - located on the top side of the model

2.3.1 Static Pressure Taps

On the top side of the model, 32 static pressure taps were located beside the microphones at a spacing of 3.2 mm center to center. The static pressure taps were secured in counter-bored holes, as shown in Figure 2.6, using a non-conductive adhesive. A through hole equal to the 1 mm (0.08 h) inside diameter of the tap was drilled through to the top surface of the I-plate, shown in Figure 2.6. This ensured a smooth top surface and avoided the curvature mismatch between the taps and the top surface. The Urethane tubing for the static pressure taps was threaded through the 12.7 mm clearance inside the model and through the shroud to the Scanivalve, mechanical, pressure scanner. The Scanivalve system used is described in Hudy[3].

The remaining 24 static pressure taps were placed in three arrays of eight taps located on the two sides and bottom of the model as seen in Figure 2.7. These pressure tap holes were spaced 9.5 mm (0.8 h) apart center to center with the first tap starting at 19.05 mm (1.6 h) downstream of the step. The I-plates were secured to the model using two ¼-20 screws at each end. The tubing for the taps was routed through the inside of the model and the shroud out to the Scanivalve.

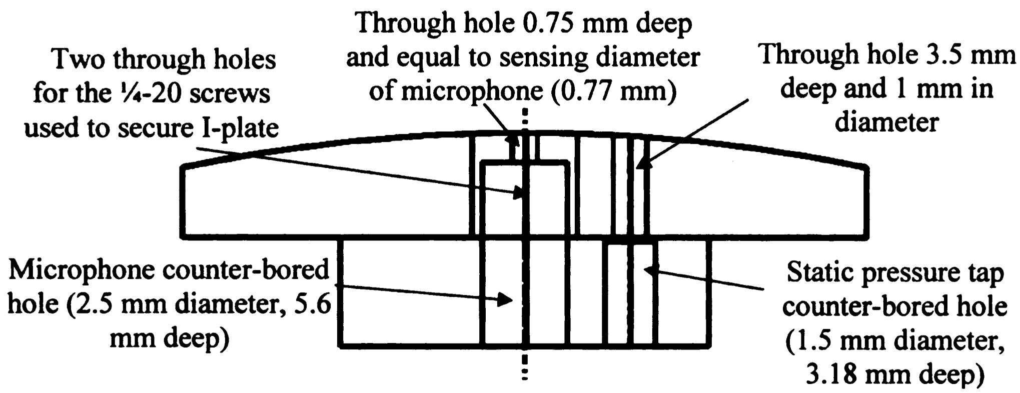

Figure 2.6 View of the I-plate showing provisions for embedding the microphones and static pressure into the I-plate

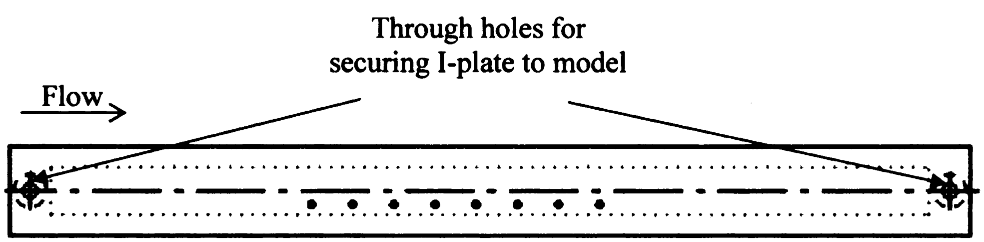

Figure 2.7 Schematic of instrument plate containing only static pressure taps

The output port of the Scanivalve was connected to one of two pressure transducers from the Setra 239 series. One transducer measured differential pressure in the range of 0-12.7 mm H_2O, outputting a corresponding 0-5 V signal. The other transducer ranged from 0-127 mm H_2O over the same voltage range. The output port of the pressure scanner was connected to the negative input of one of the transducers depending on the expected pressure range of the measurements. In turn, the positive pressure port of the transducer was connected to a reference pressure tap located in the side wall of the wind-tunnel contraction section at its exit.

2.3.2 Microphones

The microphones used in the experiment were Emkay (FG-3629-P16) Electret Condenser Microphones. The diameter of the microphones is nominally 2.6 mm (0.2 h). There were 32 microphones embedded in the I-plate with a center-to-center spacing of 4.8 mm (0.4 h). The microphones were secured in counter-bored holes, as shown in Figure 2.6, using a non-conductive adhesive. A through hole equal to the 0.77 mm (0.06 h) microphone sensing diameter was drilled through to the top surface of the I-plate. This ensured a smooth, top surface and avoided the curvature mismatch between the microphones and the top surface.

Each microphone had a nominally reported sensitivity of -53±3 dB (relative to 10 V/Pa) over the frequency range of 100-10,000 Hz (Figure 8.23 in Appendix 8.4). Since the frequency range of interest extended below 100 Hz, and to account for variations in the response of individual units, the microphones were bench calibrated between 20 and 15,000 Hz using a B&K 4226 multifunctional calibrator. Details regarding the calibration are provided in Appendix 8.4. The microphones were powered utilizing a custom-made circuit box. The box was also used to break out the output of the microphone array into 32 individual coaxial cables for connection to the A/D board, as described in Appendix 8.4.

The outputs of the microphones were connected to four National Instruments A/D boards (SCXI 1141), placed in a SCXI 1001 chassis. Each board had an input signal range of ±5V, eight differential analog-input channels, and a variable channel gain that was set to ten for this experiment. The highest sampling rate for which the board is capable is 1.25 MHz for one channel. In all, 35 channels were acquired: 32 microphone output channels, one channel for B&K reference microphone located in the ceiling, and two channels dedicated for the PIV synchronization with the microphones (see Section 2.4.3.1 for more detail). Because the channels were multiplexed, the maximum sampling rate was 35,714 Hz per channel with an inter-channel time delay of 0.8μs. This delay results in a systematic error, which is small compared to the flow convective time scale, 476μs, over a distance equal to the microphone spacing at the freestream velocity. Each channel of microphones could also be connected to an ONO SOKKI FFT Analyzer (CF940) using a matrix switch in order to spot check the data during the experiment. Data from the microphones were collected using PC software written in Visual Basic by William M. Humphreys.

2.3.3 Particle Image Velocimetry

Two-component (2C) Particle Image Velocimetry (PIV) measures two-velocity-field components at a number of points in a plane (Humphreys *et al.*[4]). There are four basic steps to PIV. First, the flow is uniformly seeded. In this test, pharmaceutical grade mineral oil was dispersed using a commercially available smoke generator. This smoke generator consisted of a shearing atomizer feeding a vaporization/condensation section and was capable of producing a cloud of smoke that could be varied in density by adjusting the atomizer supply pressure. The smoke generator was placed at the inlet section of the wind tunnel, thus allowing the incoming flow to carry the seed into the test section as shown in Figure 2.8. The mean aerodynamic size of a particle was approximately 0.2-0.4 μm. This same set-up was used in a unified instrumentation test by Fleming *et al.*[5] The group found the small particle size scattered enough light to be imaged by CCD cameras. In addition, each image contained a sufficient amount of seeding to accurately cross-correlate particles within the interrogation region, resulting in a low rate of bad velocity vectors. The particles were also evenly dispersed throughout the image and the particle diameter was consistent across the image.

Figure 2.8 Image of the fog generator used in the PIV set-up, placed upstream of the inlet section to the wind tunnel

The second step is to illuminate the particles in the flow region being studied. The illumination is from two Nd:YAG laser systems. Beams from the systems are combined through optics to form a laser sheet that is used to illuminate the flow area of interest. A record of this illuminated area is then captured using CCD cameras as the third step. The idea is that one of the laser beams is pulsed and an image is captured; then at a known time delay the other laser beam is pulsed and a second image is taken. With proper selection of the time delay, the seed particles are displaced while mostly remaining within the illuminated region.

The PIV records acquired are stored and analyzed to create a velocity vector field of the flow. The analysis requires locating the particles in one image and "matching" them with particles in the time-delayed image. This is accomplished by dividing the image into small "interrogation" windows (e.g., 16 by 16 pixels) and calculating the two-dimensional cross correlation between the first and second images for each of these sub-regions. The pixel offset at which the highest correlation is found gives the average particle displacement at the center of the interrogation cell. By dividing this displacement by the time delay between the two images, the velocity is calculated. Figure 2.9 shows an example of a PIV system set-up.

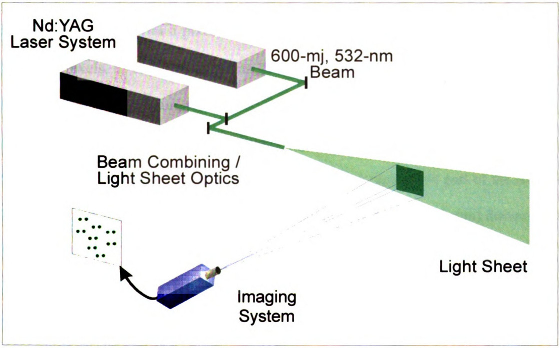

Figure 2.9 Example of a typical PIV system [Humphreys[6]]

2.3.3.1 Experimental Set-up

The PIV system used in this study was composed of two lasers, two cameras, and optical components. The two lasers were ND:YAG from the Continuum Powerlite series. Each laser was capable of producing up to 600 mJ per pulse of green light (wavelength of 532 nm) at a nominal repetition frequency of 10 Hz. The nominal pulse width for both lasers was 10 ns, and they were pulsed in synchronization with a pre-set, time separation between the lasers. The laser-lit particles were captured by two MegePlus ES-1.0 high resolution CCD cameras by Redlake. Each camera had a detector size of 1008 pixel wide by 1018 pixel high with a pixel size of 9x9 μm^2 and with a 55% fill, meaning no gap between pixels. The two cameras, shown in Figure 2.10, were used to obtain simultaneous PIV measurements over two planes that overlapped partially along the streamwise direction (about $1/16^{th}$ of the image width). This enabled coverage of all of the streamwise extent of the separating/reattaching flow region and part of the reattached boundary layer region (corresponding to a total length of 8.4h (102.5 mm) downstream of the step).

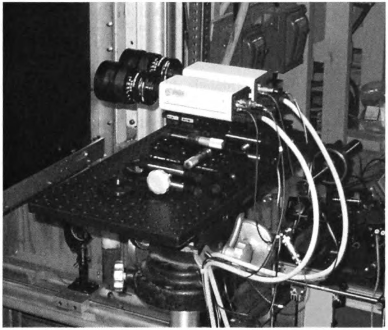
Figure 2.10 Camera set-up used in experiment

The Redlake cameras utilize the "frame-straddling" mode of image acquisition. In this technique, the first frame integration period is 250μs and the second frame integrates for a full 33.3 ms. During the integration time of the second frame, the information from the first frame is a readout of the sub-register. This method of operation allows the use of *one* camera for acquiring *two* consecutive images synchronized with the firing of each laser[7].

The time delay between the lasers was estimated based on the pixel size, the magnification factor, and the "PIV equation". The CCD size is 1018 pixels high by 1008 pixels wide and the pixel size is 9 μm on the side. Therefore, the total width of the CCD element is 9.07 mm, also called the image view. The field of view was set to be 57.2 mm. From the field of view and the image view, the magnification can be calculated as follows:

$$Magnification = \frac{i_{width}}{o_{width}} = \frac{9.07mm}{57.2mm} = 0.159 \qquad (2.1)$$

where, i_{width} represents the image width (height) and o_{width} equals the object width (height). The object in this case is the field of view along the model. The equation for extracting the velocity from displacement information is given by

$$\vec{V} = \frac{\vec{d}}{m\Delta T} \qquad (2.2)$$

where $\vec{V}$ represents the speed, $\vec{d}$ represents the displacement, m is the magnification, and ΔT is the laser pulse separation (i.e., the time delay between the light pulses from the two different lasers. A 32 by 32 interrogation box was used for the cross correlation, and the maximum displacement was estimated as approximately 40% of the interrogation window width, or 13 pixels (117 μm). Using equation (2.2) and solving for ΔT, the laser pulse separation for each test speed was calculated and is presented in Table 2.1.

Table 2.1 Laser pulse separation times for all four Reynolds numbers tested

Test Speed (m/s)	Laser pulse separation (μs)
7.4	102
10	77
18	42
23	33

The optics used to change the polarization of the lasers, form the light sheet, and direct the beam into the test section consisted of a variety of components. Turning mirrors, from CVI Laser Optics (Y2-2037-45-UNP), were used to redirect the path of the two lasers. In this case, they were used to direct the laser beams to the top of the wind tunnel. The light sheet was then formed using optics along the top of the wind tunnel and then redirected inside the test section and upstream toward the step using a turning mirror as shown in Figure 2.11. These mirrors were 50.8 mm in diameter with 9.5 mm thickness, allowing a wavelength of 532 nm to reflect with a minimum un-polarized reflectance of 99%. This means that 99% of the laser light received by the mirror is reflected, resulting in 1% loss of energy, without affecting the polarization of the beam. From the laser, one of the beams passed through a $\lambda/2$ waveplate from Newport to rotate its polarization, which was necessary in order to combine the beams using the thin, film-plate polarizer. The combined beams had perpendicular polarization with respect to each other. The CVI Laser Optics thin, film-plate polarizer (TFP-532-PW-2025-C) had a transmission efficiency of 95% at a wavelength of 532 nm. The polarized beams were then redirected to the optics on top of the wind tunnel using turning mirrors. The optics set-up is pictured in Figure 2.12. Two spherical lenses by Newport were used to focus the laser sheet on the model and limit its width. The first was a -100 mm singlet spherical lens, followed by a +150 mm bi-convex spherical lens. The distance between the two lenses was varied to change the focal point of the beam on the model. The polarized beam then passed through a BK7 cylindrical plano-concave round lens (CLCC-50.8-38.1-C-532) from CVI Laser Optics. This lens had a nominal focal length of 75 mm and was used to lengthen the laser sheet. Finally, a turning mirror was attached to the tail end of the model and used to turn the laser sheet upstream, towards the measurement region downstream of the step.

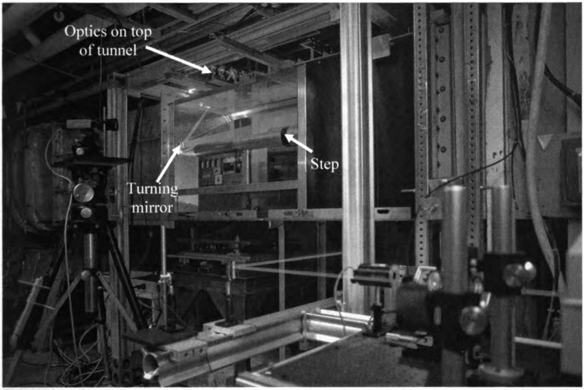

Figure 2.11 PIV set-up in SBRT

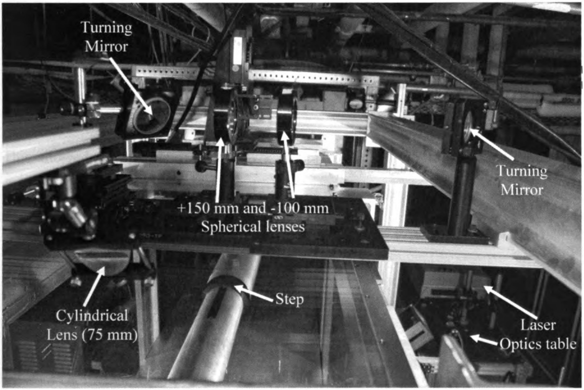

Figure 2.12 PIV optics set-up on top of the wind tunnel

2.4 Experimental Procedure

2.4.1 Static Pressure System

The static pressure taps were used to align the model inside the test section of the wind tunnel and to characterize the mean-flow field surrounding the axisymmetric backward-facing step. The static pressure measurements were acquired for 10 seconds at a sampling rate of 100 Hz. In addition, a one second, time delay was used between acquiring the pressure from consecutive ports in order to eliminate the transient effect associated with switching pressure ports on the measurements. These quantities were determined based on previous work cited in Hudy[3].

The alignment of the model inside the wind tunnel required using the static pressure ports on all four sides of the axisymmetric BFS. Twenty-four pressure taps were connected to the Scanivalve on the top side of the model, and all eight were connected on each of the remaining three sides. Data were acquired at a freestream velocity of 10 m/s. The model was secured to a traverse table (Figure 2.2) that allowed movement in all three spatial directions. In addition, the pitch and yaw angles of the model could be adjusted. This allowed for complete control over the placement of the model inside the wind tunnel. When adjustments were made to the traverse table, the piano wire was also adjusted based on the new alignment in order to provide the proper support at the leading edge of the model.

The mean-pressure profiles for all four sides are shown in Figure 2.13. Also, the average of all four cases is included in the figure (shown using a solid line). The mean-pressure coefficient, $C_p = (p_s - p_r)/(\frac{1}{2}\rho U_\infty^2)$, is plotted along the ordinate as a function of the streamwise coordinate, which is plotted on the abscissa as x/h. For definition purposes, p_s is the pressure measured along the surface of the model and p_r is the reference pressure measured with a static tap located at the exit of the wind-tunnel contraction.

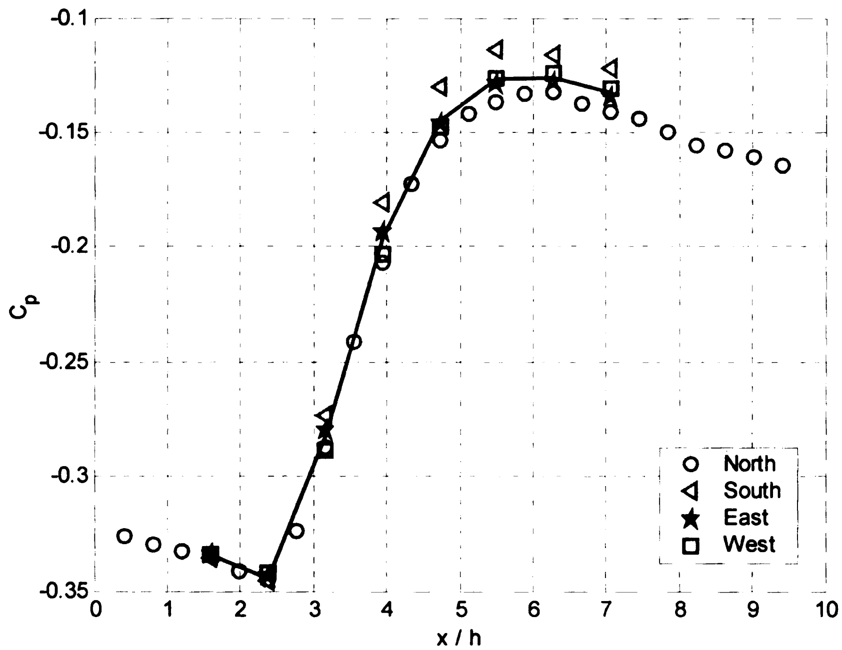

Figure 2.13 Streamwise distribution of the mean-pressure coefficient, depicting the quality of alignment of the model

The pressure distributions in Figure 2.13 collapse over the region stretching from near the step edge to approximately x/h = 3. Moving farther downstream, a difference in the pressure distribution becomes evident with a maximum deviation from the average distribution of approximately 5% occurring in the range x/h = 4.75-7. This increase in pressure seen on the south side of the model was found to be caused by the obstruction of the model support stand (Figures 2.3, 8.16, and 8.17) that is located 27h downstream of the step. As the flow approaches the stagnation line on the model stand, it begins to slow down. Thus, based on Bernoulli's principle, the freestream pressure starts to rise and the mean-pressure distribution along the model starts to differ between the north and south sides. The same affect is seen in the static pressure distribution along the false floor of the wind tunnel as shown in Figure 8.4 in Appendix 8.1.

2.4.2 Microphone Measurement System

The procedure for the microphone measurements was established after conducting a number of preliminary tests. These tests are described in Appendix 8.4. The data acquisition parameters used to record the microphone data were determined based on known information about the flow and from the necessary data collection parameters for the PIV images. Hudy[3] found that the flow frequencies of interest in a splitter-plate-with-fence geometry did not exceed 2500 Hz. This was verified using a power spectrum from the microphone closest to reattachment, where the level of the wall-pressure fluctuations was highest. Data were sampled at 12,000 Hz, and results showed that the wall-pressure spectrum vanished at frequencies higher than 1000 Hz. Since the splitter-plate-with-fence geometry produces a flow similar to the backward-facing step, these results were considered when determining the appropriate measurement parameters to use for acquiring the wall-pressure data. It was found that a similar sampling frequency of 12000 Hz was also appropriate for the present flow. Consequently, the cut-off frequency of the anti-aliasing filters employed was set to 5000 Hz (which is lower than the Nyquist frequency of 6000 to ensure proper elimination of frequencies above the Nyquist independent of the filter roll-off).

When wall-pressure and PIV measurements were acquired together, the microphone signals had to be recorded in synchronization with the PIV images, requiring the microphone time series to be at least 30 seconds, as will be explained in section 2.4.3. Therefore, microphone signals were acquired at 12000 Hz for 35 seconds.

2.4.3 Particle Image Velocimetry System

The procedure for the PIV system required imaging "dot" and "grid" cards prior to performing the experiment. These images, which were acquired every time the focus of the camera was adjusted, were used to focus the camera on the image plane and in the post-processing phase, as described in more detail in Appendix 8.5. Once these preliminary images were acquired, the PIV system was configured to acquire images of the flow field simultaneously with the microphones.

The PIV images were acquired using the program PIVACQ, written by Mark Wernet[7] from NASA Glenn Research Center. A PC with 2GB RAM was used to acquire the data. The amount of RAM available limited the number of PIV images that could be acquired during a run to 300 images. On the other hand, the PIV acquisition rate was limited by the laser repetition rate of 10 Hz. Thus, the PIV data could be acquired for 30 seconds before the images needed to be saved to the hard drive. Sampling of the microphone data started approximately two seconds before the PIV and lasted for 35 seconds to ensure overlap between the PIV and pressure information. Five runs were completed for a total of 1500 images per flow condition.

2.4.3.1 Synchronizing the PIV images and the microphones

To synchronize the microphone and PIV acquisition, a master signal and a steady 5V TTL pulse train were utilized. The timing diagram for the synchronization is shown in Figure 2.14. The detailed procedure is best described step-by-step. First, both the microphone and the PIV acquisition systems were armed to start acquiring once they receive an external trigger signal. Second, two signals were sent out from a digital-to-analog (D/A) board installed in a Dell PC laptop and driven by a LabView program: master and external-trigger signals. The master signal consisted of a *single* one millisecond pulse given 5 milliseconds into the start of the generation of the D/A output as shown in Figure 2.14. This single pulse triggered the microphone acquisition to start. The external trigger signal started two seconds after the master pulse and was sent to the PIV system to start the image acquisition. This signal consisted of a 10 Hz, TTL, 50% duty cycle pulse train, which was employed to externally trigger an NI-6602 timer board. This timer board was used to control/synchronize all of the PIV-system functions; i.e., laser timing, camera triggering, and frame-straddling synchronization.

Once the NI-6602 received an external trigger, it sent out a 67 ms wide pulse to the cameras, which opened the camera shutter to acquire the first frame. The lasers then fired on the output pulse received from the camera strobe. One laser fired within the first camera frame, which has an integration time of approximately 250 μs before it is transferred to the sub-register for readout. The second laser fired during the second camera frame, which is integrated over 33 ms. Figure 2.15 shows the timing diagram for the PIV acquisition system as detailed by Wernet[7]. Note in Figure 2.15 TPD means Transfer Pulse Delay, which determines the time interval after the camera is triggered until the current frame is transferred to the sub-register for readout. The TPD was set to 250 μs. Also, Flashlamps 1/2 and Q-switches 1/2 refer to control signals of the lasers, and Frames #1/2 are the two camera frames corresponding to the PIV image pairs.

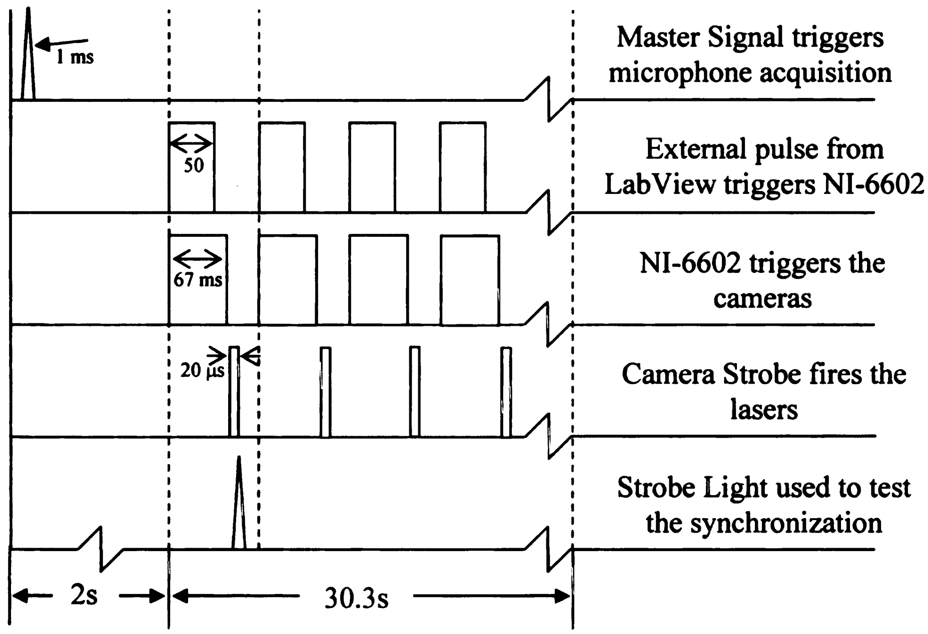

Figure 2.14 Timing diagrams showing how the microphones data and PIV images were synchronized

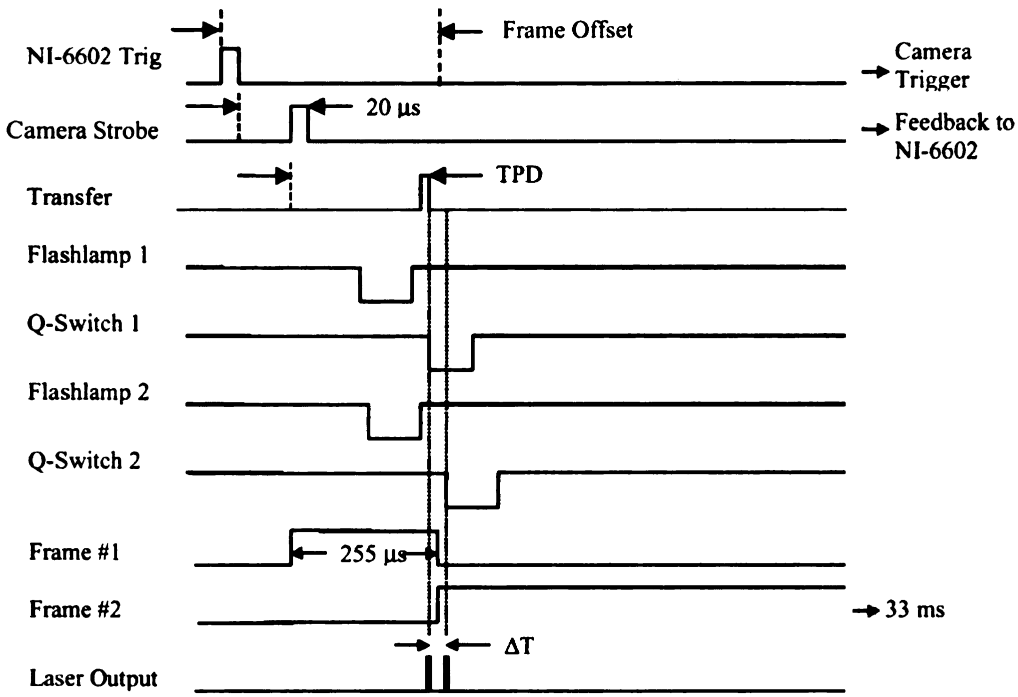

Figure 2.15 Timing diagrams for the PIV image acquisition system – Copied from Wernet[7]

The true acquisition time for the PIV images was 30.3 seconds due to both software and hardware issues. The first pulse in the external trigger signal sent by the Dell PC laptop was dropped by the NI-6602 board. In addition, the PIVACQ program dropped the first two images. Therefore, to acquire 300 images, three extra pulses needed to be added to the external trigger signal. The external trigger contained 30.3 seconds worth of pulses as seen in Figure 2.14.

The external trigger signal that was sent to the NI-6602 and the camera strobe that fired the lasers were the two extra channels acquired simultaneously with the microphone signals. Acquiring the external trigger gave the number of pulses sent by the Dell PC laptop. The camera strobe pulse train gave the pulses associated with image acquisition, and it was used to match each image with the wall-pressure pattern acquired by the microphones at the same time as the image. In the post-processing phase, the first two pulses from the camera strobe signal were ignored. The third individual pressure reading after the rising edge of the third pulse was the point in the time series that matched with the first PIV image, followed by the remaining 299 images and pulses. The third pressure reading from the rising edge was acquired 250μs after the camera strobe fired the lasers and opened the camera shutter and marked the point at which the image was transferred to the sub-register as shown in Figure 2.15. At this point, the first laser had definitely fired and the second laser was about to fire within microseconds.

In order to test the synchronization between the PIV and the microphones, a strobe light was used. The set-up for the test required a single strobe lamp that could be externally triggered. All the lights in the room containing the wind tunnel were turned off so that the only light source would be from the strobe light. A simple target was placed on the model and the strobe was set-up so it illuminated the target when triggered. A pulse train was then created in LabView that externally triggered the strobe during randomly selected frames. This trigger pulse was one millisecond in duration. The strobe only fired during the second camera frame since the integration time was longer than the duration of the strobe. For this particular test, the strobe was triggered in frames 1, 2, 8, 111, 223, and 291. Subsequent inspection of the 300 acquired images, proved that in fact an illuminated target was seen only in the second of the "PIV" image pair 1, 2, 8, 111, 223, and 291. In addition, by acquiring the strobe light trigger pulse, it was verified that the strobe pulses overlapped with the PIV synchronization TTL pulses number 1, 2, 8, 111, 223 and 291 (ignoring the first three pulses for the reasons described above). These completed the verification process of the synchronization procedure.

2.4.3.2 Post-processing the PIV images

The post-processing of the PIV images required a few steps including merging of the images, as explained in Appendix 8.5, from the two separate cameras into one image representing the full extent of the measurement domain. Once merged, the PIV images were processed using Mark Wernet's PIVPROC processing code[8] and bad vectors were removed based on Chauvenet's criterion[9]. The images were processed using a multi-pass correlation technique with 50% overlap for enhanced spatial resolution. The multi-pass approach utilized an initial 64 x 64 pixel integration box followed by a 32 x 32 pixel integration box for the second pass. This resulted in a vector spacing of 0.92 mm. Overall, the vector field map covered 101.6 mm (8.4 h) in the streamwise direction and 45.6 mm (3.8 h) in the normal direction.

2.5 Test matrix

The test matrix for the experiments done in SBRT was extensive. Four test cases, corresponding to freestream velocities (U_∞) of 7.4, 10, 18, and 23 m/s, were tested, thus resulting in a Reynolds-number, test range based on a step height of 5900-19000. This test range was selected to allow comparison with the wall-shear-stress study by Li[2] (Re_h = 4300-13000), which utilized the same axisymmetric, BFS geometry. Both microphone and PIV data were acquired at all speeds reported in the present study. A list of the cases is shown in Table 2.2 along with the corresponding Reynolds numbers based on step

height (Re_h) and momentum thickness of the separating boundary layer (Re_θ), reattachment distances divided by step height (x_r/h), and boundary layer momentum thicknesses at separation divided by step height (θ/h). Note that x_r/h was calculated using "Forward Flow Probability", or FFP. Details of FFP will be discussed in Section 3.1.

Due to the vast scope of this research project, the amount of information reported has been limited. Only two of the four 2D flow conditions will be analyzed in the following pages. A complete wall-pressure and velocity field analysis will be presented. In addition, data from the Re_h = 8081 case only will be analyzed using stochastic estimation in effort to reveal the flow structures that generate the wall-pressure signature.

Table 2.2 Experimental parameters for the four cases investigated

U_∞	Re_h	x_r/h from FFP	Re_θ	θ/h
7.4 m/s	5980	4.29	889	0.149
10 m/s	8081	4.48	1237	0.153
18 m/s	14547	4.79	1751	0.122
23 m/s	18588	4.94	1979	0.107

2.6 References

[1] Hudy, L. M., Naguib, A., Humphreys, W. M., and Bartram, S., "Particle image velocimetry measurements of a two/three-dimensional separating/reattaching boundary layer downstream of an axisymmetric backward-facing step," *43rd AIAA Aerospace Sciences Meeting and Exhibit*, AIAA-2005-0114, Reno, Neveda, January 10-13, 2005.

[2] Li, Y., "Investigation of the wall-shear-stress signature in a backward-facing-step flow using oscillating hot-wire sensors," *Ph.D. dissertation*, Michigan State University, 2004.

[3] Hudy, L.M., "Simultaneous wall-pressure array and PIV measurements in a separating/reattaching flow region," Masters thesis, Michigan State University, 2001.

[4] Humphreys, W. M. and Bartram, S. M., "Measurement of separated flow structures using a multiple-camera DPIV system," Presented at the *19th International Congress on Instrumentation in Aerospace Simulation Facilities*, 2001.

[5] Fleming, G. A., "Unified Instrumentation: Examing the Simultaneous Application of Advanced Measurement Techniques for Increased Wind Tunnel Testing Capability," *22nd AIAA Aerodynamic Measurement Technology and Ground Testing Conference, St. Louis, Missouri,* AIAA 2002-3244, June 24-26, 2002.

[6] Humphreys, W. M., "Introduction to Particle Image Velocimetry," Presented at the Wind Tunnel University workshop, NASA Langley Research Center, 2000.

[7] Wernet, M. P., *Paticle Image Velocimetry Acquisition Manual PIVACQ*, NASA Glenn Research Center, Version 2.2, 2002.

[8] Wernet, M. P., *Particle Image Velocimetry Processing Manual PIVPROC*, NASA Glenn Research Center, Version 6.03, 2002.

[9] Dally, J. W., Riley, W. F., and McConnell, K. G., *Instrumentation for Engineering Measurements*, 2nd ed., John Wiley & Sons, Inc., New York, 1984, pp. 538.

3 (

step.

the

3 General Characterization of the Flow Field

Prior to presenting the results from the experiments it is necessary to examine the characteristics of the general, flow field surrounding the axisymmetric, backward-facing step. First, the reattachment length is determined using the PIV data and compared to wall-shear-stress data acquired in the same model geometry. The average reattachment length is an important parameter in the flow field in that it gives the length of the separation bubble.

The second form of useful information presented regarding the flow field is the state of the boundary layer at separation. Sandpaper was used at the upstream end of the model in order to trip the boundary layer with the aim of establishing a turbulent boundary layer at separation. A single hotwire was used approximately 1 mm upstream of the step edge to acquire the boundary-layer velocity profile. This profile is then compared to classic, fully-developed, boundary-layer profiles from literature in order to characterize the state of the boundary layer at separation.

Finally, the mean-pressure distribution downstream of the step is presented and the Reynolds-number effect on this distribution is discussed. Note that hereafter, upper case letters represent time-averaged quantities (e.g., U indicates the mean, streamwise velocity) and lower case letters with a prime indicate fluctuating quantities (e.g., u' is the turbulent, streamwise velocity).

3.1 Reattachment Length

Two methods were used to determine the reattachment distance for all four cases listed in Table 2.2. The results from these methods were compared with results from Li and Naguib[1] who were able to determine the reattachment distance within the same axisymmetric backward-facing step geometry using an oscillating hotwire that measured the shear stress along the surface. The first method used to determine the reattachment distance was forward-flow probability (FFP), which was also employed in past studies by Spazzini *et al.*[2], Eaton[3], Westphal and Johnston[4], and Tihon *et al.*[5] FFP is the fraction of the time that the flow is in the forward direction. In each of the 1500 vector fields, the direction of the streamwise velocity measured at the lowest position of $y/h = 0.05$ ($y = 0.6$ mm) is recorded and the FFP is determined as the number of images for which the streamwise velocity is positive divided by the total number of images. The results are presented as percentages along the ordinate as shown in Figure 3.1, with the normalized streamwise distance along the abscissa. Figure 3.1 presents the FFP for all four Reynolds numbers. A 0% FFP means the flow at that particular x/h position is moving toward the step in all realizations of the 1500-sample dataset; whereas, 100% FFP indicates that the flow is moving in the downstream direction in all realizations for the same sample set. The reattachment distance is located at the streamwise position where the FFP = 50%. As a result of the slight scatter in the data, a linear fit to the data near x_r, as shown in Figure 3.1, was employed to estimate the streamwise position at which the FFP equaled 50%.

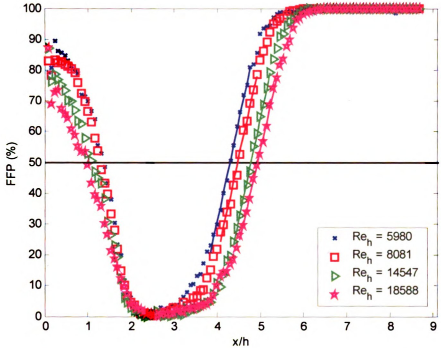

Figure 3.1 Streamwise distribution of the forward flow probability for all four Reynolds numbers

In Figure 3.1, there are two streamwise positions where the FFP = 50%. Depending on the Reynolds number, the first streamwise position is between x/h = 1 – 1.5 and the second position is roughly between x/h = 4 – 5. The first position gives the location of the secondary separation point close to the step, which separates the secondary and primary re-circulating regions. The second FFP = 50% position is the point of reattachment of the shear layer. The four cases plotted in Figure 3.1 show that increasing the Reynolds number results in a longer reattachment length and a shorter secondary separation point. Similar results were found for the same test model by Li and Naguib[1] from wall-shear measurements using an oscillating hotwire at y/h = 0.008. Spazzini *et al.*[2] also report the same trend for the Re_h range 3500 through 16000.

Li and Naguib[1] attribute this Reynolds number trend to the variation in the boundary-layer thickness. This reasoning is supported by the earlier observations of Eaton and Johnston[6] and Adams and Johnston[7], both of whom found that x_r increased as the boundary layer thickness decreased. Since in this study the Reynolds number increases by increasing the freestream velocity, the boundary-layer thickness should decrease as Re is increased. Referring to Table 2.2 and Figure 3.2, this is seen to be in fact the case for U_∞ of 10 m/s (Re_h = 8081) and higher where the value of θ is found to decrease with Re_h. However, the lowest Re_h case (U_∞ = 7.4 m/s) deviates from this trend where the momentum thickness is seen to be smaller than that at Re_h = 8081. This is attributed to possible "under stimulation" of the boundary layer at the lowest freestream speed, suggesting that the boundary layer may not be sufficiently developed to a turbulent state as in the other cases. Such a low Reynolds number effect on turbulent boundary layers established in the laboratory is typical (e.g., see Naguib[8]).

It is important to note that it would be ideal to increase Re_h without changing the ratio of the boundary-layer thickness to step height (i.e., keeping θ/h invariant). This would make the shear layer development solely dependent on the change in the freestream velocity and step height, while decoupling the connection between freestream velocity and momentum-thickness variation.

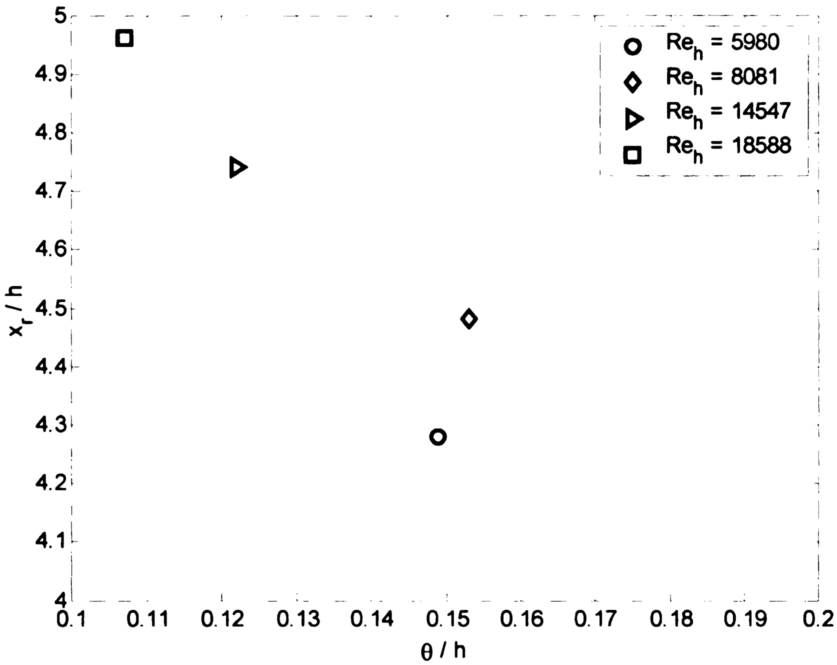

Figure 3.2 Normalized reattachment distance versus normalized momentum thickness

The second method used to estimate the mean reattachment distance required using the mean streamwise velocity component. The premise of the method is similar to that based on measurements of the mean, wall-shear stress. More specifically, the reattachment point may be determined accurately as the point of zero streamwise wall shear stress; i.e., the point at which the stress switches from a negative to positive value. Since this study had no access to wall-shear information, the analysis was conducted on the mean, streamwise velocity at the lowest y position (y = 0.6 mm). The results should be the same as that based on the wall-shear information if the y position is within the viscous sub-layer (i.e., within the region where variation of u with y is linear). If this is not true, general knowledge of the streamline pattern in this flow suggests that the results will be biased towards the upstream direction, or shorter x_r. This bias will increase with the value of y at which the analysis is done. Based on this discussion, the direction of the mean, streamwise component of the velocity (U) located at the height closest to the wall was analyzed. Figure 3.3 and Figure 3.4 show the distribution of U for the four 2D Re_h cases.

The U profile is qualitatively similar to the FFP profile shown in Figure 3.1. The U changes direction, or crosses zero (U = 0), two times. The smaller x location at which the profile crosses zero indicates the location of the secondary separation point. As seen with the FFP data, the distance between the secondary separation point and the step decreases with increasing Reynolds number as shown in Figure 3.4. When U drops below zero, this indicates the reverse flow region, or the re-circulating flow zone as shown in Figure 3.3. The larger x position at which U crosses zero is the location of the mean reattachment point. The mean reattachment distance increases with increasing Reynolds number as observed using the FFP method.

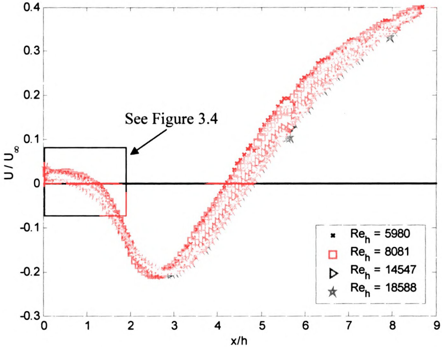

Figure 3.3 Streamwise distribution of the mean, streamwise velocity component at y/h = 0.05 for all four 2D Reynolds number

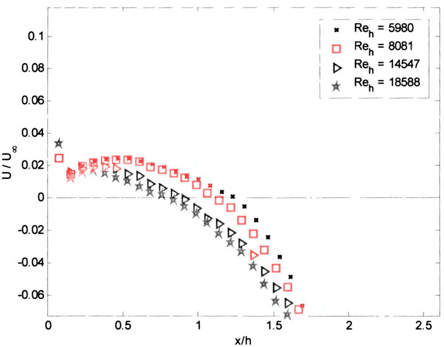

Figure 3.4 Secondary separation region from the streamwise distribution of the mean, streamwise velocity component at y/h = 0.05 for all four 2D Re

Figure 3.5 shows the reattachment distance as function of Reynolds number using both the FFP and U = 0 methods. For comparison, the results of Li and Naguib[1] are also included in the figure. All four profiles show the same trend: as the Reynolds number increases, x_r increases. Comparing the two methods, the FFP estimates a longer reattachment distance than the U = 0 method, which was also seen in the Li and Naguib[1] study. This difference may be inherent to the methods used. The FFP method determines the streamwise position that delineates where 50% of the records show the direction of the flow is in the downstream direction. This will only coincide with the location of U = 0 if the probability density function (pdf) of u is not skewed.

In addition, it is good to compare the x_r values obtained here to those from other studies in the literature, which generally find x_r to be equal to roughly 5-6h for a planar backward-facing step. Spazzini *et al.*[2] reported $x_r/h = 5.39$ in their planar BFS study at $Re_h = 5100$, Tihon *et al.*[5] found $x_r/h = 5.1$ at $Re_h = 4800$, and Jovic and Driver[9] measured $x_r/h = 6.0$ for $Re_h = 6000$. Eaton and Johnston[6] reported in their review of planar backward-facing step studies that the x_r values measured ranged from 4.9 to 8.2 step heights.

The shorter x_r values reported in this study differ from most BFS studies in the literature. However, these studies are either investigations using planar, backward-facing-step geometries or sudden-expansion pipes. Li and Naguib[1] measured the mean reattachment length in the same axisymmetric, backward-facing-step geometry employed here using an oscillating hotwire that measures the wall shear stress and found $x_r/h = 4.6$ at Re_h= 8700. They determined reattachment as the point where the wall shear stress equaled zero. Their reattachment length was also shorter than those reported in the

literature. Li and Naguib[1] attributed the shorter reattachment length to the difference in geometry, stating that even though a sudden expansion is axisymmetric, the geometry has a concave curvature and the boundary layer characteristics at separation may be different.

Comparing the current study to that of Li and Naguib[1], the x_r values measured by Li and Naguib[1] were at most 6% longer than those measured in the present study (Figure 3.5). This is expected because Li and Naguib[1] were able to measure three times closer to the wall (approximately 100μm above the wall). If data had been obtained closer to the wall in the present study, then the x_r value would be longer, in qualitative agreement with the Li and Naguib[1] data. This is because of the bias towards the upstream in the values of x_r measured at y locations that are close to the wall but above the viscous sub-layer, as discussed above. Nevertheless, it seems that the FFP method provides x_r values closer to the results of Li and Naguib[1]. Therefore, x_r values calculated using the FFP method were used throughout the present study as the best estimate of the mean reattachment length. The x_r values calculated by Li and Naguib[1] were not used in this study because the Re range used in their study stretched only from 4000-13000. In the present study, the highest Re case is 18588.

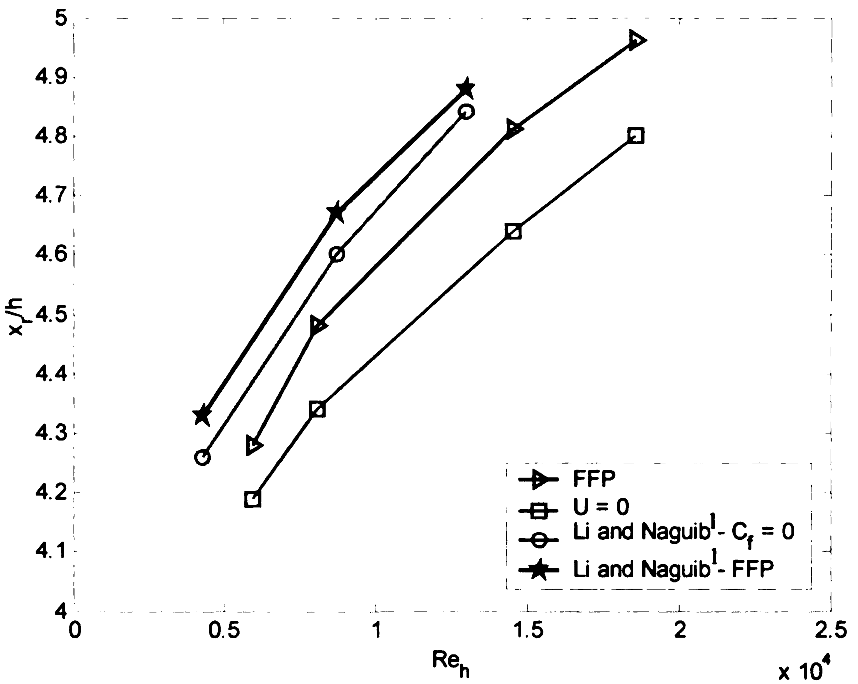

Figure 3.5 Reynolds number dependence of x_r, calculated using FFP and U = 0 and compared to Li and Naguib[1] data

3.2 Boundary Layer Velocity Profiles

Boundary layer velocity profiles were acquired using hotwire anemometry in order to characterize the state of the boundary layer at separation. As mentioned in the experimental set-up, strips of sandpaper were placed near the nose of the model in order to trip the boundary layer and accelerate its development to a turbulent, boundary layer at separation. The state of the boundary layer was determined by comparing the mean streamwise velocity profile from the current study with that from Naguib[8], who acquired hotwire measurements within a turbulent, boundary layer.

In order to make the comparison, the measured boundary-layer profiles were normalized and displayed in the classic $U^+ = U/u_\tau$ versus $y^+ = yu_\tau/\nu$ profile on a semi-log plot ($u_\tau = (\tau_w/\rho)^{1/2}$ where, τ_w is the shear stress at the wall and ρ is the fluid density). Since u_τ was not measured in the experiment, it was estimated by comparing the measured profile with the law of the wall empirical equation provided by Spalding[10]

$$y^+ = U^+ + e^{-kc}\{e^{kU^+} - 1 - kU^+ + 1/2(kU^+)^2 - 1/6(kU^+)^3\} \qquad (3.1)$$

The u_τ value used to normalize was iterated until the mean, squared error between the first five values of the measured boundary layer in the y^+ versus U^+ profile and the Spalding equation was minimized (within 2%). This percentage was determined by dividing the mean, squared error by the maximum y^+ value in the first five points. The Spalding fit and measured boundary layer profile with the calculated u_τ value are shown in Figure 3.6. This technique was first introduced by Kendall and Koochesfahani[11]. Although Clauser-fit is a common way of estimating the shear stress at the wall, it requires being able to locate the beginning and end of the log region. By using the Spalding equation, the data is fit to the boundary layer profile in wall units and stretches from the wall to the end of the log region as shown in Figure 3.6. This removes some of the uncertainties associated with determining the log region. Kendall and Koochesfahani[11] were able to use the technique to estimate the wall shear stress with an accuracy of within two percent.

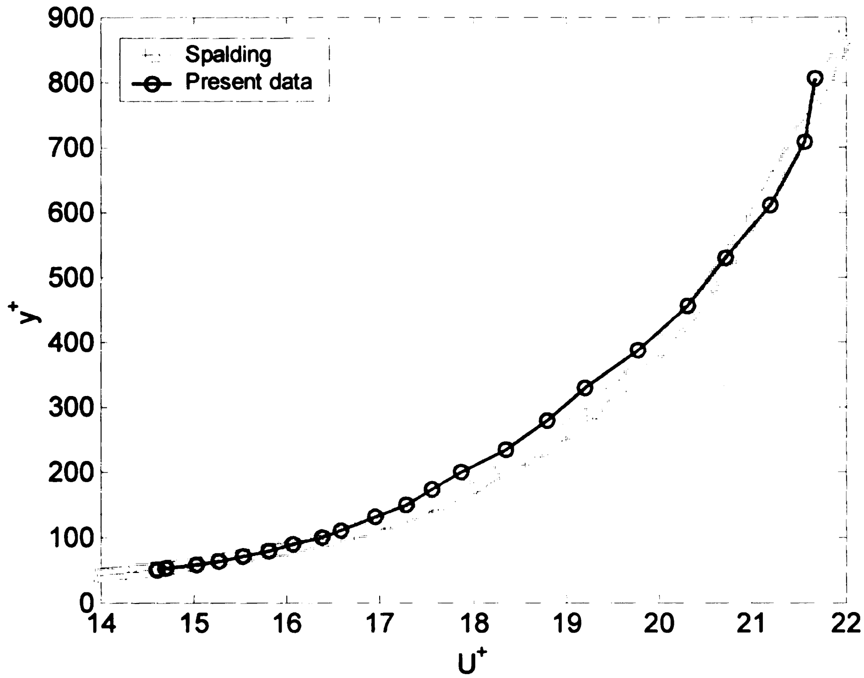

Figure 3.6 Comparison of the measured boundary layer profile with the Spalding equation

Once the u_τ was determined to be approximately 0.46 m/s, the boundary layer from the present experiment could be compared with previously measured turbulent boundary layer profiles to verify if the present boundary layer was turbulent at separation. Figure 3.7 shows this comparison between the present measurements, $Re_\theta = 1237$, and Naguib's[8] boundary layer measurements at $Re_\theta = 1577$. In Figure 3.7, mean-velocity profiles are scaled using wall variable and are plotted on a semi-log axis. In addition to Naguib's[8] data, the standard log-law in log-linear coordinates is presented, U^+ =

$2.44*\ln(y^+)+5.5$ as given in Hinze[12]. It can be observed that the present data collapse with Naguib's data and the log law over a range of $50<y^+<200$, representing a fairly small log region. Above $y^+ \sim 200$, Naguib's[8] data overshoots the log-law as expected for a fully-developed boundary layer. The y-range over which this overshoot occurs is known as the 'wake' region. In contrast, the present boundary layer does not exhibit much of a wake zone, where such an overshoot is hardly seen.

The above discussion indicates that at separation, the state of the inner portion of the boundary layer, based on the streamwise-velocity statistics, is consistent with the state of the inner portion of a fully-developed, turbulent, boundary layer, while the outer part is not. Figure 3.8 may be used to draw a similar conclusion based on the profiles of the turbulent streamwise velocity. The semi-log plot gives the normal distance to the wall along the abscissa normalized by the friction velocity and kinematic viscosity, and the u_{RMS} normalized by u_τ is represented on the ordinate. Data from both the present experiment and Naguib[8] are shown for comparison. The two sets of data collapse, starting around $y^+ > 400$. Traditionally, when comparing equilibrium boundary layers at different Reynolds numbers using wall scaling, the u_{RMS} values in this region do not collapse but increase in value with increasing Reynolds number.

To further examine the reasonableness of the estimated u_τ magnitude, Figure 3.9 shows a comparison between the friction coefficient calculated from the relationship $C_f = 2(u_\tau/U_\infty)^2$ and the Ludweig and Tillmann (Hinze[12]) empirical relation for C_f versus Re_θ ($Re_\theta = U_\infty\theta/\nu$, where θ is the momentum thickness). The Ludweig and Tillmann relation, which is based on direct wall shear stress measurements, is given by

$$C_f = 0.246\times10^{-0.678H_{12}}\,\mathrm{Re}_\theta^{-0.268} \tag{3.2}$$

where $H_{12} = \delta^*/\theta$ is the shape factor and δ^* is the displacement thickness. The relationship between parameter H_{12} and Re_θ is defined by

$$H_{12} = 1.773\,\mathrm{Re}_\theta^{-0.0276} \tag{3.3}$$

Comparing the present C_f value with the Ludweig and Tillmann relation, it can be seen that the present value falls just outside of the 5% range from the curve. This deviation is believed to be caused by "underdevelopment" of the outer-layer turbulence as discussed in the following paragraphs.

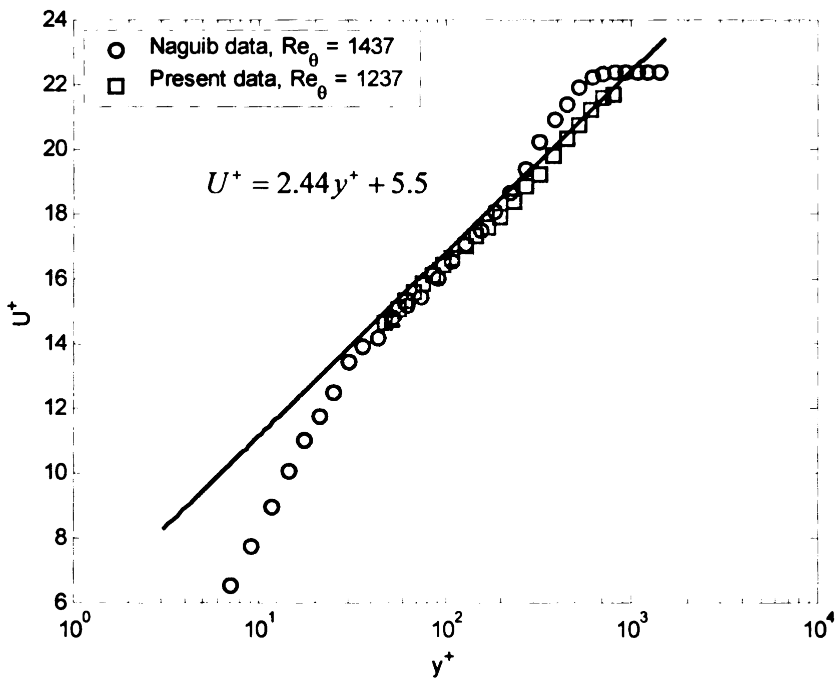

Figure 3.7 Boundary-layer mean velocity profiles from present experiment and Naguib's[8] data

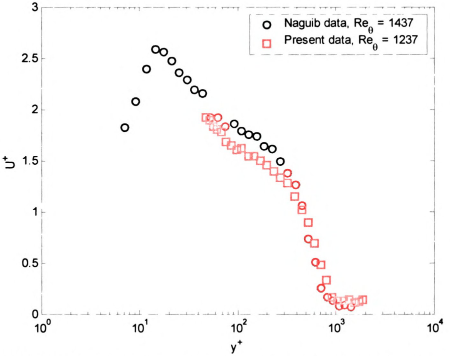

Figure 3.8 Boundary-layer turbulent-streamwise-velocity profiles from present experiment and Naguib[8] data

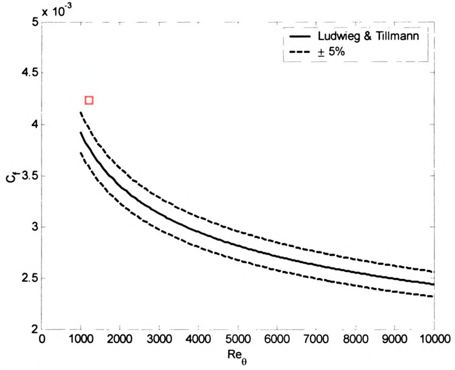

Figure 3.9 Comparison of friction coefficient value from the present experiment with the Ludweig and Tillmann relation

The

developed.

reflection

reach equ

structures

of the ou

or δ (fo

that the

from th

the inn

the tur

not sh

The finding that the boundary layer state at separation has developed into a fully-developed, or equilibrium, state in the inner portion but not in the outer region is a reflection of the need for longer boundary layer development length for the outer layer to reach equilibrium. This is consistent with the fact that the time scales of the outer-layer structures is substantially higher than that of the inner-layer turbulence. In fact, the ratio of the outer to inner time scales is the same as the ratio of the outer to inner length scales, or δ^+ (for this study, this ratio is approximately 1000). However, it is important to note that the recent study of Morris and Foss[13] has demonstrated that for shear layers resulting from the separation of a turbulent boundary layer, the dynamics of the flow is dictated by the inner layer with the outer layer playing a passive role. Therefore, whether the state of the turbulence in the outer portion of the flow is that of an equilibrium boundary layer or not should be of no particular significance to the current study.

3.3 I

Re_a = 5

pressur

pul sp

which

surface

located

a clas

betwe

of the

to rec

then c

Imme

this r

Furth

shor

Beyo

expla

3.3 Mean-pressure distribution

The mean-pressure, streamwise distribution, acquired at four Reynolds numbers (Re_h = 5980 – 18588) downstream of the axisymmetric, backward-facing step using static pressure taps, are shown in Figure 3.10. The mean-pressure coefficient, $C_p = (p_s - p_r)/(½\rho U_\infty^2)$, is plotted along the ordinate as a function of the streamwise coordinate, which is plotted on the abscissa as x/h (note that p_s is the pressure measured along the surface of the model and p_r is the reference pressure measured with a static pressure tap located at the exit of the wind-tunnel contraction). The mean-pressure distributions show a classical, backward-facing-step, pressure profile with mean reattachment located between x_r = 4-5h (x_r found from PIV analysis in Section 3.1). Immediately downstream of the step, the pressure distribution decreases until about $0.5x_r$ where the pressure begins to recover, reaching a peak slightly downstream of x_r. The mean-pressure distribution then drops slightly as the shear layer reattaches to form a boundary layer.

Comparing the four Re_h cases, a trend is easily observed in Figure 3.10. Immediately downstream of the step, the pressure drops between the step and $0.5x_r$. In this region, it can be seen that the C_p values increase with increasing Reynolds number. Furthermore, the mean-pressure distribution for the lower Re_h values recovers over a shorter distance, consistent with the shorter mean reattachment length found earlier. Beyond reattachment, the C_p values are lower for lower Re_h values. This trend is explained below.

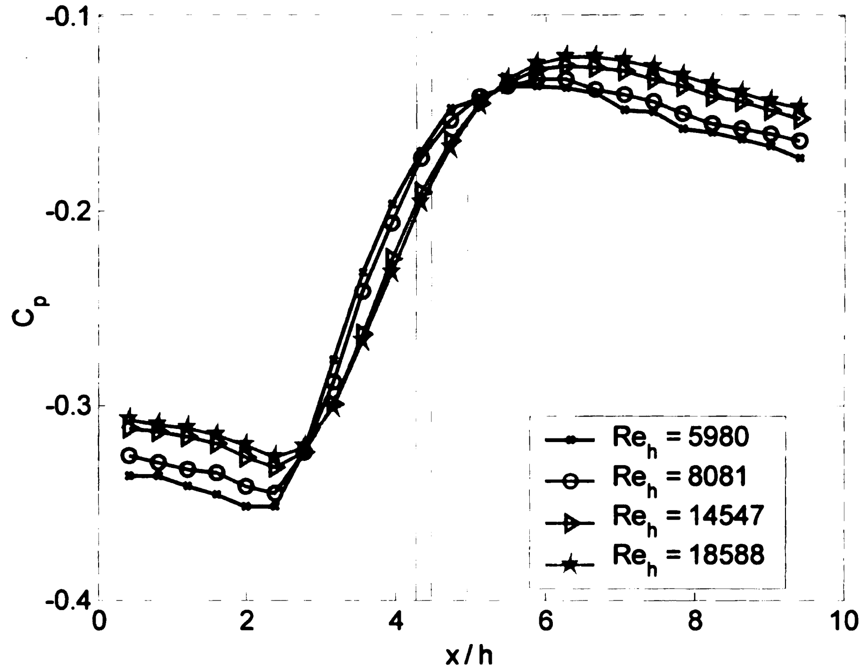

Figure 3.10 Mean-pressure distribution for all Reynolds numbers, 2D case only, with a line marking the corresponding x_r value for each case

Previous planar, backward-facing-step studies, such as Westhal[14], Roshko and Lau[15], and Adams *et al.*[16], have shown that static pressure data collapse to a universal curve when normalized using the following equation and plotted versus x/x_r

$$C_p^* = \frac{C_p - C_{p_{\min}}}{1 - C_{p_{\min}}} \tag{3.4}$$

where $C_{p_{\min}}$ is the minimum C_p in the mean-pressure distribution. Figure 3.11 shows the present static pressure data for all four Re normalized as C_p^* and plotted along the ordinate. Streamwise distance with respect to reattachment is represented on the abscissa. The C_p^* distribution for all four Re numbers collapsed through reattachment.

Adams *et al.*[16] found in their planar, backward-facing-step study that static pressure profiles for several Reynolds numbers, spanning 8500 to 41000, collapsed through reattachment. The boundary-layer thickness at separation for all cases was approximately $\delta/h = 1.1$. The pressure-recovery curves for these thick boundary layers were independent of Reynolds number. Westphal[14] and Roshko and Lau[15] found the same conclusion for thin boundary layers.

Beyond reattachment, the pressure profiles differ from each other with a larger C_p^* associated with a lower Re. The C_p^* of Adams *et al.*[16] exhibited a trend similar to that seen in Figure 3.11 and suggested that downstream pressure recovery is influenced by blockage within the wind tunnel.

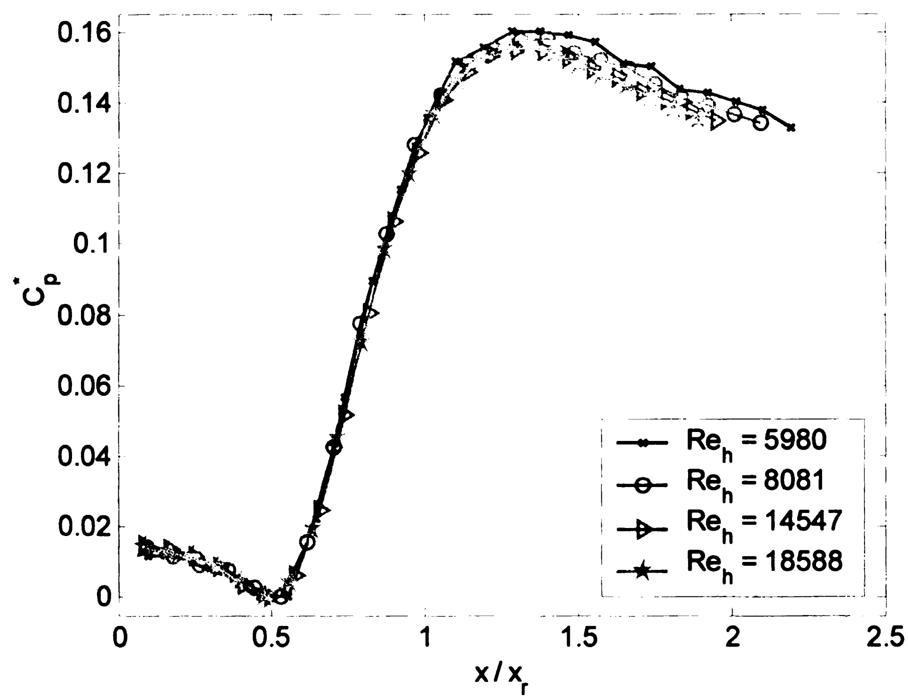

Figure 3.11 Mean-pressure coefficient distribution for the four Re cases

3.4 References

[1] Li, Y. and Naguib, A.M., "High-Frequency Oscillating-Hotwire Sensor for near-Wall Diagnostics in Separated Flows," *AIAA Journal*, Vol. 43, No. 3, 2005, pp. 520.

[2] Spazzini, P.G., Iuso, G., Onorato, M., Zurlo, N., and Di Cicca, G.M., "Unsteady behavior of back-facing step flow," *Experiments in Fluids*, Vol. 30, 2001, pp. 551-561.

[3] Eaton, J. K., "Turbulent flow reattachment: an experimental study of the flow and structure behind a backward-facing step," Ph.D. Dissertation, Stanford University, 1980.

[4] Westphal, R.V. and Johnston, J.P., "Effect of initial conditions on turbulent reattament downstream of a backward-facing step," *AIAA Journal*, Vol. 22, 1984, pp. 1727-1732.

[5] Tihon, J., Legrand, J., and Legentilhomme, P., "Near-wall investigation of backward-facing step flows," *Experiments in Fluids*, Vol. 31, 2001, pp. 484-493.

[6] Eaton, J. K. and Johnston, J.P., "A Review of Research on Subsonic Turbulent Flow Reattachment," *AIAA Journal*, Vol. 19, No. 9, 1981, pp. 1093-1099.

[7] Adams, E.W. and Johnston, J.P., "Effects of the separating shear layer on the reattachment flow structure, Part 2: Reattachment length and wall shear stress," *Experiments in Fluids*, Vol. 6, 1988, pp. 493-499.

[8] Naguib, A.M., Wark, C.E., and Juckenhöfel, O., "Stochastic estimation and flow sources associated with surface pressure events in a turbulent boundary layer," *Physics of Fluids*, Vol. 13, No. 9, 2001, pp. 2611-2626.

[9] Jovic, S. and Driver, D., "Reynolds number effect on the skin friction in separated flow behind a backward-facing step," *Experiments in Fluids*, Vol. 18, 1995, pp. 464-467.

[10] Spalding, D. B., "A Single Formula for the Law of the Wall," *Journal of Applied Mechanics*, Vol. 28, 1961, pp. 455-457.

[11] Kendall, A. and Koochesfahani, M. M., "A new method of estimating wall shear stress is turbulent boundary layers," *57th Annual Meeting of the American Physical Society Division of Fluid Dynamics*, Seattle, Washington, November 21-23, 2004.

[12] Hinze, J. O., *Turbulence: An Introduction to Its Mechanism and Theory*, McGraw-Hill Book Company, Inc., New York, 1959, pp. 486.

[13] Morris S. C., and Foss, J. F., "Turbulent boundary layer to single-stream shear layer: the transition region," *Journal of Fluid Mechanics*, Vol. 494, 2003, pp. 187-221.

[14] Westphal, R.V., "Experimental study of flow reattachment in a single-sided sudden expansion," Ph.D. thesis, Stanford University, 1983.

[15] Roshko, A. and Lau, J. C., " Some observations of transition and reattachment of a free shear layer in incompressible flow," *Proceddings of 1965 Heat Transfer and Fluid Mechanics Institute*, Stanford University Press, pp. 157-167, 1965

[16] Adams, E. W., Johnston, J. P., and Eaton, J. K., " Experiments on the structure of turbulent reattaching flow," Report MD-43, Department of Mechanical Engineering, Stanford University.

4 Wall-pressure Measurements

4.1 Introduction

The array of microphones embedded in the surface downstream of the axisymmetric, backward-facing step was utilized to investigate the space-time character of the wall-pressure field beneath the shear layer and the reattached, boundary layer. Although separated flows have been studied extensively over the years, especially in the classic geometries such as the backward-facing step, splitter plate, and splitter-plate-with-fence, most studies have been planar geometries. In addition, only a few of these studies utilized an array of microphones embedded in the surface.

Several studies over the years have investigated the flow field downstream of a planar backward-facing step. Eaton and Johnston[1], in 1981, reviewed the research done on the classic backward-facing step geometry in effort to summarize the data available at the time and to suggest areas worth investigating. Most of the studies up until that time had been conducted using hotwire, pulsed-wire, and laser anemometry. Since then, there have been a good number of studies in this classic geometry that have used more current techniques such as surface pressure sensors and particle image velocimetry (PIV). The ones containing mostly surface-pressure data are summarized below. The studies that utilized PIV will be highlighted in the next chapter (Section 5.1), which provides analysis of the velocity field.

Farabee and Casarella[2], in 1986, studied fluctuating wall pressures in a forward-facing and backward-facing step using a flush-mounted B&K 1/8in. condenser microphone to measure the surface pressure fluctuations. They characterized the backward-facing step as having an "attached shear layer" that separates from the step at the edge and reattaches on the wall a short distance later. From the root-mean-squared (RMS) turbulent pressure values, they observed the surface-pressure fluctuations to rise rapidly with increasing streamwise distance as the shear layer structures grew in strength and moved downstream. These fluctuations reached a maximum as the flow impinged on the surface of the plate at reattachment. The measurements of Farabee and Casarella[2] were compared to those from the surface beneath an equilibrium flat-plate, boundary-layer flow. The measured RMS values at reattachment were 5 times larger than those measured in the equilibrium flow farther downstream.

Using frequency domain analysis, Farabee and Casarella[2] described the characteristics of the wall-pressure field as variable with streamwise distance along the wall. Close to separation, the spectra showed the highest level of energy at very low frequencies; whereas, farther downstream the spectrum containing the largest energy was found at reattachment. This was a manifestation of the increase in the energy of the organized, turbulent structures as they convected downstream. A corresponding shift was seen in the spectrum as the dominance of the low-frequency disturbances gave way to the dominance of the high-frequency structures downstream. Farabee and Casarella[2] also stated that the energized structures diffused and decayed beyond reattachment; however, these structures were still identifiable 72 step heights downstream of the step.

In 1987, Driver *et al.*[3] identified two types of fluctuating motion in their backward-facing-step study of the time-dependent character of the separated, shear layer at a Reynolds number of 37,000, based on the step height. The first type was the flapping of the shear layer that has been identified by many researchers, and the second was a quasi-periodic vortical type motion, which, they stated, needed further investigation.

Driver *et al.*[3] noticed abnormal contraction and elongation of the separation bubble as a result of the shortening and lengthening of the reattachment length. This was labeled as the flapping motion of the shear layer with amplitude estimated to be 20% of the shear layer width, or vorticity thickness. They also found the direction of the flow to change intermittently over the range of ±1 step height from the reattachment point. In addition, Driver *et al.* identified a low frequency disturbance in the flow from surface-pressure and velocity measurements. They stated these low-frequency disturbances were random and contributed very little energy to the overall pressure fluctuations, but were believed to be associated with the shear layer flapping.

Heenan and Morrison[4] investigated wall-pressure fluctuations behind a rearward-facing step and passive control of these fluctuations using a permeable surface (at Reynolds number equal to 1.9×10^5 based on the step height) in 1998. A particularly interesting feature of Heenan and Morrison's study is that they were able to remove the low-frequency surface-pressure signature associated with shear-layer "flapping" by using the permeable surface placed downstream of the step. They attributed this success to inhibiting the re-circulating flow responsible for the upstream convection of disturbances formed at reattachment. Although the characteristics of the measured, wall pressure in the non-permeable case were consistent with that summarized earlier in this section, one difference existed. Specifically, Heenan and Morrison[4] found an *upstream* convection velocity close to separation using phase-angle analysis. They identified negative phase angles (with respect to a microphone signal measured immediately behind the step) at low frequencies and at locations from separation up to $0.4x_r$ in the impermeable case.

In 2001, Lee and Sung[5] used a 32-microphone array downstream of a planar backward-facing step to measure wall-pressure fluctuations in the streamwise and spanwise directions. Spatio-temporal statistics were extracted from this comprehensive data set for a Reynolds number of 33,000, based on the step height. Lee and Sung[5] observed the RMS pressure fluctuations rose sharply starting around $0.5x_r$ and peaked in the vicinity of reattachment, decaying beyond that point. In addition, pressure spectra revealed low-frequency dominance close to separation, presumably caused by the flapping of the shear layer. Farther downstream, the spectra were dominated by high-frequency components. In terms of the convection velocity, Lee and Sung[5] calculated a downstream convection velocity of $0.6U_\infty$ at high frequencies, and they did not find evidence of an upstream convection velocity. Although from their phase plot used to determine the convection velocity, there were many singularities (phase discontinuities) at low frequencies. This was not the case at the higher frequencies.

Also from 2001, Spazzini *et al.*[6] concentrated their investigation on the low-frequency motion identified in their backward-facing step. In their experiment, using Forward-Flow Probability (see Section 3.1 for definition) from skin friction measurements, they studied two important areas beneath the shear layer: (1) the mean, reattachment point and (2) the secondary, separation point. Similar to wall-pressure fluctuations, the maximum of the streamwise skin-friction RMS distribution was found slightly upstream of the reattachment point. Employing Fourier analysis, 75% of the total energy in the wall-shear spectra was found to be contained at low frequencies lower than $fx_r/U_\infty = 0.4$ at locations in the vicinity of the step up to 0.3 of the reattachment distance.

Farther downstream, $x/x_r = 0.7$, this same frequency range contained only 30% of the total energy. At this position, the spectra were dominated by higher frequencies.

Using a wavelet transform for more detailed analysis of the low frequency motion, Spazzini *et al.*[6] suggested that at a comparable frequency to the flapping frequency there was intense activity in the secondary, re-circulation bubble. This hypothesis was examined further using PIV measurements in a water-tunnel experiment. Based on visual observation, it was proposed that the cyclic behavior of the secondary, re-circulation bubble had a frequency corresponding to the low frequency revealed by the wavelet analysis.

In 2001 and 2003, Hudy[7] and Hudy *et al.*[8], respectively, compiled a database of wall-pressure-array measurements for studying the space-time characteristics of the surface-pressure field within a separating/reattaching flow region. The experimental geometry was a splitter-plate-with-fence that was instrumented with an array of flush-mounted microphones. Data were acquired for a Reynolds number of 7900, based on the height of the fence above the splitter plate. Two distinct regions, defined based on their location relative to the position of the mean reattachment point (x_r) of the shear layer, were identified by the authors. The first region was located upstream from the fence to $0.25x_r$. In this region, the surface-pressure signature was dominated by large-time-scale disturbances and an upstream convection velocity of $0.21U_\infty$. Beyond $0.25x_r$, turbulent structures with smaller time scales and a downstream convection velocity of $0.57U_\infty$ generated most of the pressure fluctuations.

In 2004, Daoud[9] investigated the reattached boundary layer downstream of the separation region in the splitter-plate-with-fence geometry used by Hudy[7] and Hudy *et* *al.*[8] Daoud[9] used 16 microphones embedded in the surface, starting at x/h = 37.5 and extending to x/h = 75. The reattachment point, based on step height, was measured to be $x_r = 22.5h$ and the two Reynolds-number cases investigated were $Re_h = 7600$ and 15700. Using a frequency-wavenumber analysis, Daoud[9] found only high frequency structures within the reattached boundary layer. In addition, Daoud[9] stated that these structures had a convection velocity that was independent of frequency, meaning the structures were non-dispersive. That is, structures of different scales travel at the same speed. Daoud[9] determined this speed to be $0.81U_\infty$.

The objectives for this section are to investigate only the surface-pressure signature downstream of the axisymmetric backward-facing step. Specifically, this chapter investigates the wall-pressure signature in a 2D separating boundary-layer flow field in order to understand the wall-pressure physics surrounding each case using spatio-temporally-resolved measurements of the wall-pressure. In addition, Reynolds-number effects in the 2D case are explored.

4.2 Results and Discussion

The wall-pressure data presented below were sampled simultaneously with PIV data; thus, the mirror mounted on the tail of the model was installed when these pressure measurements were made. The effect of the mirror was checked as explained in Appendix 8.4. The sampling frequency of the pressure was 12 kHz for 35 seconds. This resulted in a total of 420,000 points acquired for each flow condition.

4.2.1 Fluctuating-pressure distributions

The microphone array embedded in the wall of the model downstream of the step was used to measure the spatial distribution of the pressure fluctuations produced by the passage of various flow structures over the reattachment surface. These fluctuations represent the instantaneous deviation from the mean pressure measured by the static-pressure taps. The root-mean-square (RMS) of the pressure fluctuations (p'_{RMS}) determines a measure of the strength of the pressure deviations from the mean. Additionally, the square of the RMS pressure fluctuations presents the 'energy' of the unsteady pressure time series, thus the larger the RMS, the stronger the pressure fluctuation.

The present RMS measurements (plotted as $C_{p'} = p'_{RMS}/\frac{1}{2}\rho U_\infty^2$) are shown in Figure 4.1 for all four Re_h cases. The $C_{p'}$ is plotted along the ordinate as a function of the streamwise distance from the step, x/h, on the abscissa. A three-point average was used to smooth the RMS results shown in Figure 4.1 to reduce some data scatter associated with

in A

liter

rela

A l

RV

rea

C

with uncertainties in microphone sensitivity calibration, which is explained in more detail in Appendix 8.4.

The shape of the RMS distributions is consistent with that documented in the literature for a backward-facing step. At the point of separation, the shear layer is relatively far away from the wall-pressure sensors. Thus, at the first microphone location ($x/h = 0.43$), a low RMS pressure fluctuation is detected followed by a rapid increase of RMS pressure values with increasing downstream distance from the step up to the point of reattachment, approximately. Within this region of the flow from the step to reattachment, it is believed that the surface-pressure fluctuations are predominately associated with shear-layer vortical structures. As these structures convect downstream, growing in size and strength and moving closer to the wall, they produce an increasingly strong, wall-pressure signature. This signature reaches a maximum level in the vicinity of where the flow impinges, or reattaches, on the wall as described by Farabee and Casarella[2]. Beyond reattachment, the RMS values slowly decrease as the energized structures from the shear layer decay and diffuse downstream in the reattached boundary layer. Similar effects were recorded by Farabee and Casarella[2] in their planar backward-facing step study.

The peak in the present data occurs in the vicinity of reattachment. Heenan and Morrison[4] found their peak RMS value at approximately one step height upstream of reattachment, which was determined by using chalk/paraffin flow visualizations as well as sublayer-fence and split-film probes. The magnitude of the RMS peak spans $C_{p'}$ = 0.025-0.03 based on Re_h, which is comparable to the peak RMS found by Farabee and Casarella[2] and Driver *et al.*[3] However, these values are about half the value recorded by

Heenan and Morrison[4] in their planar BFS study. One other point worth noting is that it can be observed in Figure 4.1 that the RMS peak value decreases and shifts towards a larger streamwise position as the Reynolds number increases. This shift of the location of the peak to larger x values is consistent with the increase in reattachment length, and hence the development length, of the shear layer with Reynolds number. On the other hand, the cause of the decrease in the peak-pressure fluctuation is not known presently. Spazzini *et al.* found a similar trend in their fluctuating wall-shear-stress measurements over a Re range of 3500-16000, based on step height. The researchers plotted the normalized wall-shear-stress fluctuations as a function of x/x_r and observed that the peak skin-friction fluctuation value occurred upstream of x_r. No explanation was given regarding the decrease in skin-friction fluctuation with increasing Re. Figure 4.2 shows $C_{p'}$, on the ordinate, as a function of x/x_r, given on the abscissa, for all four Re investigated. The fluctuating-pressure distribution shows a collapse of the profile over the range stretching from separation to $x/x_r= 0.5$. After this streamwise position, the profiles split and the trend becomes evident as seen by Spazzini *et al.* The trend continues downstream of x_r until about $x/x_r = 1.75$ when the three highest Re investigated collapse again. The RMS for the lowest Re remains higher than the rest of the flow cases for the extent of the streamwise distance measured.

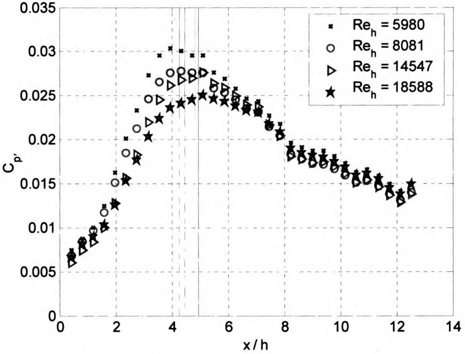

Figure 4.1 RMS pressure distribution for all Reynolds numbers with a line marking the corresponding x_r value for each case

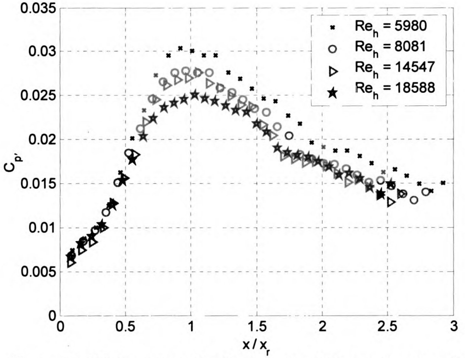

Figure 4.2 RMS pressure distributions for all Re as a function of x/x_r

4.2.2 Auto-correlations

The auto-correlation is useful in identifying the dominant time scales at a particular position in a flow field from the time series measured by a single sensor, such as a microphone. In the case of the current study, the auto-correlation could be calculated at the location of each of the microphones in the array. In addition, the spatial distribution of the auto-correlation starting just downstream of the step edge and extending approximately 12 step heights downstream can be displayed using a flooded-color, contour plot. Figure 4.3 shows the flooded-color, contour plots of the auto-correlation for two Reynolds numbers: Re_h = 8081 and 18588. Along the abscissa, the streamwise distance is normalized by the step height and along the ordinate, the time shift is normalized by the free stream velocity and the step height. The color bar indicates the magnitude of the auto-correlation, which is normalized by the RMS of the microphone signal as follows:

$$R_{p'p'} = \frac{r_{p'p'}}{p'^{\,2}_{RMS}} \tag{4.1}$$

where, $r_{p'p'}$ is the discrete-time auto-correlation function for the signal from each of the microphones and p'_{RMS} is the RMS value for that particular signal. The discrete-time auto-correlation is defined as

$$r_{p'p'}(n, x/h) = \frac{1}{N}\sum_{k_t=0}^{N-1} p'(k_t, x/h)\,p'(k_t - n, x/h) \tag{4.2}$$

where k_t represents the time index, n represents a time shift, or delay, x/h is the streamwise position, and N is the total number of points measured in the time record p'(n).

The auto-correlation for the $Re_h = 8081$ case is shown in Figure 4.3a, and four distinct regions can be seen by following the zero-contour line. The first region extends from x/h = 0, immediately downstream of the step edge, to x/h = 2. In this region, the auto-correlation function extent is wide, indicating that the pressure signature is dominated by long, time scales or low-frequency, flow disturbances. Other backward-facing-step studies, such as Eaton and Johnston[1], Heenan and Morrison[4], Driver *et al.*[3], Farabee and Casarella[2], and Lee and Sung[5], have observed similar time scales near the step. Some of these studies have attributed this low-frequency dominance to the flapping of the shear layer as explained in Heenan and Morrison[4] as well as in Eaton and Johnston[1]. Flapping refers to the unsteadiness of the shear layer trajectory, which results in variations of the reattachment point location. Equivalently, a shortening and lengthening of the separation bubble results from the flapping of the shear layer.

The second distinct region lies between x/h = 2 - 4. At about x/h = 2, the auto-correlation extent narrows, spanning $\tau U_\infty/h = -4$ to 4. The narrowing of the auto-correlation is consistent with what was observed by Hudy *et al.*[8] in their splitter-plate-with-fence study. In that particular study, Hudy *et al.*[8] found the time-scales to narrow over the $x/x_r = 0.25$-0.5 region, which translates to x/h = 1.12h-2.24h in the present study. The time-scales for which significant $r_{p'p'}$ values exist in the present study, narrow abruptly within a shorter region than in the splitter-plate-with-fence study. As explained by Hudy *et al.*[8], the narrowing of the auto-correlation extent is linked to the dominant, flow structures within the shear layer. It is within this region that the flow structures are growing in strength as well as moving closer to the wall-pressure array. Thus, these higher-frequency, flow structures begin to dominate the pressure signature as discussed in other backward-facing-step studies such as Heenan and Morrison[4].

The auto-correlation narrows once again, starting approximately around x/h = 4, to form the third distinct region. The region between x/h = 4 to 8 roughly spans from the start to the end location of a change in the time scales of the flow structures dominating $R_{p'p'}$. Within this region, the time-scales narrow as the flow structures within the shear layer impinge on the wall at x_r and the shear layer reattaches to form a boundary layer. The fourth region starts around x/h = 8 and continues downstream until the end of the microphone array. The auto-correlation extent within this region is the shortest compared to the other three regions. Thus, this region is dominated by the highest-frequency, flow structures. It is hypothesized that the narrowing of $R_{p'p'}$ over the x/h = 4 to 8 range is caused by the dominant, flow structures either convecting at a faster speed and/or changing shape in terms of getting smaller in size. In Section 4.2.4, the cross-correlation is presented, which shows an increase in the convection speed from upstream of reattachment to downstream of reattachment. Beyond x/h = 8, the contour lines remain approximately parallel to the constant τ lines showing very little change in $R_{p'p'}$ with additional increase in x.

The spatial distribution of the auto-correlation for Re_h = 18588 in Figure 4.3b is similar to that seen in Figure 4.3a; although, there are slight differences. Four distinct regions can still be seen, but each region is not as well defined as in Figure 4.3a. First, the region with low-frequency dominance extends from immediately behind the step to about x/h = 2.5. Beyond x/h = 2.5, the auto-correlation starts to narrow over a long streamwise distance, stretching from x/h = 2.5 to 8. Although the overall trend is the same in terms of the region closest to the step being dominated by low frequency and the regions farther downstream being dominated by higher-frequency, the imprint of the pressure signature paints a slightly different picture in terms of where the dominant time scales transition and how abrupt the transition is over the streamwise distance.

In order to investigate the differences in the auto-correlations between the two Reynolds numbers in more detail, the individual auto-correlations at 12 different streamwise positions were plotted for both Reynolds numbers in the same graph as shown in Figure 4.4 and Figure 4.5. Figure 4.4 gives six streamwise positions upstream of x_r, which include the following x/h = 0.822, 1.6, 2.38, 3.16, 3.96, and 4.72. The abscissa represents the time shift normalized by freestream velocity and the step height. The ordinate shows the magnitude of the auto-correlation function as given by Equation (4.1). The same axes are used in Figure 4.5 for six streamwise positions located downstream of reattachment. The positions are x/h = 5.5, 7.07, 8.63, 10.2, 11.7, and 12.5.

The first position explored in Figure 4.4, x/h = 0.822, shows that the magnitude of the auto-correlation for both cases collapses between $R_{p'p'} = 0.7 - 1.0$. In this region, the time scale is relatively short. At $R_{p'p'} < 0.7$, the auto-correlation function for the Re_h = 18588 case becomes wider than the $R_{p'p'}$ for the Re_h = 8081 case. In addition, the smaller Reynolds number crosses the $R_{p'p'} = 0$ axis at $\tau U_\infty/h = \pm 10$; whereas, in the Re_h = 18588 case the zero axis is crossed at $\tau U_\infty/h = \pm 20$, approximately. This shows that, near the step, the higher Re case experiences a longer-time-scale, pressure signature than the lower Re case, and/or that the fluctuations associated with long time scales are relatively more energetic at the higher Reynolds number. The same is true for the other streamwise positions shown in Figure 4.4 and Figure 4.5, where it seems as though the $R_{p'p'}$'s for the two cases collapse for the shorter time scales. Meanwhile, the Re_h = 18588 case depicts a stronger influence of the longer time scales compared to the other case. The difference between the two cases at large time delays is evident upstream and downstream of the reattachment position. The two $R_{p'p'}$'s converge in magnitude as x_r is approached and then slowly diverge beyond reattachment. Near x_r (x_r/h = 4.72) the two cases show nearly prefect collapse.

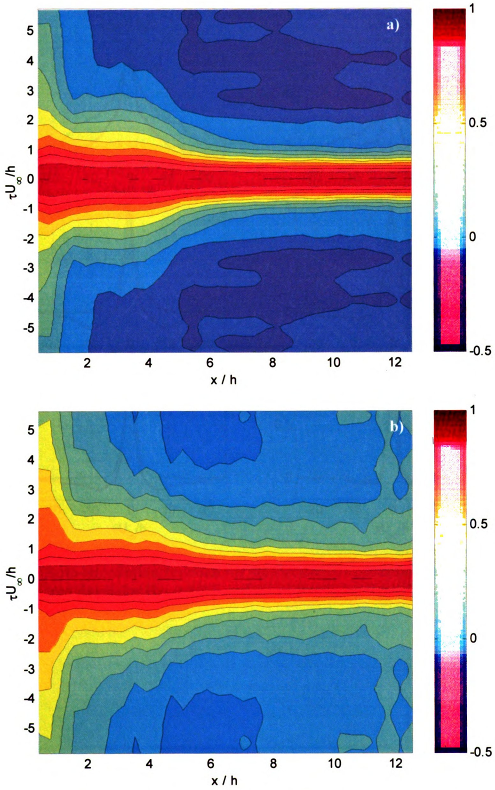

Figure 4.3 Flooded-color, contour maps of the wall-pressure auto-correlation at Re_h = a) 8081 and b) 18588

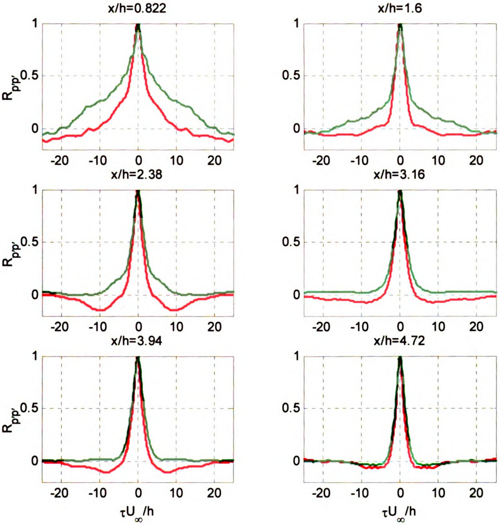

Figure 4.4 Auto-correlation function for six streamwise positions upstream of x_r – red line is for Re_h = 8081 and green line is for Re_h = 18588

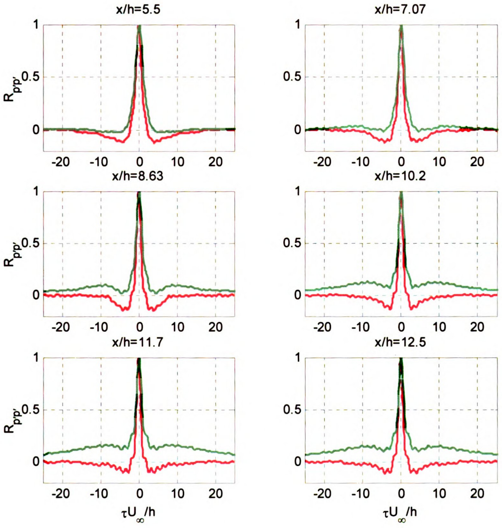

Figure 4.5 Auto-correlation function for six streamwise positions downstream of x_r - red line is for Re_h = 8081 and green line is for Re_h = 18588

4.2.3 Frequency spectra

Figure 4.6 shows the evolution of the wall-pressure frequency spectra with downstream distance. This figure contains the power spectrum plots on a logarithmic scale for both axes. The spectra are normalized by $(1/2\rho U_\infty^2)^2$ and plotted along the ordinate relative to an arbitrary reference value. The abscissa represents the frequency normalized by the fence height and freestream velocity. The use of an arbitrary reference value for the ordinate provides a means by which many spectrum plots can be displayed on the same plot without clutter. Twelve spectra from two flow cases (Re_h = 8081 and 18588) are shown in Figure 4.6. The streamwise locations of the 12 selected microphones are the same as used in the individual auto-correlation plots in Figure 4.4 and Figure 4.5.

The spectra in Figure 4.6 show the distribution of pressure-fluctuation energy with frequency and how this distribution varies with streamwise position. The spectrum at the first streamwise position (x/h = 0.82) shows a peak at the low-frequency end of the spectrum. The peak for Re_h = 8081 case is found approximately at $fh/U_\infty = 0.014 \pm 0.002$ and for Re_h = 18588 the peak is located around $fh/U_\infty = 0.011 \pm 0.0008$ (the error band is based on the spectrum resolution). In comparison with planar backward-facing-step studies, Lee and Sung[5] found a similar peak close to separation at a frequency value of $fh/U_\infty = .015$. This is comparable to values given by Heenan and Morrison[4] at fh/U_∞ = .017 and Spazzini *et al.*[6] at $fh/U_\infty = .012$. The latter authors used skin-friction spectra to determine the peak in comparison to the other studies that used wall-pressure spectra. Many studies, including the three mentioned here, have associated the low-frequency peak with the flapping of the shear layer. Farabee and Casarella[2] suggested that the energy distribution in the spectra indicates that the wall-pressure fluctuations close to separation were caused by the unsteadiness of the low-speed, re-circulating flow, rather than the highly turbulent structures in the shear layer. This is consistent with the fact that these structures are only beginning to develop in this region and are most likely weak compared to the strength of the low frequency disturbance produced by the shear layer flapping.

Farther downstream, the first noticeable shift in the peak to higher frequencies occurs at streamwise location $x/h = 2.38$ or $x/x_r = 0.53$ for $Re_h = 8081$ and $x/h = 2.77$ or $x/x_r = 0.56$ for $Re_h = 18588$. At these locations, the peak in the frequency spectra is $fh/U_\infty = 0.039 \pm 0.002$ for the $Re_h = 8081$ case and $fh/U_\infty = 0.036 \pm 0.0008$ for the $Re_h = 18588$ case. This is approximately the same location where there is a fairly abrupt narrowing of the auto-correlation in Figure 4.3. Lee and Sung[5] stated that the power spectrum in their planar BFS study reached a maximum at $fh/U_\infty = 0.068$. This peak was found in all the spectra stretching from x = 2-10h with $x_r = 7.4h$. Both Spazzini *et al.*[6] and Heenan and Morrison[4] found their maximum at $fh/U_\infty = 0.15$ and $fh/U_\infty = 0.17$, respectively. Spazzini *et al.* identifies the shift in the peak at $x/x_r = 0.5$, where the FFP value reduces to zero. Heenan and Morrison find their high-frequency peak near $x/x_r = 0.75$, which they say correlates with the maximum pressure recovery in the separation bubble based on C_p measurements. Finally, Driver *et al.*[3] recorded a peak frequency value close to $fh/U_\infty = 0.098$ at both $x/h = 5.5$ and $x/h = 8$. The reattachment length in their study was $x_r = 6.1$. This higher-frequency peak has been attributed to the structures within the shear layer, as discussed previously.

One point worth mentioning is the range of the high versus low frequency peak values reported in this study and in the literature. The values listed for the high frequency peak near reattachment vary over a range of 0.036 to 0.17, depending on the study. All of these studies, except the present study, were on planar backward-facing steps. Yet even in the planar BFS the range is relatively large compared to the differences seen in the low-frequency peak values. Both peak values are shown in Table 4.1 along with the authors and Reynolds numbers for each study. The average low-frequency value reported is $fh/U_\infty = 0.0138 \pm 0.0024$; whereas, $fh/U_\infty = 0.093 \pm 0.057$ is the average for the high frequency peak including the present study. Without the present study, the average is $fh/U_\infty = 0.12 \pm 0.05$ for the high-frequency peak. This could indicate that the low frequency peak is Reynolds number independent since all these studies were done at different Re and in different overall test conditions (boundary layer state, test-section blockage, etc.). The high-frequency peak seems to be more sensitive to the Reynolds number and/or changing test conditions.

Table 4.1 Frequency values of spectrum peaks and Re for five different studies

Study	**Re_h**	**Low frequency peak**	**High frequency peak**
Present	8081	0.014	0.039
Present	18588	0.011	0.036
Lee and Sung[5]	33000	0.015	0.068
Heenan and Morrison[4]	190000	0.017	0.17
Spazzini *et al.*[6]	16000	0.012	0.15
Driver *et al.*[3]	37000		0.098

The comparison studies reported here only discuss two peak frequencies: 1) near separation and 2) upstream of x_r. However, in this study, it was noticed that the high-frequency peak referred to above shifts to an even higher frequency, downstream of x_r, as seen in the narrowing of the auto-correlation in Figure 4.3. Figure 4.7 highlights the spectra from three streamwise positions for both Reynolds numbers in order to illustrate the frequency shift more clearly. It can be seen in the figure that the low-frequency peak at $x/h = 0.82$ shifts to a higher frequency at $x/h = 2.38$ for $Re_h = 8081$ and $x/h = 2.77$ for $Re_h = 18588$ which then shifts to an even higher frequency at $x/h = 12.14$. At that most downstream position, the peak for $Re_h = 8081$ is $fh/U_\infty = 0.106 \pm 0.002$ and for $Re_h = 18588$ is $fh/U_\infty = 0.085 \pm 0.0008$. Farabee and Casarella[2], who obtained measurements in a backward-facing step downstream of x_r, also saw a slight shift in the peak frequency to $fh/U_\infty = 0.14$ starting around $x/h = 10$ and stretching to at least $x/h = 16$. Reattachment in their flow was $x_r = 6h$. The observations regarding the frequency spectra are consistent with the findings discussed previously in regards to the auto-correlation function shown in Figure 4.3. In particular, the transition in the time scale of the wall-pressure-generating motion from large to small with streamwise distance downstream of the step up to x_r is associated with the transition in the peak of the spectrum from a low to a high frequency. Beyond x_r, another narrowing of the time scales was observed in the auto-correlation function that mirrors the second shift in the spectrum peak frequency to an even higher frequency downstream of x_r.

Another point worth mentioning deals with the low-frequency end of the spectra ($fh/U_\infty < 0.02$) and the energy associated with this range at different Reynolds numbers. In the $Re_h = 8081$ case, the low-frequency peak occurs immediately downstream of the step and is attributed to the flapping of the shear layer as previously explained. Although the same is true for the Re_h = 18588 case, there is a noticeable difference farther downstream where the energy level at the low-frequency end of the spectra *relative to* that at higher frequencies does not decay as much with increasing x. Moreover, downstream of x_r, this *relative* importance of the low-frequency, pressure fluctuations increases again. This is consistent with the auto-correlation results in Figure 4.3, where the auto-correlation function downstream of x_r is in fact wider at the higher Reynolds number than the lower one, reflecting the stronger relative dominance of the low-frequency, pressure fluctuations at the higher-Reynolds number. The origin of this increase in the low-frequency energy content at the higher-Reynolds number is not known at this time. In addition, the increase of the low-frequency content at the x/h = 4.72 position in Figure 4.6a is observed but cannot be explained at this time.

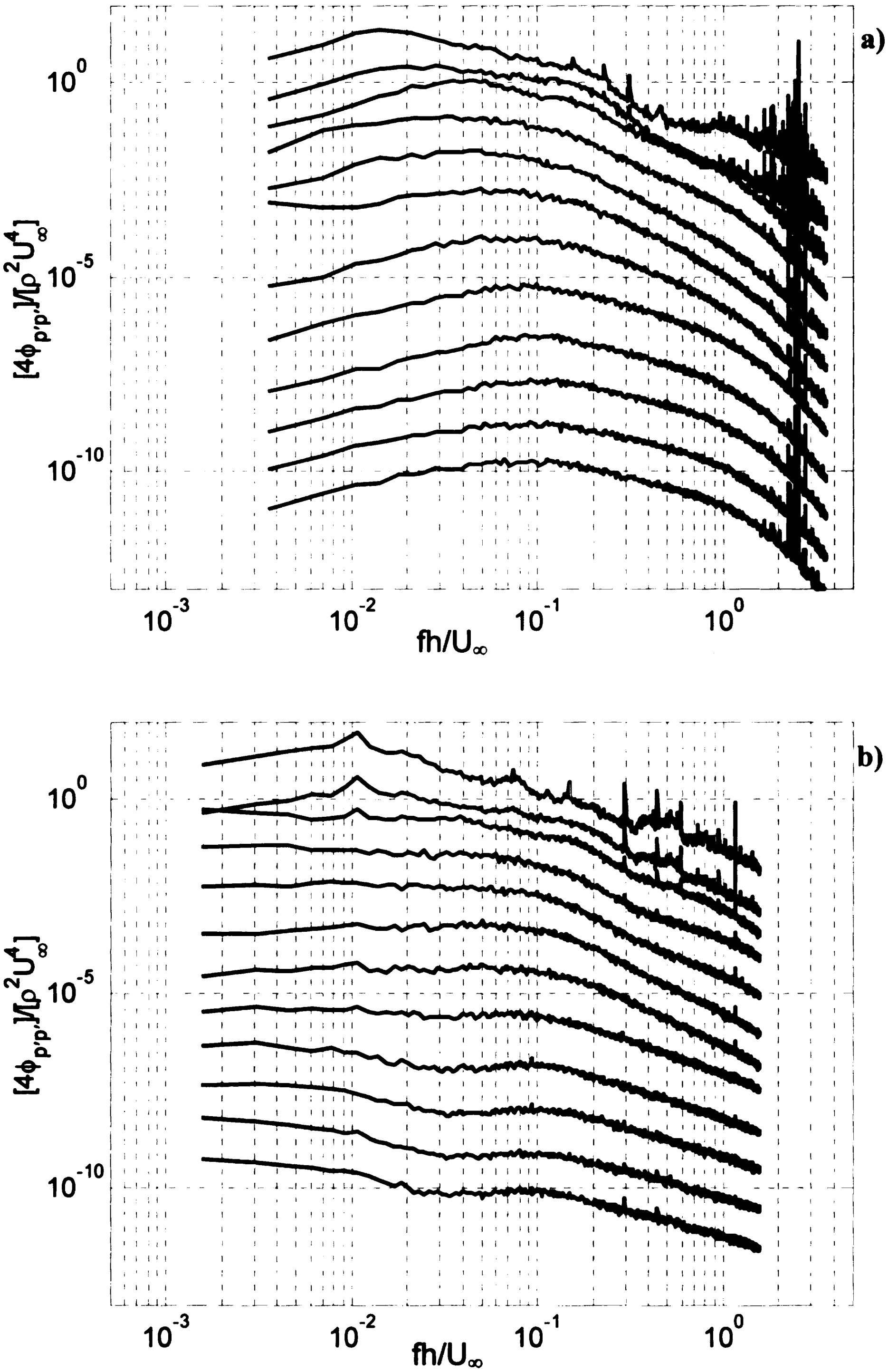

Figure 4.6 Frequency spectra for: a) $Re_h = 8081$ and b) $Re_h = 18588$. Eleven spectra are plotted relative to different origins, at the following streamwise positions starting from the top: x/h = 1) 0.822, 2) 1.60, 3) 2.38, 4) 3.16, 5) 3.94, 6) 4.72, 7) 5.50, 8) 7.07, 9) 8.63, 10) 10. 2, 11) 11.7, and 12) 12.5

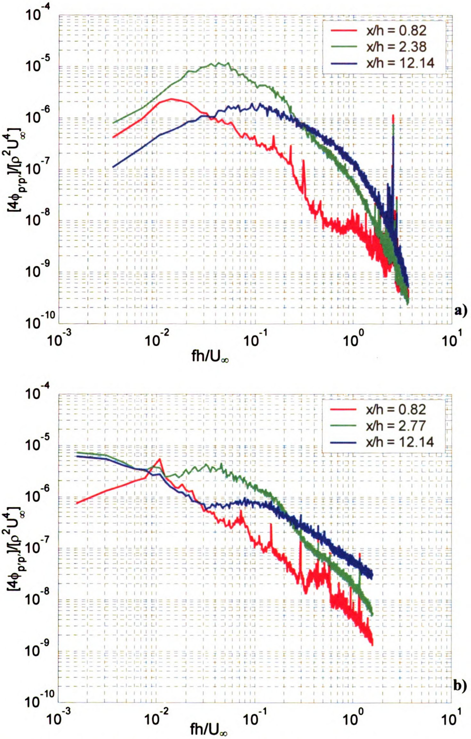

Figure 4.7 Spectra from a) $Re_h = 8081$ and b) $Re_h = 18588$ cases plotted at three streamwise positions

4.2.4 Cross-correlation with respect to the pressure signal at reattachment

The cross-correlation is obtained from two discrete-time signals to determine the similarity between them as a function of different time shifts between the signals. If the two signals are identical (i.e., $p'_1 = p'_2$), then the calculation yields the auto-correlation function, obtained earlier in Section 4.2.2. The cross-correlation values were normalized using the RMS value of p'_1 and p'_2.

$$R_{p'_1 p'_2} = \frac{r_{p'_1 p'_2}}{(p'_{1,RMS})(p'_{2,RMS})} \tag{4.3}$$

where $r_{p'_1 p'_2}$ is the cross-correlation (see Equation (4.3)) and $p'_{1,RMS}$ and $p'_{2,RMS}$ are the RMS pressure fluctuations for the two different discrete-time signals. Figure 4.8 yields the cross-correlation between the microphone nearest to reattachment and all 32 microphones in the array for two different flow cases: Re_h = 8081 and 18588. The streamwise coordinate is normalized by the step height and is presented along the abscissa. The time shift (τ) is normalized by the step height and the freestream velocity and is shown along the ordinate. The color bar represents the magnitude of the normalized cross-correlation, which was averaged over 102 records.

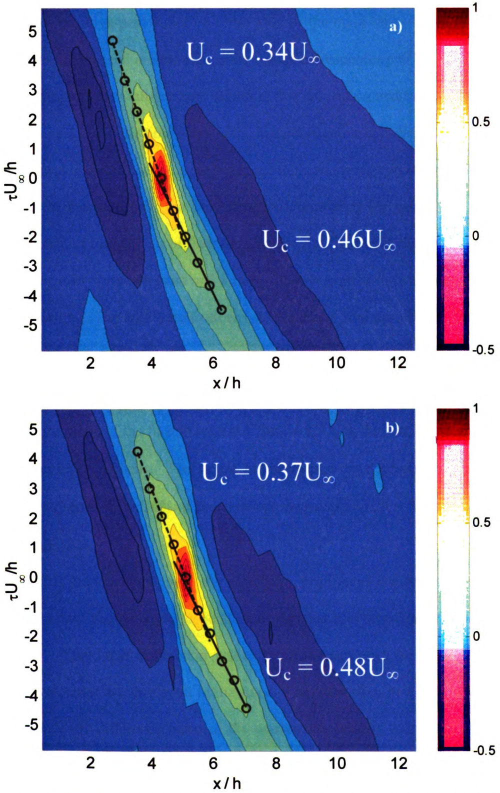

Figure 4.8 Flooded-color, contour maps of the cross-correlation and implied convection velocities at Re_h = a) 8081 and b) 18588

In each case shown in Figure 4.8, there is a main, positive-peak lobe inclined at an angle and two negative-peak lobes on either side of the main lobe. At each x location, the main peak is centered around time shift values corresponding to the largest positive correlation between the wall-pressure signal at this x location and that at reattachment. The negative peaks give the time delay to the highest negative correlation. By finding the slope of the peak locus of the main (or negative) lobe, an average downstream convection velocity can be calculated for the flow structure dominating the generation of surface-pressure fluctuations regardless of their time-scales. In Figure 4.8, the coordinates of the positive-lobe peaks were extracted and a linear fit was applied to determine the slope of the peak-locus line. The convection velocity is calculated from the slope of the fit using

$$\frac{1}{U_c} = \frac{m_s}{U_\infty} \tag{4.4}$$

where m_s is the slope of the fit line seen in Figure 4.8, U_∞ is the freestream velocity, and U_c is the convection velocity. The largest mean-squared error surrounding the linear fit lines was determined to be 10% of the smallest time step ($\tau U_\infty/h = 0.069$) within the fit range for both cases.

For both Reynolds numbers, the main-lobe, peak locus consists of two parts that are inclined at two distinct angles depending on whether x is upstream or downstream of reattachment. Thus, two convection velocities were calculated per flow case. These convection velocities are displayed in the flooded contour plots in Figure 4.8. There is approximately 30% difference between the convection velocity calculated upstream of reattachment and that obtained downstream of reattachment. This indicates that the dominant, wall-pressure-generating structures within the shear layer are convecting at a slower speed before they impinge and interact with the wall. Once the shear layer reattaches, these flow structures advect at a faster velocity, which partially explains the reduction in the dominant time scale downstream of reattachment observed in the auto-correlation contour plots in Figure 4.3. Compared to previous planar backward-facing step studies such as Heenan and Morrison[4] and Lee and Sung[5], which reported convection velocities spanning the range $0.5U_\infty$ to $0.6\ U_\infty$, the U_c values calculated here are rather low. This difference in convection velocity may be caused by the difference in geometry between a planar configuration and an axisymmetric geometry. Li and Naguib[10] investigated the wall-shear-stress signature in the same axisymmetric backward-facing step geometry and reported "local" convection velocities upstream of reattachment, as low as $0.35U_\infty$. In addition, Li and Naguib[10] found the "local" convection velocity to increase beyond reattachment up to about $0.5U_\infty$. The "local" U_c values were calculated from the slope of the peak locus of the two-point cross-correlation of the fluctuating wall-shear stress.

4.2.5 Frequency-wavenumber spectra

The frequency-wavenumber (f-k_x) spectrum is obtained from the two-dimensional, Fourier transformation of the auto-correlation of the space-time wall-pressure signal ($p'(x,t)$). As a result, this spectrum decomposes the energy content of the wall-pressure field into contributions at different frequency and wavenumber combinations. All 32 microphones, sampled at 12 kHz for 35 seconds, were used in the f-k_x spectra. A total of 417,792 (102×2^{12}) wall-pressure samples were used out of the 420,000 acquired at each microphone. Thus, a 417,792 x 32 (time x space) two-dimensional array made up the entire data set, which then was divided into sub-arrays of 2048 rows x 32 columns. This allowed averaging of the spectrum over 204 records and produced a random uncertainty error of $(204^{-0.5})100 = 7\%$ in the spectral estimation. The frequency-wavenumber spectrum of each record was calculated by taking the Fast Fourier Transform (FFT) of the 2048 x 32 array relative to the dimension representing time and multiplying by the complex conjugate. This changes the representation of the data from the time to the frequency domain. A second FFT is calculated along the space dimension (32) in order to change the spatial domain representation to one based on wavenumber. The space dimension was padded with zeros so that the FFT was computed on an array of 2048 x 128. This helps to obtain the resulting spectrum at smaller wavenumber increments via interpolation. The resolution of the dimensionless frequency and wavenumber is 0.007 and 0.08, respectively, for the $Re_h = 8081$ case and 0.003 and 0.08 for the $Re_h = 18588$ case. Note that the resolution value for the wavenumber is that based on the true rather than the interpolated (zero-padded) spatial information.

Figure 4.9 shows two flooded-color, contour plots of the frequency-wavenumber spectra for each of the Re cases. The color bar indicates the magnitude of the spectrum divided by the maximum peak magnitude, making the scale zero to one. On the abscissa, the normalized wavenumber is shown and the ordinate gives normalized frequency. Depicted in each plot is a concentration of energy forming a ridge of peak spectrum values inclined at an angle and located in the right half plane, or $k_x>0$. The peak locus of this ridge is practically linear and does not pass through the origin of the plot. The mean-squared error around the linear fit line was determined to be 0.1% of the lowest frequency ($fh/U_\infty = 0.021$) in the fit range for both Re cases. Since the convection speed at a given f and k_x point is the slope of a straight line drawn from the origin of the f-k_x spectrum to the point, the ridge represents downstream (positive) traveling disturbances.

The offset between the origin and the intercept of the peak locus with the k_x axis results in frequency (wavenumber) dependent convection velocities for different points along the ridge. These convection velocities were calculated by determining the equation of a least-squares line fit to the ridge (seen in Figure 4.9) and dividing through the frequency to obtain the convection velocity as a function of frequency. Equation (4.5) shows the details behind the calculation.

$$\left.\frac{U_c}{U_\infty}\right|_{ridge} = \frac{f}{k_x} = \frac{f(h)/U_\infty}{m_s(f(h)/U_\infty)+b} \tag{4.5}$$

where, U_c represents the convection velocity, fh/U_∞ is the normalized frequency, m_s is the slope of the least-squares line that fits the ridge, and b is the intercept of the least squares line. Figure 4.10 shows a plot of the results for both Re_h cases. The dependence of the convection velocities on frequency suggests that the structures in the flow are dispersive, meaning that flow structures of different scales travel at different speeds in the downstream direction. However, as will be shown in Chapter 6 this dependence is actually related to the acceleration of large-scale structures that have formed in place at approximately $1/2x_r$ before shedding downstream.

At negative wavenumbers, two localized peaks (shown by arrows in Figure 4.9) in the $f\text{-}k_x$ spectra are visible in the lower frequency range at $fh/U_\infty \approx 0.021 \pm 0.004$ and 0.012 ± 0.002 for the $Re_h = 8081$ and 18588 respectively. These peaks are found at a negative wavenumber of $k_x(h) \approx -0.10$ for both cases, indicating an upstream convection velocity of $U_c \approx -0.21U_\infty$ for the $Re_h = 8081$ and $-0.12U_\infty$ for $Re_h = 18588$. These upstream convection velocities are rather rough estimates. More specifically, because of the resolution of the $f\text{-}k_x$ spectrum, the locations of the peaks could vary giving a velocity range anywhere from $-0.12U_\infty$ to $-0.41U_\infty$ for the $Re_h = 8081$ case and $-0.08U_\infty$ to $-0.23U_\infty$ for the $Re_h = 18588$ case. Thus, it is difficult to determine the actual upstream convection velocities from the $f\text{-}k_x$ spectra with high degree of confidence for these low-wavenumber/low-frequency peaks.

Hudy *et al.*[8] identified an upstream convection velocity of $0.21U_\infty$ in their splitter-plate-with-fence study in both the frequency-wavenumber spectrum and a cross-correlation plot. The Reynolds number based on fence height in the study was 7885. The peak in their study was located around $f*2H/U_\infty \approx 0.02$ and $k_x*2H \approx -0.11$ in the $f\text{-}k_x$ spectrum, where 2H equals the total height of the fence. Hudy *et al.*[8] acquired measurements starting at 0.6 "step" heights downstream of the fence, which translates to $x/x_r = 0.02$. In the present measurements, the first microphone was located at 0.4 step heights, or $x/x_r = 0.09$ and 0.08 for $Re_h = 8081$ and 18588, respectively. Hudy *et al.*[8]

stated that the strongest manifestation of the upstream propagating disturbances was located in the region $x/x_r < 0.25$. This means that in the present study only two microphones are contained within the $0.25x_r$ region for the $Re_h = 8081$ case and three microphones for the $Re_h = 18588$ case.

Figure 4.11 shows the flooded-color, cross-correlation contour plots for both Re numbers using microphone #2 ($x/h = 0.82$) as the reference microphone for the lower Re case and #3 ($x/h = 1.21$) for the higher Re case. The positive-inclined lobes in the contour plots (highlighted with broken lines) indicate an upstream convection velocity near separation. The average upstream U_c is difficult to calculate from these plots due to limited resolution, which means there are not enough peak values upstream of the reference microphones to accurately fit a linear trend line to determine the slope for calculating U_c as done in Section 4.2.4. Thus, in this study, an upstream convection velocity has been identified, but not quantified. Due to the microphone spacing, the resolution in the region of the upstream convection is low, which makes it difficult to calculate upstream U_c with confidence.

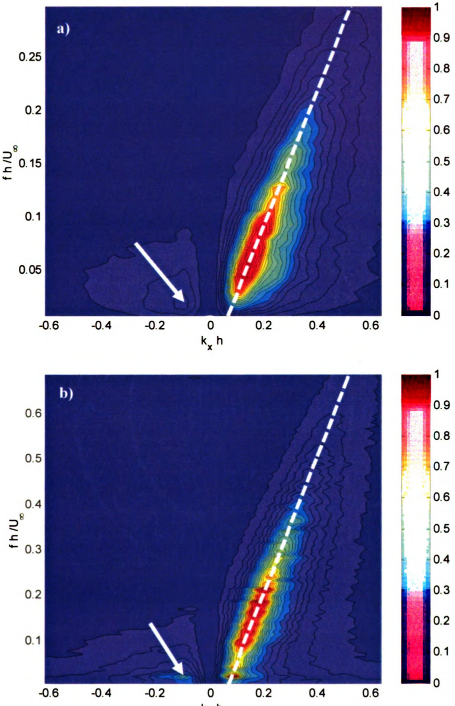

Figure 4.9 Frequency-wavenumber spectrum obtained from all 32 microphones at Re = a) 8081 and b) 18588

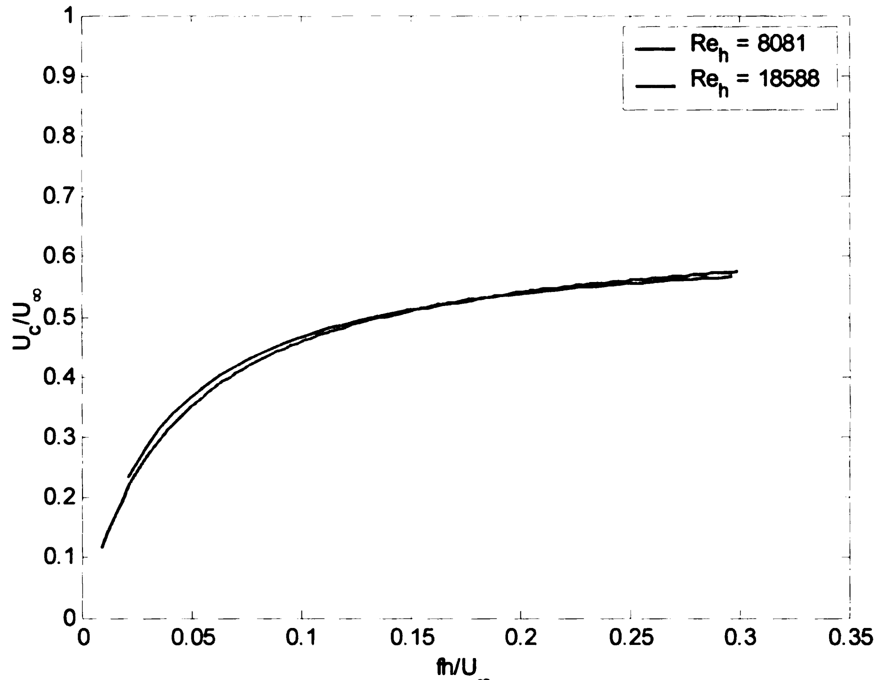

Figure 4.10 Normalized convection velocity as a function of normalized frequency for Re_h = 8081 and 18588

Lee and Sung[7] also computed a frequency-wavenumber spectrum similar to the one in Figure 4.9. Their results show a ridge associated with a downstream convection velocity as well as a stationary mode along the $k_x = 0$ axis, but they did not observe an upstream convection velocity as previously mentioned. It is believed that Lee and Sung[7] could not find a negative convection speed because their most upstream measurement location extended down to only $x/x_r \approx 0.27$. Similarly, the measurements of Farabee and Casarella[2], who also reported no upstream convection velocity, were limited to $x/x_r >$ 0.25.

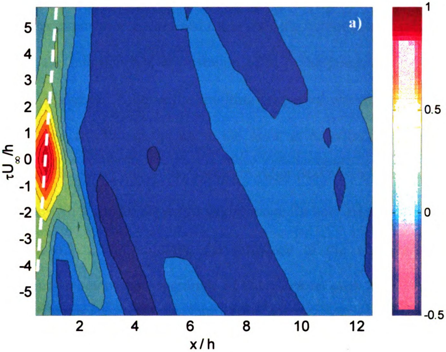

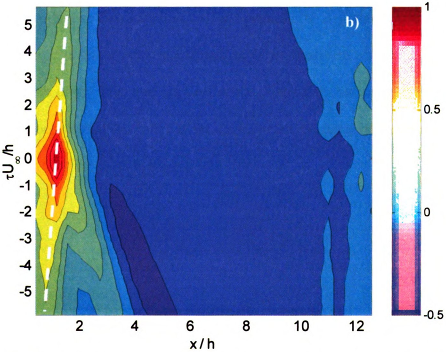

Figure 4.11 Flooded-color, cross-correlation contour plots for a) Re_h = 8081 using microphone #2 (x/h = 0.82) as the reference microphone and b) Re_h = 18588 and reference microphone #3 (x/h = 1.21)

In order to analyze the frequency-wavenumber spectra further and in more detail, the Re_h = 8081 spectrum was reprocessed using only the microphones upstream of x_r and then using only the microphones downstream of x_r. The results were similar for the higher Re case. Figure 4.12 shows the resulting frequency-wavenumber spectrum with the ordinate and the abscissa in the figure the same as described for Figure 4.8. The standard error for the linear fits to the spectrum ridge peaks was less than 0.2% of the smallest frequency ($fh/U_\infty \approx 0.028$) within the fit range for both cases.

In Figure 4.12a, by removing the influence of the wall-pressure signature downstream of reattachment, the magnitude of the spectrum peak in the negative k_x half plane becomes stronger. Thus, within this region there is a relatively strong upstream convection velocity at low frequencies. In Figure 4.12b, which shows information based only on the microphones downstream of x_r, the peak on the negative wavenumber side is weak. This suggests that a weak manifestation of the upstream traveling disturbances is found downstream of x_r. This may be a reflection of the fact that, on instantaneous basis, reverse flow velocities may be found as far downstream as approximately 5.5h (or 1.2 x_r), as depicted from the FPP plots in Figure 3.1.

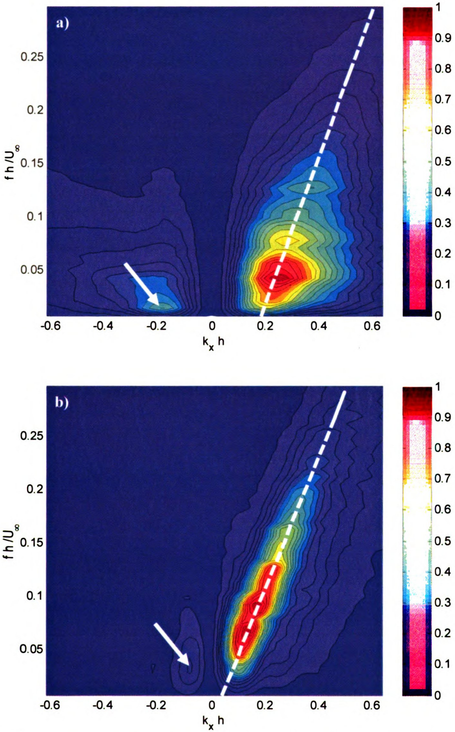

Figure 4.12 Frequency-wavenumber spectra for $Re_h = 8081$ calculated using data from the microphones located: a) upstream of x_r and b) downstream of x_r

It is also evident that the point at which the straight line determined from the peaks along the ridge crosses the abscissa in Figure 4.12b shifts to lower wavenumbers when only investigating the microphones downstream of x_r. In Figure 4.12a, the slope line crosses almost at $k_x h = 0.2$ whereas, in Figure 4.12b, the intersection point is closer to $k_x h = 0$. This shows that within the separated shear layer region the convection velocity is highly dependent on frequency. Downstream of x_r, however, the convection velocity is less dependent on frequency as the ridge line intersects the abscissa closer to zero. This relationship is shown in Figure 4.13, which displays the convection velocity as a function of frequency for the full range of microphones and for the microphones downstream of x_r. It can be seen that the line associated with the microphones downstream of x_r has a slightly flatter profile compared to the line for the full range of microphones. This shows that downstream of x_r the convection velocity is less dependent on frequency.

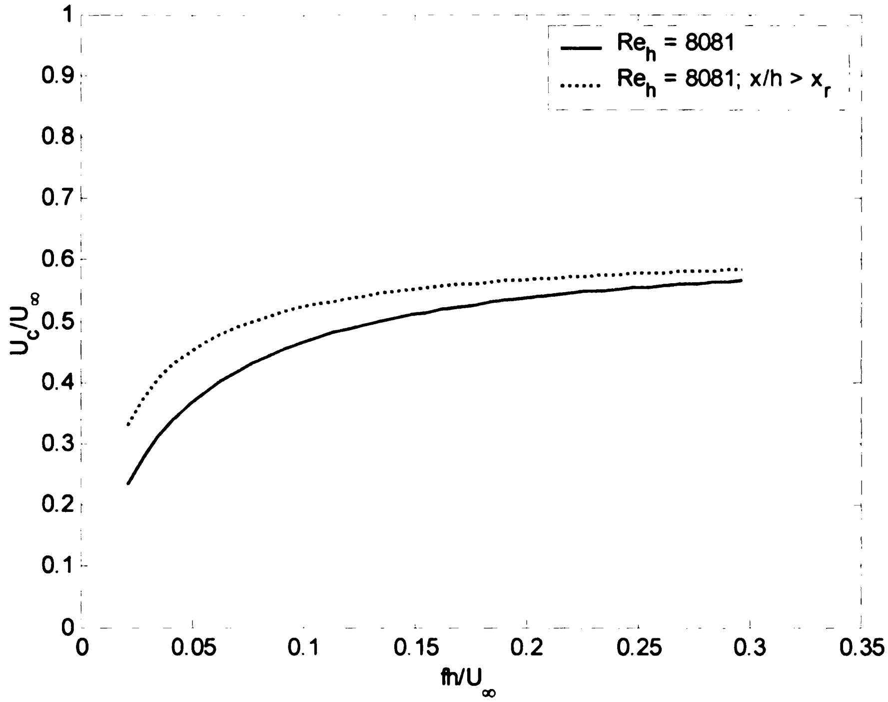

Figure 4.13 U_c versus normalized frequency for $Re_h = 8081$, comparing results from full spectrum with spectrum results from downstream of x_r

Daoud[9] investigated the reattached boundary layer downstream of a separating/reattaching flow region in a fence-with-splitter-plate configuration and found a constant convection velocity equal to 81% of the freestream velocity using the f-k_x spectrum. The convection velocity was independent of frequency in the reattached, boundary-layer region, which is not the case in the present study. However, Daoud's[9] microphone measurements started at $x/x_r > 1.7$ downstream of the fence; whereas, the results shown in Figure 4.12 and Figure 4.13 are based on measurements at *and* downstream of $x/x_r = 1.05$. This is near the beginning of the reattached, boundary-layer region. In order to compare the convection velocity of the structures within the reattached boundary layer as calculated by Daoud[9] with those from the present study, only the microphones downstream of $x/x_r = 1.7$ were used to determine the f-k_x spectrum for the Re_h = 8081 case as shown in Figure 4.14. It is found that if only the spectrum-ridge peaks located at the frequency of the global spectrum peak ($fh/U_\infty \sim 0.1$) and higher frequencies are used to determine the line fit, then in fact the line does pass through the plot's origin (see dashed line in Figure 4.14) within the resolution of the origin. For frequencies below $fh/U_\infty \sim 0.1$, the convection speed remains dependent on frequency as evident from the deviation of the ridge peaks from the dashed line in this frequency range. In an effort to compare the convection velocity found by Daoud[9] in the reattached boundary layer with the present study, the peaks along the ridge below $fh/U_\infty < 0.1$ are ignored. Figure 4.14 shows the slope of the linear fit for the peaks greater than the frequency value stated along the positive ridge in each f-k_x spectrum. The linear fit lines cross at $k_xh = 0 \pm 0.01$. The slope of the line indicates that the high-frequency structures within the reattached boundary layer have an average convection velocity of $0.59U_\infty$ independent of frequency as shown in Figure 4.15. Farabee and Casarella[2] found the convection speed within the reattached boundary to be roughly 0.65-$0.70U_\infty$. The difference between the two studies may be due to the geometry difference. Farabee and Casarella[2] used a planar BFS with assumed two dimensionality along the centerline.

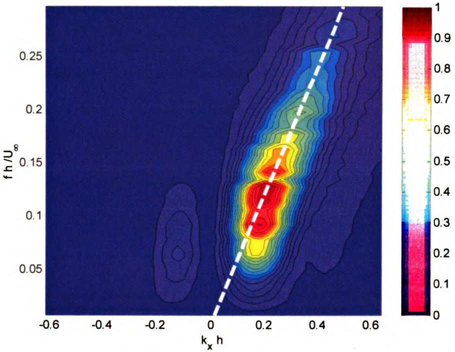

Figure 4.14 Frequency-wavenumber spectrum for $x/x_r > 1.7$ at $Re_h = 8081$ for $fh/U_\infty > 0.085$

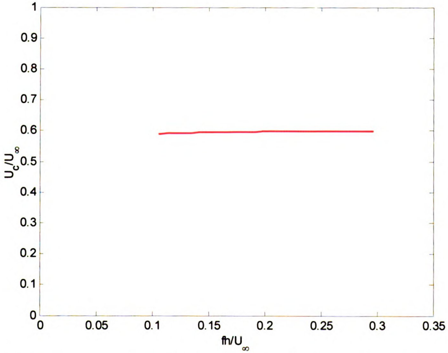

Figure 4.15 U_c versus normalized frequency obtained from microphones located at $x/x_r > 1.7$ and frequencies $fh/U_\infty > 0.086$ for $Re_h = 8081$

4.3 Conclusions

A comprehensive, wall-pressure-signature dataset has been acquired beneath the flow field downstream of an axisymmetric, backward-facing step. The dataset was acquired at four different Reynolds numbers, allowing investigation of the Reynolds-number effect.

Both the mean- and fluctuating-pressure distributions exhibited Reynolds-number dependence. The mean-pressure recovery occurred over a longer, streamwise-distance with increasing Reynolds number. Similarly, the RMS pressure fluctuations reached their peak at an x value that increases with Reynolds number. Both of these effects were consistent with the lengthening of the separation bubble with Re_h. Another Reynolds-number effect that remains unexplained at this stage is the reduction of the RMS pressure, relative to the dynamic head of the flow, as the Reynolds number increases.

The wall-pressure, auto-correlation showed a distinct region in the flow, stretching from separation to half of the reattachment distance that is dominated by low-frequency disturbances. These disturbances are characteristic of backward-facing-step flows and are associated in the literature with the flapping of the shear layer. A second noticeable region was found in the auto-correlation starting from $\frac{1}{2}x_r$ and stretching up to about x_r. This region of the flow is dominated by higher-frequency structures, which are linked to the passage of flow structures within the shear layer. Beyond x_r, up to approximately $x/h = 8$, the dominant time scale extracted from the auto-correlation results narrows again as the shear layer reattaches on the surface and becomes a boundary layer. The fourth distinct region delineated in the auto-correlation contour plots starts beyond $x/h = 8$. It is in this region that the time scales are the shortest over the entire streamwise extent measured. These time scales do not change over the remainder of the region measured and indicate that this region may be dominated by flow structures that may be smaller in size and may be convecting at a faster speed than the flow structures in the shear layer upstream of reattachment.

An increase in the convection speed between upstream and downstream of reattachment was seen in the wall-pressure cross-correlation results relative to a reference signal measured near reattachment. The speed increased from approximately $0.35U_\infty$ upstream of x_r to about $0.5U_\infty$ downstream of x_r, seemingly independent of Reynolds number. The convection velocity value upstream of reattachment is lower in magnitude than reported in planar backward-facing step studies. Overall, a weak effect was seen in terms of Reynolds number in both the auto-correlation and cross-correlation analysis.

The frequency-wavenumber spectra showed that for both Reynolds number cases that the downstream convection velocity was dependent on frequency. This dependence of the convection velocities on frequency suggests that the structures in the flow are dispersive. However, as will be seen in Chapter 6, this dependence reflects the acceleration of the large-scale structures once they form. In addition, an upstream convection velocity was identified in the f-k_x spectra; although, U_c was difficult to quantify due to the limited wavenumber resolution of the spectra.

4.4 References

[1] Eaton, J. K. and Johnston, J.P., "A Review of Research on Subsonic Turbulent Flow Reattachment," *AIAA Journal*, Vol. 19, No. 9, 1981, pp. 1093-1099.

[2] Farabee, T.M., and Casarella, M.J., "Measurements of fluctuating wall pressure for separated/reattached boundary layer flows," *Journal of Vibration, Acoustics, Stress, and Reliability in Design*, Vol. 108, 1986, 301-307.

[3] Driver, D.M., Seegmiller, H.L., and Marvin, J.G., "Time-dependent behavior of a reattaching shear layer," *AIAA Journal*, Vol. 25, No. 7, 1986, pp. 914-919.

[4] Heenan, A.F. and Morrison, J.F., "Passive control of pressure fluctuations generated by separated flow," *AIAA Journal*, Vol. 36, No. 6, 1998, pp. 1014-1022.

[5] Lee, I. and Sung, H.J., "Characteristics of wall pressure fluctuations in separated and reattaching flows over a backward-facing step," *Experiments in Fluids*, Vol. 30, 2001, pp. 262-272.

[6] Spazzini, P.G., Iuso, G., Onorato, M., Zurlo, N., and Di Cicca, G.M., "Unsteady behavior of back-facing step flow," *Experiments in Fluids*, Vol. 30, 2001, pp. 551-561.

[7] Hudy, L.M., "Simultaneous wall-pressure array and PIV measurements in a separating/reattaching flow region," Masters thesis, Michigan State University, 2001.

[8] Hudy, L.M., Naguib, A.M., and Humphreys Jr., W.M., "Wall-pressure-array measurements beneath a separating/reattaching flow region," *Physics of Fluids*, Vol. 15, No. 3, 2003, pp. 706-717.

[9] Daoud, M.I., "Stochastic Estimation of the flow structure downstream of a separating/reattaching flow region using wall-pressure array measurements," Ph.D. Dissertation, Michigan State University, 2004.

[10] Li, Y. and Naguib, A.M., "High-Frequency Oscillating-Hot-Wire Sensor for near-Wall Diagnostics in Separated Flows," *AIAA Journal*, Vol. 43, No. 3, 2005, pp. 520.

5 Velocity Measurements using PIV

5.1 Introduction

Although the backward-facing-step flow field has been investigated extensively over the past few decades, the majority of these studies have utilized time, rather than space, resolved measurements. Only during the last decade have a few PIV studies (summarized below) of the BFS flow become available. All of these have been conducted in a planar flow geometry, which suffers from the inability to establish a truly two-dimensional mean flow because of end effects as discussed in the Introduction. The objective of this study is to explore the statistics of the velocity field above the surface using PIV measurements in a geometry that allows for axisymmetric separating boundary layer conditions. This information will give better understanding of the flow structures that develop in the shear layer beyond separation as well as provide a database that is suitable for benchmarking of computational codes based on periodic, boundary conditions in the spanwise direction.

Spazzini *et al.*[1] acquired digital PIV measurements in a planar BFS at Reynolds numbers based on step height spanning 3500-16000. These measurements were completed in a water tunnel and provided quantitative information about the flow field as well as qualitative visualizations. In addition, time-resolved skin-friction measurements were obtained in a companion experiment using a wall-mounted double hot-wire probe. Data from both velocity and wall-shear-stress measurements revealed a strong dependence between x_r and Re_h with the length of reattachment growing with increasing Reynolds number. In addition, Spazzini *et al.*[1] found that the location of the secondary separation point was weakly dependent on Reynolds number, moving closer to the step with rising Re_h.

In 2002, Kostas *et al.*[2] acquired PIV measurements in a planar backward-facing-step geometry at Re_h = 4660. From their measurements, the mean-velocity field in the plane parallel to the streamwise and wall-normal coordinates revealed both primary and secondary recirculation regions. The mean-reattachment point recorded was 4.8h ± 0.2h, which is the location that the streamline originating at the step edge impinges onto the wall. Kostas *et al.*[2] stated x_r could not be accurately obtained because the PIV data did not extend to the wall. In addition, Kostas *et al.*[2] found x_r to be shorter than reported in literature, and they attributed this to the high level of turbulence near the wall in the upstream boundary layer. Reynolds-stress components $\overline{u'^2}, \overline{v'^2}, \overline{u'v'}$ normalized by U_∞^2 were also presented. Kostas *et al.*[2] found appreciable, Reynolds stress values starting around two step heights downstream of separation at a vertical height of y = h. They also reported that the largest levels of Reynolds stress were located roughly one-step height upstream of reattachment at y = 0.7h. Beyond reattachment, Kostas *et al.*[2] observed a decline in the Reynolds stress levels. They also investigated the out-of-plane (spanwise) vorticity, observing that negative vorticity was contained within the shear-layer region with a peak, vorticity value of $\omega_z^* = \omega_z h/U_\infty = -3.4$. At separation, the vorticity is concentrated in a thin layer that grows in width with increasing streamwise distance until it takes on a more bulbous shape between x/h = 2-5 as a result of the high-degree of mixing in the region. Downstream of reattachment, the authors observed a decrease in vorticity as the reattached boundary layer began to relax back to equilibrium.

Scarano and Riethmuller[3] published a study in 1999 describing an improved algorithm for interrogating PIV images. In the paper, they presented PIV data in the form of mean velocity and Reynolds stress quantities from a planar backward-facing-step study at Re_h = 5000. The mean velocity profiles with streamlines show both a primary and secondary re-circulation region and a reattachment distance of x_r = 5.9h. Reynolds stress contour maps show that the maximum values observed for u_{RMS}, v_{RMS}, and $\overline{u'v'}$ were located along the centerline of the shear layer, which was defined as the locus of inflection points for the mean streamwise velocity plots. Scarano and Riethmuller[3] found the maximum u_{RMS} value of 17% of the freestream velocity at approximately one-step height upstream of x_r. As for v_{RMS} and $\overline{u'v'}$, the maximum values occurred at x/h = 5 and had a magnitude of 12% and -1.2%, respectively, when normalized using U_∞.

In the remainder of this chapter, the velocity field downstream of the axisymmetric, backward-facing step is investigated using PIV measurements. The primary focus is the examination of the Reynolds number effect on the velocity-field statistics.

5.2 Results and Discussion

Details of the PIV measurements analyzed here were described in the test matrix in Section 2.4. Results presented include the mean-velocity field, the streamwise and normal fluctuating-velocity fields, the Reynolds shear stresses, and the mean-spanwise-vorticity field. Reynolds-number effects are explored between $Re_h = 8081$ and 18588.

5.2.1 Mean-Velocity Field

The mean-velocity vector fields and streamlines above the surface downstream of the axisymmetric backward-facing step are shown in Figure 5.1a-b for two of the four Reynolds numbers investigated: $Re_h = 8081$ and 18588. The streamwise coordinate, x/h, is along the abscissa and the coordinate normal to the wall, y/h, is represented along the ordinate. The vector maps show a classical backward-facing step mean-velocity field. The boundary layer separates at the edge of the step forming a shear layer that reattaches at a distance downstream of the step. The streamlines curve towards the wall with increasing x until the shear layer reattaches at x_r. Beneath the shear layer there is a clockwise recirculation zone located near the wall that stretches from $x/h \approx 1.1$, depending on Reynolds number, to x_r. The reattachment point was captured for all tested Reynolds numbers and, as seen earlier in the FFP and U = 0 plots in Figures 3.1 and 3.3, the reattachment length increases with increasing Reynolds number. Near the step, within the x/h = 0-1.1 region, the streamlines indicate a secondary recirculation zone, which is a characteristic feature in BFS flows. Scarano and Riethemuller[3] along with Kostas et al.[2] were also able to capture the secondary recirculation zone in their recent

PIV studies of a planar BFS. As observed in the FFP analysis as well as recorded in studies by Spazzini *et al.*[1] and Li and Naguib[4], there is a reduction in the size of the secondary re-circulation region with increasing Reynolds number. Beyond reattachment, the shear layer forms a reattached boundary layer as shown in Figure 5.1 for both Reynolds numbers.

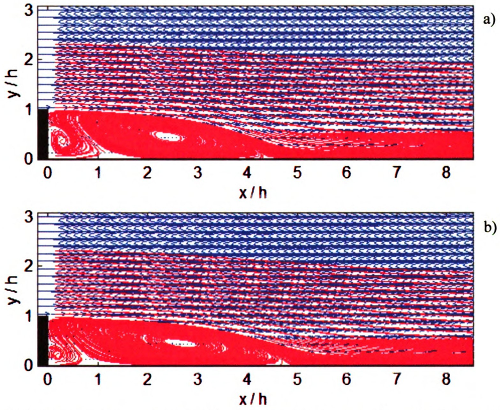

Figure 5.1 Mean-velocity vector fields and associated streamlines for Re_h = a) 8081 and b) 18588

To take a closer look at the mean-velocity-field characteristics, mean-velocity profiles extracted from the planar PIV data at six different x/h positions are shown in Figure 5.2 for Re_h = 8081 and 18588. The six positions are located at x/h = 0.85, 2.08 3.54, 4.23, 6.07, and 8.06. These same six positions will be used throughout the remainder of the chapter. Along the abscissa, the normalized velocity is presented as U/U_∞ and along the ordinate the distance normal to the wall is given as y/h for all six x/h positions. In general, the top three plots are located downstream of separation and upstream of the reattachment point. These three plots show the reverse flow below the step height, the shear layer region, and the relatively unchanged boundary layer-like profile above a y/h value that is slightly larger than 1. For the fourth plot, x/h = 4.22 is near reattachment and at this point slightly more reversed flow is seen at Re_h = 18588 than Re_h = 8081 since for the former the flow reattaches 0.48h farther downstream. The last two velocity-profile plots are located downstream of reattachment. It is in this region that the flow reattaches and begins to relax towards an equilibrium boundary layer state.

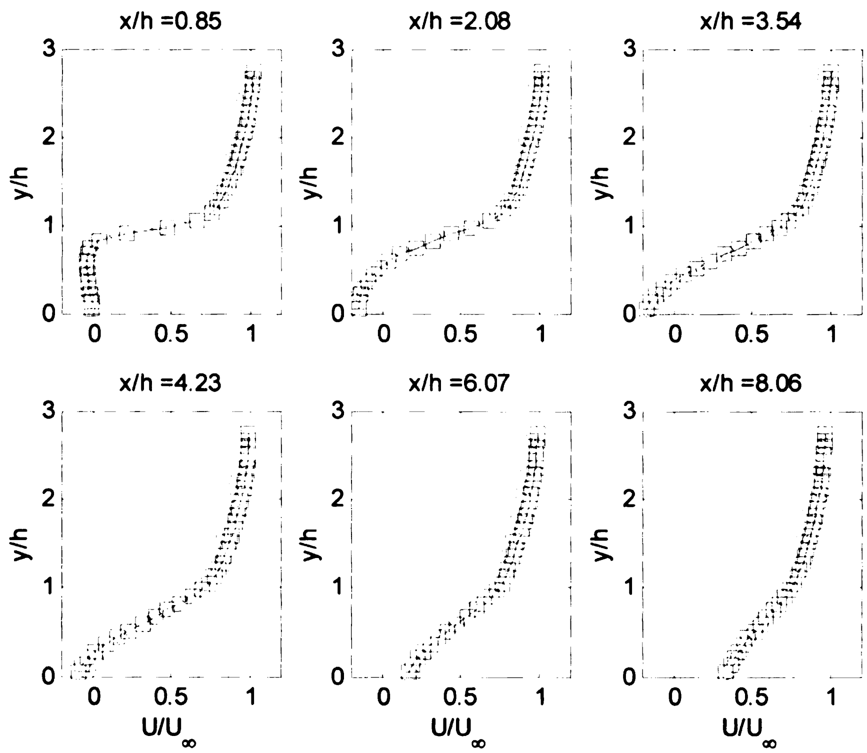

Figure 5.2 Mean-streamwise-velocity profiles at selected streamwise locations: (O)Re_h = 8081, and (□) Re_h = 18588

To elaborate further, starting with the x/h = 0.85 plot located downstream of the step, the two profiles show the reverse flow beneath the step height, y/h = 1. Around y/h = 1, the velocity changes rapidly over a very short y distance, corresponding to the shear-layer region. This is consistent with the idea that near the step, the shear layer is thin; that is, a large velocity gradient exists. At y/h > 1, the velocity profile takes on a profile similar to that of the boundary layer upstream (not shown here) away from the near-wall region. This gives indication that the boundary layer once it separates remains unaffected except in the region close to the wall. In their study of a single-stream shear layer, Morris and Foss[5] introduced the idea that the initial shear layer instability originates only from within the near-wall region of the boundary layer, forming a "sub-shear layer" immediately downstream of separation. The rest of the boundary layer remains intact until farther downstream when the sub-shear layer grows sufficiently to affect the full width of the flow domain. Morris and Foss[5] stated that the mean profiles are identical for $y/\theta > 2$ for a streamwise distance between $0 < x/\theta < 29$ (where θ is the separating boundary layer momentum thickness). The first four plots in Figure 5.2 have x/θ equal to 5.5, 13.6, 23.1, and 27.6 for $Re_h = 8081$. The current study provides evidence that the ideas of Morris and Foss seem to also hold for shear layers separating over a back step. Further discussion of this point will be given in Section 5.2.2 of the Results and Discussion.

Farther downstream, the steep velocity gradient in the shear-layer region relaxes and the shear layer spreads out. This can be seen in the next two plots, x/h = 2.08 and 3.54, where the velocity gradient around y/h = 1 is not as steep. In addition, the vertical height of the reverse-flow region becomes smaller as the shear layer curves toward the wall. At x/h = 4.23, the reverse-flow region is almost non-existent as the shear layer nears the reattachment point. Beyond reattachment, the two profiles are similar as seen in Figure 5.2 at x/h = 6.07 and 8.06.

5.2.2 Fluctuating-velocity field: u_{RMS} and v_{RMS}

Figure 5.3-Figure 5.4 show the longitudinal (u_{RMS}) and vertical (v_{RMS}) turbulent fluctuations for Re_h = 8081 and 18588. Each figure is a flooded-color, contour map with the streamwise distance downstream of the step, x/h, along the abscissa and the distance normal to the wall, y/h, along the ordinate. These axes will be used on all flooded-color, contour plots in this chapter. The color bar on the bottom of the contour plot indicates the magnitude of the particular turbulent RMS velocity normalized by U_∞. For all plots in Figure 5.3-Figure 5.4, the peak root-mean-square values are located within the separating-shear layer, with the highest peak along the center of the shear layer near the separation edge. The data presented in Figures 5.3 and 5.4 compare well, qualitatively, with Scarano and Riethmuller[3] in their PIV study of a planar, backward-facing step. In addition, the general behavior observed is consistent with the findings of Castro and Haque[6] as well as Ruderich and Fernholz[7] in their investigations of a fence-with-splitter-plate flow. Both studies employed the maximum loci in the turbulent intensity plots to determine the center of the separating-shear layer. Quantitatively, the RMS magnitudes in the current study are higher than in Scarano and Riethmuller's[3] study. In particular, the u_{RMS} and v_{RMS} values are almost double the values found by those authors. It is interesting to note that, in contrast to a free-shear layer, which spreads gradually and smoothly with increasing x, the reattaching, shear layer initially diverges smoothly until approximately x/h ~ 2 when a "sudden" divergence occurs and the shear layer grows to a thickness approximately equal to the step height. This is also the streamwise location at which the width of the wall-pressure auto-correlation reduces somewhat abruptly (see Figure 4.3). The RMS results show that in fact this transition in the wall-pressure field

characteristics is associated with the shear-layer structures approaching the wall. This was hypothesized through inference using the wall-pressure data alone. The velocity field data confirm the hypothesis.

In Figure 5.3a-b, the u_{RMS}, contour maps outline the shear layer and the "boundary layer" (i.e., the portion of the flow that seems to remain similar to the boundary layer at separation) distinctly for both Reynolds-number cases. Within the separating, sub-shear layer (the thin region of high shear near y/h = 1, immediately downstream of the step), the u_{RMS} values change dramatically over a short x distance as a result of the high shear in the region. Above this sub-shear layer, starting around y/h = 1.25, the u_{RMS} values decrease slowly over a large, streamwise distance in the downstream direction. That is, within this zone very little change is observed in the turbulence activity from that in the outer part of the separating, boundary layer, and hence the flow-structure characteristics are likely to be similar to those in the boundary layer. At the edge of the boundary layer, $\delta = 1.73h$, u_{RMS}/U_∞ values are less than 0.02 as the boundary layer merges with the free stream. In Figure 5.3a-b, distinct u_{RMS} bands can be seen at the different heights above the shear layer. These u_{RMS} values decrease with increasing radial distance as expected. In addition, the u_{RMS} bands show a slight curvature toward the wall upstream of reattachment. Beyond reattachment, the bands become parallel to the wall as the shear layer transitions to a reattached, boundary layer. In addition, the turbulence within the shear layer loses energy once the shear layer reattaches as can be seen by the reduction in u_{RMS} magnitude beyond reattachment.

A point of interest is the two peaks in the u_{RMS} contour maps that can be seen within the shear layer at x/h ~ 0.1-1 and 4.2. The peak closest to separation increases in magnitude with increasing Reynolds number and has a higher magnitude than the second peak. This local maximum value close to separation has also been seen by Morris and Foss[5] in their single-stream, shear-layer study. Morris and Foss[5] found a local maximum value located roughly at $x/\theta \sim 2$ and $y/\theta \sim 0.15$. Such a local maximum value has been observed in the literature only in laminar separating boundary layers. Hence, it appears that the present data support the findings of Morris and Foss[5], whose boundary layer was also turbulent at separation, suggesting that the sub-shear-layer region is dominated by viscous effects from the near-wall at separation. Nonetheless, caution should be exercised since the region immediately downstream of the separation point is a high-shear region and the accuracy of the PIV results there may be questionable. Therefore, to check that the peak near separation is not an artifact of the PIV processing, the data near separation need to be re-processed using iterative methods, such as particle image distortion (Huand and Fidler[8]) that have been developed to remedy high-shear effects on PIV measurements.

The second u_{RMS} peak occurs slightly upstream of reattachment, $x/h \sim 4.2$. Scarano and Riethmuller[3] find their maximum u_{RMS} value about one-step height upstream of reattachment. The same trend has also been recorded in surface-pressure studies in planar BFS. For example, Heenan and Morrison[9] observed in their study that the maximum p_{RMS} value is located approximately one step height upstream of reattachment. In the present study, the p_{RMS} value occurs close to reattachment as seen in Figures 4.1 and 4.2 and, due to data scatter near the peak, it is possible that the peak p_{RMS} occurs slightly upstream of reattachment.

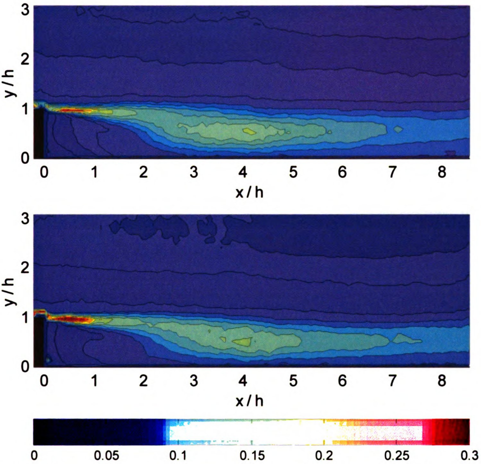

Figure 5.3 Flooded-color, contour maps of u_{RMS}/U_∞ at Re_h = a) 8081 and b) 18588

The comparison between the two Re_h cases shows no noticeable difference in the u_{RMS} distribution. This can be seen more clearly in the u_{RMS} profiles plotted in Figure 5.5 for the same six streamwise positions displayed in Figure 5.2. In the first plot at x/h = 0.85, there are slight differences between the two profiles in both the separation region and near the free stream. At the remaining five streamwise positions, Figure 5.5 shows the profiles at the two different Reynolds numbers collapsing over both the separation region and the shear layer, with only slight differences near the freestream where the Re_h = 8081 case shows more streamwise fluctuations.

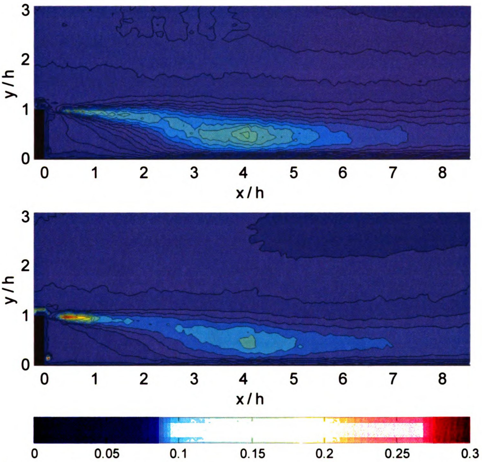

Figure 5.4 Flooded-color, contour maps of v_{RMS}/U_∞ at Re_h = a) 8081 and b) 18588

Flooded-color, contour maps of v_{RMS} for the two different Reynolds numbers are shown in Figure 5.4a-b. The contour maps have similar characteristics compared to the longitudinal turbulent intensity maps as evidenced by the higher intensity values being contained within the shear layer. In addition, v_{RMS} bands can be seen located above the shear layer with slight curvature toward the wall; although, these bands are not as clearly defined as the u_{RMS} bands. Nonetheless, the v_{RMS} values decrease with increasing height within the region of remaining boundary-layer turbulence.

The effect of increasing Reynolds number is evident in the vertical, turbulent-intensity, contour maps. One of the most noticeable characteristics of increasing

Reynolds number is that the magnitude of the peak value, located at x/h ~ 0.1-1 as seen in the u_{RMS} contour maps, increases. The v_{RMS} profiles for both Re_h cases are shown in Figure 5.6 at the selected streamwise locations. The only difference between the two cases is that the magnitude of the peak near separation is greater for the Re_h = 18588 case than the Re_h = 8081 case as can be seen in the x/h = 0.85 plot. Beyond this streamwise position, the profiles collapse for the remaining x/h locations investigated.

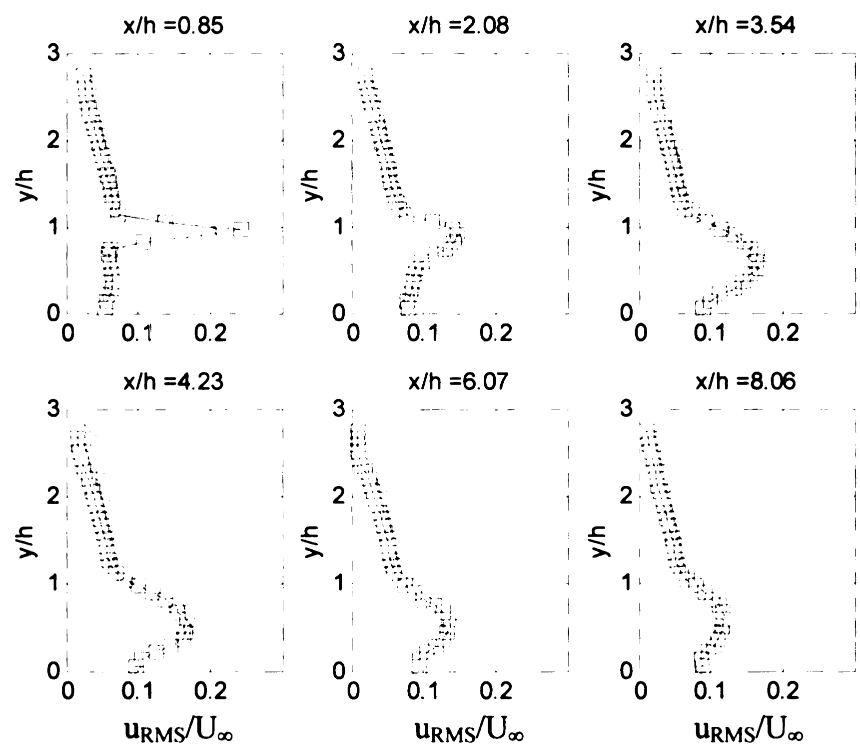

Figure 5.5 Streamwise-velocity RMS profiles: (O)Re_h = 8081 and (□) Re_h = 18588

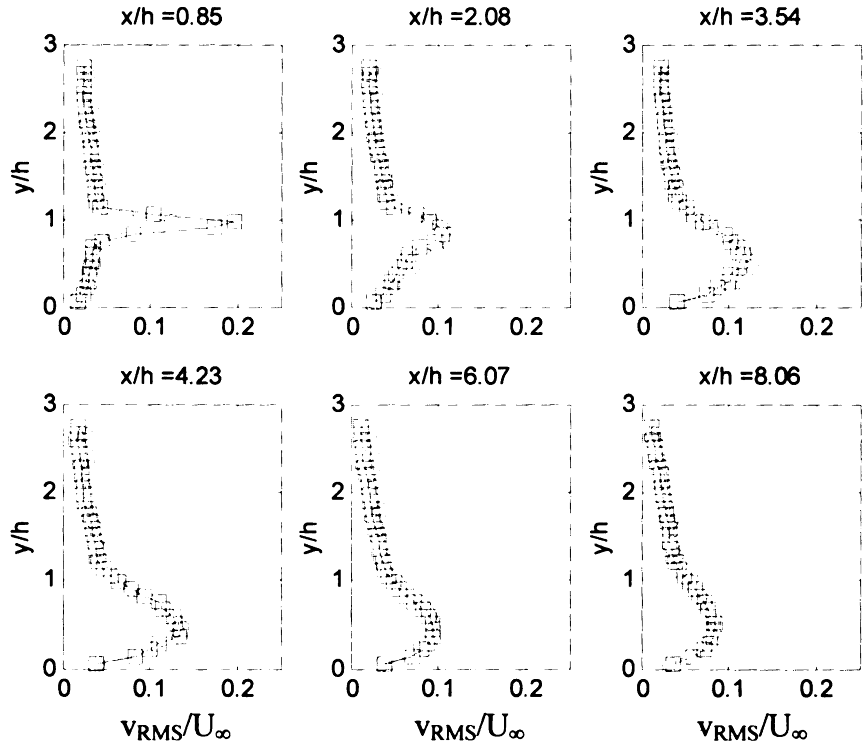

Figure 5.6 Normal-velocity RMS profiles: (O)Re_h = 8081 (□) Re_h = 18588

5.2.3 Reynolds Shear Stress

Figure 5.7 and Figure 5.8 provide the Reynolds shear stress, $-\overline{u'v'}/U_\infty^2$, information for the axisymmetric backward-facing step. Figure 5.7a-b contains the flooded-color, contour maps for the Reynolds-shear-stress for two Reynolds numbers. The axes for the contour plots are the same as seen previously with other contour plots. The color bar below the maps gives the magnitude of the normalized Reynolds stress. Figure 5.8 provides individual $-\overline{u'v'}/U_\infty^2$ profiles at selected streamwise locations. In these profile plots, $-\overline{u'v'}/U_\infty^2$ is plotted along the abscissa and the ordinate shows the normal coordinate normalized by the step height.

Starting with the color, contour maps in Figure 5.7, it is interesting that the magnitude of the non-dimensional, Reynolds-shear-stress decreases as the Reynolds number is increased. This may be explained by looking at the scaling used in the contour maps. The Reynolds stress values in the contour maps are all normalized by U_∞^2. However, Morris and Foss[5] suggested that the Reynolds stresses in a single-stream shear layer should scale with the separating boundary-layer friction velocity (i.e., wall-shear stress), at least close to separation. Thus, since the skin-friction coefficient of the boundary layer (which is proportional to the square of the friction velocity divided by U_∞^2) decreases with increasing Reynolds number, then the ratio of friction velocity to free stream velocity decreases with Re_h as well. This means that the free stream velocity changes faster than the friction velocity with increasing Re_h. Thus, if $-\overline{u'v'}/U_\infty^2$ (u_τ is the friction velocity) does remain invariant with Reynolds number as hypothesized by Morris and Foss[5], then $-\overline{u'v'}/U_\infty^2$ should decrease with increasing Reynolds number.

The individual $-\overline{u'v'}/U_\infty^2$ profiles in Figure 5.8, for the same six different streamwise positions employed earlier to display u_{RMS} and v_{RMS} profiles, provide a clearer support for the above observations. First, the peak for the Re_h = 8081 case near separation is almost double the magnitude of the peak for the Re = 18588 case. This is consistent with, but does not prove, the idea that the turbulence within the shear layer, especially near separation, scales on u_τ and not U_∞. Throughout the shear layer, upstream of reattachment, as shown in the first four plots in Figure 5.8, the lower Reynolds number case has a larger, Reynolds-stress magnitude than the higher Re case. The gap between the two decreases, however, with increasing x/h distance. Beyond reattachment, the profiles collapse, which suggests that in this region $-\overline{u'v'}/U_\infty^2$ is the proper non-dimensional quantity.

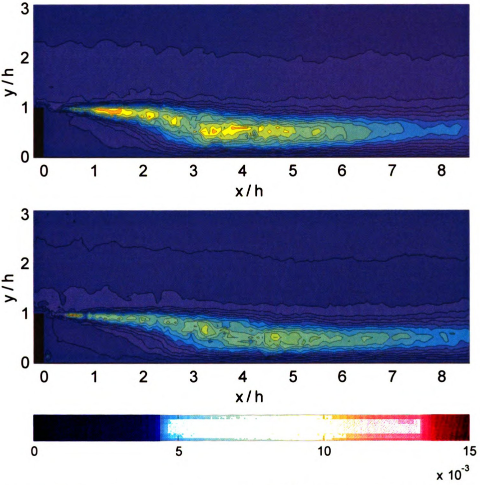

Figure 5.7 Flooded-color, contour maps of $-\overline{u'v'}/U_{\infty}^{2}$ at Re_h = a) 8081 and b) 18588

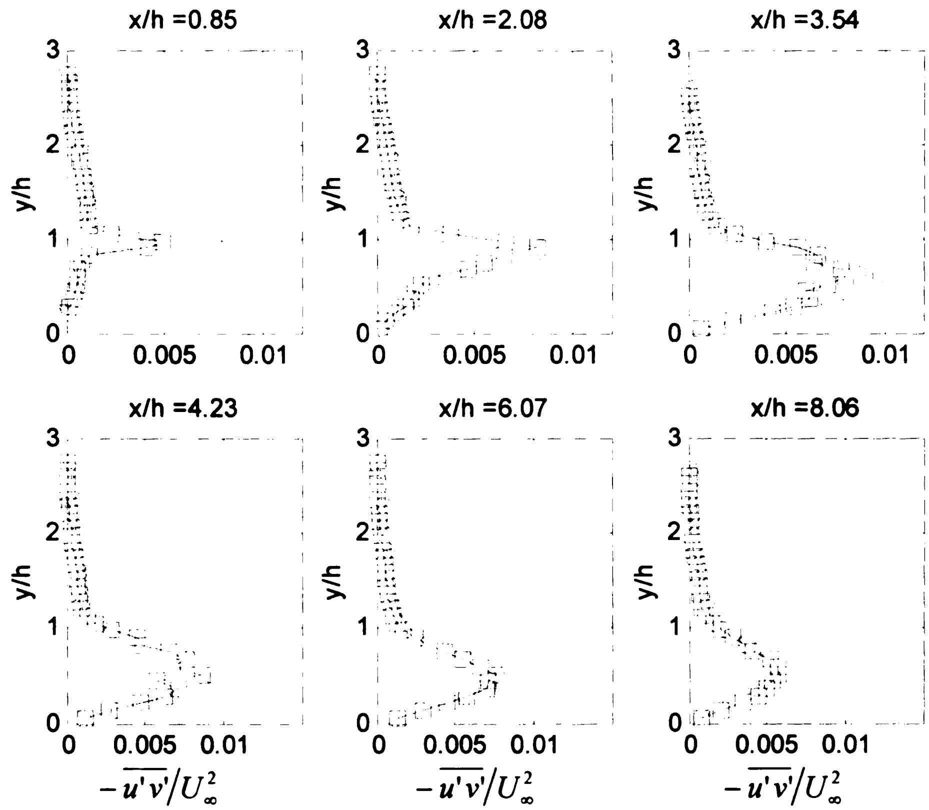

Figure 5.8 Reynolds-shear-stress profiles: (O)Re_h = 8081 and (□) Re_h = 18588,

5.2.4 Vorticity and shear-layer thickness

Vorticity is used to describe the local rotational characteristics of fluid particles. The vorticity is calculated from the velocity field using

$$\vec{\omega} = \nabla \times \vec{V} \tag{5.1}$$

where, $\vec{\omega}$ is the vorticity vector, ∇ is the "del" differential operator, and $\vec{V}$ is the velocity vector field. For this study, velocity measurements were acquired in the x-y coordinate plane; and, therefore, only the vorticity component in the z-direction, i.e., out of plane, can be calculated. This component is given by

$$\omega_z = \left(\frac{\partial v}{\partial x} - \frac{\partial u}{\partial y} \right) \tag{5.2}$$

where, ω_z is the out-of-plane vorticity component. From equation (5.2), it is clear that large vorticity is associated with regions containing large velocity gradients; i.e., regions of high shear. Therefore, the vorticity distribution would be valuable in highlighting the flow within the separated shear layer.

The vorticity downstream of the axisymmetric backward-facing step was calculated using the PIV data. Although the velocity gradients required to obtain the vorticity can be calculated using a finite difference scheme, a circulation-based method for calculating vorticity was used here based on the recommendation of Raffel *et al.*[10]. This relies on the fact that vorticity is related to circulation through the Stokes theorem. More specifically, the *average* vorticity within a particular area can be estimated by calculating the circulation along a contour surrounding the area and dividing the result by the enclosed area. Here, the vorticity estimate is calculated based on the circulation estimate around eight neighboring points as shown in Figure 5.9.

$$(\omega_z)_{i,j} = \frac{\Gamma_{i,j}}{4\Delta X \Delta Y} \tag{5.3}$$

where ΔX and ΔY represent the grid spacing in the streamwise and normal directions, respectively, and

$$\begin{aligned}\Gamma_{i,j} &= \frac{1}{2}\Delta X(U_{i-1,j-1} + 2U_{i,j-1} + U_{i+1,j-1}) \\ &+ \frac{1}{2}\Delta Y(V_{i+1,j-1} + 2V_{i+1,j} + V_{i+1,j+1}) \\ &- \frac{1}{2}\Delta X(U_{i+1,j+1} + 2U_{i,j+1} + U_{i-1,j+1}) \\ &- \frac{1}{2}\Delta Y(V_{i-1,j+1} + 2V_{i-1,j} + V_{i-1,j-1})\end{aligned} \tag{5.4}$$

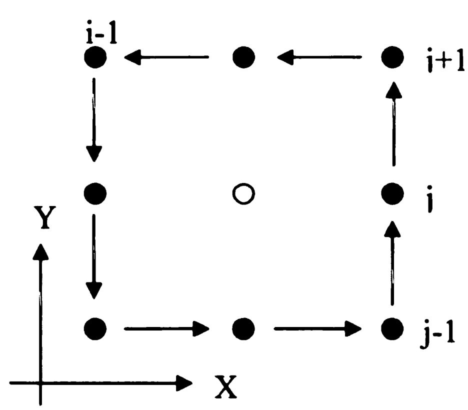

Figure 5.9 Demonstration of the eight-point grid used to calculate the circulation for estimating the vorticity at point (i, j). Copied from Raffel *et al.*[10]

Figure 5.10 shows mean-vorticity, flooded-color, contour plots for the two Reynolds number cases being compared: Re_h = 8081 and 18588. The mean vorticity was calculated from the mean-velocity field shown in Figure 5.1. The axes are the same as given in Figure 5.3. The magnitude of the vorticity, normalized as $\omega_z^* = \omega_z h/U_\infty$, is given by the color bar. Finally, the solid and dashed black lines mark the point where the vorticity is 8% of the global peak vorticity. These lines were determined by finding, for each streamwise location, the vertical position at which the vorticity equaled 8% of the peak vorticity in the flow (these positions are displayed using open circles in Figure 5.10). A 7th order polynomial fit of these locations was then used to obtain the two solid black lines and a 3rd-order polynomial fit was used for the dashed white line. The order of the polynomial was selected to provide a good fit quality. The fits are found to be good for the most part except near reattachment. The solid, black line along the top of the shear layer traces the outer edge of the shear layer from the step to all the way downstream. The bottom edge of the shear layer can only be traced with confidence up to reattachment. Beyond x_r, the dashed line indicates where the lower edge of the shear layer may be located. It is difficult to determine the lower edge of the shear layer beyond reattachment since once the flow reattaches a new boundary layer begins to develop beneath the reattached flow. The point that delineates the two regions is difficult to determine.

Looking at the mean-vorticity distribution for the two cases, the concentration of substantial negative vorticity within the flow field is confined to the shear-layer region. Within the shear layer, there is a local vorticity peak seen slightly downstream of the separating edge. At this point the shear layer is the thinnest and the vorticity is the highest. The vorticity distribution grows in width in the downstream direction, and at the same time the intensity level of the vorticity decreases. The spread rate of the vorticity distribution in the wall-normal direction is particularly pronounced around x/h = 1 to 2, which is consistent with the lateral spread of the distribution of the RMS velocities and the Reynolds stress (Figure 5.3, Figure 5.4, Figure 5.7). Kostas *et al.*[2], who investigated the flow field downstream of a backward-facing step using PIV for $Re_h = 4660$, referred to the shape as bulbous and attributed the shape to the large degree of mixing in the region. Downstream of reattachment, the level of vorticity continues to decrease as the reattached shear layer begins to diffuse and a new boundary layer begins to develop.

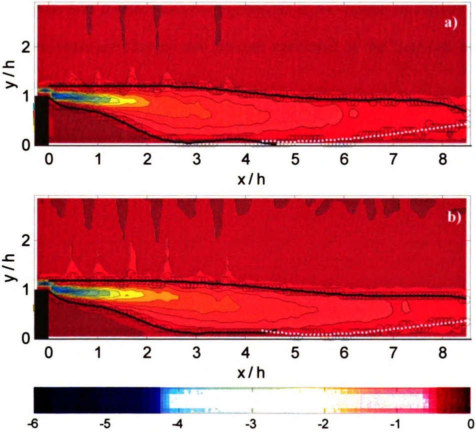

Figure 5.10 Flooded-color, contour plots of vorticity, $\omega_z^* = \omega_z h/U_\infty$, for Re_h = a) 8081 and b) 18588

A comparison can be made between the results for the two Reynolds numbers using both the color, contour plots in Figure 5.10 and the individual vorticity profiles shown in Figure 5.11. Figure 5.11 shows vorticity profiles for both Reynolds number at the same six streamwise positions used for the RMS and Reynolds stress analysis. The normalized vorticity is shown along the abscissa, and along the ordinate, the normal direction divided by the step height is given. The peak vorticity, located near separation ($x/h = 0.008$), for the $Re_h = 8081$ case was $\omega_z^* = -4.7$ and for the $Re_h = 18588$, $\omega_z^* = -5.2$. Kostas *et al.*[2] found their peak vorticity value near the step to be $\omega_z^* = -3.4$. Although the peak levels differ slightly, overall the vorticity magnitude of the two cases is of the same order. There is very little difference between the shear-layer edge lines shown in Figure 5.10 for both cases as highlighted in more detail in Figure 5.12. This shows that the shear-layer spread rate remains unaffected by the Reynolds number (at least over the Re range covered in this study).

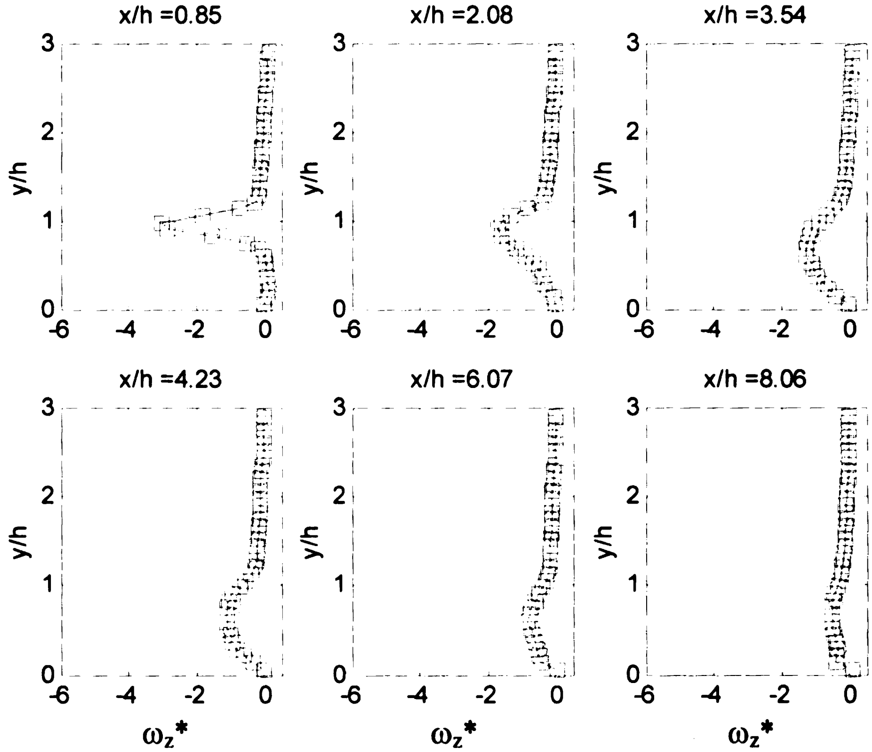

Figure 5.11 Vorticity, $\omega_z^* = \omega_z h/U_\infty$, profiles as selected streamwise locations : (O)Re_h = 8081 and (□) Re_h = 18588

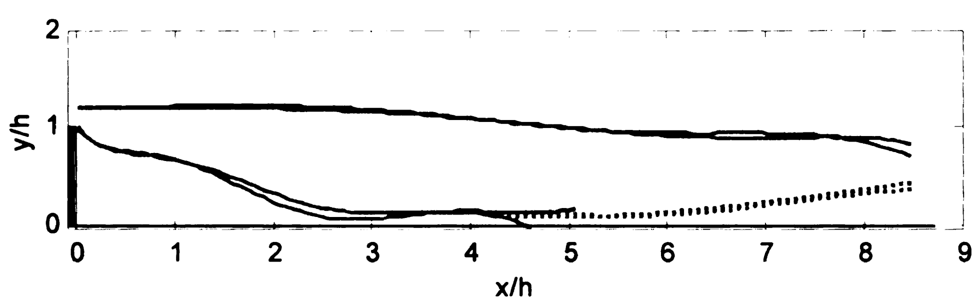

Figure 5.12 Shear-layer edges from Figure 5.10: Re_h = 8081 (red line) and Re_h = 18588 (green line)

5.3 Conclusions

An extensive, planar PIV dataset of the flow field downstream of an axisymmetric backward-facing step was acquired for four different Reynolds numbers in the 2D separating boundary layer case. Reynolds-number effects have been investigated using a portion of the 2D data (specifically for $Re_h = 8081$ and 18588).

The mean-velocity, streamline plots and profiles of the shear layer and the recirculation zone above the wall revealed that both the reattachment length and the location of the secondary, separation point are Reynolds-number dependent. As Re_h increased, the reattachment distance grew while the secondary separation point moved closer to the step. As mentioned in Chapter three, the Reynolds-number effect on the reattachment length may be attributed to variation in the boundary layer momentum thickness as suggested by Eaton and Johnston[11] and Adams and Johnston[12].

The streamwise and wall-normal, turbulent, RMS-velocity, contour maps also indicated Reynolds number dependence near separation, where a peak in the turbulent intensity values was observed at $x/h \approx 0.1 - 1$. The existence of the peak may be explained by the findings of Morris and Foss[5] in a single-stream shear layer, who suggested that the sub-shear layer region is dominated by viscous effects from the near-wall at separation. This local maximum value near separation increased in magnitude with rising Reynolds number. Nonetheless, specialized PIV routines need to be used to verify that the observed peak is not an artifact of high-shear effects on PIV measurements. A second peak was also identified in u_{RMS} and v_{RMS} contour maps. This peak was located slightly upstream of reattachment and increased slightly in magnitude with rising Re_h in u_{RMS} maps but not in the v_{RMS} maps.

The effects of changing Reynolds number were also seen in the Reynolds stress contour maps. The magnitude of the Reynolds stress decreased with increasing Re_h, indicating that near separation $-\overline{u'v'}$ possibly scales on u_τ as suggested by Morris and Foss[5]. This observation requires further testing by directly measuring the wall-shear stress at separation.

The mean-vorticity distribution was used to identify the upper and lower edges of the separating/reattaching shear layer. It was found that the extent of the shear layer, and hence its spread rate, remained unaffected by Reynolds number.

5.4 References

[1] Spazzini, P.G., Iuso, G., Onorato, M., Zurlo, N., and Di Cicca, G.M., "Unsteady behavior of back-facing step flow," *Experiments in Fluids*, Vol. 30, 2001, pp. 551-561.

[2] Kostas, J., Soria, J., and Chong, M.S., "Particle Image Velocimetry Measurements of a Backward-facing Step," *Experiments in Fluids*, Vol. 33, 2002, pp. 838-853.

[3] Scarano, F. and Riethmuller, M. L., "Iterative Multigrid Approach in PIV Image Processing with Discrete Window Offset," *Experiments in Fluids*, Vol. 26, 1999, pp. 513-523.

[4] Li, Y. and Naguib, A.M., "High-Frequency Oscillating-Hot-Wire Sensor for near-Wall Diagnostics in Separated Flows," *AIAA Journal*, Vol. 43, No. 3, 2005, pp. 520.

[5] Morris S. C., and Foss, J. F., "Turbulent boundary layer to single-stream shear layer: the transition region," *Journal of Fluid Mechanics*, Vol. 494, 2003, pp. 187-221.

[6] Castro, I.P. and Haque, A., "The Structure of a Turbulent Shear Layer Bounding a Separation Region," *Journal of Fluid Mechanics*, Vol. 179, 1987, pp. 439-468.

[7] Ruderich, R. and Fernholz, H. H., "An Experimental Investigation of a Turbulent Shear Flow with Separation, Reverse Flow, and Reattachment," *Journal of Fluid Mechanics*, Vol. 163, 1986, pp. 283-322.

[8] Huang, H.T. and Fiedler, H. E., "A DPIV Study of a Starting Flow Downstream of a Backward-facing Step," *Experiments in Fluids*, Vol. 23, 1997, pp. 395-404.

[9] Heenan, A.F. and Morrison, J. F., "Passive Control of Pressure Fluctuations Generated by Separated Flow," *AIAA Journal*, Vol. 36, 1998, pp. 1014-1022.

[10] Raffel, M., Willert, C., and Kompenhans, J., *Particle Image Velocimetry: A Practical Guide*, 3rd ed., Springer-Velag, Berlin, 1998, pp. 160-163.

[11] Eaton, J. K. and Johnston, J.P., "A Review of Research on Subsonic Turbulent Flow Reattachment," *AIAA Journal*, Vol. 19, No. 9, 1981, pp. 1093-1099.

[12] Adams, E.W. and Johnston, J.P., "Effects of the separating shear layer on the reattachment flow structure, Part 2: Reattachment length and wall shear stress," *Experiments in Fluids*, Vol. 6, 1988, pp. 493-499.

6 Pressure and Velocity Measurements

6.1 Introduction

Few authors have investigated the flow mechanisms that generate a specific wall-pressure signature. Most of these investigations have been done in a turbulent boundary layer (e.g. Thomas and Bull[1], Snarski and Lueptow[2], and Johansson *et al.*[3]). Conditional sampling techniques for the pressure signature and the velocity field were used to identify these mechanisms.

One of the few studies that looked at the velocity field *and* surface pressure measurements in a separating/reattaching flow geometry was Lee and Sung[4]. In 2002, they investigated the spatio-temporal characteristics of the wall-pressure fluctuations of the separating/reattaching region downstream of a planar, backward-facing step in a wind tunnel with Re_h = 33000 based on step height. The authors used a one-dimensional array of 29 electret condenser microphones spaced over nine step heights in the streamwise direction, starting two step heights downstream of the separating edge. Pressure measurements were simultaneously acquired with velocity measurements using two split-film probes traversed over a grid of 37 x 21 that extended over $2.0 \le x/h \le 11.0$ and $0.01 \le y/h \le 1.6$.

The simultaneous pressure-velocity measurements were used to analyze the interrelation between the flow field above the surface and the pressure signature on the surface. Lee and Sung[4] cross-correlated both the u and v components of the velocity field with the pressure signature acquired at zero time delay. Results from the cross-correlation between the pressure and u ($R_{u'p'}$) showed a main positive peak inclined at a negative angle with two similar negative peaks on either side. With the $R_{v'p'}$, a negative correlation peak was located directly above the pressure position with a positive peak on either side. The highest correlation was found near the streamwise location of the wall-pressure microphone. In addition, these simultaneous measurements were used to reconstruct the flow field by conditionally averaging the velocity measurements based on specific wall-pressure conditions that were obtained from a new wavenumber filtering technique. The reconstructed flow field showed a well-organized, spanwise, vortical structure with $0.6U_\infty$ convection speed. They also examined the unsteadiness of the reattachment length and were able to analyze the flapping motion of the shear layer. The authors linked the enlargement and shrinkage of the recirculating zone to the low-pass filtered component of the pressure fluctuations.

Another approach for obtaining conditional averages is stochastic estimation (SE). Most of the existing SE studies have utilized velocity measurements at one or more points in the flow field to estimate the flow velocity elsewhere (i.e. Adrian[5], Tung and Adrian[6], Guezennec[7], Cole and Glauser[8], and Stokes and Glauser[9]). In 2001, Naguib *et al.*[10] was the first study to use SE to estimate the flow field from the wall-pressure signature in order to determine the flow sources associated with surface pressure events in a turbulent boundary layer. Simultaneous microphone and hot-wire measurements were acquired over a Reynolds number range of $1437 \leq Re_\theta \leq 5670$, based on momentum thickness. The velocity measurements were obtained in the buffer and logarithmic regions of the flow field. The study estimated the velocity above the surface using both linear and quadratic stochastic estimation (LSE and QSE, respectively). Results showed that it was necessary to include the quadratic term for estimating the flow field as LSE did not capture the conditional average accurately, but the quadratic estimate showed good representation.

In 2002, Murray and Ukeiley[11] used stochastic estimation models for resolving the temporal evolution of the velocity field above the surface from surface-pressure information in a 2D, open-cavity flow. The authors generated their surface pressure and velocity data using numerical simulation in order to test the ability of SE to estimate the flow structures in a separating-flow geometry. The flow Mach number was 1.5 and the cavity had a length to depth ratio of six. Fluctuating velocity, turbulent kinetic energy, and spanwise vorticity were used to compare the estimated and simulated results. Both single-point and multi-point, linear and quadratic SE were used to predict the flow field from the wall-pressure information.

Murray and Ukeiley[11] reported that the estimation strongly depends on the location of the pressure measurement. They found that adding more pressure measurement locations in the LSE only improves the estimation in regions close to where the pressure measurements were acquired. Murray and Ukeiley[11] also found that the linear estimate was able to predict the majority of the flow field, but that adding the quadratic term was necessary to accurately represent the turbulent energy of the flow. In terms of vorticity, the linear term estimated most of the vorticity. However, the addition of the quadratic term was necessary to capture the finer details. Finally, the authors were able to time-resolve the flow evolution using SE and noted that the quadratic estimate predicted the dominant features in the flow very well when compared to the instantaneous simulated data. Later in 2005, the same authors[12] acquired simultaneous PIV and pressure measurements in a Mach 0.2 cavity flow with two different length to depth ratios of 5.16 and 1.49. Using wall-pressure-based quadratic stochastic estimation, they were successful in using this technique to characterize the time-dependent flow behavior within the cavity from the experimental measurements.

To the best of the author's knowledge, no studies have investigated the relation between the velocity field and the wall-pressure in an axisymmetric backward-facing step in order to identify the flow mechanisms generating the surface-pressure signature. Thus, the objectives for this chapter are to identify the flow structures that generate the surface-pressure signature using wall-pressure-based single-point linear and quadratic stochastic estimation and multi-point linear stochastic estimation. Based on the instantaneous spatial pressure distribution, proper orthogonal decomposition is also used to highlight the dominant mode shapes in the pressure signature. These dominant shapes are then used along with stochastic estimation to explore the time evolution of the large-scale flow structures that are linked to the wall-pressure-generation-process within the shear layer and downstream of reattachment. For brevity, the coupling of the flow field with the surface pressure using stochastic estimation will be presented for the Re_h = 8081flow case only.

6.2 Results and Discussion

6.2.1 Average Wall-pressure Signature versus Mean Velocity Field

The purpose of this section is to compare the wall-pressure signature with the velocity field above the surface. Thus far, the pressure signature has been presented in Chapter 4 and the velocity field has been analyzed in Chapter 5. This section combines the two and looks at possible links between the behavior of the wall-pressure statistics and those of the above-surface flow field.

Figure 6.1 gives the auto-correlation from the wall-pressure signature in the top plot and the u_{RMS}/U_∞ of the velocity field in the bottom plot for the $Re_h = 8081$. The auto-correlation, contour plot and axes are the same as those given in Figure 4.3 and are described in detail in Section 4.2.2. The u_{RMS}/U_∞ contour plot and axes are presented in Figure 5.3 and described in Section 5.2.2. Both plots are reprinted here for ease of discussion. In addition, the two plots cover the same streamwise extent and are lined up with respect to each other. By aligning the two plots, a comparison between the wall-pressure and the velocity field streamwise development can be made. In addition, inferences made about the velocity field using the pressure signature in past literature by Heenan and Morrison[13], Driver *et al.*[14], and Hudy *et al.*[15], to name a few, can be verified.

It can be seen in Figure 6.1 that the abrupt transitions seen in the auto-correlation, contour plot are also evident in the u_{RMS}/U_∞, contour plot at the same streamwise locations. Near the step and immediately downstream of separation ($0 < x/h < 2$), as described in Section 4.2.2, the region is dominated by a low-frequency disturbance that has been associated with the flapping of the shear layer in literature. It has been assumed that this region is dominated by low frequency disturbances because the shear layer over this streamwise extent is narrow and far away from the microphone array. Therefore, the disturbances that form in the shear layer due to the Kelvin-Helmholtz instability do not affect the pressure signature since they are weak and far away from the embedded wall-array. Examining the u_{RMS}/U_∞, contour plot over the same streamwise extent, it can be seen that the shear layer within the $0 < x/h < 2$ region is relatively thin and that most of the intense turbulent activity occurs within the shear layer. In addition, the shear layer within this region is far away from the wall-pressure array. This comparison does not affirm that the low-frequency is associated with the flapping of the shear layer but does give reason as to why the pressure signature is not dominated by high-frequency fluctuations from structures within the shear layer.

The second region in Figure 6.1, $2 < x/h < x_r$, is dominated by higher frequencies relative to that seen in the region upstream of $x = 2h$ in the auto-correlation. The abrupt transition seen in the auto-correlation around $x = 2h$ mirrors the transition seen in the u_{RMS}/U_∞ contour plot. At this point in the mean-velocity field, the shear layer is seen to spread vertically over a very short streamwise extent. The vertical spread of the shear layer is roughly equal to the height of the step. It has been inferred from pressure measurements that the reason the auto-correlation is dominated by shorter time scales in this region is due to the proximity of the shear layer with respect to the wall-pressure array. This is confirmed by the observation that the peak, u_{RMS}/U_∞ values seen in this region are in fact closer to the wall-pressure array compared to the location of the peak, u_{RMS}/U_∞ values in the shear layer near separation. Thus, the structures within the shear layer dominate the pressure signature in the $2 < x/h < x_r$ region as stated in literature.

Beyond x_r, the time scales in the auto-correlation gradually become even shorter, indicating that this region is dominated by even higher frequency structures compared to the $2 < x/h < 4$ region. As suggested in Section 4.2.2, it is hypothesized that the narrowing of $R_{p'p'}$ over the $x/h = 4$ to 8 range is caused by the dominant flow structures either convecting at a faster speed and/or changing shape in terms of getting smaller in size. What is evident from the u_{RMS}/U_∞, contour plot is that the vertical extent of the shear layer narrows as the shear layer pulls away from the wall on the lower end and the contours curve toward the wall on the upper end of the shear layer. The y/h position of the center of the shear layer, taken at the postion of the peak u_{RMS}/U_∞ value at each streamwise location and marked by "x" in Figure 6.1, increases slightly in the region downstream of reattachment. To understand more about this region, it is necessary to look at Figure 6.2.

Figure 6.2 gives the same auto-correlation, contour plot as shown in Figure 6.1. In addition, a U/U_∞ versus x/h plot is also given. The velocity values plotted in this figure are the local U values at the center of the shear layer, shown in the bottom plot of Figure 6.1. In free, shear-layer studies, such as Ho and Huerre[16] and Brown and Roshko[17], it is recognized that the average velocity at the center of the layer is approximately equal to the convection velocity of flow structures within the shear layer. Thus, as an estimate, it may be assumed that the velocity at the center of the shear layer in this BFS flow is an approximation of U_c of the flow structures within the shear layer. Focusing only on the U/U_∞ values downstream of x_r, it can be seen that the local, mean velocity at the center of the shear layer increases with increasing streamwise distance. This supports the hypothesis that downstream of reattachment the dominant structures in the flow are convecting faster with increasing x (i.e., accelerating) and therefore a shift in dominance towards smaller times scales (or higher frequencies) of the corresponding wall-pressure signature is observed.

Upstream of reattachment, the local mean velocity at the center of the shear layer is around $U \approx 0.45U_\infty$, in the $0 < x/h < 2$ region, except for the two streamwise locations that show a dip in the velocity roughly around x = 0.3h and 0.5h (Figure 6.2, bottom). This dip most likely is due to an error in the PIV measurements since the locations of these measurements are near the step and PIV has difficulty with near-wall accuracy. At the downstream end of this region, the first transition in the convection velocity is observed when the shear layer balloons out toward the wall. Morris and Foss[18] found U_c to increase steadily through $x/\theta = 120$ in their single-stream shear layer study. Here, the local convection velocity shows a dramatic decrease in the velocity at $x/h \approx 2$ ($x/\theta = 13$), as the shear layer spreads out and the dominant flow structures slow down. The local mean velocity at the center of the shear-layer transitions again and starts to increase around x/h = 3. In investigating the u_{RMS}/U_∞, contour plot in Figure 6.1 again, it appears that the shear layer reaches its full vertical extent at the streamwise location of x/h = 3. It is difficult to verify this in the mean-vorticity-based shear-layer edges plot shown in Figure 5.10. Although it is evident that the shear layer reaches the wall beyond x/h = 2. Once the shear layer reaches its full extent, the flow structures start to increase in speed and continue to do so beyond reattachment.

Another interesting comparison is the local, mean-velocity plot with the wall-pressure cross-correlation contour plot from Figure 4.8 for the $Re_h = 8081$. This comparison is shown in Figure 6.3. In Chapter 4, the cross-correlation, contour plot was used to identify an average, convection velocity upstream and downstream of reattachment. It was found that the average convection velocity upstream of reattachment was lower than U_c downstream of x_r. This same trend is found in the local, mean-velocity plot in Figure 6.3. By averaging the local, mean velocities over the same region from which the convection velocities were calculated, the results showed an increase downstream of x_r. More specifically, from the cross-correlation, U_c was found to be $0.34U_\infty$ upstream of x_r and $0.46U_\infty$ downstream of x_r. From averaging the local mean velocities, $U_c = 0.26U_\infty$ and $0.41U_\infty$ for upstream and downstream of x_r, respectively. While the trend of U_c increasing downstream of x_r is the same between the two methods, the actual calculated convection velocity values differ. This difference could be due to how the two U_c values were calculated from the cross-correlation contour plot, as explained in the following paragraph.

Figure 6.4 investigates the convection velocity calculated from the positive peaks in the cross-correlation contour plot and compares the results with the local mean velocity values located at the center of the shear layer. The center of the shear layer in Figure 6.4 has been defined based on: 1) the peak of the u_{RMS}/U_∞ at each x/h location, and 2) the peak of the mean vorticity at each x/h location. It can be seen that the local, mean velocities at the center of the shear layer based on peak, mean vorticity are greater in value than the velocities at the center of the shear layer based on the location of the peak u_{RMS}/U_∞ values. On the other hand, the convection velocity of the dominant wall-pressure-generating flow structures were calculated in two ways using the peaks of the positive lobe from the cross-correlation shown in Figure 6.3. The first method involved fitting a linear trend to the positive peaks as described in Section 4.2.4. This gives two convection velocities: 1) upstream of x_r, $U_c = 0.34U_\infty$, and 2) downstream of x_r, $U_c = 0.46U_\infty$. The other method explored fitting a parabola to the positive peaks of the cross-correlation. The results from the parabola fit are given in Figure 6.4. It can be seen that while the U_c values from the linear fit do a decent job estimating the convection velocity within the particular streamwise extent, the U_c versus x/h line from the parabola describes the velocity variation along the shear layer center line more accurately within the region. In addition, it seems as though the parabolic fit describes U_c within the reattached boundary layer better than in the shear-layer region. Collectively, the above analysis establishes on a firm basis what has been inferred in the past from wall-pressure or limited wall-pressure/velocity measurements concerning the relationship between the shear layer flow structures and the wall-pressure signature.

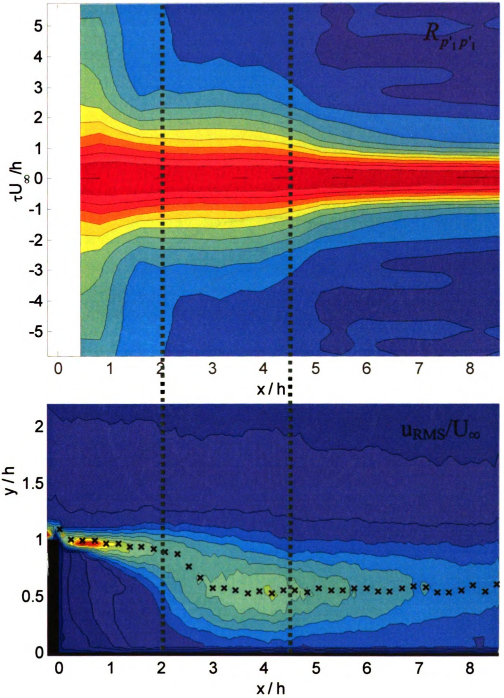

Figure 6.1 Auto-correlation from wall-pressure signature (top plot) and u_{RMS}/U_∞ of the velocity field (bottom plot) for Reh = 8081

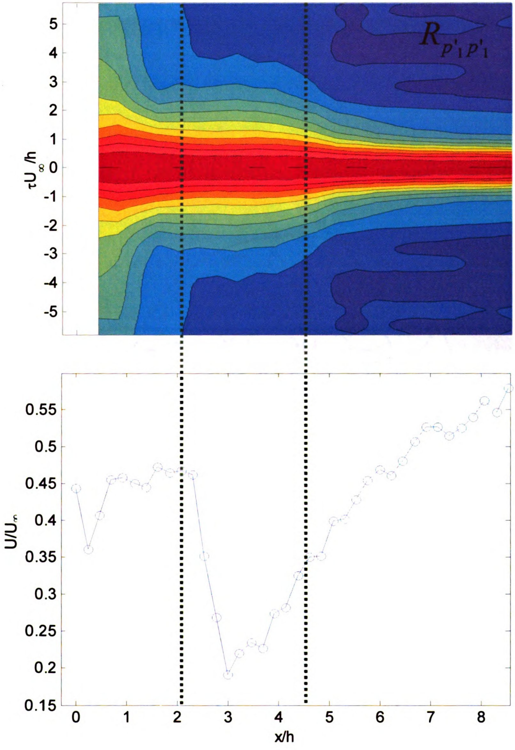

Figure 6.2 Auto-correlation from wall-pressure signature (top plot) and local mean velocity at the center of the shear layer versus streamwise position (bottom plot) for $Re_h = 8081$

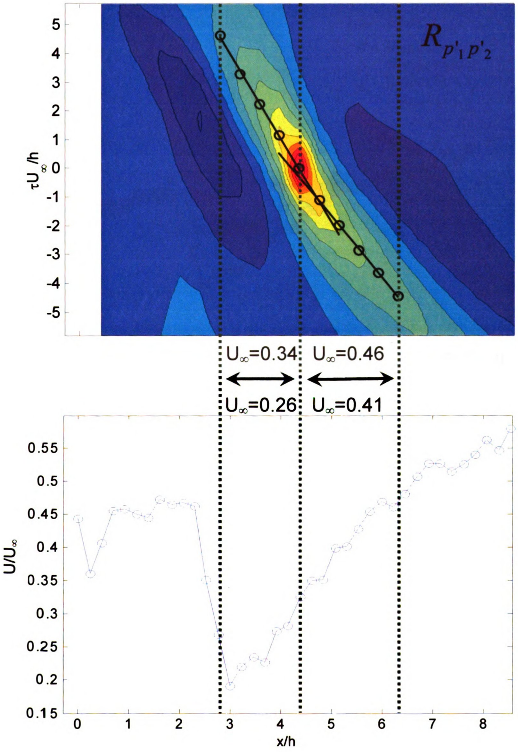

Figure 6.3 Cross-correlation from wall-pressure signature (top plot) and local mean velocity versus streamwise position (bottom plot) for Re_h = 8081

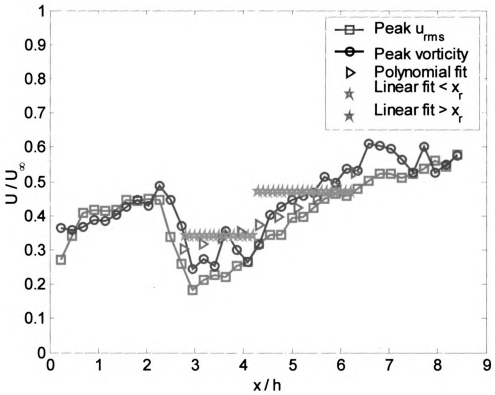

Figure 6.4 Local, mean velocities from velocity field and average convection velocities calculated from wall-pressure, cross-correlation peaks for $Re_h = 8081$

6.2.2 Single-point Linear and Quadratic Stochastic Estimation

Linear stochastic estimation was used to estimate the u' and v' components of the velocity based on a known wall-pressure signature according to

$$\tilde{u}'(x_o+\Delta x, y_o+\Delta y, t) = A_u(\Delta x, \Delta y; x_o, y_o)p'(x_o, y_o, t) \quad (6.1)$$

$$\tilde{v}'(x_o+\Delta x, y_o+\Delta y, t) = A_v(\Delta x, \Delta y; x_o, y_o)p'(x_o, y_o, t) \quad (6.2)$$

where $\tilde{u}'$ and $\tilde{v}'$ are the estimated streamwise and normal fluctuating velocities, respectively, x_o is the streamwise position of the known variable (wall-pressure condition), Δx is the streamwise distance between the known and estimated variables, y is the normal coordinate (also the normal distance between the known and estimated variables), t is the instant in time the pressure event occurs, p' is the measured fluctuating pressure on the wall, and A_u and A_v are the linear estimation coefficient terms for $\tilde{u}'$ and $\tilde{v}'$ respectively. For more detailed information regarding single-point linear stochastic estimation, refer to Appendix 8.6.

Single-point, linear, stochastic estimation requires information from the cross-correlation between the fluctuating pressure signature at one streamwise position and the fluctuating velocity field in order to determine the linear-estimation coefficient. Figure 6.5 shows the flooded-color, contour plots of the cross-correlation between the fluctuating pressure at a particular streamwise position and the mean-removed, streamwise-velocity component (i.e., $R_{u'p'}$) at every node in the flow field. Figure 6.6 display similar plots for the mean-removed, normal-velocity component (i.e., $R_{v'p'}$). The cross-correlations are shown for three different streamwise positions of wall-pressure measurements, x/h = 3.51, 4.68, and 5.46 at Re_h = 8081. The first position is located upstream of reattachment, and the last position is located downstream of reattachment as indicated by the arrows in the figures. The middle position, x/h = 4.68, is located near reattachment, approximately x/h = 0.20 downstream of x_r. These positions were selected in order to highlight the main correlation features at different points in the flow field including within the separated shear layer, around the mean reattachment point, and in the reattached boundary layer. In addition, it is known that in these regions the wall-pressure fluctuations are generally high as shown in the RMS pressure distributions in Figures 4.1 and 4.2.

In Figure 6.5 and Figure 6.6, the streamwise coordinate is shown on the abscissa as x/h and the normal direction is plotted along the ordinate as y/h. The color bar, which gives the magnitude of the cross-correlation normalized by $(\frac{1}{2}\rho U_\infty^2)U_\infty$, has been custom-made so that the transition from red to blue indicates the narrow region around zero correlation. The normalization used for the cross-correlation allowed for identification of correlation regions that are strong globally (i.e., over the entire flow domain). The traditional means of normalization using the local u_{RMS} and p_{RMS} proved difficult to use to compare between the strength of the correlation at different locations in the flow because of the variation in RMS values from one point to another. However, RMS-based normalization is useful in judging the significance of the calculated, correlation values. Thus, it is mentioned here that when normalized by local RMS values, the $R_{u'p'}$ and $R_{v'p'}$ correlations yielded values between -0.4 to 0.4. In Figure 6.5 and Figure 6.6, only correlation values below/above the uncertainty level (correlation value of ±0.00008) are shown in order to highlight the significant correlations in the flow field (note again the apparently small values in the figure are due to normalization by the freestream velocity).

Finally, an arrow with the label p' indicates the streamwise position for the microphone used in each of the correlations.

Starting with the first position, x/h = 3.51, the correlation between the flow field and the pressure is strong as seen in Figure 6.5. A positive, peak correlation can be seen, inclined at an angle, at the x/h = 3.51 microphone location. This positive peak stretches from x/h = 2 - 4.5 and from y/h = 0 – 1.0, indicating good, positive correlation between the streamwise velocity within this region and the pressure at the x/h = 3.51. A negative correlation region can also be seen in Figure 6.5 downstream of x/h = 3.51. It is found inclined at an angle mirroring the positive peak and stretches from x/h = 2.5 – 8, over the y/h = 0 – 2.0 range. The same observations can be made for the other two streamwise positions, x/h = 4.68 and 5.46, shown in Figure 6.5. Note, though, that in all cases the highest correlation value is found very close to the location of observation of the wall pressure. Additionally, the negative correlation region is confined closer to the wall for wall-pressure observations near and downstream of reattachment in comparison to the most upstream location of pressure observation. Finally, a small region of negative correlation upstream of the positive correlation region is found near the wall for x/h = 3.51.

Figure 6.6 shows the $R_{v'p'}/(\frac{1}{2}\rho U_\infty^3)$ contour plots for Re_h = 8081 at the same three streamwise positions. Both positive and negative peaks can be seen in the correlation plots; although, in opposition to the $R_{u'p'}$ results, the main, negative peak is now located directly above the microphone used for the correlation, and the main, positive peak is located farther downstream.

One point worth noting is that the peak correlation values, both positive and negative, at x/h = 4.68 are noticeably stronger than those at the other streamwise positions. This location is about 0.2h downstream of x_r when the structures within the reattached boundary layer are very energetic and are close to the wall. The correlation is expected to be high in this region.

Using the cross-correlation results between pressure and velocity in Figure 6.5-Figure 6.6, the linear, estimation coefficients at each node in the flow field could be calculated (see Equation (8.7) in Appendix 8.6). Once the coefficients were determined, the estimation of the flow field could be performed based on a single-point pressure event. Thus, the flow field was estimated based on the condition that the pressure at a particular streamwise position was five times the RMS. This was computed for both a negative and positive pressure event for all three streamwise locations shown in the cross-correlation, contour plots.

Specifically, SE was used to estimate the mean-removed velocities associated with the pressure events. Subsequently, the mean-velocity field was added to the estimated field to provide an estimation of the full flow field rather than the turbulent field alone. The vorticity and strain rate (ξ_{ij}) fields were then calculated to allow the observer to better see the coherent motions in the flow field. These two measures were used because they are calculated from velocity gradients and therefore, unlike velocity-vector field observations, they are independent of the choice of the translation velocity of the frame of reference. The difficulty in viewing the flow field from a convective frame of reference is in determining the appropriate convection velocity of the flow structures associated with the pressure signature used in the estimate. Subtracting the incorrect convection velocity from the estimated field would give false information regarding the true nature of the flow features. Moreover, as seen in section 6.2.1, the convection velocity of the flow structures responsible for the generation of the wall pressure depends on the streamwise location. Hence, a particular choice of the convection velocity may be suitable for proper observation of the estimated velocity field at one point in the flow but not at others.

The description of vorticity and the equations used in its calculation were given in Section 5.2.4. On the other hand, strain rate is a measure of the rate of geometrical distortion of a fluid element. Rate of strain is a symmetric, second-order tensor, and hence is fully described using six different components (three corresponding to shear and three to elongation). With the availability of planar, velocity-field data in the current study, it was possible to compute only one shear and all three elongation, strain components. The computed shear strain rate component is the in-plane one (ξ_{xy}). Because this component was found to be substantially larger than the elongation components, only the former is presented here. The equations used to calculate the in-plane shear strain are given in Appendix 8.7, with additional information available from Raffel *et al.*[19]

Figure 6.7 – Figure 6.12 show the results of linear, stochastic estimation using vorticity and in-plane shear strain rate (hereafter referred to as just "strain" for brevity). In addition, results from the quadratic stochastic estimation (QSE), which is explained in more detail below, are also shown. The vorticity and strain from both the LSE and QSE for a negative-pressure event at the streamwise position x/h = 3.51 are shown in Figure 6.7 and for a positive pressure event in Figure 6.8. The same results are shown in Figure

6.9 and Figure 6.10 for the streamwise position x/h = 4.68 and in Figure 6.11 and Figure 6.12 for x/h = 5.46. The abscissas and the ordinates for the vorticity and strain fields are the same as described in the cross-correlation results in Figure 6.5 and Figure 6.6. The color bar indicates the magnitude of the vorticity ($\omega_z^* = \omega_z h/U_\infty$) and shear strain ($\xi_{xy}^* = \xi_{xy} h/U_\infty$). The magnitudes were plotted on a scale of -4 to 4. Vorticity and shear strain levels between -0.4 and 0.4 were set at zero in order to minimize noise in the contour plots and enhance the visibility of the dominant features in the flow field.

The single-point, quadratic, stochastic estimation was used as a means of verifying the accuracy of the single-point LSE. QSE was used as a check to see what additional information the quadratic term provides in the flow field and, more importantly, how well does LSE estimate the flow field. The equations used to estimate the u' and v' components of the velocity based on the pressure signature using quadratic stochastic estimation are the following:

$$\tilde{u}'(x_o + \Delta x, y_o + \Delta y, t) = A_{u,quad}(\Delta x, \Delta y; x_o, y_o) p'(x_o, y_o, t) + B_u(\Delta x, \Delta y; x_o, y_o) p'^2(x_o, y_o, t) \qquad (6.3)$$

$$\tilde{v}'(x_o + \Delta x, y_o + \Delta y, t) = A_{v,quad}(\Delta x, \Delta y; x_o, y_o) p'(x_o, y_o, t) + B_v(\Delta x, \Delta y; x_o, y_o) p'^2(x_o, y_o, t) \qquad (6.4)$$

where $\tilde{u}'$ and $\tilde{v}'$ are the estimated streamwise and normal fluctuating velocities in the flow field respectively, x_o is the streamwise position of the known variable, Δx is the streamwise distance between the known and unknown variables, y_o is the normal position of the known variable, Δy is the normal distance between the known and unknown variables, t is the instant in time the pressure event occurs, p' is the magnitude of the wall-pressure event, $A_{u,quad}$ and $A_{v,quad}$ are the linear estimation coefficient terms, and B_u and B_v are the quadratic estimation coefficient terms. More details regarding QSE, including the equations for the coefficients, are given in Appendix 8.6.

At x/h = 3.51, shown in Figure 6.7 and Figure 6.8, the top two plots give the vorticity and strain fields from LSE and the bottom two plots show QSE results. In Figure 6.7a, a region of localized negative-vorticity concentration is shown directly above the microphone used in the estimation. The concentration of vorticity can be seen more clearly in the QSE results in Figure 6.7c, suggesting the presence of a vortical structure immediately on top of the point of observation of the negative pressure event. Inspection of the corresponding strain maps (both linear and quadratic) indicates no particular features in the immediate vicinity of the negative-pressure event. Instead, a hint of a localized strain peak downstream of the event location is found in the QSE results (Figure 6.7d). This feature is smeared in Figure 6.7b where the LSE results are shown. The above suggests that the generation of negative-pressure events on the wall is linked to the passage of large-scale (order h) vortical features.

A comparison between the LSE and QSE results shows that the global flow features are the same as found using LSE, but the features are enhanced and magnified by the addition of the quadratic term. Nonetheless, the basic structure of the estimated flow field is the same by both techniques. LSE is able to capture the large-scale structures with some smearing, while QSE defines the details of the large-scale structures more clearly.

In Figure 6.8, the same results are seen for a positive pressure event. The LSE vorticity field in Figure 6.8a shows that the estimation using this positive pressure signature at x/h = 3.51 produces localized concentration of vorticity upstream and downstream of this streamwise position. Again, this is better defined in the QSE results in part c of the same figure. Whereas, in Figure 6.8 b & d, a region of high strain is found directly above x/h = 3.51. This localized strain-rate peak being found in-between two vertical structures suggest its association with the high-strain region of a saddle point between two vortices.

The above findings are consistent with the study of Naguib and Koochesfahani[20] who found that for the flow field of an axisymmetric vortex ring impinging on a flat wall, strong positive-pressure-generation was associated with the large strain-rate resulting from the interaction of the primary and secondary vortices. Additionally, they also identified the core of the vortex structures to be associated with strong generation of negative pressure. These findings were related to the earlier study of Bradshaw and Koh[21] in which it was shown that, in general, positive pressure generation can be solely attributed to fluid strain while negative pressure production arose due to vorticity.

Similar results can be seen at the remaining two positions, x/h = 4.68 and 5.46, given in Figure 6.9 – Figure 6.12. One interesting observation made in Figure 6.11c and Figure 6.12c is the existence of a region of *positive* vorticity downstream of reattachment. In Figure 6.11c, this region extends roughly in the range x/h = 4.5 – 5.2 and is found very close to the wall just upstream of the vortex structure immediately above the negative-pressure event. In Figure 6.12c, the positive vorticity region is found downstream of a localized negative-vorticity structure upstream of the event location, but farther away from the wall ($y \sim h$). It is hypothesized here that the region of positive vorticity near the wall is associated with the generation of an opposite-sign secondary vortex near and downstream of reattachment via the interaction of the large-scale negative-vorticity structures with the wall. Subsequently, the secondary vortex gets "pulled away" from the wall by the primary structure. Thus, the originally near-the-wall positive-vorticity feature orbits the primary structure reaching $y \sim h$. The described scenario, which is derived from the observations of Gendrich *et al.*[22] of the interaction of an axi-symmetric vortex ring with a flat wall, was also observed in, at least, one instance of a movie of time-resolved multi-point LSE of the flow field (the multi-point estimation and associated flow field is addressed in section 6.2.4).

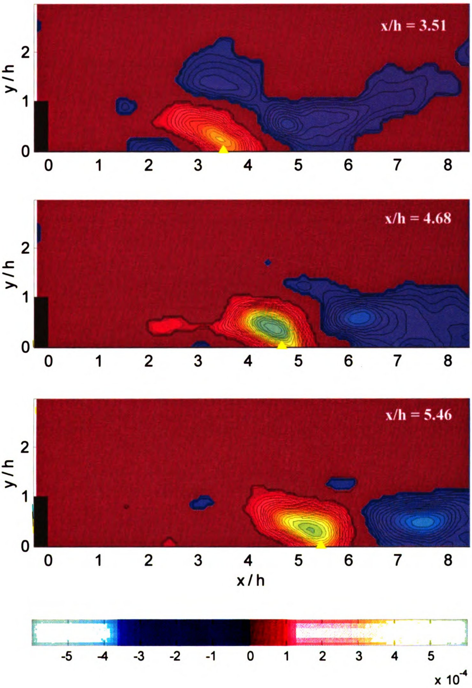

Figure 6.5 Flooded-color, contour plots of $R_{u'p'}/(\frac{1}{2}\rho U_\infty^3)$ for $Re_h = 8081$

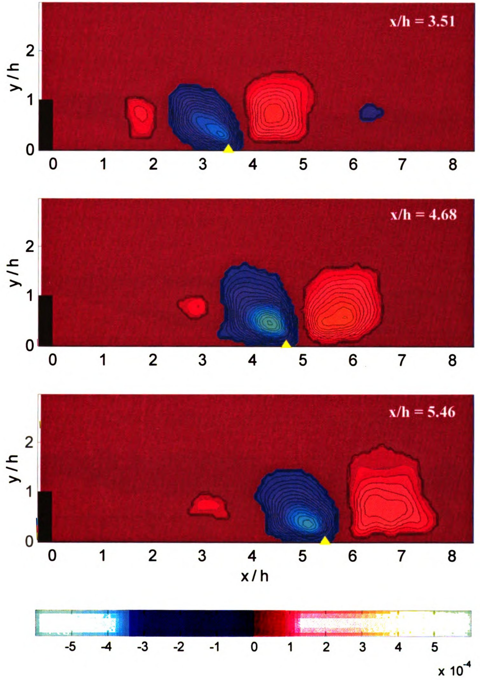

Figure 6.6 Flooded-color, contour plots of $R_{v'p'}/(\frac{1}{2}\rho U_\infty^3)$ for $Re_h = 8081$

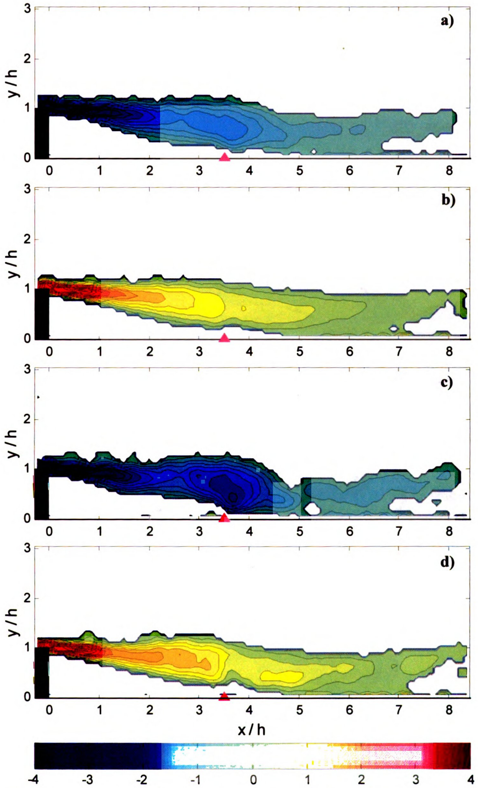

Figure 6.7 Single-point stochastic estimation results for a negative pressure event ($p' = -5p_{RMS}$) at x/h = 3.51 for Re_h = 8081. Linear results: a) vorticity and b) shear strain rate. Quadratic results: c) vorticity and d) shear strain rate.

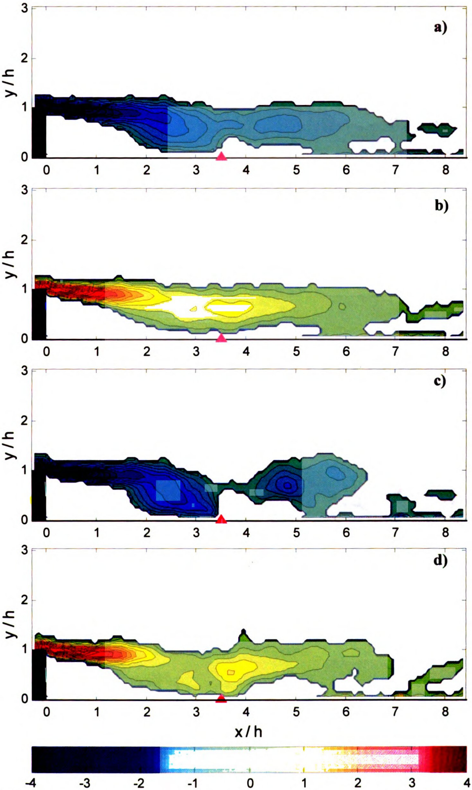

Figure 6.8 Single-point stochastic estimation results for a positive pressure event ($p' = +5p_{RMS}$) at x/h = 3.51 for $Re_h = 8081$. Linear results: a) vorticity and b) shear strain rate. Quadratic results: c) vorticity and d) shear strain rate.

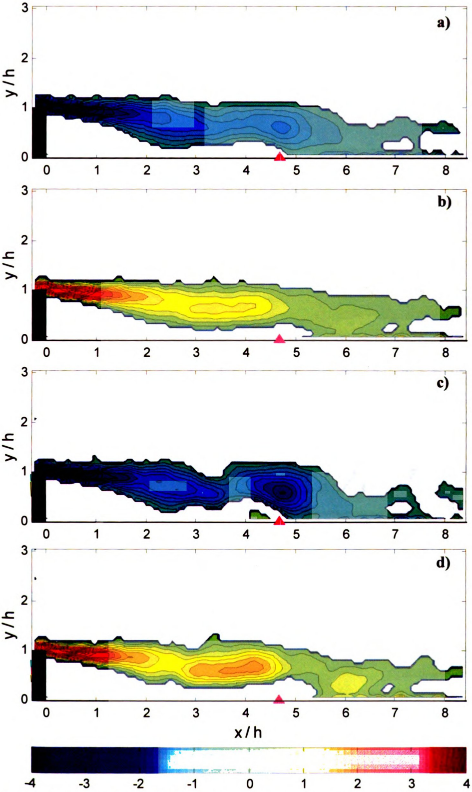

Figure 6.9 Single-point stochastic estimation results for a negative pressure event ($p' = -5p_{RMS}$) at x/h = 4.68 for Re_h = 8081. Linear results: a) vorticity and b) shear strain rate. Quadratic results: c) vorticity and d) shear strain rate.

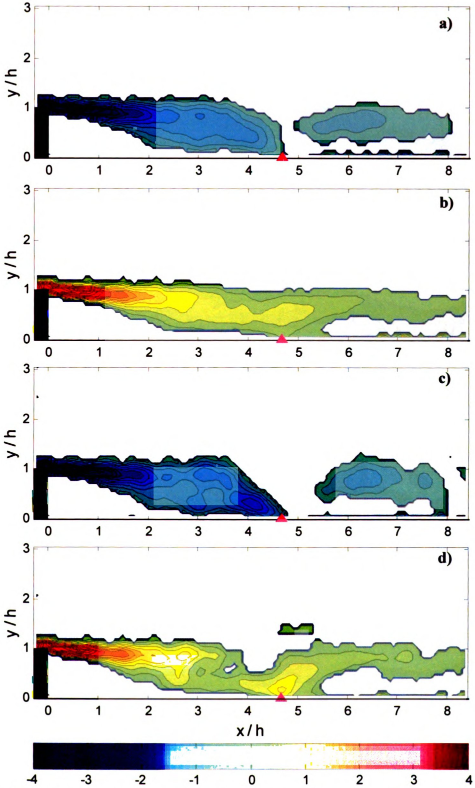

Figure 6.10 Single-point stochastic estimation results for a positive pressure event ($p' = +5p_{RMS}$) at $x/h = 4.68$ for $Re_h = 8081$. Linear results: a) vorticity and b) shear strain rate. Quadratic results: c) vorticity and d) shear strain rate.

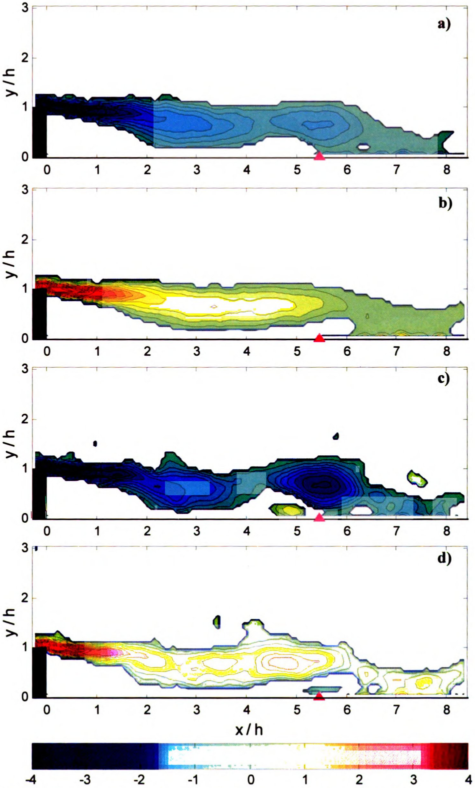

Figure 6.11 Single-point stochastic estimation results for a negative pressure event ($p' = -5p_{RMS}$) at $x/h = 5.46$ for $Re_h = 8081$. Linear results: a) vorticity and b) shear strain rate. Quadratic results: c) vorticity and d) shear strain rate.

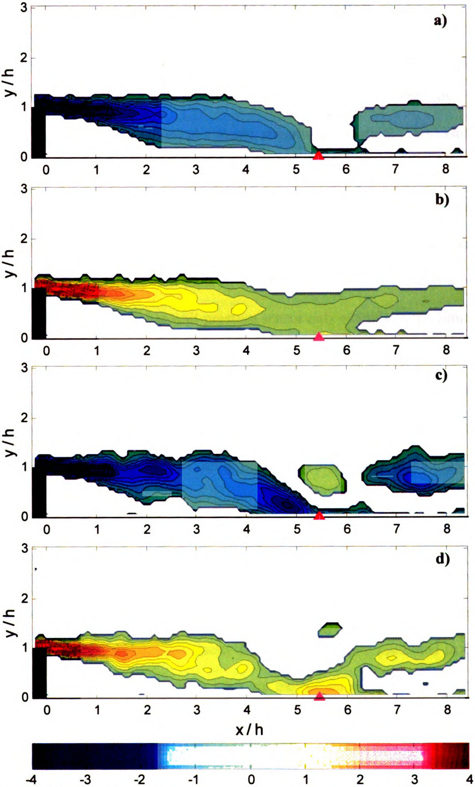

Figure 6.12 Single-point stochastic estimation results for a positive pressure event ($p' = +5p_{RMS}$) at $x/h = 5.46$ for $Re_h = 8081$. Linear results: a) vorticity and b) shear strain rate. Quadratic results: c) vorticity and d) shear strain rate.

6.2.3 Instantaneous, Pressure-Signature Characteristics

6.2.3.1 Instantaneous, pressure signature

Although the above single-point analysis gives information regarding the flow structures associated with the generation of strong, wall-pressure events, the results are biased to one particular microphone at a single, streamwise location. This assumes that a flow structure only affects a single sensor and therefore, only the pressure signature from that sensor is needed to reconstruct the associated flow field. In general, however, flow structures will imprint a pressure signature on multiple microphones. Additionally, it can be seen from the cross-correlation plots in Figure 6.1 and Figure 6.2 that a correlation between the velocity and a single wall-pressure sensor only extends over a limited part of the velocity field. Therefore, in order to estimate the flow structures over the entire flow field, it is necessary to have several sensors at various streamwise locations. The array of 32 microphones embedded in the wall of the axisymmetric backward-facing step model provided this level of detail by measuring the pressure signature at multiple points in space.

The pressure signature from the microphone array was analyzed statistically in Chapter 4 and an average spatio-temporal picture of the pressure field was drawn based on the auto-correlation, the cross-correlation, and the frequency-wavenumber contour plots. The statistics regarding the velocity field have also been presented in Chapter 5. The question that remains, however, is what are the *instantaneous* characteristics of the flow structures that are associated with various instantaneous spatial pressure imprints? In other words, what flow field characteristics produce the observed pressure signature and how do these flow features develop?

Answering these questions requires investigating the spatial pressure signature and corresponding velocity field over time. Starting with the instantaneous, spatial-pressure distribution, Figure 6.13 - Figure 6.14 show examples of the pressure signature over all 32 microphones at different instants in time. The abscissa gives the streamwise distance and the ordinate gives the unsteady pressure in Pascals. Each signature was band-pass filtered between 20-160 Hz (fh/U_∞ = 0.024-0.19). According to past literature as explained in Section 4.2.3 and seen in the frequency spectra in Figure 4.6, the most energetic part of the pressure fluctuations occurs within this bandwidth. This frequency range is mostly beyond the flapping frequency and is where the frequencies associated with the passage of the shear-layer structures occur. Thus, the band-pass filtering allows one to focus the analysis on the flow features associated with the shear layer; i.e., those associated with the downstream-traveling pressure disturbances corresponding to the main spectrum ridge in the right half plane of the wall-pressure frequency-wavenumber (see Figure 4.9a)

Looking at all six spatial-pressure signatures presented in Figure 6.13 and Figure 6.14, it can be seen that the general, signature shape changes along with magnitude. At certain instances in time, the pressure signature seems random in distribution and relatively low in magnitude as seen in Figure 6.13a, Figure 6.13c, and Figure 6.14c. These signatures show low-pressure levels, roughly between -1 to +1 Pascals, over most of the spatial extent. In addition, spatially, the pressure distribution seems unorganized compared to, for example, the signatures in Figure 6.13b and Figure 6.14a-b, where a certain level of organization, almost a modulated "sinusoidal-like" distribution, can be seen. The corresponding pressure magnitude spans a larger range (-4 to 4 Pascals) than seen with the random signatures.

Similar observations were made by Cherry *et al.*[23] in their investigation of the flow around a thick, splitter plate at Re = 32,000 based on model thickness. Two Setra 237 low-pressure transducers were mounted inside their model and were used to measure the fluctuating pressures on the wall. Smoke visualization was used to monitor the flow field simultaneously as the pressure fluctuations were acquired. From their dataset, Cherry *et al.*[23] synchronized the pressure traces with the flow visualization and were able to describe the pressure signature in time as having various shedding phases. These phases were defined by observations made by Cherry *et al.*[23] One such observation was the shedding of pseudo, periodic trains of vortical structures from the reattachment zone. The smoke visualization showed that these structures had a characteristic spacing of approximately 60-80% of the reattachment zone. Large-scale vorticity was also observed to have an irregular shedding pattern and there were quiescent periods where no large-scale shedding occurred. These quiescent periods in the flow field were found to be synchronized with periods in the pressure trace where the pressure fluctuations were random and low in magnitude. During a shedding phase, the pressure signature was found to be energetic, showing higher peaks and lower valleys (in magnitude) than in the quiescent phase. Based on their observations, Cherry *et al.*[23] stated that the pressure signature of a single microphone in time showed substantial variation.

The same is true for the pressure traces measured in the current study. It is very evident from these six pressure signatures that the spatial shape of the pressure distribution varies in time between a quiescent, random signature and a more organized energetic phase. Within the latter a modulated, sinusoidal-like shape seems to recur (Figure 6.13b and Figure 6.14a-b). This offers reason to believe that there is an underlying pattern to the energetic, pressure distributions that appears ever so often in the flow field. In order to investigate such an idea, a mathematical technique that extracts the various mode shapes (spatial shapes) of the most energetic pressure signature was utilized to conduct further analysis. The results of applying the technique, which is known as Proper Orthogonal Decomposition (POD), are given in the following section.

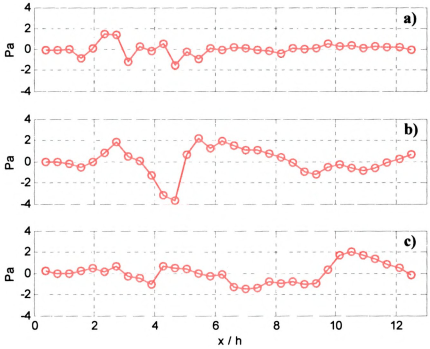

Figure 6.13 Spatial, pressure signature for Re_h = 8081 case at three instants of time: a) 12.00 s, b) 12.01 s, and c) 12.02 s

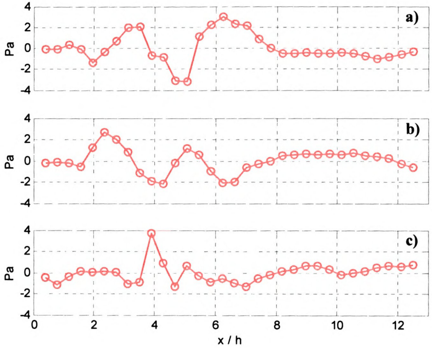

Figure 6.14 Spatial, pressure signature for $Re_h = 8081$ case at three instants of time: a) 8.80 s, b) 8.81 s, and c) 8.84 s

6.2.3.2 Proper Orthogonal Decomposition

Proper Orthogonal Decomposition (POD) is an unbiased technique for extracting organized signatures (or mode shapes), which was first introduced in 1967 by Lumley[24] for use in problems of turbulence. More specifically, the technique identifies the more energetic structures in a flow field. The idea behind POD is that it assumes that a random field can be represented by a set of deterministic, spatial functions superposed with coefficients (or amplitudes) that are random functions of time. Fourier decomposition assumes the same ideology, except that the functions are predetermined to be sinusoidal and are made to fit by solving for coefficients that would make the functions define the random field. The uniqueness of POD stems for its ability to extract both the functions and the coefficients used to define the random field based on statistical properties of the field.

In essence, for the purposes of the current study, POD allows the random field to dictate the modal shapes that make up the spatial pressure field. In addition, POD "ranks" each mode according to its contribution to the wall-pressure signature with the first mode providing the most energetic contribution, followed by the second one and so on. Hence, POD was used in this study to find the dominant spatial pressure distributions underlying the measured pressure field and to rank these distributions according to their average contribution to the pressure field. For more information regarding the background of POD and the implementation of the technique, refer to Berkooz *et al.*[25]

The results for the POD analysis are shown in Figure 6.15, which gives the first four modal shapes plotted as a function of streamwise distance (x/h). A total of 32 modes were calculated using POD since there were 32 wall-pressure sensors. In order to be able to discuss these shapes in their full context, it is necessary to look at the contribution of each mode to the pressure signature. Figure 6.16 shows the percentage of the fluctuating-pressure-field energy recovered from the POD representation, plotted versus the number of POD modes used to represent the pressure signature. The inclusion of all 32 modes in the representation recovers 100% of the energy in the signal. What can be seen from the percent energy distribution in Figure 6.16 is that mode one and mode two, combined, make up almost 40% of the energy content in the signal. Modes three and four make up an additional 20% of the energy content, with each mode representing approximately 10%. This is significant in that 60% of the energy in the pressure signatures can be described using *only* the first four modes from the POD analysis. The next two modes, five and six, add an additional 10%. Thus, 70% of the pressure signature can be recovered using six out of the 32 modes. This helps to simplify the analysis of the pressure signature and allow for focus on the most dominant spatial pressure distributions.

Modes one and two in Figure 6.15 represent the largest energy content and are noticeably similar in spatial distribution. The difference between the two modes is that mode two is shifted to the right with respect to mode one. For instance, notice that when mode one peaks, mode two crosses zero approximately. The same is true when mode two peaks, mode one crosses zero as shown at x/h = 4. The similarity between the two modes with only a streamwise shift difference indicates that the two together represent a single mode that is convecting‡. The same observation can be made for modes three and

‡ It can be shown that POD analysis of a convecting sinusoidal wave gives only two modes: sine and cosine (i.e., sine with 90 degrees phase shift) functions. The combination of the sine and cosine functions with different weights (i.e., amplitudes) can then produce the proper instantaneous phase of the wave.

four in Figure 6.15. This is consistent with the observation that the pairs of modes have similar energy percentage in Figure 6.16. Thus, it can be stated that a convecting mode with a spatial shape given by some weighted average of modes one and two in Figure 6.15 produces 40% of the fluctuating-pressure energy. Moreover, another convecting mode, given by the combination of modes three and four in Figure 6.17, is responsible for the generation of an additional 20% of the unsteady-pressure energy. Based on this analysis, the first four modes will be the focus of the velocity field analysis undertaken in the next section. In addition, since mode one and two represent parts of a convective mode, the two modes are added together with appropriate weighting factors (as will be seen shortly) to form the convecting mode called mode A. The same can be done for modes three and four. The addition of these two modes is called mode B for discussion purposes.

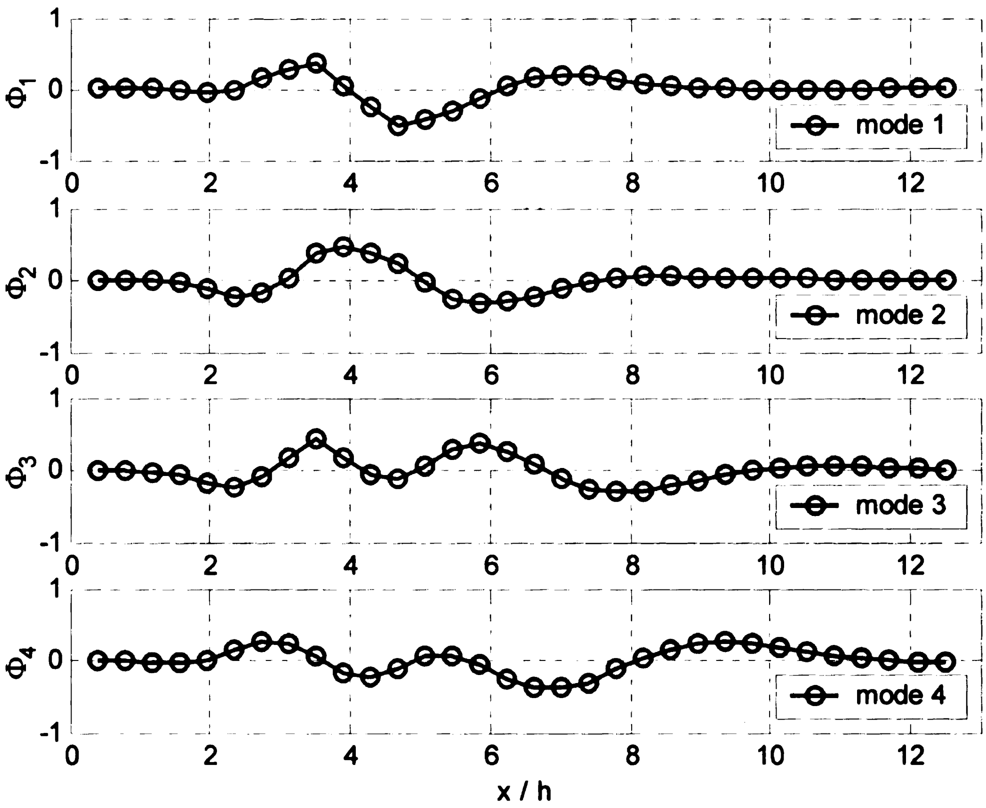

Figure 6.15 First four mode shapes defined by POD for the pressure distribution at Re_h = 8081

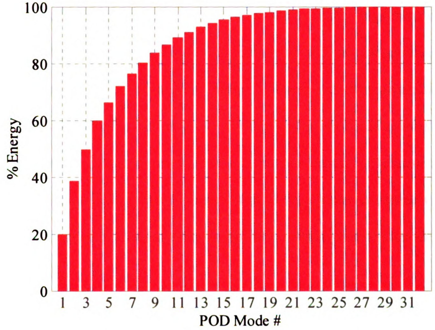

Figure 6.16 The cumulative distribution of energy over all 32 modes for the pressure distribution at Re_h = 8081

It is important to point out that the relative importance of the different modes as shown in Figure 6.16 represents an average over time. For example, although mode one is the most dominant on average there are time instants at which this mode may not be observed at all. Thus, each mode has a time-dependent coefficient, or amplitude $a_n(t)$, that is employed in superposition of all modes to reconstruct the instantaneous pressure signature. The reconstruction is given by the following equation:

$$p(x,t) = a_1(t)\phi_1(t) + a_2(t)\phi_2(t) + a_3(t)\phi_3(t) + \ldots + a_{32}(t)\phi_{32}(t) \quad (6.5)$$

where p(x,t) is the instantaneous spatial wall-pressure signature and $a_1 - a_{32}$ are the amplitude coefficients for each of the mode functions, which are defined as ϕ_1 - ϕ_{32}. The advantage of equation (6.5) is that by limiting the summation to one or a few modes, the space-time evolution of the mode(s)'s pressure signature can be created. For example, if only the first two terms on the right hand side of equation (6.5) are used, one would obtain the spatio-temporal-pressure signature of mode A. This signature can then be combined with LSE to investigate the development of the large-scale structures associated with this mode. However, before looking at the large-scale-structure development, it is instructive to examine the vorticity and strain fields associated with the individual mode shapes, focusing only on the first four modes. Because a particular mode is defined based on the pressure values at all 32 microphones, these vorticity and strain fields were estimated using multi-point LSE employing the mode's pressure signature (as seen in Figure 6.15).

6.2.4 Multi-point Linear Stochastic Estimation

6.2.4.1 Velocity field associated with the pressure signature of POD modes

Multi-point, linear, stochastic estimation is an extension of the single-point LSE equations as shown in Section 6.2.2

$$\tilde{u}' = A_{uo}p'(x_o,t) + A_{u1}p'(x_1,t) + A_{u2}p'(x_2,t) + \ldots + A_{un}p'(x_n,t) \qquad (6.6)$$

$$\tilde{v}' = A_{vo}p'(x_o,t) + A_{v1}p'(x_1,t) + A_{v2}p'(x_2,t) + \ldots + A_{vn}p'(x_n,t) \qquad (6.7)$$

where, A_{u0}-A_{un} and A_{v0}-A_{vn} are the linear-estimation coefficients for each pressure point used in the LSE. For more detailed information, including how the coefficients are calculated, refer to Appendix 8.6. Note that the multi-point, linear, stochastic estimation is used to investigate the flow field associated with the spatial, pressure signature instead of single-point, LSE due to its increased accuracy in estimating the instantaneous flow field as will be shown in Section 6.2.4.3.

Figure 6.17 - Figure 6.24 display the vorticity and shear strain field contour plots for each of the first four modes. The abscissa and the ordinate give the streamwise and normal direction, respectively, normalized by the step height. The color bar shows the magnitude of the vorticity and shear strain, ranging from -4 to +4. The contours plotted are between -4 and -0.5 for vorticity and between +0.5 to +4 for shear strain. This is in an effort to clean up the plots by removing some of the background noise associated with the accuracy of evaluating the derivatives and to highlight regions dominated by high levels of vorticity and shear strain. Beneath each contour plot is the mode-pressure signature used to estimate the vorticity and shear strain fields. The mode is given in Pa and is plotted as a function of streamwise distance.

Figure 6.17 shows the vorticity field associated with the first mode from the POD analysis and Figure 6.18 gives the in-plane shear strain field. It is evident in the vorticity field that a negative peak in the mode's pressure signature (at x/h = 2 and x/h = 4.6) is associated with localized concentration of vorticity as found in the single-point LSE and QSE analysis. At the same streamwise positions in the shear strain field, these negative pressure peaks line up with a region of low shear strain. The reverse is true with the positive pressure peak at roughly x/h = 3.5 in Figure 6.17 and Figure 6.18. The positive pressure peak is associated with an area of low vorticity in Figure 6.17 and a region of peak positive shear strain in Figure 6.18. Farther downstream, a second, positive peak is seen in the mode-pressure signature within the reattached, boundary-layer region. However, both the vorticity and shear strain fields do not show a flow feature associated with this positive peak. This could be due to the level of estimation used. Multi-point QSE may be able to define this region with more clarity as mentioned in the single-point LSE versus QSE discussion. Collectively, the observations in Figure 6.17 and Figure 6.18 suggest that mode one is related to two vortical structures that are located at x/h = 2 and 4.6 with a high-strain, or saddle point, in between.

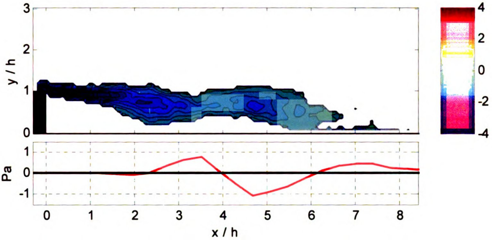

Figure 6.17 Vorticity field associated with mode-one, pressure signature

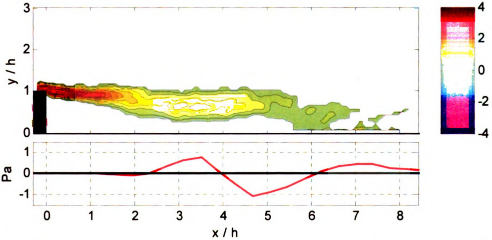

Figure 6.18 Shear strain field associated with mode-one, pressure signature

Figure 6.19 and Figure 6.20 show the same results for mode two as seen in the previous two figures for mode one. The results seem quite similar to those of mode one with the exception of a downstream shift. In particular, the vorticity field shown in Figure 6.19 is no more than the vorticity field shown in Figure 6.17 shifted downstream such that the localized focusing of vorticity is now found at x/h = 2.5 and 6. A similar shift is found for the shear strain field in Figure 6.18 and Figure 6.20. In summary, mode two appears to reflect the same flow structure as mode one after the translation of the latter farther downstream. Thus, a linear combination of both modes can be used to represent the advection of the mode, as reasoned earlier based on the pressure signature alone.

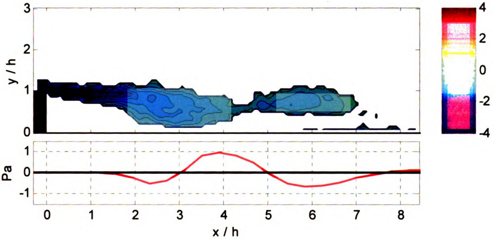

Figure 6.19 Vorticity field associated with mode-two, pressure signature

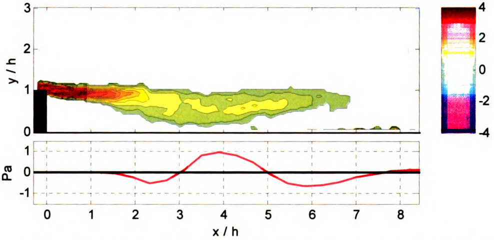

Figure 6.20 Shear-strain field associated with mode-two, pressure signature

Figure 6.21 and Figure 6.22 display the vorticity and shear-strain field, respectively, for mode three. This mode shape has lower negative and positive peak magnitudes then those seen in modes one and two. Additionally, mode three's pressure signature shows two positive peaks and three negative peaks over the streamwise extent investigated. Mode one had two positive pressure peaks and one negative; whereas, mode two had the opposite of mode one. Based on the single-point, SE findings, the number of negative-pressure peaks may be used to indicate the number of vortical-flow structures associated with the particular mode shape. In Figure 6.21, is can be seen that the three negative-pressure peaks are associated with three vortical structures; whereas, in Figure 6.22, the positive peaks line up with the spaces in between the structures.

An interesting observation may be made at this point. Recognizing the association of negative-pressure peaks with vortical structures, it appears that it may be possible to create a potential flow model of a train of convecting vortical structures that would produce the same mode-pressure signatures seen in Figure 6.21 and Figure 6.22. More specifically, it is known from potential flow theory that as a vortex core passes over a wall it leaves a negative pressure imprint. A series of such vortices would then produce a corresponding train of negative pressure peaks with positive pressure between the vortices. A similar model for representing the wall-pressure field downstream of reattachment was proposed by Daoud[26].

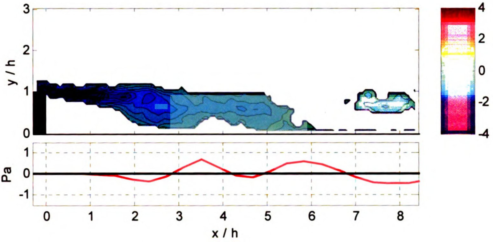

Figure 6.21 Vorticity field associated with mode-three, pressure signature

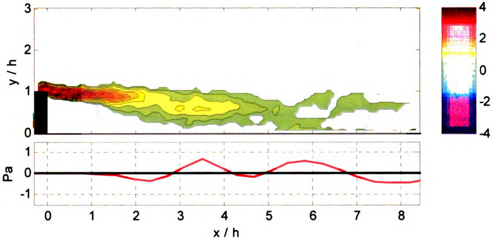

Figure 6.22 Shear strain field associated with mode-three, pressure signature

The vorticity and shear strain fields associated with the mode-four, pressure signature are shown in Figure 6.23 and Figure 6.24 respectively. The fields are the same as seen in mode three but shifted in the streamwise direction due to the convective nature of the structures that the modes represent.

Finally, it is interesting to note that the vorticity field is able to capture a structural feature in the reattached boundary layer when there is a negative pressure peak at such a streamwise location (see Figure 6.19 at x/h = 6 and 6.22 at x/h = 8). However, the shear strain field does not display any features in the reattached, boundary-layer region. These observations are also consistent with the single-point-estimation results (see Figure 6.10 and Figure 6.11b) where it is seen that the localization of the shear strain is more evident in the shear layer than in the reattached, boundary layer. However, the single-point QSE results within the same region (Figure 6.10 and Figure 6.11d) are successful in capturing the localization of the strain field. Hence, it appears that whereas LSE does a good job in representing localization in vorticity, it is not as good in capturing localization of strain. The reason for this is currently unknown and requires further investigation.

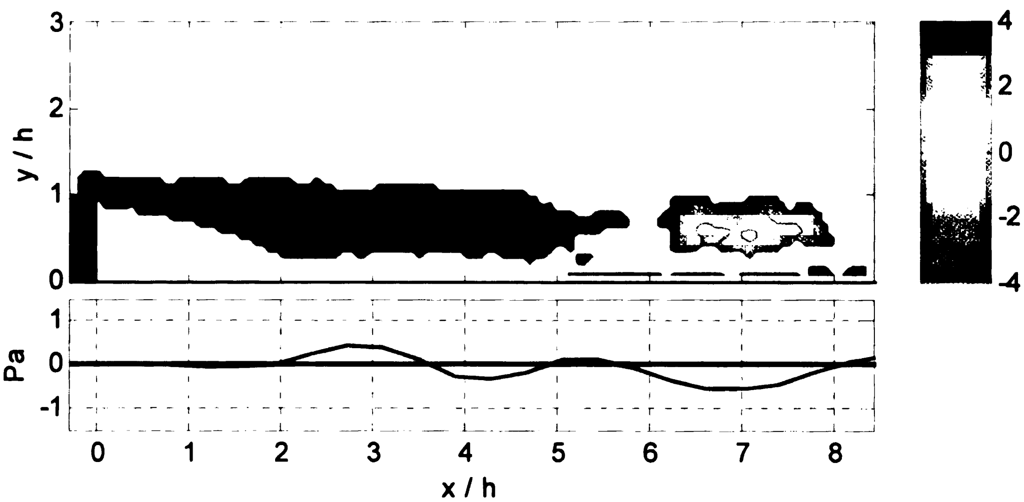

Figure 6.23 Vorticity field associated with mode-four, pressure signature

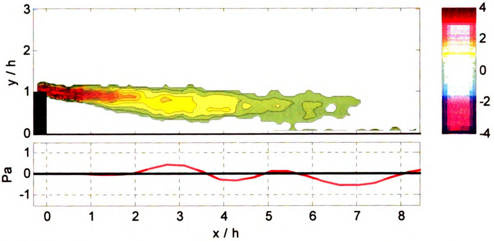

Figure 6.24 Shear strain field associated with mode-four, pressure signature

6.2.4.2 The evolution of large-scale structures in the flow field

Figure 6.25 shows the evolution of the vorticity field using multi-point LSE based on the pressure signature of mode A. Only the vorticity field is shown since it gives the same information as the shear strain field and seems to better reveal structures within the reattached, boundary layer. The axes in Figure 6.25 are the same as given in Figure 6.23, including the color bar. The pressure signature used in the estimations starts 8.81 seconds (image 67) into the acquisition sequence and ends after an elapsed time of 125 ms. Numbers associated with arrows are used in the figure to identify coherent structures, which are defined as regions of vorticity concentration.

In all four plots in Figure 6.25, it can be seen that immediately downstream of separation there exists a thin region of vorticity that extends to approximately x = 1.5-2h. This region is dominated by the mean vorticity field seen in Figure 5.10a. Multi-point LSE reveals the mean-removed quantities in regions where the correlation between the pressure signature and the flow field is high. Due to the relatively large separation between the shear layer in this region and the wall-pressure sensors, the correlation in this region is low; and, therefore, no particular flow featured is captured. This can also be seen by the low magnitude of the pressure signature used in the estimation in this region shown in all four contour plots in Figure 6.25. Beyond x/h = 2, the correlation between the flow field and pressure signature is good (Figure 6.5 and Figure 6.6) and the magnitude of the pressure signature is higher; therefore, the vorticity field estimation begins to reveal some of the underlying, turbulent structures.

As discussed in Section 6.2.3.1, the pressure field seems to alternate between periods of random, quiescent, pressure signatures and organized active ones. In the quiescent phase, the magnitude of the pressure signature is relatively low and the estimated, vorticity field looks similar to the mean-vorticity field shown in Figure 5.10a for reasons just explained above. Figure 6.25a shows the end of a relatively quiet phase compared to the other vorticity fields shown in Figure 6.25. Nonetheless, some strengthening in the shear layer has occurred and, as can be seen in Figure 6.25a, a large concentration of vorticity (1) seems to start to develop.

During an active phase, the magnitude of the pressure signature is strong and the coherent structures in the vorticity field are well defined. As shown in Figure 6.25b, the evolution of the shear layer shows a spatial growth of vorticity that forms a coherent structure (2) between x/h = 2-3 while the large concentration of vorticity (1) sheds from the shear layer and travels downstream. This sequence of events occurs approximately 3.75 ms after Figure 6.25a. In time-dependent estimation (not shown here), the large-scale structure (2) is then seen to move downstream to approximately x/h = 3 where it shows weakening. Twelve milliseconds after Figure 6.25b, the coherent structure (2) has moved to x/h = 3-4 where it remains stationary while growing in size, shape, and strength

(Figure 6.25c). At this point, coherent structure (1) has moved even farther downstream and seems to have decayed. This shows a limitation of the POD technique in that the spatial modes 1 and 2 are equal to zero beyond x/h = 8 (Figure 6.15). Therefore, using mode A pressure signature in multi-point LSE would not be useful in estimating mean-removed quantities at streamwise positions greater than x/h = 8. That is, the coherent structure (1) in Figure 6.25c most likely has not completely decayed as shown, but, in terms of POD, is likely to now be defined by a higher mode shape. In Figure 6.25d, which was taken 6 ms after Figure 6.25c, coherent structure (1) is no longer in the streamwise extent shown and large-scale structure (2) is seen to be shedding from the shear layer. At the same time instant, coherent structure (3) starts to form upstream between x/h = 2-3. The concentration of vorticity (2) eventually moves downstream past the mean, reattachment point and into the reattached, boundary layer.

A similar pattern can be described for the time evolution of the large-scale structures based on mode B pressure signature. The time-sequenced, estimated-vorticity fields for mode B are shown in Figure 6.26. These vorticity fields were estimated starting 17 ms before image 67 was acquired and ran 1.7 ms after the image acquisition. The region between separation and x/h = 1.5-2 is the same as described for mode A. An initial roll-up of a large-scale structure (3) occurs between x = 2-3h as seen in Figure 6.26a. Weaker coherent structures (1) and (2) are also evident in the vorticity field. Coherent structure (2) has just passed through the average reattachment point. The evolution of coherent structure (3) shows that the structure moves downstream once it reaches approximately the size of one step height. It then shows weakening between x/h = 3-4 for a moment before growing stronger as shown in Figure 6.26b (8.3 ms after

Figure 6.26a). Meanwhile, the concentration of vorticity (2) near the wall in Figure 6.26a has convected downstream and picked up strength in Figure 6.27b. This same structure (2) is then seen 5.4 ms later to have convected downstream as in Figure 6.27c along with the large-scale structure (3). Both of these concentrations of vorticity formed well-defined structures and shed from the shear layer. In addition, another large-scale coherent structure (4) is starting to form between x/h = 2-3 in Figure 6.26c. In Figure 6.26d, 3.3 ms later, both coherent structures (3) and (4) lose strength as seen in the vorticity field and in the mode B pressure signature. It is possible that the fast decay of the strength of the structures may be due to the structures switching to a higher mode shape; but more likely, it is related to the phenomenon of switching between active and inactive, flow periods. The physical mechanisms leading to this switching remains a mystery at the present time.

Modes A and B, pressure signatures are combined in Figure 6.27, and the associated vorticity fields are shown for the same time sequence as used with the mode B pressure signature. The modes A and B combined are responsible for 60% of the pressure-fluctuation energy on average. Estimating the vorticity field from both modes A and B can provide additional information since the strength of the coefficients for modes 1-4 can vary with time. For example, at a particular instant in time, one of the modes may be more dominant or both could be equally important.

In Figure 6.27, the same sequence of events described for the individual modes A and B can be seen when both modes are combined. Two coherent structures (1) and (2) are evident in Figure 6.27a. Both convect farther downstream 2.1 ms later in Figure 6.27b, while a concentration of vorticity (3) starts to form at streamwise location x/h = 2-

3. The roll-up of the large-scale vortex (3) continues 2.9 ms later in Figure 6.27c and coherent structure (2) is seen to have moved farther downstream. It is interesting to note here that the streamwise extent between the two concentrations of vorticity (2) and (3) is equivalent to approximately $0.67x_r$. Cherry *et al.*[23] found the characteristic spacing between structures shedding from the reattachment zone to be between 60% - 80% of the separation bubble length. In Figure 6.27d, 6.25 ms later, coherent structure (3) increases in strength between x/h = 3-4 and at the same time the large-scale vortex (2) is decaying in the reattached boundary layer. One observation that can be made in the estimation using mode AB pressure signature is the period of weakening noticed in the individual mode pressure signatures does not seem to exist. This suggests that the weakening of the structures is associated with the disappearance of energy from one mode and its appearance in the other. Since the POD modes are generally mathematical, it is likely that this is a mathematical artifact. That is, modes A and B may simply be a mathematical decomposition of the same physical structure.

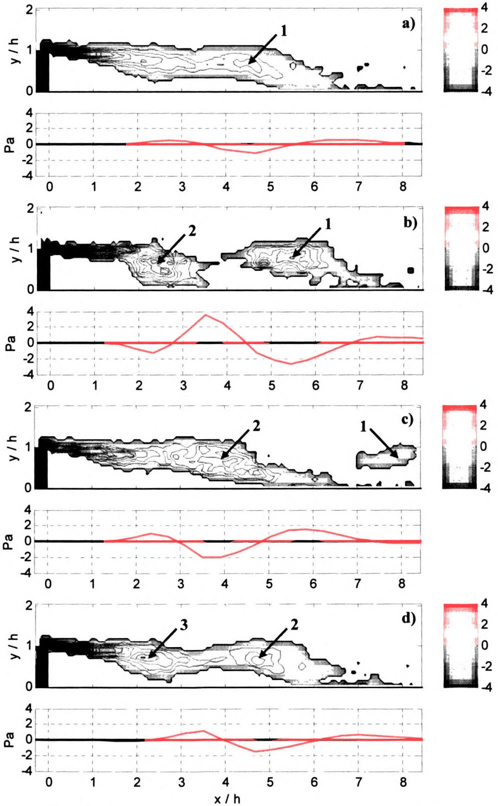

Figure 6.25 Multi-point LSE of the velocity field associated with mode A pressure signature

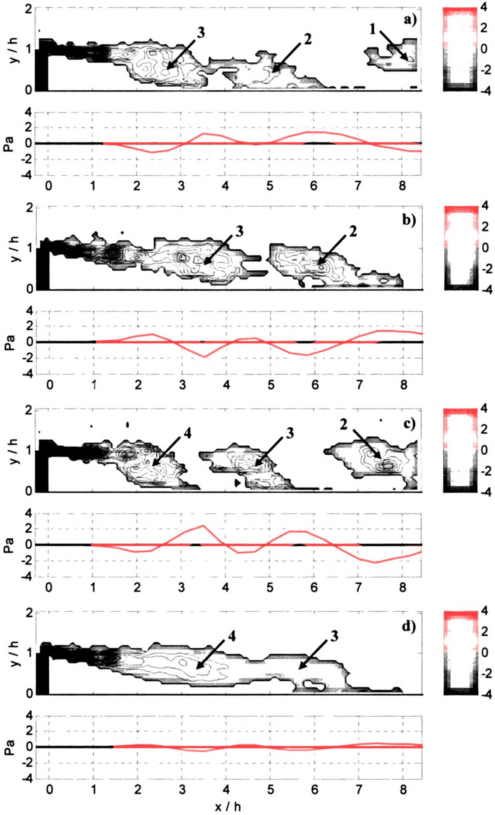

Figure 6.26 Multi-point LSE of the velocity field associated with mode B pressure signature

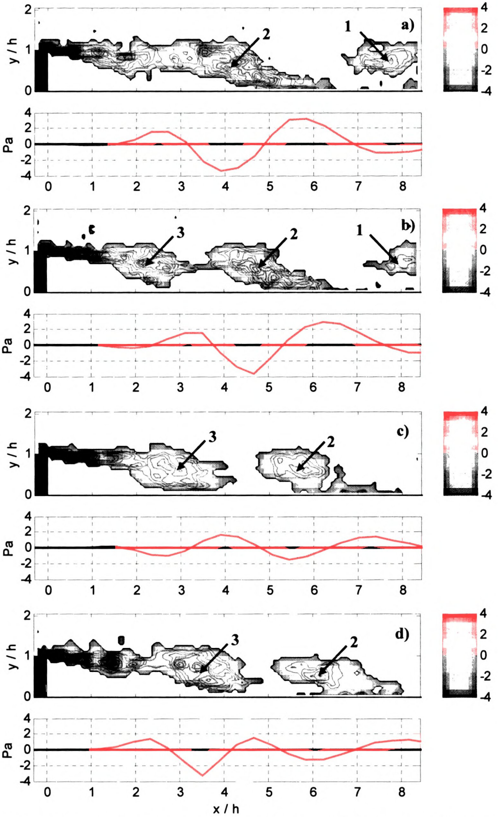

Figure 6.27 Multi-point LSE of the velocity field associated with mode AB pressure signature

As mentioned previously, it is best to show the evolution of the flow structures using a movie or multiple frames. Figure 6.25, Figure 6.26, and Figure 6.27 show the overall picture seen regarding the evolution of the flow structures. However, the flow-field frames given in these figures are separated by a rather coarse time step. To provide a clearer picture of the evolution of the flow features, a series of 36 plots of the vorticity field separated by a time offset of 0.4 ms between plots are shown in Figure 6.28. The axes and the color bar (not shown) are the same as described in Figure 6.27. In Figure 6.28, the flow structure of interest is marked by an "X" by *visually* locating the highest vorticity value within the flow structure. Note that without the fitting of a curve to the vorticity distribution in order to locate the peak vorticity, a minimum uncertainty equal to the grid spacing of the PIV data (0.92 mm or 7.5% of the step height) is assumed in identifying the structure location. Additionally, the visual process of identification is likely to increase this uncertainty by a factor of two or three. Therefore, it is estimated here that the identified structure location is known with 15% - 20% uncertainty. Overall, detailed formation and subsequent evolution of the marked vortex structure is depicted in Figure 6.28. To see this more clearly, the streamwise coordinate of the vortex is plotted as a function of time in Figure 6.29. The figure shows the flow structure of interest remaining stationary, within the uncertainty of the data, between x/h = 2-3 for the duration of the first four to five vorticity fields (2 ms) before it starts to accelerate downstream. Finally, Figure 6.30 shows the streamwise and normal position of the flow structure of interest as it is tracked downstream in the multiple frames shown in Figure 6.28.

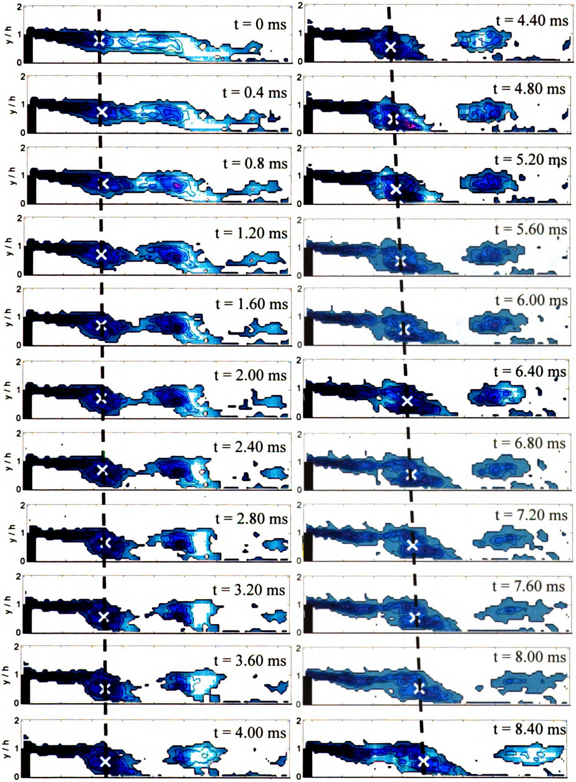
t = 0 ms
t = 0.4 ms
t = 0.8 ms
t = 1.20 ms
t = 1.60 ms
t = 2.00 ms
t = 2.40 ms
t = 2.80 ms
t = 3.20 ms
t = 3.60 ms
t = 4.00 ms
t = 4.40 ms
t = 4.80 ms
t = 5.20 ms
t = 5.60 ms
t = 6.00 ms
t = 6.40 ms
t = 6.80 ms
t = 7.20 ms
t = 7.60 ms
t = 8.00 ms
t = 8.40 ms
y / h

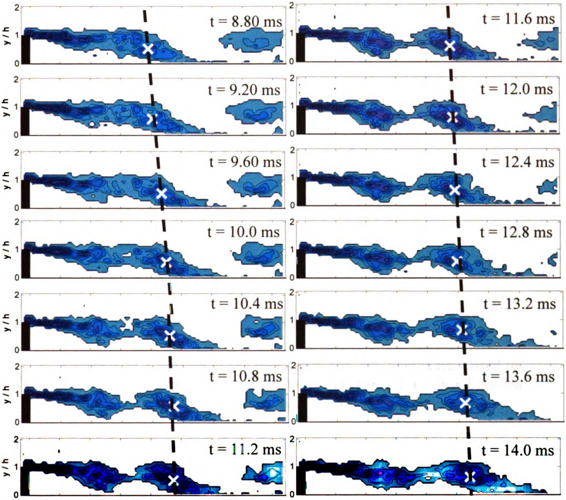

Figure 6.28 Frames showing evolution of flow structure, $\Delta t = 0.4$ ms

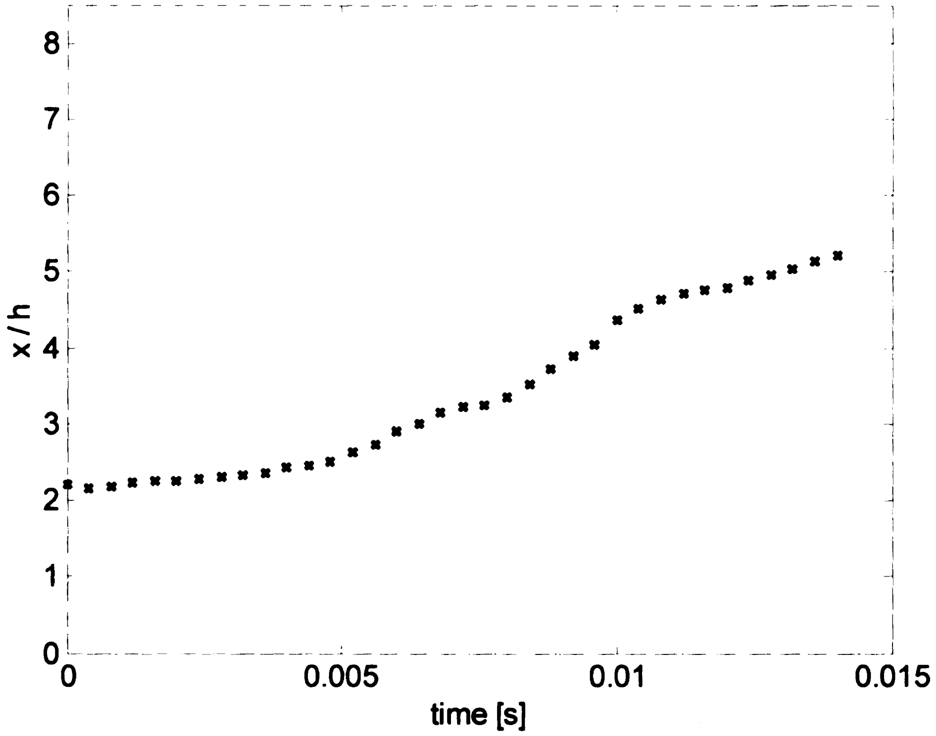

Figure 6.29 Location of the flow structure, x/h, versus time used in tracking the evolution of a flow structure developing between x/h = 2-3

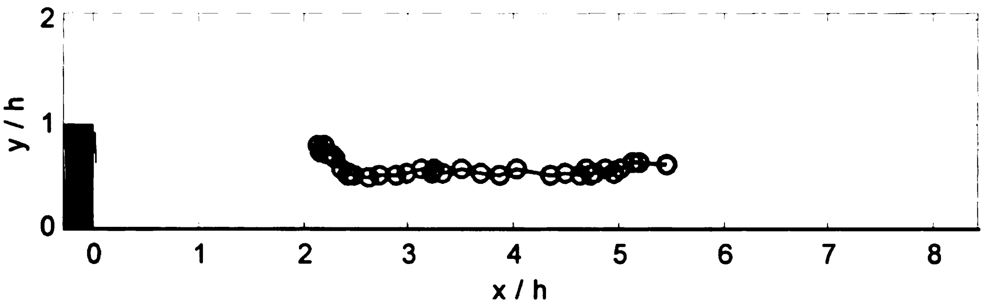

Figure 6.30 Tracking the location of a flow structure as it forms between x/h = 2-3 and then accelerates downstream

6.2.4.3 Instantaneous versus estimated flow field

As mentioned previously and explained in detail in Appendix 8.6, under certain conditions, the multi-point LSE can satisfactorily estimate the instantaneous, velocity field. Multi-point LSE imposes a strict spatial condition for estimating the average flow field by using a particular, spatial-pressure-distribution condition. The estimate is stricter with this condition compared to a single-point, pressure condition and is less likely to deviate from the instantaneous flow field. This would be particularly true for flow fields where the pressure generation is dominated by coherent motions. Thus, multi-point LSE allows for a more "realistic" estimation of the instantaneous, flow field. Cole and Glauser[8] addressed the accuracy of multi-point, LSE compared to single-point, LSE in their jet mixing layer study. In their study, they used velocity measurements to estimate the entire flow field using LSE. From their results, they found that single-point, velocity estimates did not adequately estimate the instantaneous, flow field and that at least two reference points were needed to represent the flow field well. The present study utilizes surface-pressure to estimate the flow field. The degree to which the estimate represents the instantaneous flow field will be assessed in this section.

The instantaneous pressure signatures shown in Figure 6.13b and Figure 6.14b were simultaneously acquired with PIV images 1299 and 67, respectively. The instantaneous vorticity fields associated with the pressure signatures are shown in Figure 6.31a and Figure 6.32a. The instantaneous vorticity fields have been smoothed using a 3x3 filter in order to remove the effect of small-scale random turbulence and some of the noise resulting from calculating derivatives. The abscissa, the ordinate, and the color bar are the same as described for Figure 6.23. In Figure 6.31b and Figure 6.32b, the vorticity fields estimated using multi-point LSE based on the instantaneous pressure signatures occurring simultaneously with the sampling of images 1299 and 67, respectively, are displayed. Finally, the vorticity fields estimated using multi-point LSE based on one of the dominant mode shapes is shown in Figure 6.31c and Figure 6.32c. The mode shape used for image 1299 is mode A and for image 67 is mode B, as will be explained below.

The instantaneous vorticity field in Figure 6.31a shows small-scale concentrations of vorticity spread across the streamwise and normal extent measured by the PIV. The vorticity field shown in Figure 6.31b gives an estimate of both small- and large-scale structures. Since the technique used was LSE, the large-scale structures are better defined. The organization of the flow field is difficult to see in Figure 6.31a, yet the instantaneous, pressure signature suggests some organization and Figure 6.31b shows large-scale structures. This organization is similar in shape to the spatial pressure distribution shown for modes one and two. Since these modes form the convective mode A, the pressure signature for mode A at the time image 1299 was acquired is shown in Figure 6.31c along with the estimated flow field from multi-point LSE. Comparing the three vorticity fields in Figure 6.31 shows that while mode A does not capture all the small-scale coherent structures, it does give a good representation of the large-scale organization of the flow field, which was seen in Figure 6.31b. One item to note is that the magnitude of the mode A, pressure signature is smaller compared to the magnitude of the instantaneous pressure signature. Wee *et al.*[27] used POD to analyze BFS flow and found that the reconstruction accuracy of the flow field is dependent on the dominant dynamics at a location and the number of modes used in the reconstruction. The more significant the higher frequencies, the larger the number of modes needed to accurately reconstruct the flow field. This seems to be the case in Figure 6.31.

Figure 6.32a shows that at the instant of time that image 67 was acquired the flow field was dominated by large-scale concentrations of vortical structures. Three distinct structures can be identified near x/h = 1.5, 4, and 6.5. This distribution of the coherent structures in the flow field matches the instantaneous, pressure signature, which shows three minimum peaks at the same streamwise positions. The multi-point, linear, stochastic estimation of the vorticity field in Figure 6.32b shows a similar large-scale vortical distribution as seen in the instantaneous, vorticity field. Looking at the spatial, pressure signature, it can be seen that the distribution is similar to that seen in mode B. Thus, at this moment in time mode B is more dominant in the pressure signature. The pressure signature associated with the large-scale structures is captured in mode B from POD and estimated using multi-point LSE. The reconstruction of the flow field from mode B in Figure 6.32c gives a good estimate of the instantaneous flow field in Figure 6.32a. This discussion is not to say that mode A or B are physical representations of the instantaneous flow field, but it is encouraging to see how well each represent the flow field at certain time instances. At times both modes are needed to represent the flow field and still at other times modes beyond A and B are needed.

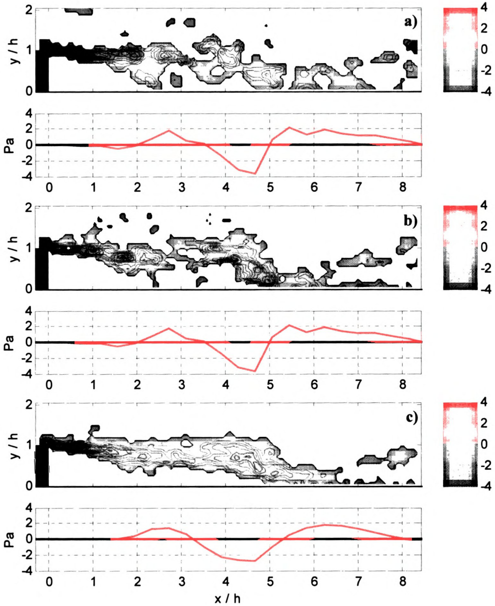

Figure 6.31 Vorticity field at instant of acquisition of PIV image #1299: a) instantaneous, vorticity field and pressure signature, b) multi-point LSE using instantaneous, pressure signature, and c) multi-point LSE using mode A, pressure signature

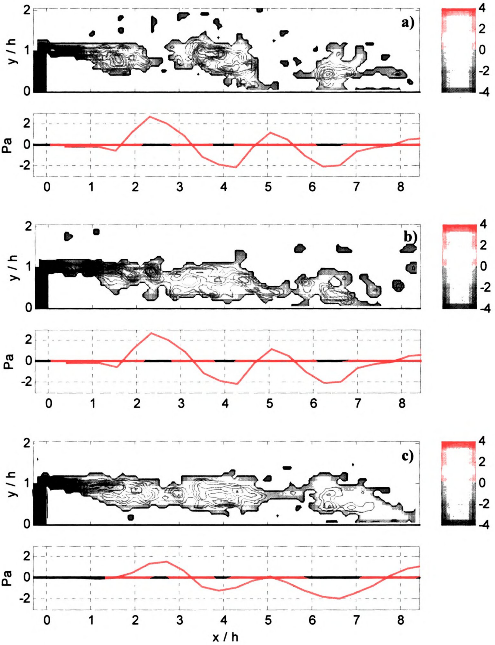

Figure 6.32 Vorticity field at instant of acquisition of PIV image #67: a) instantaneous, vorticity field and pressure signature, b) multi-point LSE using instantaneous, pressure signature, and c) multi-point LSE using mode B, pressure signature

6.3 Conclusions

The goal of this chapter was to investigate the flow features that generate the wall-pressure signature motivated by the physical link between these features and flow-induced vibration and noise in practical applications. Comparing statistics from the simultaneously acquired wall-pressure and above-surface-velocity measurements showed that the abrupt transitions seen in the wall-pressure characteristics are also evident in the velocity field. The links between these wall-pressure and velocity field characteristics associated with the transition regions have been inferred in previous literature from wall-pressure information alone or in conjunction with limited velocity information. Here, these links have been verified as well as expanded based upon the comprehensive wall-pressure and velocity measurements that have been measured.

The simultaneously acquired database was also used to estimate the coherent structures in the flow field based on the wall-pressure signature. Linear stochastic estimation was used to highlight the flow structures associated with various types of the wall-pressure signature. Single-point LSE revealed that a negative pressure event was associated with the passage of vortices; whereas, a positive pressure event correlated with a saddle point between two vortices. Single-point QSE was used to verify the accuracy of the single-point LSE. Although QSE does add additional flow-field information, particularly in relation to clearly identifying localized regions of large strain rate, LSE was able to estimate the global features of the large-scale, vortical structures in the flow field.

One interesting finding from the single-point QSE analysis was the possible existence of a secondary vortex that is formed due to the interaction of a passing, large-scale vortex with the wall at or downstream of the point of reattachment. This secondary vortex was seen when a negative pressure event was applied approximately one step-height downstream of the mean, reattachment location. In addition, when a positive pressure event was applied at the same location, the secondary vortex was found farther away from the wall in the reattached boundary layer region.

Proper Orthogonal Decomposition (POD) was used to determine the spatial modes that dominated the generation of the fluctuating-pressure signature. Spatial-pressure distribution patterns were noticed in the instantaneous, pressure signature, suggesting periods of active and organized, flow features followed by periods of quiescent and random activity. POD helped extract the modes of organization in efforts to analyze each more closely. It was found that the first four POD modes were responsible for 60% of the energy in the instantaneous, pressure signature. In addition, POD also revealed that modes one and two formed convective mode A and modes three and four formed convective mode B.

Multi-point, linear, stochastic estimation was then used to estimate the flow field based on the spatial-pressure distribution for each mode shape. Valleys in the mode-pressure signature showed concentrations of vorticity and absence of shear strain in the respective fields at nominally the same streamwise locations; whereas, mode-pressure signature peaks showed voids of vorticity in the vorticity field and local concentrations of shear strain in the shear-strain, contour plots at nominally the same streamwise locations.

The evolution of the flow structures within the flow field was investigated using LSE based on modes A and B and the combination of the two modes. The analysis revealed quiescent and active periods in the flow. In addition, a pattern from the active phase of the flow seemed to emerge for all modes. Between x/h = 2 - 3, a concentration of vorticity grows and reaches a height roughly equal to the step height before moving downstream. It was then seen that the coherent structure moves to x/h = 3-4 where it remains stationary while growing in size, shape, and strength. The coherent vorticity concentration then sheds downstream as another coherent structure starts to form between x/h = 2-3.

Finally, a comparison between the instantaneous vorticity fields and those estimated using multi-point LSE based on the instantaneous pressure signature and the pressure signature of modes A or B was presented for two instances in time. Results revealed that the multi-point LSE provides a reasonable estimate of the large-scale organization in the vorticity field using either the instantaneous or mode pressure signature. Nonetheless, it is evident that details due to small-scale contributions are lost; and, therefore, it may be necessary to use either a higher-order, estimation technique or number of modes in the reconstruction of the flow field. It is also noted that the success of multi-point LSE in capturing the flow features is closely related to the periods when large flow organization takes place. During these times, the pressure fluctuations are well correlated with the coherent structures and therefore are able to reflect the global characteristics of these structures. On the other hand, at times where the flow is in an apparently random state and the pressure fluctuations are weak, LSE would be useless in trying to shed light on the flow state.

6.4 References

[1] Thomas, A.S.W. and Bull, M.K., "On the role of wall-pressure fluctuations in deterministic motions in the turbulent boundary layer," *Journal of Fluid Mechanics*, Vol. 128, 1983, pp. 283-322.

[2] Snarski, S. and Lueptow, R.M., "Wall pressure and coherent structures in a turbulent boundary layer on a cylinder in an axial flow," *Journal of Fluid Mechanics*, Vol. 286, 1995, pp. 137-171.

[3] Johansson, A.V., Her J., and Haritonidis, J.H., "On the generation of high-amplitude wall-pressure peaks in turbulent boundary layers and spots," *Journal of Fluid Mechanics*, Vol. 175, pp. 119-142.

[4] Lee, I. and Sung H.J., "Multiple-arrayed pressure measurement for investigation of the unsteady flow structure of a reattaching shear layer," *Journal of Fluid Mechanics*, Vol. 463, 2002, pp. 377-402.

[5] Adrian, R.J., "Conditional eddies in isotropic turbulence," *Physics of Fluids*, Vol. 22, 1979, pp. 2065-2070.

[6] Tung, T.C. and Adrian, R.J., "Higher-order estimates of conditional eddies in isotropic turbulence," *Physics of Fluids*, Vol. 23, No. 7, 1980, pp. 1469-1470.

[7] Guezennec, Y.G., "Stochastic Estimation of coherent structures in turbulent boundary layers," *Physics of Fluids A*, Vol. 1, 1989, pp. 1054-1060.

[8] Cole, D.R. and Glauser, M.N., "Applications of stochastic estimation in the axisymmetric sudden expansion," *Physics of Fluids*, Vol. 10, No. 11, 1998, pp. 2941-2949.

[9] Stokes, S. and Glauser M., "Multi-point measurement techniques used in the study of separated flows," *30th AIAA Fluid Dynamics Conference*, AIAA 99-3518, Norfolk, VA, June 28 – July 1, 1999.

[10] Naguib, A.M., Wark, C.E., and Juckenhöfel, O., "Stochastic estimation and flow sources associated with surface pressure events in a turbulent boundary layer," *Physics of Fluids*, Vol. 13, No. 9, 2001, pp. 2611-2626.

[11] Murray, N. and Ukeiley, L., "Estimating the Shear Layer Velocity Field Above an Open Cavity from Surface Pressure Measurements," *32nd AIAA Fluid Dynamics Conference and Exhibit*, AIAA 2002-2866, St. Louis, Missouri, June 24-26, 2002.

[12] Ukeiley, L. and Murray, N., "Velocity and surface pressure measurements in an open cavity," *Experiments in Fluids*, published on-line April 6, 2005.

[13] Heenan, A.F. and Morrison, J. F., "Passive Control of Pressure Fluctuations Generated by Separated Flow," *AIAA Journal*, Vol. 36, 1998, pp. 1014-1022.

[14] Driver, D.M., Seegmiller, H.L., and Marvin, J.G., "Time-dependent behavior of a reattaching shear layer," *AIAA Journal*, Vol. 25, No. 7, 1986, pp. 914-919.

[15] Hudy, L.M., Naguib, A.M., and Humphreys Jr., W.M., "Wall-pressure-array measurements beneath a separating/reattaching flow region," *Physics of Fluids*, Vol. 15, No. 3, 2003, pp. 706-717.

[16] Ho, C. and Huerre, P., "Perturbed Free Shear Layers," *Annual Review of Fluid Mechanics*, Vol. 16, 1984, pp. 365-424.

[17] Brown, G. L. and Roshko, A., "On density effects and large structure in turbulent mixing layers," *Journal of Fluid Mechanics*, Vol. 64, No. 4, pp. 775-816, 1974.

[18] Morris S. C., and Foss, J. F., "Turbulent boundary layer to single-stream shear layer: the transition region," *Journal of Fluid Mechanics*, Vol. 494, 2003, pp. 187-221.

[19] Raffel, M., Willert, C., and Kompenhans, J., *Particle Image Velocimetry: A Practical Guide*, 3rd ed., Springer-Velag, Berlin, 1998, pp. 160-163.

[20] Naguib, A. M. and Koochesfahani, M. M., "On wall-pressure sources associated with the unsteady separation in a vortex-ring/wall interaction," *Physics of Fluids*, Vol. 16, No. 7, 2004, pp. 2613-2622.

[21] Bradshaw, P. and Koh, Y.M., "A note of Poisson's equation for pressure in a turbulent flow," *Physics of Fluids*, Vol. 24, 1981, pp. 777.

[22] Gendrich, C. P., Bohl, D. G., and Koochesfahani, M. M., "Whole-field measurements of unsteady separation in a vortex ring wall interaction," *28th AIAA Fluid Dynamics Conference*, AIAA Paper No. 97-1780, Snowmass, CO, June 29 – July 2, 1997.

[23] Cherry, N. J., Hillier, R., and Latour M. E. M., "Unsteady measurements in a separated and reattaching flow," *Journal of Fluid Mechanics*, Vol. 144, 1984, pp. 13-46.

[24] Lumley, J. L., "The structure of inhomogeneous turbulence," *Atmosphere Turbulence and Wave Propagation*, Yaglom and Tatarsky eds., Nauka, Moscow, 1967, pp. 166-178.

[25] Berkooz, G., Holmes, P., and Lumley, J. L., "The proper orthogonal decomposition in the analysis of turbulent flows," *Annual Review of Fluid Mechanics*, Vol. 25, 1993, pp. 539-575.

[26] Daoud, M.I., "Stochastic Estimation of the flow structure downstream of a separating/reattaching flow region using wall-pressure array measurements," Ph.D. Dissertation, Michigan State University, 2004.

[27] Wee, D., Park, S., Yi, T., and Annaswamy A.M., "Reduced-order modeling of reacting shear flow," *40th Aerospace Sciences Meeting and Exhibit*, AIAA 2002-0478, Reno, NV, January 14 – 17, 2002.

7 Conclusions with Discussion and Future Work

The purpose of this chapter is to integrate the individual findings of previous chapters into a common view of the dominant flow features in the back-step flow that relates to the wall-pressure generation process. For more detailed information on the specific observations of the research, the reader is directed to the conclusion section of the end of the previous chapters. Additionally, recommendations for future follow-up investigations are provided in this chapter.

7.1 Conclusions with Discussion

Overall, the experimental data presented gives a detailed look at both the wall-pressure signature and the velocity field downstream of an axisymmetric, backward-facing step. Both the pressure and velocity measurements have been individually analyzed and found to be consistent with the results reported in the literature. The two datasets have also been analyzed together in terms of how the wall-pressure signature relates to the velocity field. Of particular significance is the first-time investigation of the dominant flow features in the BFS flow through utilization of multi-point linear stochastic estimation coupled with wall-pressure array information (Chapter 6). From this analysis, a view different from the widely accepted one seems to have emerged.

From literature, it is known that at the step edge, the turbulent boundary layer separates and forms a thin, shear layer. Due to Kelvin-Helmholtz instability, the shear layer rolls up to form small vortices of a size equivalent to the thickness of the shear layer. As the vortices continue to move downstream, they start to pair, triple, or even quadruple according to Smits[1], who states that this appears to be the rapid growth mechanism in the shear layer. This initial roll-up of the shear layer resembles the structure of a simple mixing layer as stated by Smits[1]. At approximately half of the reattachment distance, the small-scale structures continue to pair and form larger-scale, coherent structures. Smits[1] states that these coherent structures that are pairing continue downstream, roll around each other, and form a single, large-scale, vortical structure prior to reattachment.

The view discussed by Smits[1] corresponds to the widely accepted view of the BFS flow in which the growth of the shear layer structures occurs *spatially*; i.e., as the structures travel downstream. However, it can be seen in the present analysis that a large-scale, coherent structure actually forms while ***remaining stationary*** between x/h = 2-3. Figures 6.26- 6.28 depict this development of a large-scale coherent structure. In particular, it can be seen that a large-scale coherent structure grows in place (i.e., *temporally*) before reaching a height equivalent to the step height. At this point, the coherent structure sheds and by necessity accelerates to its ultimate convection speed in the downstream direction.

This temporal growth of the flow structures is similar to the development of the vortex structures in the wake of a bluff body (e.g., vortex shedding from a cylinder) than it is to a simple mixing layer. Therefore, to contrast the two view points, the scenario arrived at in this study will be referred to as "wake mode" versus the traditional one, which will be termed "shear-layer mode". It is important to realize that regardless of which of the two modes is prevalent, the flow structures ultimately grow to a scale of the order of the step height and they travel downstream with a certain convection velocity. Hence, the distinction of the two modes is likely to primarily affect the flow characteristics within the separation bubble rather than downstream of reattachment.

Figure 7.1 and Figure 7.2 provide an idealized sketch of the coherent structures developing in the separation bubble for the shear-layer mode and the wake mode respectively.

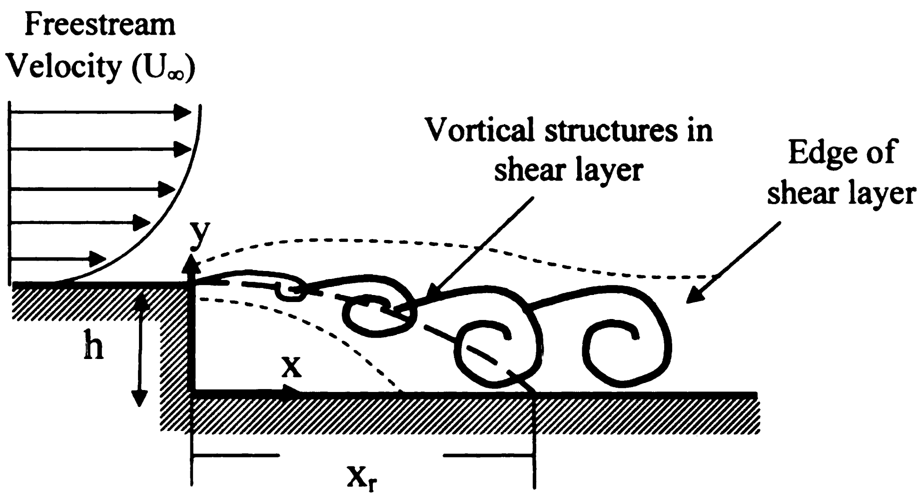

Figure 7.1 Idealized sketch of the flow structures developing in "shear-layer mode" downstream of a backward-facing step

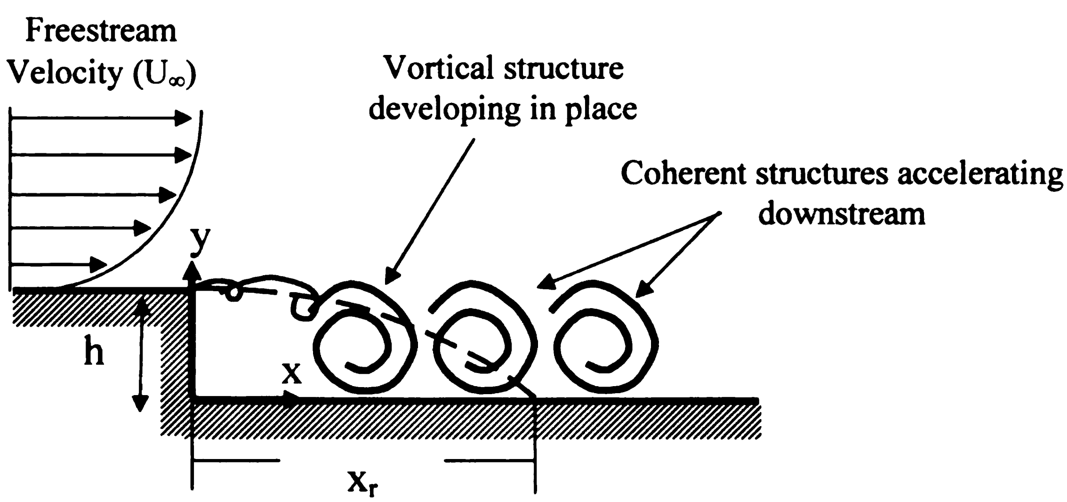

Figure 7.2 Idealized sketch of the flow structures developing in "wake mode" downstream of a backward-facing step

Only one other recent study indicates a scenario similar to that identified here. The study is conducted by Wee *et al.*[2,3] using Random Vortex Method, numerical simulations of the flow field downstream of a sudden expansion. Wee *et al.*[2,3] found that large-scale vortices periodically formed at the middle of the reattachment zone before shedding downstream. More interestingly, they also linked this temporal evolution of the structures downstream of the step to the existence of an absolute instability of the flow. Subsequent linear stability analysis showed that the location of maximum instability growth rate was found in the middle of the reattachment zone (in agreement with the location of formation of the vortices). Wee *et al.*[2,3] state that absolute modes are most likely to originate in a region with strongest backflow. Around x/h = 2-3 in the axisymmetric backward-facing step, the backflow is the strongest ($U/U_\infty \approx -0.2$) as seen in the near-wall velocity plot in Figure 3.3. In addition, Huerre and Monkewitz[4] found that a two-stream, mixing layer is absolutely unstable when the velocity ratio, defined as the velocity of one freestream divided by the velocity of the other freestream, was less than -0.136. As shown in Figure 3.3, the ratio of the maximum, reverse velocity to the freestream in this study has a value of $U/U_\infty \approx -0.2$ in the x/h = 2-3 region, which is lower than the critical value found by Huerre and Monkewitz[4]. Thus, within this location, it is likely that an absolute instability exists, which leads to the roll-up of the large-scale vortex. The absolute instability mechanism suggested by Wee *et al.*[2,3] and its relation to the formation of large-scale structures in the back-step flow is similar to the flow behavior in the wake of bluff bodies where the process of vortex shedding has been linked to the existence of an absolute-instability mechanism as well (Oertel[5]).

It is useful to note here that wake and shear-layer modes have in fact been identified in open-cavity flows since 1987 (Gharib and Roshko[6]). Moreover, a link between absolute instability and the wake mode has also been proposed in this case (Rowley *et al.*[7]). Particularly interesting in the cavity flow case is that, with the exception of axisymmetric flow geometry (Gharib and Roshko[6]), observations of the wake mode remain confined to computational studies (Najm and Ghoniem[8] and Rowley *et al.*[7]). This has led to a recently developing belief (Naguib[9]) among researchers of cavity flows that the observation of a wake mode may require idealized or close to idealized two-dimensional-flow geometry. This may provide a rationale for the commonly held belief that the vortical structures within the separation bubble develop as in a simple mixing layer rather than in a wake flow.

Finally, unlike the behavior of the flow in the wake of bluff bodies where vortex shedding is regular, the process seems to be highly intermittent in the back-step flow. Specifically, as noted in Chapter six, the back-step, flow field seems to alternate between phases of organization (where vortex formation and shedding takes place) and randomness. An interesting question that arises is what mechanism that is unique to the back-step flow (i.e., not found in the wake of a bluff body) "turns on/off" the vortex shedding process? The answer to this question is currently unknown and requires further research. It is noted though, that this is perhaps a case of "confused identity", where the flow, for unknown reasons, switches between the shear-layer and wake modes. Such switching behavior has been identified in numerical computations of cavities (Rowley *et al.*[7]) under certain conditions.

If the mode-switching scenario were true, then the period of random inactive wall-pressure activity found in Chapter six would correspond to the existence of a shear-layer mode. This suggests that when a shear-layer mode exists, it does not have a significant, wall-pressure imprint; and, therefore, wall-pressure-based LSE cannot accurately predict the associated flow field. Figure 7.3 shows an example of a low-magnitude, pressure signature and the associated, instantaneous, vorticity field (obtained from the PIV data concurrent with the pressure signature). The instantaneous, vorticity field shows distinct coherent structures in the flow field that are, however, smaller than those found in Figure 6.30a and are located farther away from the wall. The observed features are more descriptive of a shear-layer-like mode than a wake mode (although one could not tell with certainty in the absence of temporal evolution information).

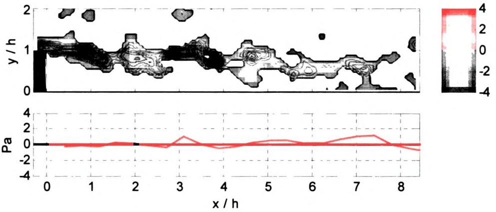

Figure 7.3 Instantaneous, pressure signature and associated, vorticity field

The development of the large-scale structures in place provides a more logical explanation than that given in Chapter four (based on the accepted view) for the abrupt transition seen around x/h = 2 in the autocorrelation. At x/h = 2, the time scales are seen to decrease over a very short distance. In addition, beyond x_r, there is a gradual transition in the length scales as the structures accelerate downstream. Figure 6.2 shows this in more detail. In the autocorrelation, the abrupt transition at x/h = 2 is associated with the in-place (“sudden”) formation of the vortex structures between (x/h = 2 – 3). Beyond x/h = 3, the large-scale structure starts to accelerate from the stationary position and continues to accelerate through x/h = 8. This acceleration, which can be seen in the average streamwise velocity at the center of the shear layer in Figure 6.2, is most likely responsible for the gradual change of the time scales in the autocorrelation in Figure 6.2 between x/h = 4 to 8.

7.2 Future Work

In closing, there are a few other suggested items that could be investigated in order to refine the present study:

1. Estimate the flow field from the pressure signature using multi-point, *quadratic*, stochastic estimation. As noted in Section 6.2.2, the quadratic term adds finer details to the flow field that the linear term cannot estimate (particularly in defining regions with local concentration of strain and capturing the generation and evolution of the secondary vortices arising from the interaction of the shear-layer vortices with the wall). Thus, a more detailed vorticity field could be estimated that will highlight features beyond the large-scale structures.
2. Determine the convection velocities associated with different POD modes, which could give insight into the convection velocities determined by the cross-correlation contour plots of the wall-pressure signature.
3. Estimate how often the dominant POD modes that are associated with organized phases of the flow field occur. This could be useful in terms of knowing at what frequency to apply flow control techniques. If flow control techniques do not need to applied often, then that can save energy in the overall operating system.
4. Generate the time series of the convective-mode-pressure signature and determine the frequency spectrum for each microphone in the array. Early analysis of this item indicates that the strongest convective mode (mode A) dominates the energy in the spectra at reattachment; whereas, in the reattached, boundary layer, mode B dominates most of the energy in the spectra.

5. Calculate the flow sources of pressure (the forcing function in Poisson's equation) and their distribution from the instantaneous and stochastically-estimated, flow fields.
6. Obtain the turbulent-velocity-field statistics (RMS velocities, Reynolds stresses, etc.) from the stochastically-estimated-velocity field and compare it to those obtained from the instantaneous PIV shots.

7.3 References

[1] Smits, A. J., "A visual study of a separation bubble," *International Symposium on Flow Visualization*, Bochum, Germany, September 9-12, 1980.

[2] Wee, D., Park, S., Yi, T., Annaswamy, A. M., and Ghoniem, A. F., "Reduced order modeling of reacting shear flow," *AIAA 40th Aerospace Sciences Meeting and Exhibit*, AIAA 2002-0478, Reno, Nevada, January 14-17, 2002.

[3] Wee, D., Yi, T., Annaswamy, A. M., and Ghoniem, A. F., "Self-sustained oscillations and vortex shedding in backward-facing step flows: simulation and linear instability analysis," *Physics of Fluids*, Vol. 16, No. 9, 2004, pp. 3361-3373.

[4] Huerre, P. and Monkewitz, P.A., "Absolute and convective instabilities in free shear layers," *Journal of Fluid Mechanics*, Vol. 159, 1985, pp. 151-168.

[5] Oertel, H., "Wakes behind blunt bodies," *Annual Review of Fluid Mechanics*, Vol. 22, 1990, pp. 539-562,

[6] Gharib, M. and Roshko, A., "The effect of flow oscillations on cavity drag," *Journal of Fluid Mechancis*, Vol. 177, pp. 501-530.

[7] Rowley, C. W., Colonius, T., and Basu, A. J., "On self-sustained oscillations in two-dimensional compressible flow over rectangular cavities," *Journal of Fluid Mechancis*, Vol. 455, 2002, pp. 315-346.

[8] Najm, H. N. and Ghoniem, A. F., "Numerical simulation of the convective instability in a dump combustor," *AIAA Journal*, Vol. 29, No. 8, 1991, pp. 911-919.

[9] Naguib, A., private communications.

8 Appendix

8.1 Wind Tunnel Facility

The Subsonic Basic Research Tunnel (SBRT) is an open-circuit wind tunnel located at NASA Langley Research Center in Hampton, Virginia. A schematic of the tunnel is shown in Figure 8.1. The intake side of the tunnel is surrounded on three sides with a semi-circular, entrance lip that enables the incoming flow to stay attached to the wall. The upper lip is removed due to space constraints inside the tunnel room.

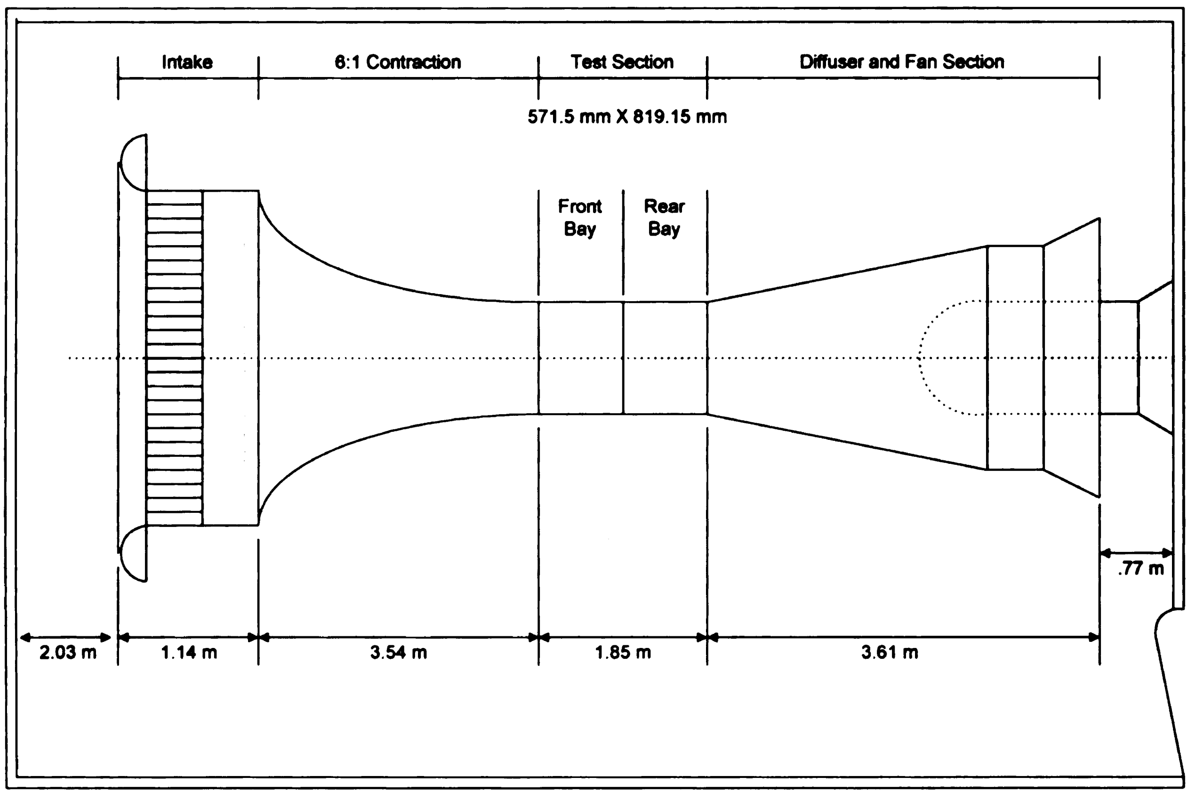

Figure 8.1 Subsonic Basic Research (Wind) Tunnel at NASA Langley

The inlet dimensions are 1.52 m wide by 1.82 m high. Air entering the tunnel flows through 0.2 m of aluminum honeycomb flow straigtheners that use 12.7 mm cells designed to remove any flow swirl. The flow then moves through a double row of wire mesh turbulence screens, separated by 76.2 mm. These screens are located approximately 0.2 m downstream of the honeycomb and are 0.254 mm in diameter at about 8 meshes per 10 mm. The intake section stretches 1.14 m leading into a 6:1 contraction section that measures 3.54 m in length. Located downstream of the contraction is a 0.57 m wide by 0.82 m high by 1.85 m long newly-constructed test section. The new test section was constructed prior to the experiment in order to improve flow quality in the test area. As a result, the corresponding turbulence intensity at flow conditions used in this study was less than 1%. The walls of the new test section consist of plywood, Plexiglas, and glass as shown in Figure 8.2. The glass side was used for high-quality, flow visualization and Particle Image Velocimetry (PIV). Finally, the diffuser and fan section measure 3.6 m in length. The fan is driven by a 200 hp motor enabling flow speeds in the wind tunnel up to 70 m/s (M = 0.2, where M is the Mach number). For more details concerning the wind tunnel specifications refer to Howerton[1].

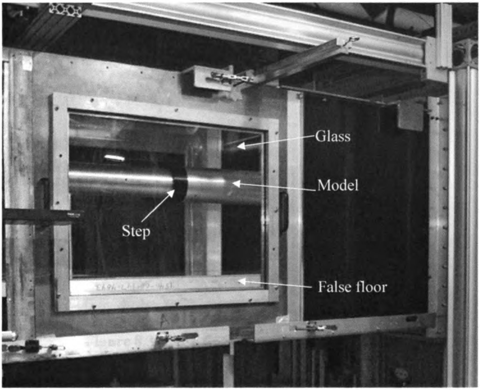

Figure 8.2 Axisymmetric, backward-facing step inside the test section of SBRT

The test section of the wind tunnel had a moveable false floor that could be used to eliminate the streamwise, pressure gradient associated with flow acceleration inside the test section. Figure 8.3 shows the false floor in the test section. The height of the test section with the false floor installed was 0.62 m.

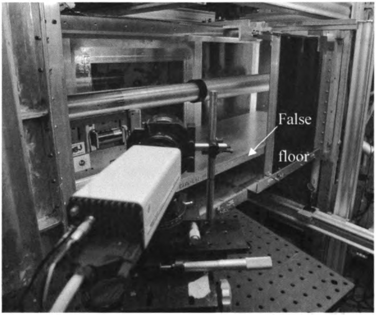

Figure 8.3 False floor in test section of SBRT

The false floor was embedded with 18 static-pressure taps that were used to determine the pressure gradient within the test section. The pressure readings from these taps are plotted as C_p versus the streamwise distance, x/h, in Figure 8.4. Starting at the upstream end of the model, the pressure along the floor is increasing over a 20h distance. This low pressure region may be caused by separation at the leading edge of the false floor. The pressure recovers over the 20h distance upstream of the rotating section (rotator) of the model. Although within the first 18h in the rotator region, the pressure is still recovering slightly. Nonetheless, the pressure varies less than 3% in this region, making the pressure gradient in the rotator region approximately zero. At the downstream end of the rotator region, the pressure starts to increase. This is partly due to the slight flow area increase associated with the flow over the step. More significantly, there is a pressure increase associated with the flow slowing down as it approaches the shroud that covers the leading edge of the model stand. Nonetheless, it is evident by the pressure distribution shown in Figure 8.4 that the boundary layer prior to separation develops under a mostly zero-pressure-gradient condition.

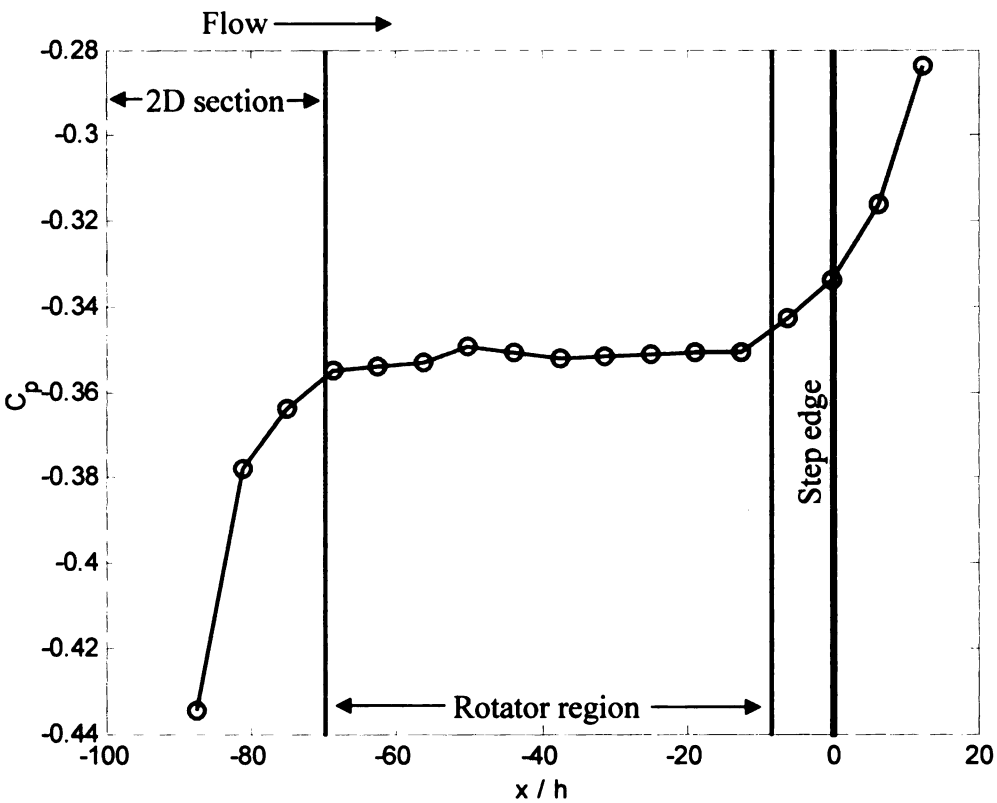

Figure 8.4 Static pressure distribution along false floor in SBRT test section

8.2 Axisymmetric BFS Design

The axisymmetric, backward-facing step was partially modeled after an axisymmetric-boundary-layer-model design studied by Driver and Johnston[2]. There are several components that make up the axisymmetric, backward-facing-step configuration: skeleton shaft, nose, 2D section, rotator, step, instrument plates, motor and drive, tail, wire supports, and support stand. Each of these will be discussed in detail in the following sections. Some of these components are shown in Figure 8.5.

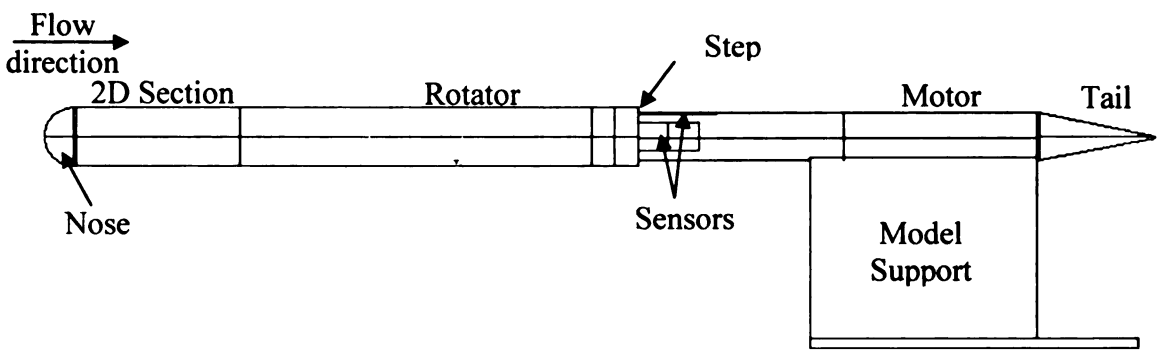

Figure 8.5 Side view of the axisymmetric, backward-facing step

8.2.1 Skeleton shaft

The skeleton shaft is made of solid steel ground to a 0.25 μm to 0.41 μm surface finish, with a Rockwell rating of 60-65C. The skeleton shaft runs almost the entire length of the model, minus the nose and tail sections. The total length of the 25.4 mm diameter shaft is 1.94 m. This shaft provides the main support for the model, and all stationary components rest directly on the shaft. For the rotating section, bearings are placed between the rotator component and the skeleton shaft so it can rotate freely. At both ends of the skeleton shaft, a 25.4 mm deep tapped hole is used with a ½-13 allen screw to tighten all the components along the shaft. The two screws are located in the stationary and motor components of the model. The location and function of these threaded holes will become more evident in the sections where these components are discussed.

The 25.4 mm diameter solid stainless steel shaft was selected based on its deflection properties. Since the model is designed as a long cantilever beam, it was important to ensure that the amount of deflection in the model was minimal in order to ensure axisymmetry. The model was actually supported over a length of 482.6 mm at the downstream end where the support stand was connected to the model. Thus, the overall cantilever beam length was 1457.4 mm. The maximum deflection of the beam was estimated to be 0.006m using the Modulus of Elasticity for cold-rolled stainless steel equal to 190 GPa. This may seem to be a large deflection, but it is important to recognize the length and diameter of the shaft and the fact that the estimate is based on a cantilever beam analysis, where the beam is fixed only at the tip of one end. In addition, this analysis was done without considering the extra support from other model pieces, which when assembled on the skeleton shaft increase the overall moment of inertia at a given cross section and therefore provide more support. Once completed, the manufacturer of the model measured the actual, overall, vertical displacement of the model nose to be 0.381 mm. This deflection was removed by the wire support system in the front of the model, which is described in more detail below.

8.2.2 Nose

The purpose of the nose is to provide a smooth transition for the flow as it approaches the model. The nose is hemi-spherical in shape as shown in Figure 8.6, which results in a step discontinuity in the radius of curvature at the junction between the nose module and the stationary 2D section. Nonetheless, a turbulent boundary layer is desired at separation, meaning that any flow disturbance caused by a discontinuity would in fact be beneficial in accelerating the development towards a turbulent state.

The nose was constructed out of solid aluminum with a radius of roughly 70mm. It is positioned at the upstream end of the axisymmetric BFS and is attached by a male-female fit between the nose and the stationary section. A set screw is then used to secure the nose in place. Figure 8.6 shows the nose configuration with dimensions.

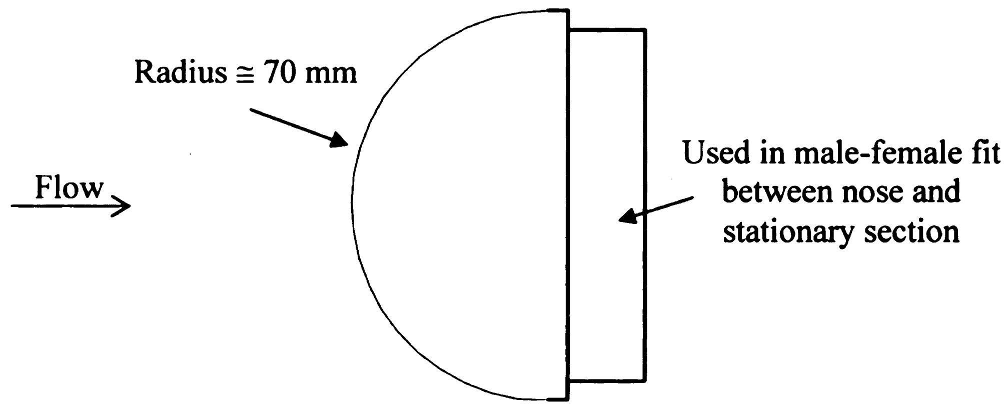

Figure 8.6 Schematic of nose section

8.2.3 Upstream Stationary Section

The stationary section is located downstream of the nose and upstream of the rotating section. It is made from 0.35 m long aluminum tubing with an outside diameter of 0.124 m and an inside diameter of 0.11 m. Figure 8.7 shows a schematic of the stationary section. With the two donuts (0.11 m diameter cylindrical spacers, 25.4 mm thick) on either end supporting the tubing, the skeleton shaft can be threaded through the 25.4 mm diameter holes drilled in the center of each of the donuts. Thus, the stationary section rests on the non-rotating skeleton shaft.

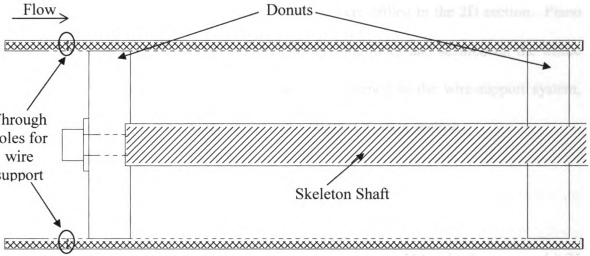

Figure 8.7 Schematic of the stationary section

Located on the upstream portion of the 2D section is sandpaper, which was used to trip the boundary layer. Due to the long, development length needed to obtain a turbulent, boundary layer and the lack of space in the test section for such a length, the boundary layer was tripped with three pieces of sandpaper. The piece farthest upstream was located 70 mm downstream of the nose tip. This first piece was 38.1 mm wide and 120 grit. The second piece was 150 grit, measured 50.8 mm in width, and was located 115 mm downstream of the nose tip. Finally, the third piece was 50.8 mm in width, 150 grit, and placed 25.4 mm downstream of the second piece of sandpaper. Results showing the characteristics of the turbulent boundary layer established at separation may be found in Section 3.2.

The last function of the stationary section was in the support system of the axisymmetric BFS. The upstream portion of the model was supported by four piano wires located at 45° with respect to the centerline of the model. The position of the holes can be seen in Figure 8.7. Without the wire support the model acted like a cantilever beam. Holes at the 45° mark, 1 mm in diameter, were drilled in the 2D section. Piano wire (≈ 1 mm in diameter) were threaded through the holes and secured on the inside with a nut. The piano wire was pulled taut and fastened to the wire-support system, which is discussed in further detail in the Wire-Support System section.

8.2.4 Rotating Section

The rotating section, shown in Figure 8.8, measures 0.124 m in diameter and 0.75 m in length. It was constructed out of aluminum tubing, having a wall thickness of 6.35 mm, to minimize the overall weight. Spacers, also referred to as donuts, were press fit into the tubing on either end. These donuts were annulus in shape having an outer diameter of 114 mm with a bearing press fitted into the hole drilled through the center. The main support shaft (25.4 mm diameter) was threaded through the bearing in each donut allowing the rotating section to spin freely around the main, support shaft. These bearings were self-aligning.

The upstream donut housed a CSB series bearing (CSB 205-16) manufactured by Fafnir. This bearing is a combination bearing and collar with two set screws used to secure the collar to the skeleton shaft. By placing a bearing/collar at the upstream donut, the gap between the rotator and the section containing the step could be adjusted by sliding the bearing/collar along the skeleton shaft. Moving the bearing/collar in the upstream direction results in a wider gap and sliding in the downstream direction gives a smaller gap.

The downstream donut in the rotator supported a Precision Steel Needle-Roller Bearing (supplier: McMaster-Carr 7929K24). The bearing was made for a 25.4 mm shaft diameter and had an outside diameter of 38.1 mm with 19.05 mm width. A needle bearing was used in order to conserve space for the three bolts that were used to connect the drive shaft to the downstream rotator donut. By connecting the drive shaft to the donut, the rotator spins with the drive shaft. A flange bracket was used to make the connection as seen in Figure 8.8. The three bolts connected the bracket to the donut and two more were secured to the actual drive shaft. The three bolts actually made a loose connection in the donut. In other words, the three holes in the donut were drilled oversize so the bolts did not make a rigid connection, but still forced the rotator to spin. Through trial and error it was discovered that running the rotator with the loose, bolt connection reduced the vibration in the model compared to running the rotator with a rigid connection.

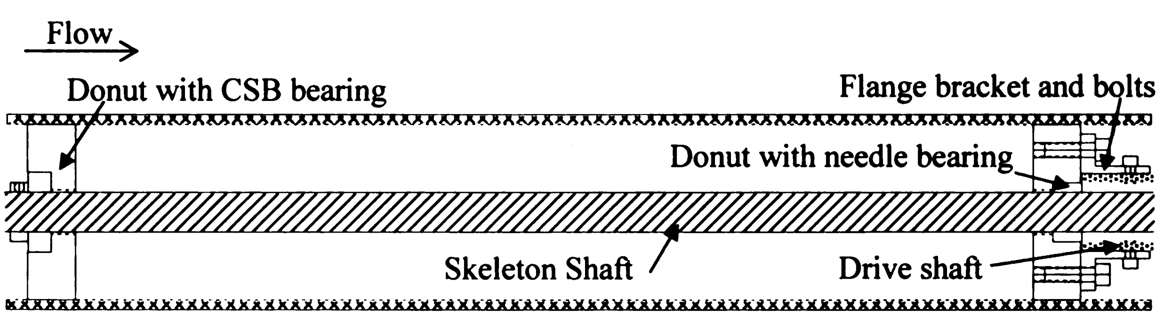

Figure 8.8 Rotator schematic

8.2.5 Step Section and Step Ring

The step portion of the model is the "area of interest" in the project. This is where the boundary layer separates and forms an unstable, shear layer that eventually reattaches downstream of the step. Figure 8.9 shows a schematic of the step region of the model. The step section is composed of several different pieces including the skeleton shaft that runs through the center of the whole model. The steel, drive shaft has a wall thickness of 7.13 mm and fits over the skeleton shaft leaving a 5.56 mm gap all the way around. A Double-Row Steel Ball Bearing (supplier: McMaster-Carr 5885K22) supports the drive shaft at the upstream end of the step section while still allowing the shaft to spin. This bearing has an outside diameter of 90 mm and an inside diameter of 50 mm with a maximum rpm rate of 4,000. A ¼-20 set screw was used to secure the double-row ball bearing in place. At the downstream end of the step section, a needle bearing (supplier: McMaster-Carr - 7929K24) was placed between the skeleton and drive shaft. On the outer side of the drive shaft, the CMT pulley (manufacturer: CMT 42-XL-037-3-A-312) with a pitch diameter of 67.9 mm was used to rotate the shaft. The pulley was connected to a timing belt, which wrapped around the same type of pulley that was press fit on the motor shaft. Details of the motor and timing belt are given in Motor and Drive section. Finally a thrust bearing (supplier: McMaster-Carr 5909K36) and two thrust washers (supplier: McMaster-Carr 5909K63) were placed at the downstream end of the drive shaft to absorb any axial loading caused by the rotating drive shaft.

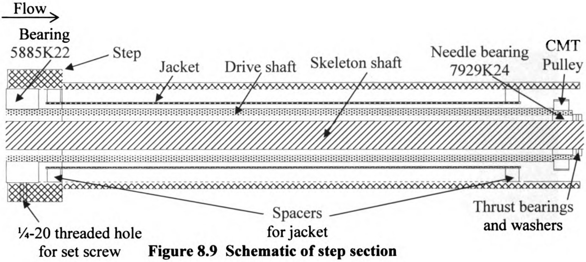

Figure 8.9 Schematic of step section

The instrument plates that housed the static pressure taps and the microphones were placed in the step section immediately downstream of the step. These plates are explained in further detail in Section 2.3. A step ring measuring 0.124 m in outside diameter and 50.8 mm in width was secured around the step section of the model as shown in Figure 8.10.

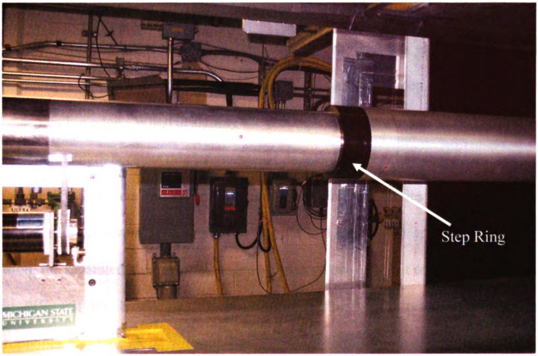

Figure 8.10 Picture of step ring on model

The step ring was constructed out of two halves so the ring could be easily taken off and put on the model if the instrument plates needed to be accessed. The gap between the step ring and the step section was less than 0.254 mm. The step ring was anodized to reduce surface glare in the Particle Image Velocimetry images. A step ring was used in order to keep flexibility in the model design. By using the concept of a step ring the distance between the rotating section and the edge of the step could be adjusted by machining additional step rings of varying width. Changing the width of the step ring or removing it all together varies the length over which the 3D boundary layer relaxes. This affects the strength of the cross flow at the separating edge.

The height of the step was a key parameter in the design of the model. Out of the three classic separating/reattaching geometries (backward-facing step, splitter plate, and splitter-plate-with-fence) the backward-facing step has the smallest separation bubble as noted in Hudy[3]. Eaton and Johnston[4] reported that for a planar BFS the reattachment distance varied from 4.9 to 8.2 step heights for approximately 23 experiments reviewed by the authors. Generally, the reattachment length is around 6 step heights downstream of the separation edge. When designing the model, careful consideration was given to the reattachment length because this length would dictate the size of the separation bubble. It was necessary to have a "good sized" separation bubble so a series of microphones and static pressure taps would fit under the bubble and give good spatial resolution. In addition, the separated-flow region needed to be large enough so it could be resolved well using PIV. If the bubble were too small then that would restrict the number of microphones and taps along with the number of velocity vectors that could be captured beneath or inside the bubble. If the bubble were too large then, in terms of PIV, multiple views would need to be set-up to capture the entire separation bubble region, which is very time consuming.

Besides separation bubble size, blockage ratio was another limiting factor in terms of determining the maximum diameter of the model. Blockage ratio is defined as the frontal area as seen by the flow divided by the total area of the test section perpendicular to the flow direction. Because a section of the model needed to rotate and sensors were to be embedded in the model, space inside the model was necessary and a limiting factor regarding how small in diameter the model could be in order to fit all the components. The other issues were the overall cost of the materials and manufacturing the model. Based on these design constraints, it was decided that a 101.6 mm outside diameter tubing with 6.35 mm wall thickness could house the 25.4 mm diameter skeleton shaft with the 50.8 mm diameter drive shaft and still have a 12.7 mm clearance for the electronics. In addition, the step height was optimized to be 12.7 mm, which gives a reattachment length of 76.2 mm based on the $x_r = 6h$ and a blockage ratio of 3.6%. The thirty-two microphones, each with a diameter of 2.54 mm, were spaced 2.2 mm apart, edge to edge. The microphone spacing resulted in a total measurement distance along the centerline of approximately 150 mm, which ensured that the reattachment point would be contained within the extent of the microphone array.

Once the step height was determined, the rest of the model's dimensions could be calculated based on the information presented by Driver and Johnston[2]. Driver and Johnston[2] used an axisymmetric model to develop a three-dimensional, shear-driven, turbulent, boundary layer. The total axisymmetric BFS model length was 187h. The long length of the model used in this study not only ensured a reattachment point on the model but also aided in reducing the effects of downstream disturbances that could propagate upstream, i.e., acoustically, and change flow conditions in the measurement region. Farabee and Casarella[5] observed, in their backward-facing-step study, energized structures from the shear layer up to 72 step heights downstream of the step. The point where the wake develops is so far downstream of the measurement region that the probability of the acoustics from the weak disturbances convecting upstream to the region of interest is small.

One other important item to mention in this section is the jacket shown in Figure 8.9. The jacket was used to separate the tubing and wiring from the drive shaft in the step region. The jacket was made out of a 0.8 mm thick aluminum sheet that was rolled to make a cylinder. It was secured to the inside walls of the step section using spacers as shown in Figure 8.9.

8.2.6 Instrument Plates (I-plates)

Both static pressure taps and the Emkay microphones were housed in the north instrument plate seen in Figure 2.5. The north instrument plate is beneath the main area of measurement. PIV measurements were taken above this plate in a plane perpendicular to the microphones. The details surrounding the construction and the instrumentation of the I-plates are described in Section 2.3.

8.2.7 Motor Section

The motor section of the model stretches 0.41 m in length with a 101.6 mm outside diameter. This section is made out of 15.9 mm thick steel tubing. Two donuts at either end support the skeleton shaft. In the downstream end a ½-13 allen screw is used in the threaded hole at the end of the skeleton shaft to tighten all the model components. The clamp collar (supplier: McMaster-Carr 6435K18) prevents any axial shift of the pulley. The motor section fits into the step section using a male-female fitting as shown in Figure 8.11.

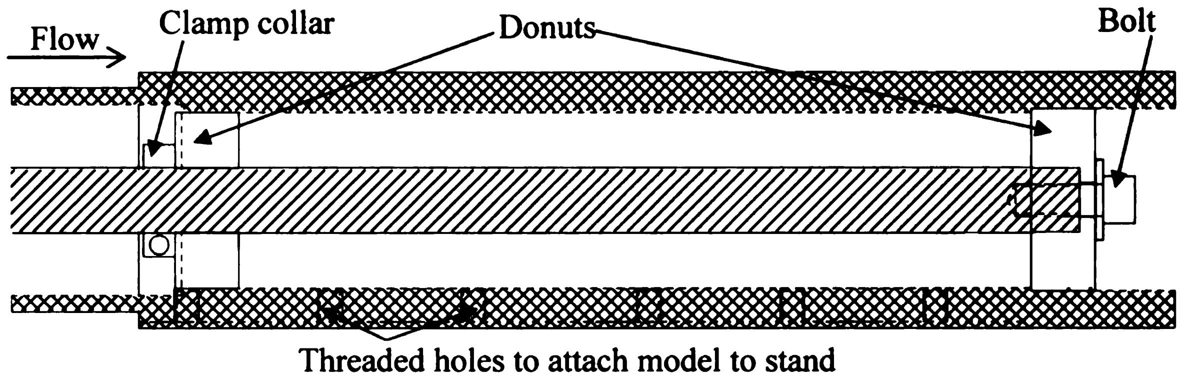

Figure 8.11 Motor section schematic

8.2.8 Drive Shaft and Motor

The drive shaft was constructed out of aluminum. It measures 557.2 mm long and 50.8 mm in diameter. Figure 8.12 shows a schematic of the drive shaft. On the upstream edge, two tapped holes are shown. These two holes were used to attach the flange bracket (Figure 8.8) to the donut inside the rotator. By making this connection, the rotator spins when the drive shaft spins. Farther upstream, there is a change in diameter from roughly 50 mm to 50.8 mm. The junction between the two diameter sizes is a shoulder for the double-row steel ball bearing (5585K22). The upstream portion of the shaft was machined to fit the bearing. On the downstream edge, there is another shoulder 17.6 mm long that was machined to fit the pulley. Inside the drive shaft, two needle bearings were used to support the drive shaft on the skeleton shaft while still allowing the drive shaft to rotate.

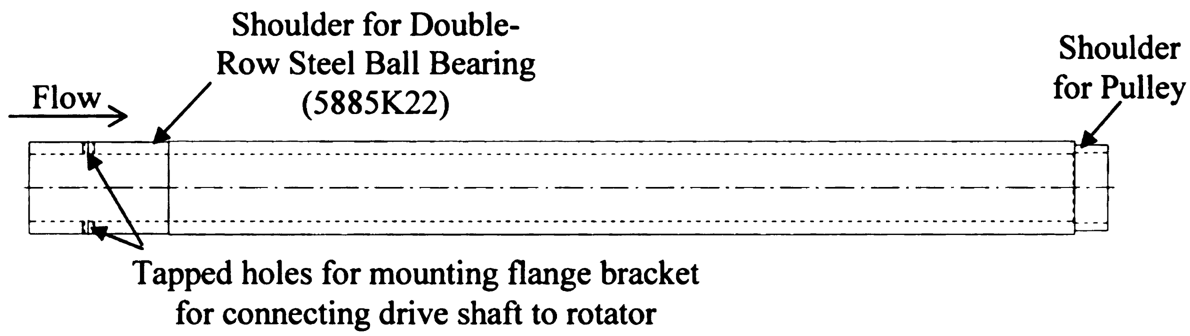

Figure 8.12 Schematic of drive shaft

A dc motor (M1110015) from Leeson was used to drive the shaft that spun the rotator. The motor was a sub-fractional-horsepower, DC, permanent-magnet motor. It was designed for use with full-wave, nonfiltered, SCR controls for adjustable-speed applications requiring dynamic braking and constant torque throughout the speed range. (Information based on catalog.) It had a full load RPM of 3500 at 90 Vdc. The motor was powered using a direct-current, power supply from Instek (Model GPR-11H30D). The power supply had a 0.01% high regulation, constant voltage and current operation, internal select for continuous or dynamic load, and low ripple and noise. It was capable of output 0 to 110 volts over 0 to 3 amps. The motor was connected to the same pulley described in the Step Section using a timing belt, thus resulting in a one-to-one ration between the motor and the drive shaft. An optical sensor (TPU-H5A) from Dart Controls was used to monitor the pulley and thus, the rotator in order to determine the rotations per minute.

8.2.9 Tail

The tail section was used to reduce possible downstream disturbances by gradually tapering the model thickness to a point. This would moderate the step-like feature at the end of the model that may create disturbances. These disturbances could propagate upstream, i.e. acoustically, and change the flow conditions in the separating/reattaching zone of interest.

The tail of the model was attached to the motor section using a male-female fitting. It was constructed out of solid aluminum and conical in shape. The height of the cone is 266.7 mm with a 101.6 mm base diameter. The tip of the tail was fastened on by a 10-24 screw. This allowed for the option of removing the tip to screw on a turning mirror for positioning the laser beam upstream during PIV measurements. A sketch of the tail is shown in Figure 8.13.

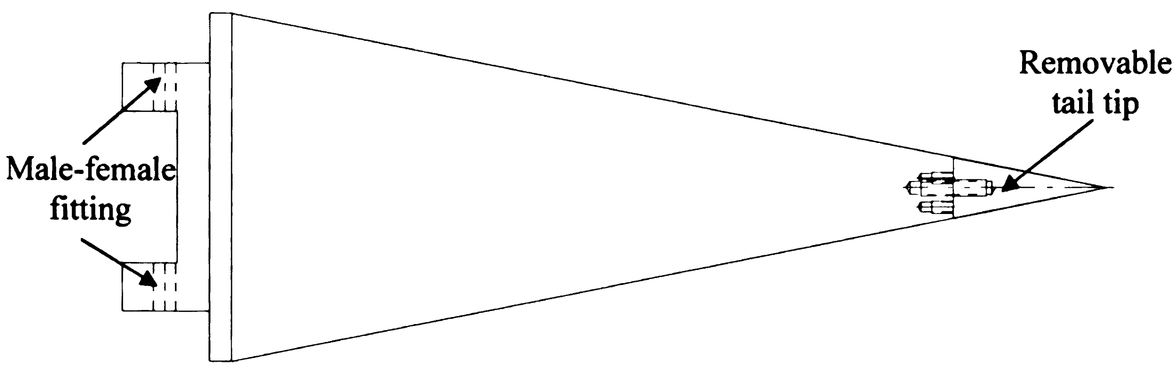

Figure 8.13 Sketch of tail section

8.2.10 Wire-Support System

The wire support system was used to support the most upstream end of the model. It consisted of four cylinders, 0.99 mm diameter piano wire, four swivels, four hanger screws, and some washers and nuts. The piano wire was strung through each of the 1 mm holes drilled at 45° angles with respect to the normal and spanwise planes in the stationary section of the model (Figure 8.7). These holes were located 38.1 mm downstream of the end of the nose section. Nuts were tied at the end of the piano wire so the wire would not slip through the holes. The piano wire was then stretched outside the tunnel at the 45° angles and fitted around the swivels, which were directly connected to the hanger screws. Each hanger screw was threaded through the cylinder that had a flat top with a centered hole. Washers and nuts were used to secure the hanger screw and tighten the wire. Figure 8.14 shows a picture of one corner of the wire support system and Figure 8.15 shows one side of the support system in use at SBRT. The actual system itself was connected to perforate square bar using threaded rod and nuts. The advantage of this system was its versatility. The angle of the cylinders could be adjusted as well as the length of the piano wire and the amount of tension applied to the model. The nuts on top of each of the cylinders were adjusted until the model spun freely and was level with respect to the tunnel floor.

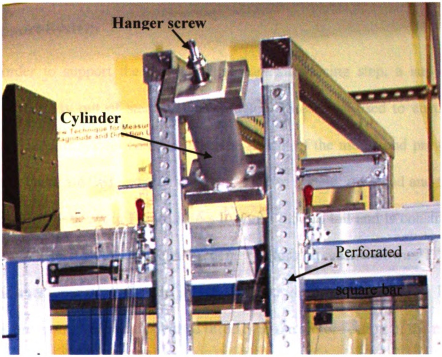

Figure 8.14 View of one corner of the wire-support system

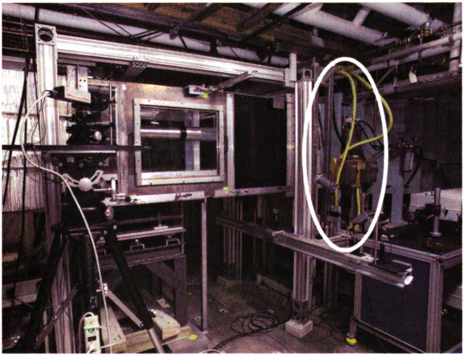

Figure 8.15 View of the wire-support system in use in SBRT

8.2.11 Support System

In order to support the axisymmetric backward-facing step, a support system made almost entirely out of steel was constructed. Steel was used to ensure that the weight of the support system could counter the weight of the model and prevent it from tipping over. There are two parts to the model, support system: the stand and the traverse table. The stand is shown in Figure 8.16. It stands 0.52 m tall and is constructed from two 19.05 mm thick steel sheets welded together to form an upside-down "T." The base of the stand measures 0.50 m wide in the spanwise direction and 0.70 m long in the streamwise direction. The stand is bolted directly to the motor section of the model using 8 bolts. It houses the motor, as seen in Figure 8.16, used to drive the shaft that spins the rotator. A shroud was placed at the upstream edge of the stand to round the leading edge, reducing the possibility of disturbances that could propagate upstream into the measurement region. Inside the shroud, the microphone wiring and static-pressure tap tubing were hidden from the free stream and directed outside the model to be connected to the appropriate instrument.

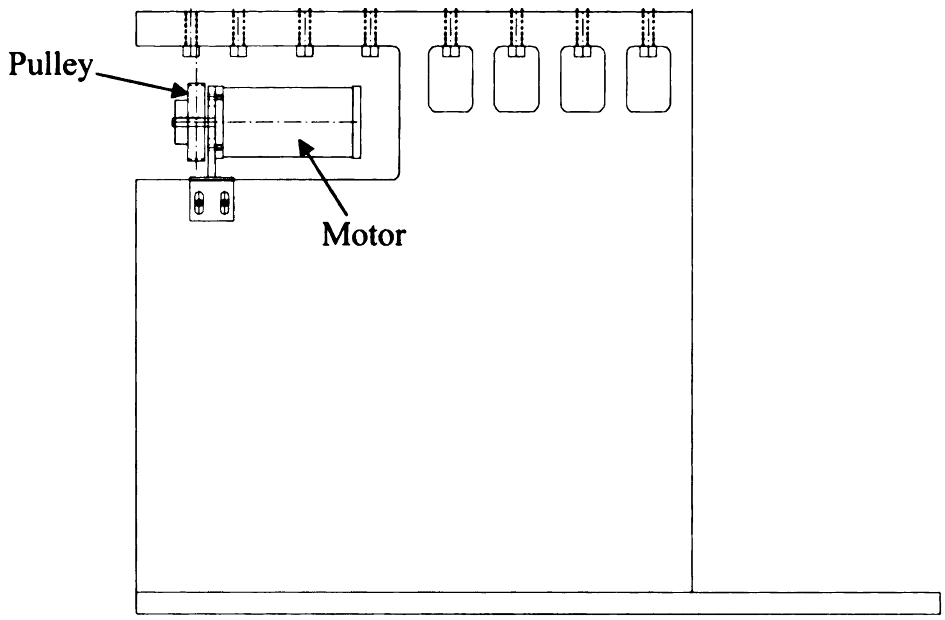

Figure 8.16 Model support stand

The second part of the model, support system is the traverse table shown in Figure 8.17. The traverse table is made almost entirely out of steel. Its purpose is to vertically and horizontally traverse, rotate, and/or change the pitch angle to align the model in the test section. The pitch angle is defined as the angle between the streamwise axis that is parallel to the floor and the centerline of the model in a vertical plane. For example, if the nose is higher than the tail, the model is at a positive pitch angle. The model stand was bolted directly on the traverse table, which was leveled with respect to gravity before starting to align the model in the test section.

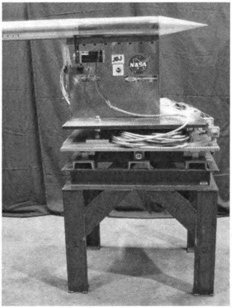

Figure 8.17 Picture of the stand used to support the model

At NASA Langley the model, support stand was raised 177.8 mm in order to center the stand in the test section. To accomplish this, a 177.8 mm tall by 503.8 mm thick by 762 mm long piece of steel was bolt to the stand. Figure 8.18 shows the extension added to the model stand at Langley.

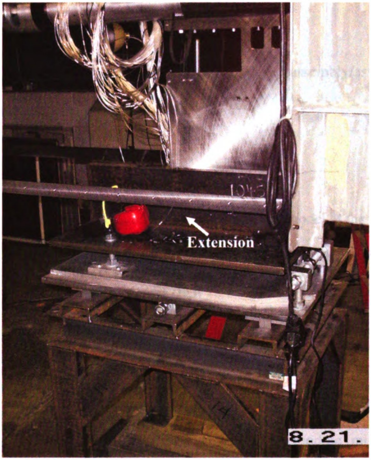

Figure 8.18 Model-stand set-up in SBRT at NASA Langely

8.2.12 Model Assembly

The following is a rough procedure for disassembly/assembly of the axisymmetric, backward-facing step.

Disassemble the model

1. Remove the set-screw - located on the outside of the model at the upstream end of the 2D section. It is used to secure the nose in place.
2. Remove the nose – this may require applying careful pressure (tight fit)
3. Loosen the ½" bolt inside the model (exposed by removing the nose)
4. Slide the 2D Section off the center shaft
5. Remove the set-screws (there should be 3) inside the upstream end of the rotator, which are used to secure the donut inside the rotator to the center shaft
6. Slide the rotator off using LIGHT up and down pressure (may have a tight fit)
7. The three bolts used to connect the rotator with the drive shaft should not make a rigid connection. These should slide in and out of oversized holes.
8. To remove the step module for access to the pulley and timing belt, this should require first matching the red lines between drive shaft and step module
9. Remove the set-screw at the upstream part of the step module (might need slide hammer to remove set-screw)
10. Use slide hammer to take out 3 set-screws in the downstream part of the step module
11. There should be one bolt to remove
12. At this point, there should be easy access to the pulley.
13. The tail tip can also be removed see Figure 8.13

Re-assemble the model

1. Reverse disassembly steps
2. Replace step, bolt and set-screws
3. Replace rotator module
4. Make sure to use a 0.015" shim between the step and the rotator modules
5. Tighten the 3 set-screws inside the upstream end of the rotator
6. Slide the 2D Section into place along the center shaft
7. Tighten the ½" bolt inside the model at the upstream end of the 2D Section
8. Replace the nose
9. Tighten the set-screw used to hold the nose in place

8.3 Azimuthal Uniformity

To verify the alignment of the axisymmetric BFS in SBRT, the azimuthal uniformity of the flow was checked using a hotwire probe. The sensor was placed approximately 6.35 mm upstream of the step at five different heights: 6.35, 9.53, 12.7, 19.1, and 25.4 mm. This translates to y/θ = 3.4, 5.1, 6.8, 10.2, and 13.6 for the Re_h = 8081 case, which was the only case used in this test. To position the sensor, a second ring designed similar to the step ring was used to hold and rotate the probe around the model. The inner diameter of the ring was equal to the outer diameter of the model downstream of the step. Figure 8.19 shows an image of the hotwire set-up for the azimuthal uniformity test. A pitot probe was also placed in the free stream at the same streamwise position as the hotwire probe and was rotated with the hotwire sensor. The pitot probe provided total pressure data at the same streamwise location as the probe was rotated around the model. The two probes were rotated through 16 angles of 22.5° increments for a total of 360°.

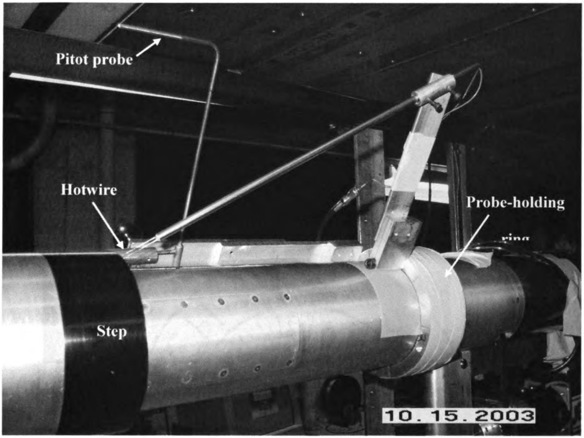

Figure 8.19 Set-up for azimuthal, uniformity test

Prior to running the azimuthal, uniformity test, the azimuthal uniformity associated with the rotation of the ring holding the hotwire probe was checked. This was done using a dial gauge indicator secured to the probe-holding ring. Figure 8.20 shows the dial gauge test set-up. The results are plotted in Figure 8.21, where the reading of the dial gauge was set to zero at the north position ($\phi = 0^o$). As seen from the figure, the azimuthal traversing uniformity is within ± 30% of the momentum thickness for the Re_h = 8081 case. This variation could be due to the lack of concentricity of the first and/or second step ring, which is difficult to decouple. The height differences resemble that of a sine wave with peak high variations occurring at angles 50 and 200 degrees and a low peak near 125 degrees.

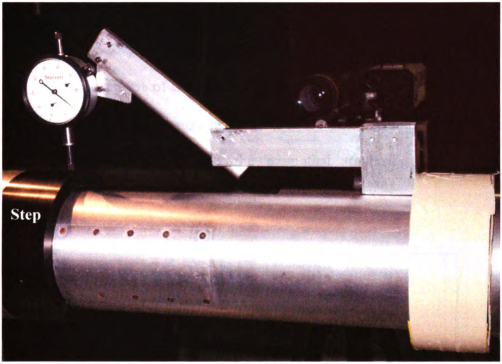

Figure 8.20 Dial-gauge-test set-up

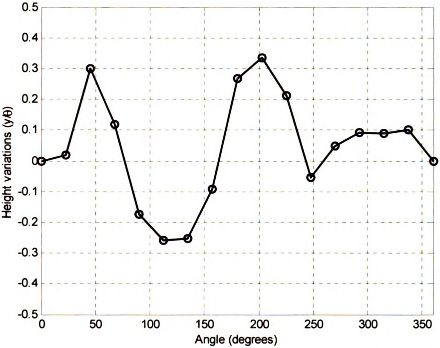

Figure 8.21 Results from the dial-gauge test

The results for the mean-streamwise-velocity, azimuthal-uniformity test are shown in Figure 8.22 for all 5 heights tested. The variations measured in the azimuthal symmetry are within ± 10% of the azimuthal-average value of the measurements. This variation could be due to the change in position of the probe within the boundary layer associated with the inaccuracies of the azimuthal traversing mechanism used. Nonetheless, the variation is reasonably small.

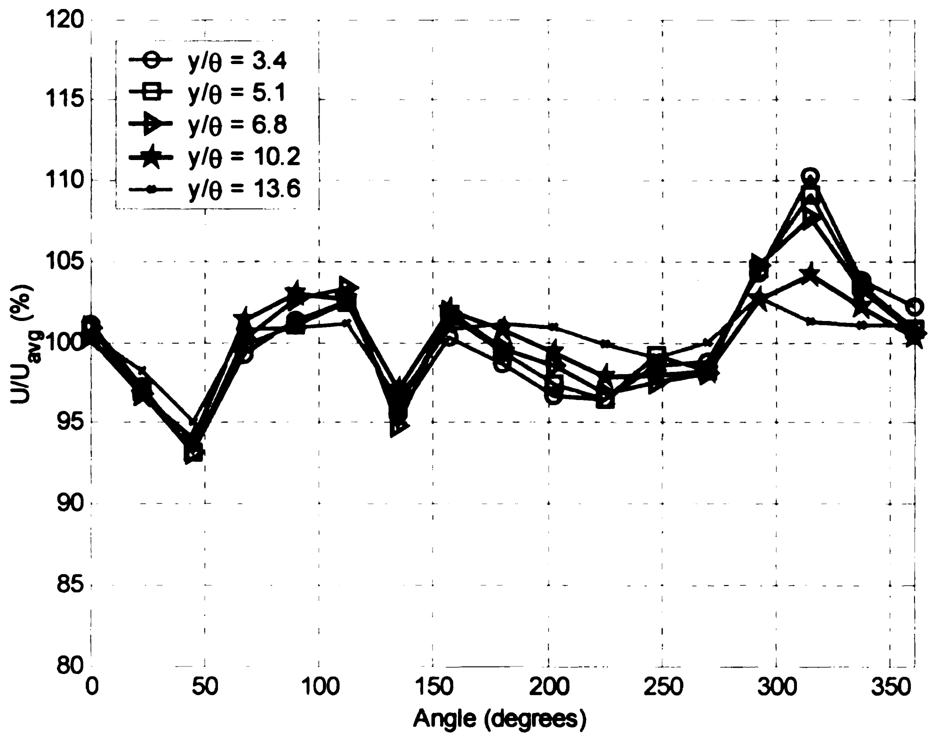

Figure 8.22 Azimuthal symmetry of the flow "at" separation for Re_h = 8081

8.4 Additional Microphone Information

8.4.1 Microphone Specifications

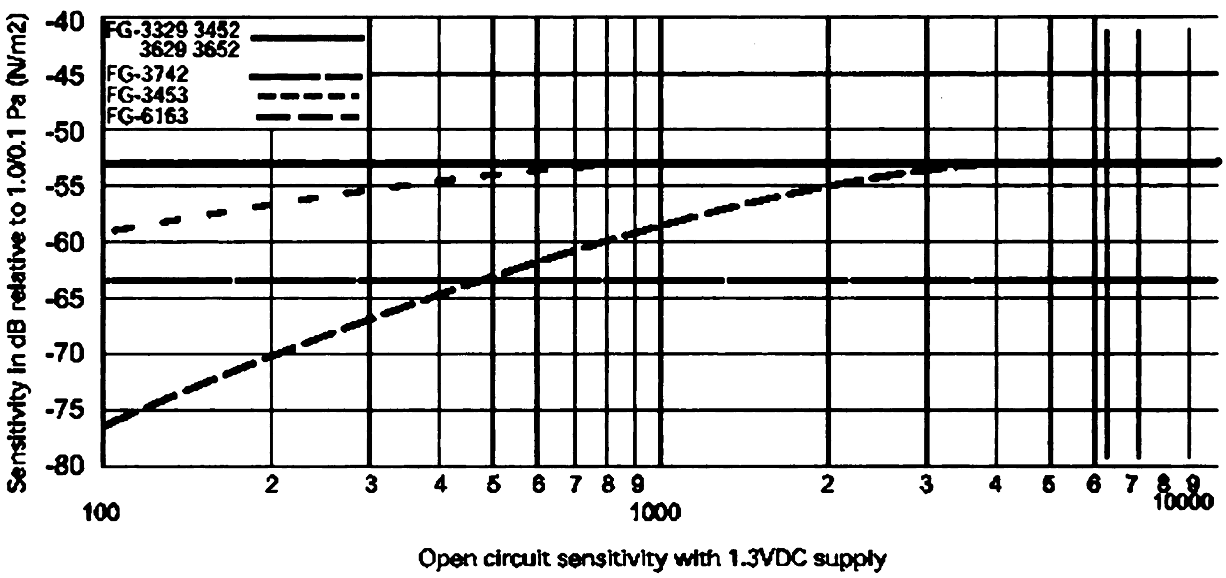

Figure 8.23 Typical FG-3629-P16 Frequency-Response, Curve – Emkay data sheet

8.4.2 Circuitry

Figure 8.24 shows a picture of the wiring for the microphone array that was embedded in the I-plate located downstream of the axisymmetric BFS. Each microphone had three 25.4 mm leads (for more microphone detail, see Section 2.3.2): power (V_{cc}), ground, and output. Copper tape was laid on the underside of the I-plate and was used as a ground bus. In addition, a printed-circuit board was cut to the appropriate length and width so it would fit inside the I-plate slot on the model. On the copper board there was a V_{cc} bus and individual plugs used to connect the output from each microphone. The three leads from each microphone were soldered to the appropriate bus or pin (Figure 8.24). There was one common ground and V_{cc} on the I-plate and 32 individual output signals.

Therefore, there were 34 wires coming from the I-plate to the circuit box, which was used to power the microphones and break out the output cables for individual microphones.

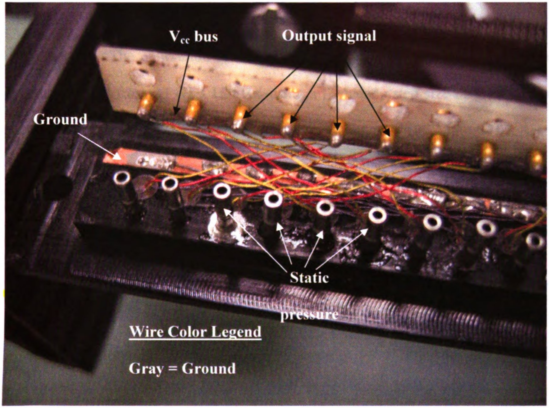

Figure 8.24 Wiring for the I-plate

The circuitry to operate the microphones required a 1.5V voltage regulator to supply power to all 32 microphones via the single supply (V_{cc}) line. The output signal lines from the microphones were AC coupled with BNCs using a 0.1 μF capacitor. These BNCs were then directly connected to the anti-aliasing low-pass filters and digitizers inside the control room. In the original design, the signal outputs were sent through an amplifier board before connecting to the BNC outputs. However, there were grounding issues with the circuitry; and, therefore, the direct connection was made instead since the lengths of the coax cables were not too long and onboard amplification was not essential.

8.4.3 Calibration

A bench calibration was performed on each microphone before placing the microphones in the model in order to determine the individual sensitivity and phase reponse. The microphones were calibrated using a B&K 4226 multifunction calibrator at NASA Langley. The calibration assembly is shown in Figure 8.25. The calibration frequencies extend from 20 Hz - 15 kHz, using a frequency step size of 5 Hz over the range of 20 - 100 Hz and a step size of 250 Hz over the range of 100 - 15000 Hz. Results for each microphone showed sensitivity values similar to that plotted in Figure 8.26, plus a 180-degree phase shift between the calibrator and the microphone output. The phase is constant over all frequencies with an RMS deviation of 5° or less for all microphones. The individual sensitivity values for each microphone used in the data analysis are plotted in Figure 8.27.

One other point to mention is that 20 Hz was the lowest frequency that calibration data could be acquired reliably using the B&K 4226. Nonetheless, the low-end of the measured frequency was below the frequency response range of the microphones. A similar situation was seen by Hudy[3]. Because the microphone sensitivity below 20 Hz decreases, a reduction in the amount of energy recorded in the signal from the surface pressure fluctuations below 20 Hz is expected. This primarily affects the energy level for the microphones closest to the step, where the low-frequency fluctuations are dominant. However, a very small effect, if any, is expected on the shape of the wall-pressure spectra seen in Section 4.2.3.

Because the A/D channels were multiplexed, there is an average time delay between each sampling microphone, which results in a systematic error in the sampled data. The time delay was estimated from the phase calibration data to be 336 μs at the frequency where the wall-pressure spectra exhibited a peak ($fh/U_\infty = 0.039$). This value is compared to the convective time scale over the length of the entire array of microphones, which is 15 ms. This is two orders of magnitude larger than the time delay of the microphones.

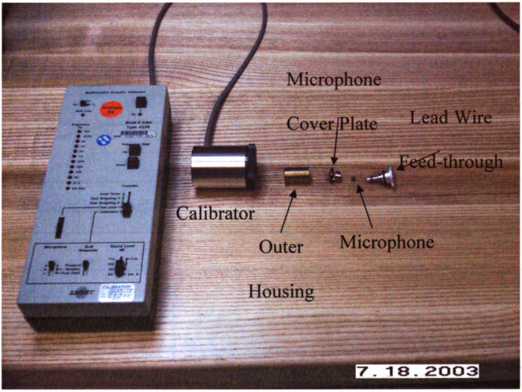

Figure 8.25 Microphone, calibration assembly

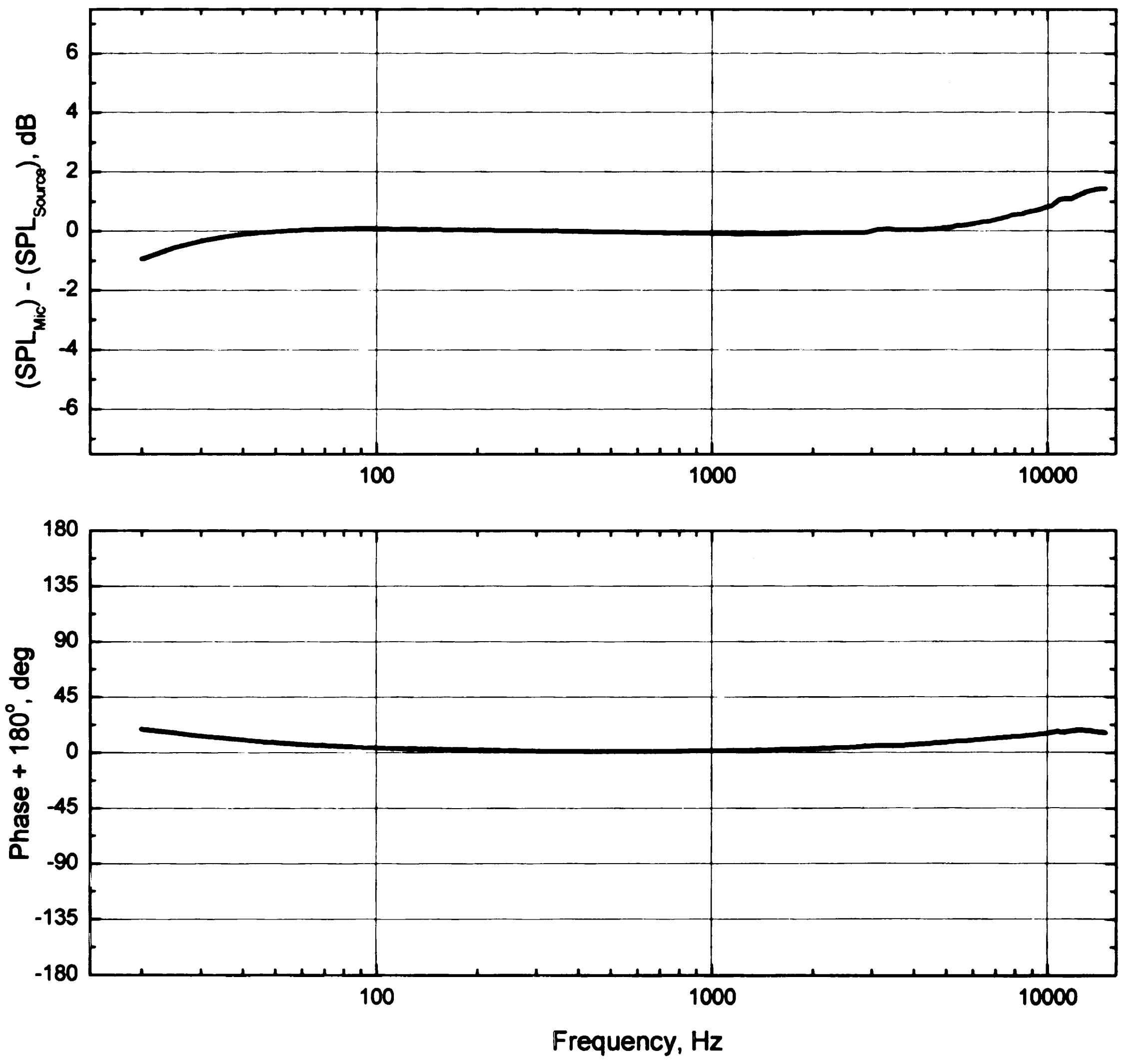

Figure 8.26 Sample of calibration results for the FG-3629 microphone

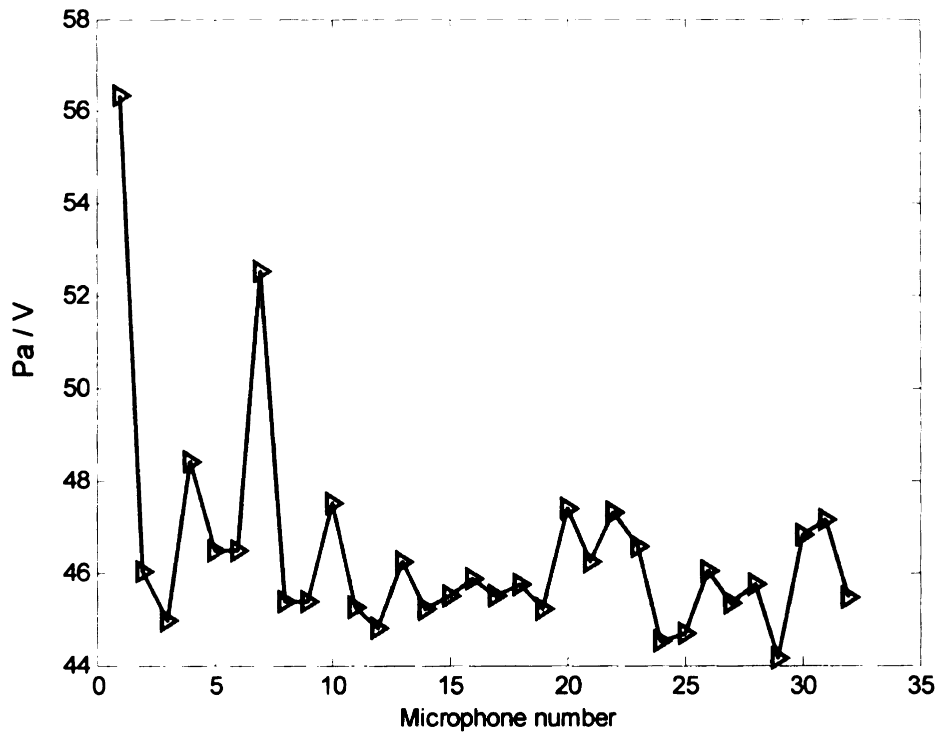

Figure 8.27 Microphone sensitivities from bench calibration

8.4.4 Preliminary tests

Several preliminary tests were completed in effort to establish the proper, microphone, experimental procedure. These tests included cross talk check, laser noise, and mirror interference. Below is a brief description of each test along with the results.

8.4.4.1 Cross talk check

Because of the multi-channel nature of the microphone measurements, the microphones had to be checked for cross talk. Cross talk is defined as the 'leakage' of the signal from one microphone into the neighboring channel of another microphone by electric means (e.g., electromagnetic or capacitive coupling). In order to test for cross talk, the hand-held B&K 4226 multifunction calibrator was used to generate a harmonic sound signal at 250 and 1000 Hz. The signal was fed to a single microphone using the calibrator shown in Figure 8.25. Data were acquired for all 32 channels, and the auto-spectrum of each channel was calculated and used to estimate the relative strength of the cross talk signal at the channels other than where the sound was applied. The acquisition rate per channel used was 6000 kHz. The results showed that the maximum amount of cross talk observed was about 35-40 dB lower than the input signal at 1 kHz. That is, if one channel receives 1 kHz sound signal and the spectrum obtained at this channel was normalized so that the spectral peak at 1 kHz is 0 dB, then the other 31 channels would read no higher than –35-40 dB at 1 kHz. This means that there is almost two orders of magnitude difference between the input signal recorded on a single microphone and leakage recorded by the other microphones. Thus, the cross-talk that may occur is very small and not a concern.

8.4.4.2 Laser Noise

Because microphone and PIV measurements were conducted simultaneously, it was important to check that the laser did not induce a noise signal in the microphone at the laser repetition frequency. Such a signal could be produced by electromagnetic coupling since the laser sheet was immediately above the centerline microphones or by the audible sound heard when the lasers were pulsed. Figure 8.28a, b, and c show the surface-pressure power spectrum obtained at microphones 2, 11, and 26 respectively. Inspection of Figure 8.28a, b, and c clearly shows that the measured surface-pressure auto-spectra contain no peaks at the laser frequency (10 Hz) or its harmonics. Therefore, no special filtering needed to be done for the laser noise.

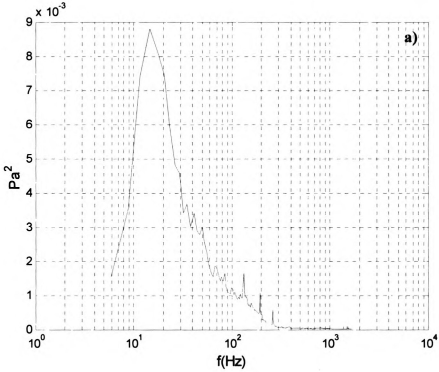
x 10^-3
a)
Pa^2
f(Hz)

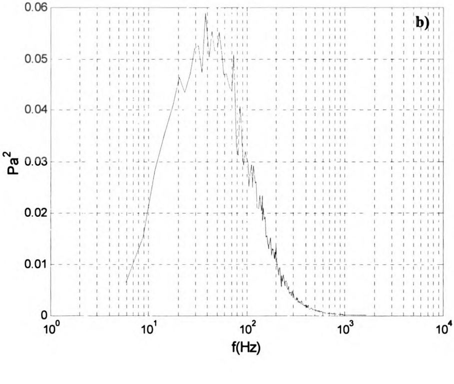
b)
Pa^2
f(Hz)

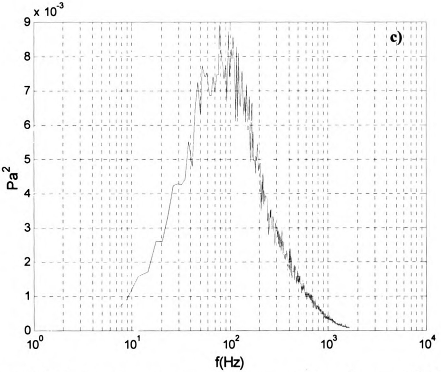

Figure 8.28 Surface-pressure power spectra at microphones: a) 2, b) 11, and c) 26

8.4.4.3 Mirror Interference

As discussed in Section 2.3.3.1, the region of the PIV measurements was illuminated with the laser sheet using a mirror that was mounted to the tail of the model. Figure 8.29 shows a picture of the mounted mirror. Due to the abrupt shape of the mirror and mount, it was desired to check if any disturbances produced by the protruding mirror affected the surface pressure measurements. Additionally, the mean pressure distribution was checked to verify that there was no effect on the mean flow as well. To this end, the microphone as well as the static pressure tap data were checked before and after the mirror was mounted on the model in the tunnel. Figure 8.30 shows the static pressure data for the two conditions for the Re_h = 8081. Although there was a slight increase in the static pressure along the surface when the mirror was placed in the tunnel, there was no change in the characteristics of the flow. In addition, reattachment remained at practically the same position for both conditions.

Figure 8.29 Mirror mounted on tail of model

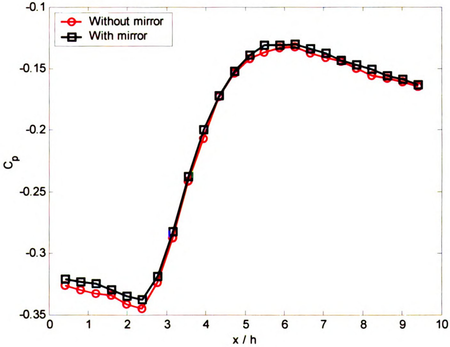

Figure 8.30 Static pressure data with and without mirror in tunnel for the Re_h = 8081

Surface-pressure, spectra data were compared with and without the mirror in the tunnel for the microphone closest to the step and the microphone nearest to reattachment, Figure 8.31a-b respectively. The data shown are for Re_h = 8081. Wall-pressure data were acquired for 60 seconds at a 12 kHz sample rate independent of PIV measurements. As seen from Figure 8.31, there is a small increase in the overall level of pressure fluctuations (corresponding to 12% in the RMS level). Nonetheless, the shape and dominant peaks of the spectra remain unchanged. Only the magnitudes of the peaks increase with the addition of the mirror, which could be due to the fact that the pressure signatures were acquired on different days. The percent change in RMS level between two different days with the mirror installed was 5% over all microphones, suggesting that the microphones may have been affected by such outside factors as relative humidity between the two days. This systematic influence seems to have affected the magnitude and not the frequency content.

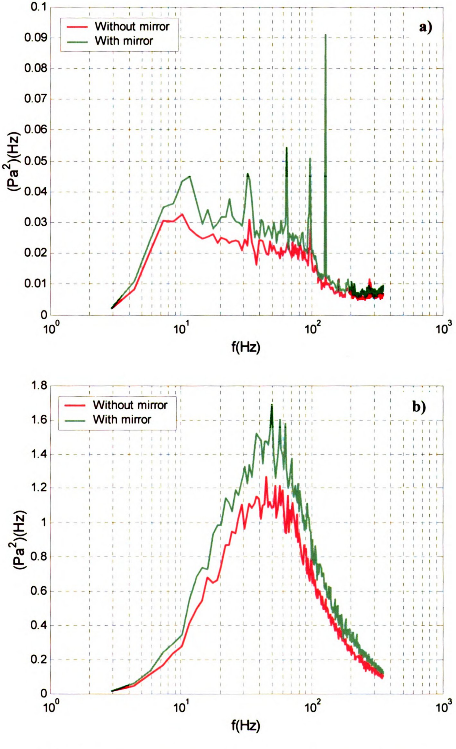

Figure 8.31 Auto spectra of microphone data with and without mirror: a) microphone closest to the step and b) microphone nearest to reattachment

8.5 Additional PIV Information

8.5.1 Dot Card

The dot card, shown in Figure 8.32, was used in the post-processing of the images. The image shown in Figure 8.32 is reversed in the streamwise direction compared to how the results are presented in this paper. All the PIV imaging was done with the flow moving from right to left; however, the results are presented with the flow moving from left to right, which is the typical way to display such results.

The region of interest in the flow stretched about 8.4h downstream of the step and -0.5h upstream of the step. In order to have good resolution in the PIV images, especially in the high shear regions of the separating, boundary layer, the field of view for one camera stretched only 4.5h. Thus, two cameras were needed to capture a large portion of the region of interest. With the two cameras, the flow field captured stretched from roughly -0.5h to 8.4h in the streamwise direction as shown in Figure 8.33.

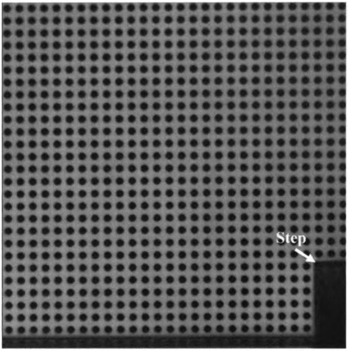

Figure 8.32 Example of dot card image from camera #1

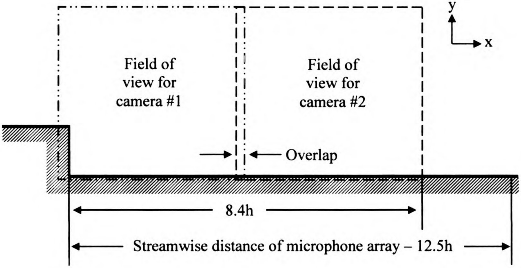

Figure 8.33 Flow regions captured by the two cameras used

Because two cameras were used, the two images needed to be merged in order to show the full region of interest. The images were merged before processing the vector fields. Prior to merging the PIV images, a piecewise, bilinear, dewarping technique was employed to remove perspective and optical distortions. This technique of "straightening" the image was developed for Doppler Global Velocimetry by Meyers[6]. The dewarping technique required dot card images in order to set-up the correct transformation between the old image and the new dewarped image. The images were then merged by removing the pixel columns that overlapped. The number of columns to be removed was determined from the grid card, which is explained in the next section.

8.5.2 Grid card

The grid cards, shown in Figure 8.34, were used in two ways: 1) to determine the number of pixel columns to drop in order to merge the images, and 2) to calibrate the field of view of the cameras in order to determine the physical units per pixel. First, the grid cards were dewarped as described in the previous section. Then overlapping columns were removed from each image and a new matrix describing the image was formed. Figure 8.35 shows an example of a merged, grid-card image. The settings used to remove the columns for the grid card images were used on the PIV images after dewarping and prior to processing the vector fields.

The grid card was also used to calibrate the field of view. The calibration was done on a merged, image grid-card, similar to the one shown in Figure 8.35. To calibrate the field of view, the number of pixels was counted between grid lines. The spacing between each grid line was 10 mm. The number of pixels was divided into 10 mm to determine the calibration constant of mm/pixel. The calibration constant was determined to be 0.0569 mm per pixel.

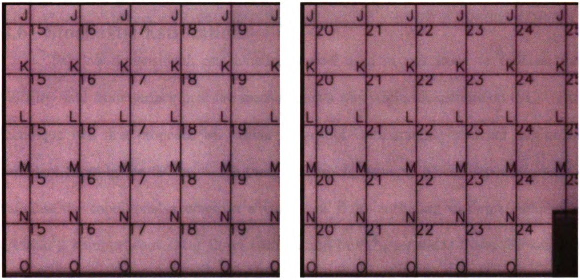

Figure 8.34 Grid cards from cameras 1 and 2 - after dewarping, prior to merging

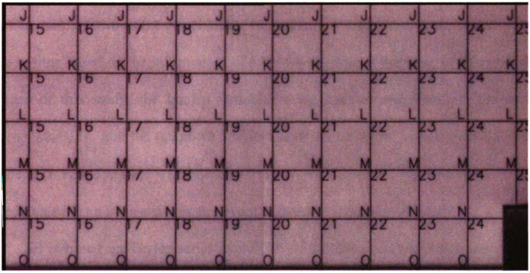

Figure 8.35 Example of merged, grid card from PIV set-up

8.6 Stochastic Estimation

The low-dimensional, mathematical model used in this study to estimate the velocity field from surface pressure measurements was stochastic estimation (SE). The technique was first proposed by Adrian[7] as a tool for extracting coherent motion in turbulent flows in the 1970s. Since then, the low-dimensional model has been used to estimate the conditional average in a variety of flows including isotropic turbulence (Adrian[7]), homogeneous shear flows (Adrian and Moin[8]), separated flows (Stokes and Glauser[9]), and turbulent wall-bounded flows (Adrian *et al.*[10], Guezennec[11], and Naguib *et al.*[12]).

Stochastic estimation is a conditional, averaging technique that uses unconditional statistics, namely two-point correlations, to estimate a variable at a particular point in space or time based on the information of a known variable at the same or other point. In the case of this study, the known variable is the pressure signature on the surface, $p'(x_o,y_o=0,z_o=0,t)$, and the unknown variable is in the turbulent velocity field above the surface, $u'(x_o+\Delta x,\Delta y,t)$ and $v'(x_o+\Delta x,\Delta y,t)$. Thus, the turbulent flow field above the wall was estimated from a known pressure event or events located on the wall.

SE is based on Taylor series expansion of the unknown variable in terms of the known variable:

$$\tilde{u}'(x_o+\Delta x, y_o+\Delta y, t) = A_u(\Delta x, \Delta y; x_o, y_o)p'(x_o, y_o, t) + B_u(\Delta x, \Delta y; x_o, y_o)p'^2(x_o, y_o, t) + O(p'^3) \quad (8.1a)$$

$$\tilde{v}'(x_o+\Delta x, y_o+\Delta y, t) = A_u(\Delta x, \Delta y; x_o, y_o)p'(x_o, y_o, t) + B_u(\Delta x, \Delta y; x_o, y_o)p'^2(x_o, y_o, t) + O(p'^3) \quad (8.1b)$$

where $\widetilde{u}'$ and $\widetilde{v}'$ is the estimated streamwise and normal fluctuating velocity in the flow field, respectively, x_o is the streamwise position of the known variable, Δx is the streamwise distance between the known and unknown variables, y_o is the normal position of the known variable, Δy is the normal distance between the known and unknown variables, t is the instance in time the pressure event occurs, p' is the measured fluctuating pressure on the wall, A_u is the linear estimation coefficient term, and B_u is the quadratic estimation coefficient term. From Equation (1), the estimation coefficient terms can be determined by minimizing the average squared error between the estimated flow field and the measured velocity field at each node in the flow field.

$$E\{e^2\} = < [\widetilde{u}'(x_o + \Delta x, y_o + \Delta y, t) - u'(x_o + \Delta x, y_o + \Delta y, t)]^2 > \quad (8.2a)$$

$$E\{e^2\} = < [\widetilde{v}'(x_o + \Delta x, y_o + \Delta y, t) - v'(x_o + \Delta x, y_o + \Delta y, t)]^2 > \quad (8.2b)$$

where u' is the measured fluctuating velocity component in the flow field, e is the error between the estimated and measured fluctuating velocity components, and E is the expectation or average of the square of the error. Minimization requires setting the derivative of the expectation to zero and solving for the coefficients A_u and B_u, etc.

$$\frac{\partial E\{e^2\}}{\partial A_u} = \frac{\partial E\{e^2\}}{\partial B_u} = \ldots = 0 \quad (8.3a)$$

$$\frac{\partial E\{e^2\}}{\partial A_v} = \frac{\partial E\{e^2\}}{\partial B_v} = \ldots = 0 \quad (8.3b)$$

The number of estimation coefficients to use in the SE of a velocity field was first investigated by Tung and Adrian[13] who looked at higher-order estimates of conditional eddies in isotropic turbulence. The researchers compared first to fourth-order expansions of the SE equation using velocity measurements at one point to estimate the conditional eddies in the flow field. Based on their findings, Tung and Adrian[13] concluded that linear, stochastic estimation (LSE) was the highest order required to satisfactorily describe large-scale features of the two-point conditional eddy field. Guezennec[11] also investigated using linear versus non-linear estimates and found little improvement when using the non-linear estimates to predict the flow field in a turbulent boundary layer. Although the author felt that the quadratic term did convey additional information that would be important when the probability density function (pdf) of the velocity was highly skewed. Guezennec[11] also investigated making time-dependent estimations of the turbulent boundary layer using multiple velocity reference points as proposed by Adrian *et al.*[10] These multi-point, conditional averages were computed in order to force a length scale on the estimated flow field, which allowed the author to focus on structures of a particular length scale in the boundary layer. As a result of the author's findings, Guezennec[11] suggested that using multi-point, conditional estimates coupled with measured velocity time sequences could lead to more "realistic" estimations of the evolution of the instantaneous velocity field. Cole and Glauser[14] reaffirmed the idea of using multi-point SE by investigating utilizing multiple reference velocity points in their estimation of the dominant structures in a jet mixing layer. They presented their results in terms of percentage of energy captured by the multi-point estimates. The authors found that single-point estimates did not adequately estimate the instantaneous flow field and that at least two reference points located on opposite sides of the shear layer did represent the flow field well. Thus, from this discussion, it can be concluded that multi-point, linear, stochastic estimation can satisfactorily estimate the velocity field. However, the estimations in these studies used a velocity point within the flow field to estimate the entire flow field. In the present study, the wall-pressure signature is used to estimate the flow field.

The Naguib *et al.*[12] study was the first that investigated using stochastic estimation to determine the flow structures associated with surface pressure events in a turbulent boundary layer. In their study, they used the pressure signal that was acquired simultaneously with hot-wire measurements to estimate the flow field above the surface. The group concluded that the quadratic term was needed to accurately represent the conditional velocity field and attributed this to the influence of the turbulent-turbulent (non-linear) pressure source term. In the present study, single- and multi-point, linear estimation has been utilized for the estimation of the flow field. In addition, single-point quadratic SE, as suggested by Naguib *et al.*[12], has been computed to assess the sufficiency of the linear estimations in capturing the details of the flow features. Future work includes expanding the single-point QSE to a multi-point estimation.

Thus, linear, stochastic estimation was used to estimate the u' and v' components of the velocity based on the wall-pressure signature according to

$$\tilde{u}'(x_o + \Delta x, y_o + \Delta y, t) = A_u(\Delta x, \Delta y; x_o, y_o) p'(x_o, y_o, t) \tag{8.4a}$$

$$\tilde{v}'(x_o + \Delta x, y_o + \Delta y, t) = A_v(\Delta x, \Delta y; x_o, y_o) p'(x_o, y_o, t) \tag{8.4b}$$

where $\tilde{u}'$ and $\tilde{v}'$ is the estimated fluctuating velocity components, and A_u and A_v are the linear terms for the estimation of u' and v', respectively. Employing Equations 8.2 and 8.3, and after some algebra, A_u and A_v terms are found as shown below

$$\tilde{u}' = \left(\frac{\overline{u'p'}}{p'^{2}_{RMS}} \right) p' \tag{8.5a}$$

$$\tilde{v}' = \left(\frac{\overline{v'p'}}{p'^{2}_{RMS}} \right) p' \tag{8.5b}$$

where, p'_{RMS} is defined as the root-mean-squared of the fluctuating pressure. Both linear coefficients are a function of the cross-correlation between the fluctuating velocity components and the fluctuating pressure on the surface. These two-point correlations are computed at zero time delay between the pressure signature and the flow field; and, therefore, it is necessary to acquire both the pressure and velocity data simultaneously. An important point to recognize is that with stochastic estimation if there is no correlation between the flow field and the pressure signature, the estimation has no significant physical value. The technique provides information about the flow structures that are directly related to the pressure signature. Thus, SE gives a physical interpretation of the dominant the flow structures associated with the pressure generation on the surface.

In addition to single-point, multi-point LSE was used to estimate the velocity field in the present study since a coherent motion, depending on its size and strength, will most likely affect more than just one microphone. The single-point, linear, stochastic-estimation equation given above can easily be extended to the multi-point LSE.

$$\widetilde{u}' = A_{uo}p'(x_o,t) + A_{u1}p'(x_1,t) + A_{u2}p'(x_2,t) + \ldots + A_{un}p'(x_n,t) \quad (8.6a)$$

$$\widetilde{v}' = A_{vo}p'(x_o,t) + A_{v1}p'(x_1,t) + A_{v2}p'(x_2,t) + \ldots + A_{vn}p'(x_n,t) \quad (8.6b)$$

where, A_{u0}-A_{un} and A_{v0}-A_{vn} are the linear estimation coefficients for each pressure point used in the LSE. These are obtained from

$$\begin{bmatrix} A_{u0} \\ A_{u1} \\ A_{u2} \\ \vdots \\ A_{un} \end{bmatrix} = \begin{bmatrix} \overline{p'_0 p'_0} & \overline{p'_0 p'_1} & \overline{p'_0 p'_2} & \cdots & \overline{p'_0 p'_n} \\ \overline{p'_1 p'_0} & \overline{p'_1 p'_1} & \overline{p'_1 p'_2} & \cdots & \overline{p'_1 p'_n} \\ \overline{p'_2 p'_0} & \overline{p'_2 p'_1} & \overline{p'_2 p'_2} & \cdots & \overline{p'_2 p'_n} \\ \vdots & \vdots & \vdots & \ddots & \vdots \\ \overline{p'_n p'_0} & \overline{p'_n p'_1} & \overline{p'_n p'_2} & \cdots & \overline{p'_n p'_n} \end{bmatrix}^{-1} \begin{bmatrix} \overline{u' p'_0} \\ \overline{u' p'_1} \\ \overline{u' p'_2} \\ \vdots \\ \overline{u' p'_n} \end{bmatrix} \quad (8.7a)$$

$$\begin{bmatrix} A_{v0} \\ A_{v1} \\ A_{v2} \\ \vdots \\ A_{vn} \end{bmatrix} = \begin{bmatrix} \overline{p'_0 p'_0} & \overline{p'_0 p'_1} & \overline{p'_0 p'_2} & \cdots & \overline{p'_0 p'_n} \\ \overline{p'_1 p'_0} & \overline{p'_1 p'_1} & \overline{p'_1 p'_2} & \cdots & \overline{p'_1 p'_n} \\ \overline{p'_2 p'_0} & \overline{p'_2 p'_1} & \overline{p'_2 p'_2} & \cdots & \overline{p'_2 p'_n} \\ \vdots & \vdots & \vdots & \ddots & \vdots \\ \overline{p'_n p'_0} & \overline{p'_n p'_1} & \overline{p'_n p'_2} & \cdots & \overline{p'_n p'_n} \end{bmatrix}^{-1} \begin{bmatrix} \overline{v' p'_0} \\ \overline{v' p'_1} \\ \overline{v' p'_2} \\ \vdots \\ \overline{v' p'_n} \end{bmatrix} \quad (8.7b)$$

In general, flow structures will imprint a pressure signature on multiple microphones. Thus, when estimating the flow field above the surface from the wall-pressure field, the multi-point, linear, stochastic estimation uses the pressure signature from an array of two or more microphones as the condition on which to estimate the flow field. The number of microphones to use in the estimate depends on the correlation of the velocity with the pressure field. In some cases a flow structure may affect the pressure seen by five or six microphones only; and, therefore, only those microphones would be needed in the estimation. However, it is difficult to know exactly how many microphones are appropriate for reconstructing the flow field based on the pressure distribution. This problem can be remedied by using a large array of microphones extending beyond the spatial range of interest for the estimation.

Overall, using multi-point LSE can increase the accuracy of the estimate compared to single-point LSE as explained by Cole and Glauser[14]. With the single-point LSE, the flow field is being estimated based on a single condition at one point at the wall. Thus, it is unknown in the estimate how the pressure varies spatially up and downstream of the location of the pressure event at the single, streamwise position. Thus, the spatial pressure pattern associated with the single-point-pressure value is generally random. By using the multi-point, LSE technique, the flow field is estimated based on a particular, spatial-pressure, distribution condition. Thus, the condition for the estimate is stricter; and, therefore, the estimate is more likely not to deviate substantially from the instantaneous flow field (especially for flow fields where the pressure generation is dominated by coherent motion).

Being able to impose a strict, spatial condition for estimating the average, flow field is easier to do using multi-point, stochastic estimation than using conventional, conditional averaging. The difficulty with the conventional technique is the amount of data that must be acquired to ensure being able to obtain a converged average of the flow field based on the spatial pressure condition. With multi-point SE, the same spatial pressure events can be used as the condition, but the average can be found with smaller data sets since all the samples are used in the two-point correlations. This can be advantageous when handling large, two- or three-dimensional data sets as a majority of the calculation only needs to be performed once, regardless of the number of conditions or the complexity of the conditions to be analyzed.

Nonetheless, it is necessary to check the accuracy of the stochastic estimation by comparing the estimated velocity field results with the conditionally averaged flow field since the stochastic estimation should converge to the conditional average. One way to check if the estimation does converge is by performing the conditional average of the flow field. However, as explained previously, this requires a large data set that may not be easy to acquire. Therefore, another method for checking the accuracy of the stochastic estimation is to do both the linear SE and the quadratic SE. If the quadratic SE shows very little deviation from the linear-term estimation, then this provides some measure of confidence that the LSE converged to the conditional average.

Thus, quadratic, stochastic estimation was used to estimate the u' and v' components of the velocity based on the wall-pressure signature according to

$$\tilde{u}'(x_o + \Delta x, y_o + \Delta y, t) = A_{u,quad}(\Delta x, \Delta y; x_o, y_o) p'(x_o, y_o, t) + B_u(\Delta x, \Delta y; x_o, y_o) p'^2(x_o, y_o, t) \qquad (8.8a)$$

$$\tilde{v}'(x_o + \Delta x, y_o + \Delta y, t) = A_{v,quad}(\Delta x, \Delta y; x_o, y_o) p'(x_o, y_o, t) + B_v(\Delta x, \Delta y; x_o, y_o) p'^2(x_o, y_o, t) \qquad (8.8b)$$

where $\tilde{u}'$ and $\tilde{v}'$ is the estimated fluctuating velocity components, and $A_{u,quad}$ and $A_{v,quad}$ are the linear terms and B_u and B_v are the quadratic terms for the estimation of u' and v', respectively. Employing Equations 8.2 and 8.3, and after some algebra, $A_{u,quad}$, $A_{v,quad}$, B_u, and B_v terms are found as shown below

$$A_{u,quad} = \frac{\overline{u'p'} - B_u \overline{p'^3}}{\overline{p'^2}} \tag{8.9a}$$

$$A_{v,quad} = \frac{\overline{v'p'} - B_v \overline{p'^3}}{\overline{p'^2}} \tag{8.9b}$$

$$B_u = \frac{\overline{p'^2}\left(\overline{u'p'^2}\right) - \overline{p'^3}\left(\overline{u'p'}\right)}{\left(\overline{p'^4}\right)\left(\overline{p'^2}\right) - \left(\overline{p'^3}\right)^2} \tag{8.10a}$$

$$B_v = \frac{\overline{p'^2}\left(\overline{v'p'^2}\right) - \overline{p'^3}\left(\overline{v'p'}\right)}{\left(\overline{p'^4}\right)\left(\overline{p'^2}\right) - \left(\overline{p'^3}\right)^2} \tag{8.10b}$$

Both quadratic coefficients are a function of the cross-correlation between the fluctuating, velocity components and the fluctuating pressure on the surface similar to the linear coefficients. In addition, however, the quadratic coefficients are also a function of the cross-correlation between the fluctuating, velocity components and the square of the fluctuating pressure on the surface. More information regarding QSE is provided by Naguib *et al.*[12] and Daoud[15].

Another advantage of SE that is pertinent to the present study is the ability to compare the estimated flow field to the instantaneous measurements. Particle Image Velocimetry (PIV) was used to acquire the velocity field above the surface. Details about the technique are described in Section 2.3.3. PIV allows for acquisition of the velocity over the "entire" flow field instantaneously. This enables a comparison between the estimated flow field at a particular time instant and the instantaneous flow field acquired at the same instance in time.

Finally, one other powerful tool that comes out of using stochastic estimation is that the evolution of the estimated, flow structure can be time-resolved even if the flow field was not sampled at a rate that is fast enough to resolve the frequency of the dominant structures in the flow. With current PIV capability, it is difficult to sample the velocity information at a fast enough rate to time-resolve the dominant structures in air flows. By using stochastic estimation, flow features can be time-resolved because the estimation is based on the pressure signature, which can be sampled at a fast enough rate to resolve the coherent motions. This has the advantage of not only being able to examine the time evolution of the flow structures, *but also* to focus attention on the organized motion that is *directly* linked to the wall-pressure generation. In other words, even if one is able to resolve the flow-field temporally, instantaneous, flow fields are likely to contain influences of random, small-scale turbulence and other details that may obscure the nature of the flow organization as well as the motions that are relevant to the wall-pressure generation.

8.7 Shear Strain

Angular distortion or deformation results in a change in the shape of a fluid element and is referred to as shear strain. Shear strain is used to describe the local angular distortion of fluid particles and is calculated from the velocity field. For this study, velocity measurements were acquired in the x-y coordinate plane, and therefore only the in-plane (ξ_{xy}), out-of-plane (ξ_{zz}), and linear (ξ_{xx} and ξ_{yy}) strain components can be calculated. These components are given by

$$\xi_{xy} = \frac{1}{2}\left(\frac{\partial u}{\partial y} + \frac{\partial v}{\partial x}\right) \tag{8.11}$$

$$\xi_{zz} = -\frac{1}{2}\left(\frac{\partial u}{\partial x} + \frac{\partial v}{\partial y}\right) \tag{8.12}$$

$$\xi_{xx} = \frac{\partial u}{\partial x} \tag{8.13}$$

$$\xi_{yy} = \frac{\partial v}{\partial y} \tag{8.14}$$

where, ξ_{xy} is the in-plane, shear-strain component, ξ_{zz} is the out-of-plane, shear-strain component or the normal strain, and ξ_{xx} and ξ_{yy} are the linear strain rates in the streamwise and normal directions respectively. From equations (8.11) and (8.12), it is clear that large shear strain is associated with regions containing large velocity gradients, meaning regions of high shear. Therefore, the shear strain distribution would be valuable in highlighting the flow within the separated, shear layer. In the case of this study, only the in-plane component is calculated.

As with the vorticity, the shear strain downstream of the axisymmetric BFS was calculated using the PIV data. An integral method was used to calculate vorticity as highlighted in Section 5.2.4. A related method[16] is used for determining shear strain from the velocity gradients in the flow field PIV data. The shear-strain estimate is calculated based on eight neighboring points as shown in Figure 8.36.

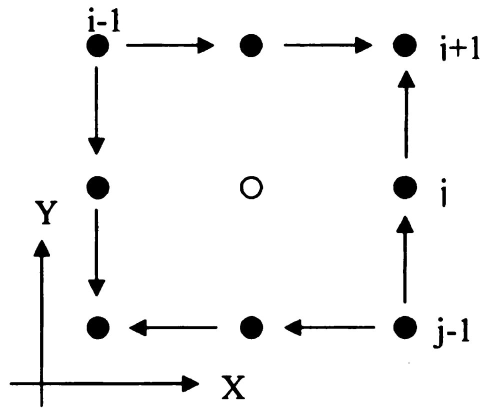

Figure 8.36 Path of integration used to calculate the shear strain at point (i, j). Copied from Raffel *et al.*[16]

The equations used to calculate the shear strain from the PIV data are from Raffel *et al.*[16] and are given below.

$$\xi_{xy} = \left(\frac{\partial U}{\partial Y} + \frac{\partial V}{\partial X}\right)_{i,j} = -\frac{(U_{i-1,j-1} + 2U_{i,j-1} + U_{i+1,j-1})}{8\Delta Y} + \frac{(U_{i+1,j+1} + 2U_{i,j+1} + U_{i-1,j+1})}{8\Delta Y} - \frac{(V_{i-1,j+1} + 2V_{i-1,j} + V_{i-1,j-1})}{8\Delta X} + \frac{(V_{i+1,j-1} + 2V_{i+1,j} + V_{i+1,j+1})}{8\Delta X} \tag{8.15}$$

8.8 Appendix References

[1] Howerton, B. M., "Development of a passive horseshoe vortex control device as applied to semi-span wind tunnel testing," Masters thesis. North Carolina State University, 1998.

[2] Driver, D. M. and Johnston, J. P., "Experimental study of a three-dimensional shear-driven turbulent boundary layer with streamwise adverse pressure gradient," NASA Technical Memorandum #102211, May 1990.

[3] Hudy, L.M., "Simultaneous wall-pressure array and PIV measurements in a separating/reattaching flow region," Masters thesis, Michigan State University, 2001.

[4] Eaton, J. K. and Johnston, J.P., "A Review of Research on Subsonic Turbulent Flow Reattachment," *AIAA Journal*, Vol. 19, No. 9, 1981, pp. 1093-1099.
[5]Farabee, T.M., and Casarella, M.J., "Measurements of fluctuating wall pressure for separated/reattached boundary layer flows," *Journal of Vibration, Acoustics, Stress, and Reliability in Design*, Vol. 108, 1986, 301-307.

[6] Meyers, J.F., "Doppler Global Velocimetry – The Next Generation?," *AIAA Paper 92-3897*, 1992.

[7] Adrian, R.J., "Conditional eddies in isotropic turbulence," *Physics of Fluids*, Vol. 22, 1979, pp. 2065-2070.

[8] Adrian, R.J. and Moin, P., 'Stochastic estimation of organized turbulent structure: homogeneous shear flow," *Journal of Fluid Mechanics*, Vol. 190, 1988, pp. 531-559.

[9] Stokes, S. and Glauser M., "Multi-point measurement techniques used in the study of separated flows," *30th AIAA Fluid Dynamics Conference*, AIAA 99-3518, Norfolk, VA, June 28 – July 1, 1999.

[10] Adrian, R.J., Moin, P., and Moser, R.D., "Stochastic estimation of conditional eddies in channel flow," Report CTR-S87, Center for Turbulence Research, NASA Ames/Stanford, 1987.

[11] Guezennec, Y.G., "Stochastic Estimation of coherent structures in turbulent boundary layers," *Physics of Fluids A*, Vol. 1, 1989, pp. 1054-1060.

[12] Naguib, A.M., Wark, C.E., and Juckenhöfel, O., "Stochastic estimation and flow sources associated with surface pressure events in a turbulent boundary layer," *Physics of Fluids*, Vol. 13, No. 9, 2001, pp. 2611-2626.

[13] Tung, T.C. and Adrian, R.J., "Higher-order estimates of conditional eddies in isotropic turbulence," *Physics of Fluids*, Vol. 23, No. 7, 1980, pp. 1469-1470.

[14] Cole, D.R. and Glauser, M.N., "Applications of stochastic estimation in the axisymmetric sudden expansion," *Physics of Fluids*, Vol. 10, No. 11, 1998, pp. 2941-2949.

[15] Daoud, M.I., "Stochastic Estimation of the flow structure downstream of a separating/reattaching flow region using wall-pressure array measurements," Ph.D. Dissertation, Michigan State University, 2004.

[16] Raffel, M., Willert, C., and Kompenhans, J., *Particle Image Velocimetry: A Practical Guide*, 3rd ed., Springer-Velag, Berlin, 1998, pp. 160-163.